



UNIVERSIDADE FEDERAL DO CEARÁ

CENTRO DE CIÊNCIAS

DEPARTAMENTO DE QUÍMICA ANALÍTICA E FÍSICO-QUÍMICA

PROGRAMA DE PÓS-GRADUAÇÃO EM QUÍMICA

RAFAEL MELO FREIRE

**MAGNETIC NANOPARTICLES AND CARBON QUANTUM DOTS:
INTERDISCIPLINARY NANOPARTICLES FOR SENSING AND/OR EDUCATION**

FORTALEZA

2016

RAFAEL MELO FREIRE

MAGNETIC NANOPARTICLES AND CARBON QUANTUM DOTS:
INTERDISCIPLINARY NANOPARTICLES FOR SENSING AND/OR EDUCATION

Doctoral thesis submitted to the Programa de Pós-graduação em Química of the Universidade Federal do Ceará as a requirement for the degree of doctor of chemistry. Area: Inorganic Chemistry

Advisor: Prof. Dr. Pierre Basílio Almeida Fachine

FORTALEZA
2016

Dados Internacionais de Catalogação na Publicação
Universidade Federal do Ceará
Biblioteca Universitária

Gerada automaticamente pelo módulo Catalog, mediante os dados fornecidos pelo(a) autor(a)

F935m Freire, Rafael Melo.

Magnetic nanoparticles and carbon quantum dots: interdisciplinary nanoparticles for sensing and/or education / Rafael Melo Freire. – 2016.
180 f. : il. color.

Tese (doutorado) – Universidade Federal do Ceará, Centro de Ciências, Programa de Pós-Graduação em Química, Fortaleza, 2016.

Orientação: Prof. Dr. Pierre Basílio Almeida Fechine.

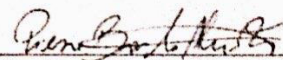
1. Mixed ferrites. 2. Carbon quantum dots. 3. Identification . 4. Protein. I. Título.

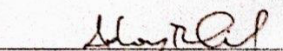
CDD 540


Esta Tese foi apresentada como parte dos requisitos necessários à obtenção do Grau de Doutor em Química, área de concentração Química, outorgado pela Universidade Federal do Ceará, e em cuja Biblioteca Central encontra-se à disposição dos interessados.


Rafael Melo Freire


Tese aprovada em: 21/10/2016.


Dr. Pierre Basilio Almeida Fechine
(Orientador-UFC)


Dr. Adonay Rodrigues Loiola
(UFC)


Dr. Amauri de Paula Jardim
(UFC)


Dra. Gisele Simone Lopes
(UFC)


Dr. Pedro de Lima Neto
(UFC)

Dedication

I dedicate this work to my wife and daughter, Maria Socorro Gonçalves da Costa and Ana Maria Gonçalves Freire, my parents, Jonivaldo Freire de Souza e Maria Rosario Melo, my brother, Tiago Melo Freire, and my dear friends who have helped me to become the professional I am today.

ACKNOWLEDGMENTS

Firstly, I would like to thank God for all opportunities in my personal and professional ways. I am very thankful for each one I have passed through, which also includes the unsuccessful ones. Since I was able to learn and become a better man and professional. Secondly, my family was really important. The constant support, as well as the unconditional love were the most important features to make me move forward. My wife, Maria Socorro Gonçalves da Costa, and my daughter, Ana Maria Gonçalves Freire, are the fuel to make me get up in the morning, the fuel that makes me want to be a better person and researcher. My father, Jonivaldo Freire de Souza, the person who always is there to provide the support I need. My brother, Tiago Melo Freire, for the support as well, but the valorous friendship too. I cannot forget his fiancé, Jessica Miranda Abreu, who also support me when I need.

From the Universidade Federal do Ceará, I would like to express my sincerest gratitude to my advisor and one of my best friends, Pierre Basílio Almeida Fechine. No doubt, his patient to guide me in the way to obtain the master and doctor degree was essential to make me the researcher I am today. Furthermore, I should say be the one of the Pierre's students for 6 years was extremely pleasant. All our conversation, as well as his advices to me when I needed were so valuables. I am quite sure I would be a different person today if I was not one of the Pierre's students. Other professors of the chemistry course were also important. In special, I would like to thank the Professors Antoninho Valentini and Elisane Longhinotti for their support and advices. I could not forget my advisor from University of Massachusetts – Amherst, MA, United States, Vince M. Rotello, who changed my vision about the research. Upon my period in his laboratory, I am a better researcher for sure.

From Grupo de Química de Materiais Avançados (GQMat), I have got dear friends for all my life and I am so grateful for this. Therefore, my warm thanks to Antônio César Honorato Barreto, Davino Machado Andrade Neto, Elayne Valerio Carvalho, Janaína Sobreira Rocha, Natália Dantas Gomes de Souza, Denis Valony Martins Paiva, Wesley dos Santos Galvão, Eduardo José Juca Mallmann, Victor Moreira da Costa, Anderson Valério Chaves, Manuela Chaves Loureiro Cândido, Antonio Alvernes Carneiro Cruz, Fernando Lima de Menezes, Jessica Sales Barbosa, Suderlan Freire de Moraes, Ticiane Alencar Magalhães, Leandro Torres Rodrigues, Valdirene Oliveira da Costa and Rafael Andrade Sampaio. Each one of them has contributed a lot to make

me the person and researcher I am today. I would like also to thank all my friends outside GQMat. Maybe, having so many good people around me be the key to make the life less stressful, the key to make the life much more enjoyable.

I would like to thank the Universidade Federal do Ceará itself. I am very grateful for the opportunity to learn chemistry. Furthermore, the Universidade Federal do Ceará was the place I met my wife for the first time. For this, I have no words to express my feelings given the huge impact in my life. I could not forget to be thankful for the structural and financial support to keep my research always on. In this sense, I also thank Coordenação de Aperfeiçoamento de Pessoal de Nível Superior (CAPES) and Conselho Nacional de Desenvolvimento Científico e Tecnológico (CNPq) for the fellowships provided during 6 years, which makes possible the dream to be a doctor.

Finally, once again I thank my family for all unconditional support and love, but I would like to make a special acknowledgement to my mother, Maria do Rosario Melo. She is not with me anymore in Earth since 2013. However, I am quite sure she is very proud of me for what I have been done in my life, but I must be grateful to have her example in my life. All her life work was valuable for my professional career.

RESUMO

Neste trabalho, uma estratégia para detecção e identificação de proteínas incluindo nanopartículas magnéticas (MNPs) e pontos quânticos de carbono (CQDs) foi desenvolvida. Assim, ferritas mistas de fórmula $M_{0.5}Zn_{0.5}Fe_2O_4$ (M=Mn or Ni) foram inicialmente investigadas. Neste sentido, suas sínteses foram feitas utilizando diferentes condições (solvente, tempo reacional e concentração de base). Logo, baseado nas propriedades magnéticas das MNPs sintetizadas, escolheu-se a $Mn_{0.5}Zn_{0.5}Fe_2O_4$ (MnZn) sintetizada em água por mostrar grande potencial, uma vez que essa amostra apresentou alto valor de magnetização de saturação ($M_s \cong 50$ emu/g) em comparação com outras ferritas de composição semelhante, baixo tamanho de cristalito por volta de 12 nm e comportamento superparamagnético. Com a primeira parte do trabalho concluída, a próxima etapa foi encontrar uma sonda fluorescente. Assim, realizou-se a síntese dos CQDs funcionalizados com grupamentos amina (CQDs.BPEI). Quando testada contra 8 diferentes proteínas (4 metálicas e 4 não-metálicas), apresentou variação da emissão para concentrações na faixa de 5 – 40 nM. Titulações fluorescentes também foram realizadas e observou-se que a supressão da fluorescência ocorre via mecanismo colisional a partir de resíduos aminoácidos na superfície da proteína. Para adicionalmente checar o potencial dos CQDs.BPEI, foi desenvolvida abordagem para identificar proteínas utilizando materiais Cu^{2+} e o ácido etilenodiamino tetraacético. No total, a estratégia desenvolvida foi capaz de identificar corretamente 6 diferentes proteínas a 40 nM. A precisão da identificação encontrada foi 90% para as amostras desconhecidas. Contudo, vale ressaltar que os 10% de engano foram apenas entre BSA e HSA, duas proteínas albumínicas muito similares. Os resultados obtidos nessa parte do trabalho evidenciam o alto potencial de CQDs.BPEI para detecção e identificação de proteínas. Observando os resultados do trabalho como um todo, pode-se afirmar que MnZn e CQDs.BPEI são capazes de compor excelente abordagem para detecção e identificação de proteínas. Adicionalmente, foi explorada a utilidade dos CQDs para o campo educacional. Dessa forma, foi também desenvolvido e aplicado (mais de 70 estudantes de graduação oriundos dos cursos de biotecnologia, farmácia, engenharias e geologia) um experimento de laboratório para demonstrar fenômenos quânticos relacionados com a luz.

Palavras-chave: Ferritas mistas. Pontos quânticos de carbono. Identificação. Proteína.

ABSTRACT

In this work, a sensing strategy for detection and identification of proteins with magnetic nanoparticles (MNPs) and carbon quantum dots (CQDs) was developed. In this sense, mixed ferrites of general formula $M_{0.5}Zn_{0.5}Fe_2O_4$ (M=Mn or Ni) were first investigated. Therefore, the hydro/solvothermal synthesis of these magnetic nanoparticles was performed under different conditions (solvent, reaction time and base concentration). Based on the magnetic properties of the two MNPs investigated, the mixed ferrite of formula $Mn_{0.5}Zn_{0.5}Fe_2O_4$ (MnZn) synthesized using water showed the greatest potential for sensing. Since among all synthesized MNPs, this sample displayed the highest saturation magnetization value ($M_s \cong 50$ emu/g), lower crystallite size around 12 nm and superparamagnetic behavior. Once the first part of the doctoral thesis was concluded, the next step was to find a fluorescence probe. In this regard, it was performed the synthesis, as well as the application of branched polyethylenimine-functionalized carbon quantum dots (CQDs.BPEI). These new carbon-based nanoparticles were found to be protein-responsive. Since CQDs.BPEI were able to detect eight different proteins (four metallic and four non-metallic) even using concentrations in the range of 5 – 40 nM. Fluorescence titrations performed at 298 and 310 K displayed the fluorescence quenching through collisional mechanism. Therefore, it was also possible to conclude that the fluorescence quench comes from the amino acid residues on the surface of the proteins. To further check the potential of the CQDs.BPEI, it was developed a “nose” based methodology to identify proteins. Using materials as cheap as Cu^{2+} and ethylenediaminetetraacetic acid, the chemical “nose” approach was able to discriminate six different proteins at 40 nM concentration in phosphate buffered saline (PBS, pH 7.4). The identification accuracy of the random unknown set was 90% with all misclassification occurring for albumin proteins (e.g., Bovine Serum Albumin and Human Serum Albumin). The displayed results evidence the great potential of CQDs.BPEI as a protein-responsive probe to detect and identify proteins. Taken together, MnZn and CQDs.BPEI were capable to build up a powerful protein sensing approach. In addition, realizing the great potential of CQDs in the educational field, it was also developed and successfully applied (for more than 70 students from from biotechnology, pharmacy, engineers and geology courses) a lab experiment to demonstrate light-related quantum phenomena.

Keywords: Mixed ferrites. Carbon quantum dots. Identification. Protein

LIST OF FIGURES

Figure 1.1. Applications of MNPs in different technological fields	17
Figure 1.2. Schematic illustration of luminescence modulation via Förster resonance energy transfer (FRET) within the context of pattern recognition based on competitive binding between indicator and anionic analyte on the surface of the lanthanide (Ln^{3+})-doped NPs	21
Figure 1.3. Illustration presenting CQDs properties, as well as potential research fields	22
Figure 2.1. XRD for samples of the system $(\text{H}_2\text{O})_{1-x}:(\text{EG})_x$, where x denotes the amount of the EG used to compose the solvent. The corresponding x values are reported in each diffractogram. The black dots reveal the experimental data, while the red line denotes the calculated data. The green line displays the difference between experimental and calculated data.....	37
Figure 2.2. Particle size describe in function of the x values, which denotes the amount of the EG used to compose the solvent.....	38
Figure 2.3. Results of the stabilization test for different precursors metallic used in the synthesis. On the left side of each series of tests the relative metalis reported. The x values for the system $(\text{H}_2\text{O})_{1-x}:(\text{EG})_x$ are presented only in the case of Zn series, but can be straightforwardly expanded for Mn and Fe	40
Figure 2.4. IR spectra of the tests realized with different x in the system $((\text{H}_2\text{O})_{1-x}:(\text{EG})_x)$ for metallic precursors	41
Figure 2.5. FTIR for samples of the system $(\text{H}_2\text{O})_{1-x}:(\text{EG})_x$, where x denotes the amount of the EG used to compose the solvent. The corresponding x values are reported in each spectrum.....	42
Figure 2.6. K values for tetrahedral (K_T) and octahedral (K_O) site plotted as a function of x	44
Figure 2.7. Mössbauer spectra (left) and quadrupole (Δ) distribution (right) for samples of the system $(\text{H}_2\text{O})_{1-x}:(\text{EG})_x$, where x denotes the amount of the EG used to compose the solvent. The corresponding x values are reported beside spectrum.....	46

Figure 2.8. Magnetic measurements for samples of the system $(\text{H}_2\text{O})_{1-x}:(\text{EG})_x$. Inset reports M_s plotted as a function of the x	48
Figure 2.9. Zero field cooled-field cooled curves of samples with $x = 0, 0.4$ and 1.0 ...	49
Figure 2.10. TEM micrographs for samples of the system $(\text{H}_2\text{O})_{1-x}:(\text{EG})_x$, where x denotes the amount of the EG used to compose the solvent. The corresponding x values are reported in the image.....	51
Figure 3.1. PXRD patterns for samples MNP1 – 7 as well as the fit made using the Rietveld Method	65
Figure 3.2. FT-IR for samples MNP1 – 7	69
Figure 3.3. Mössbauer spectrum for MNP3 – 7	71
Figure 3.4. Size distribution graph for MNP3 – 7. The black solid line denotes the distribution curve made using a normal distribution to fit the data	74
Figure 3.5. High magnification TEM images for samples MNP3 – 7.....	76
Figure 3.6. Magnetization curves at 300 and 5K for MNP3 – 7	78
Figure 3.7. ZFC/FC measurements for MNP3 – 7	82
Figure 4.1. TEM image of CQDs.BPEI. Inset: distribution size graph based on the measurements of 150 particles randomly chosen	95
Figure 4.2. Surface properties of CQDs.BPEI. (a) FT-IR spectrum of CQDs.BPEI. XPS analysis (c) Survey scan, (d) C1s analysis and (e) N1s analysis	96
Figure 4.3. Optical properties of CQDs.BPEI. (a) UV/Vis absorption spectra of CQDs.BPEI. (b) The excitation-wavelength independent fluorescence spectra of CQDs.BPEI. (c) Fluorescence intensity as function of pH values and (d) Photobleaching experiment: fluorescence intensity recorded during 60 min at room temperature	97
Figure 4.4. Fluorescence response of the CQDs.BPEI upon addition of protein at 40 nM (concentration in the well)	99
Figure 4.5. Fluorescence titration performed at 298 and 310K for non-metallic (a) and metallic (b) proteins	101
Figure 5.1. Normalized fluorescence intensity of the CQDs.BPEI ($2 \mu\text{g}\cdot\text{mL}^{-1}$) against $250 \mu\text{M}$ of several metal ions in PB 5 mM (pH 7.4)	123
Figure 5.2. Fluorescence titration performed at 298 K for Cu^{2+}	124

Figure 5.3. Schematic picture illustrating the two-plate “nose”-based strategy developed in this work. I and II denote two different 96-well plates. As it can be seen, the plate I was used to obtain the first discrimination event. The second and third interactional events were obtained in the plate II	125
Figure 5.4. Detection of metallic proteins in PB 5 mM (pH 7.4). (left) Fluorescence response pattern of the proteins evaluated. Each value of average as well as standard deviation was calculated based on 6 replicates. (right) Canonical score plot for the fluorescence patterns as obtained from LDA clustering process	127
Figure 5.5. Detection of non-metallic proteins in PB 5 mM (pH 7.4). (left) Fluorescence response pattern of the proteins evaluated. Each value of average as well as standard deviation was calculated based on 6 replicates. (right) Canonical score plot for the fluorescence patterns as obtained from LDA clustering process	129
Figure 5.6. LDA plots for metallic proteins using the concentration as a parameter to be classified	130
Figure 5.7. Canonical score plots for non-metallic proteins using the concentration as a parameter to be classified	131
Figure 5.8. Canonical score plots classifying eight proteins at different concentrations (10, 20 and 40 nM)	133
Figure 5.9. Schematic picture illustrating the one-plate “nose”-based strategy developed in this work	134
Figure 5.10. Detection of eight different proteins in PB 5 mM (pH 7.4). (a) Fluorescence response pattern of the proteins evaluated. Each value of average as well as standard deviation was calculated based on 6 replicates. (b) Canonical score plot for the fluorescence patterns as obtained from LDA utilizing the two most significant factors	135
Figure 5.11. Detection of eight different proteins in PBS. (a) Fluorescence response pattern of the proteins evaluated. Each value of average as well as standard deviation was calculated based on 6 replicates. (b) Canonical score plot for the fluorescence patterns as obtained from LDA utilizing the two most significant factors	137

Figure 5.12. (a) Fluorescence titration performed at 298 K using different human serum concentrations. Fluorescence response pattern obtained spiking the proteins tested in 0.1 (b), 0.5 (c) and 1% (V/V) (d) human serum concentrations. Each value of average as well as standard deviation was calculated based on 6 replicates	138
Figure 5.13. Optimization of the conditions for the one-plate methodology in 1% (V/V) human serum. (a) Improvement of the amount of CQDs.BPEI and (b) Cu ²⁺ fluorescence titration performed at 298 K	139
Figure 5.14. Detection of eight different proteins spiked in human serum 1% (V/V) using the optimized conditions. (a) Fluorescence response pattern acquired for the proteins tested. Each value of average as well as standard deviation was calculated based on 6 replicates. (b) Canonical score plot for the fluorescence patterns as obtained from LDA utilizing the two most significant factors	140
Figure 6.1. Course of time for the lab experiment proposed in this work. The experiment was divided into three blocks. The first block takes 40 min, while the second and third 25 min each. This is also represented by orange, green and blue colors, respectively. The words inside the circles are the point what was done in each block ...	153
Figure 6.2. Schematic illustration of the thermal decomposition process to obtain CQDs. The pictures (a) and (b) displays citric acid inside 10 mL glass vial before and after the thermal process, respectively. The gray, blue and white balls denote the elements carbon, oxygen and hydrogen, respectively	155
Figure 6.3. Demonstration of quantum phenomenon related to the emission and scattering of the light. (a) Front side view of the light scattering result of the red Laser going through the dispersion colloidal containing the CQDs synthesized. (b) Spontaneous blue emission of the dispersion colloidal while is illuminated from down side using the 3 in 1 Laser light pointer. (c) Both spontaneous emission and light scattering of the red Laser. In this case, the 3 in 1 pointer was positioned at the left side of the recipient	156
Figure 6.4. UV-Vis absorption spectrum recorded at room temperature. The illustration inside the graph denotes the irradiation of CQDs presenting –OH and –COOH groups on the surface, as well as the sp ² domains in the core	158

Figure 6.5. (a) TEM micrograph of the synthesized CQDs. (b) Distribution size graph built using over 90 NPs randomly selected 160

Figure 6.6. Schematic illustration representing the basic mechanism to describe photoluminescence. Once the absorption process (a) does not present spontaneous emission, the excitation of the electron (e-) is colorless. By contrast, blue light can be seen as a result of the de-excitation process, i.e. emission process (b) 161

Figure 6.7. Normalized fluorescence intensity of the as-synthesized CQDs recorded at room temperature from 350 to 600 nm using different excitations wavelengths (315 – 405 nm) 162

LIST OF TABLES

Table 2.1. x values and label of the samples obtained in this work	34
Table 2.2. Values of x , ν_T , ν_O , K_o and K_T for all samples synthesized	44
Table 2.3. Hyperfine parameter for samples synthesized in this work	47
Table 3.1. Label for all the samples as well as the used conditions (NaOH concentration and time)	63
Table 3.2. Values of average crystallite size (D), microstrain (ϵ), network parameter, Rwp and S for the samples that showed spinel phase	67
Table 3.3. Mössbauer parameters for MNP3 – 7 samples	72
Table 4.1. Values of K_Q , n , ΔG , ΔH and ΔS found for non-metallic proteins	104
Table 4.2. Values of K_Q , n , ΔG , ΔH and ΔS found for metallic proteins	107
Table 4.3. Values of M_w of the analyte proteins targeted	109

TABLE OF CONTENTS

1 INTRODUCTION AND OBJECTIVES	16
1.1 Introduction	16
1.1.1 Magnetic Nanoparticles	16
1.1.2 Carbon Quantum Dots	18
1.2 Objectives.....	23
1.2.1 General	23
1.2.2 Specifics	23
1.2.2.1 Magnetic Nanoparticles	23
1.2.2.2 Carbon Quantum Dots	23
References	24
2 EFFECT OF SOLVENT COMPOSITION ON THE STRUCTURAL AND MAGNETIC PROPERTIES OF MnZn FERRITE NANOPARTICLES OBTAINED BY HYDROTHERMAL SYNTHESIS	31
Abstract	31
2.1 Introduction	32
2.2 Experimental	33
2.2.1 Materials and Methods	33
2.2.2 Synthesis of MnZnFe ₂ O ₄ nanoparticles	33
2.2.3 Stabilization of the metallic precursors from EG	34
2.2.4 Characterization of the MNPs	35
2.3 Results and discussion	35
2.3.1 X-ray powder diffraction (PXRD)	35
2.3.2 Stability of metallic chlorides with EG	38
2.3.3 Infrared Spectroscopy	41
2.3.4 ⁵⁷ Fe Mössbauer Spectroscopy	45
2.3.5 Magnetic Measurements	47
2.3.6 Transmission Electron Microscopy (TEM)	49
2.4 Conclusion	52
References	52

3. MORPHOLOGIC AND MAGNETIC PROPERTIES OF SUPERPARAMAGNETIC NiZn FERRITES OBTAINED BY HYDROTHERMAL ROUTE	60
Abstract	60
3.1 Introduction	61
3.2 Experimental	62
3.2.1 Material and methods	62
3.2.2 Synthesis of NiZnFe ₂ O ₄ MNPs	62
3.2.3 Characterization of nanoparticles	63
3.3 Results and discussion	64
3.3.1 PXRD	64
3.3.2 FTIR measurements	67
3.3.3 ⁵⁷ Fe Mössbauer Spectroscopy	70
3.3.4 TEM	73
3.3.5 Magnetic measurements	76
3.4 Conclusion	84
References	84
4. NH₂-RICH CARBON QUANTUM DOTS: A POWERFUL PROTEIN-RESPONSIVE PROBE	90
Abstract	90
4.1 Introduction	91
4.2 Materials and Methods	92
4.2.1 Materials	92
4.2.2 Synthesis of CQDs.BPEI	92
4.2.3 Characterization of CQDs.BPEI.....	93
4.2.4 Detection Experiments	93
4.3 Results and Discussion	94
4.3.1 CQDs Characterization	94
4.3.2 Detection of proteins using CQDs.BPEI	98
4.4 Conclusions	110
References	111

5. DEVELOPMENT OF “NOSE”-BASED STRATEGY TO IDENTIFY PROTEINS USING NH₂-RICH CQDs	117
Abstract	117
5.1 Introduction	118
5.2 Materials and Methods	119
5.2.1 Materials	119
5.2.2 Sensing Experiments	120
5.3 Results and Discussion	122
5.3.1 Chemical nose/tongue approach	122
5.4 Conclusion	140
References	141
6. CARBON QUANTUM DOTS: A SAFE TOOL TO LEARN ABOUT QUANTUM PHENOMENON IN NANOMATERIALS	146
Abstract	146
6.1 Background	147
6.2 Overview	148
6.3 Experimental Design	149
6.3.1 Chemical and Materials required	149
6.3.2 Procedure	149
6.3.3 Safety	150
6.4 Results	151
6.4.1 Synthesis of CQDs	151
6.4.2 Tyndall Effect and Emission	152
6.4.3 Absorption Spectra	154
6.5 Discussion	157
6.6 Conclusion	160
6.7 Supporting data	161
6.7.1 Student Version	161
6.7.2 Instructor Version	165
References	170
7. GENERAL CONCLUSIONS	177

CHAPTER 1

1 INTRODUCTION AND OBJECTIVES

1.1 Introduction

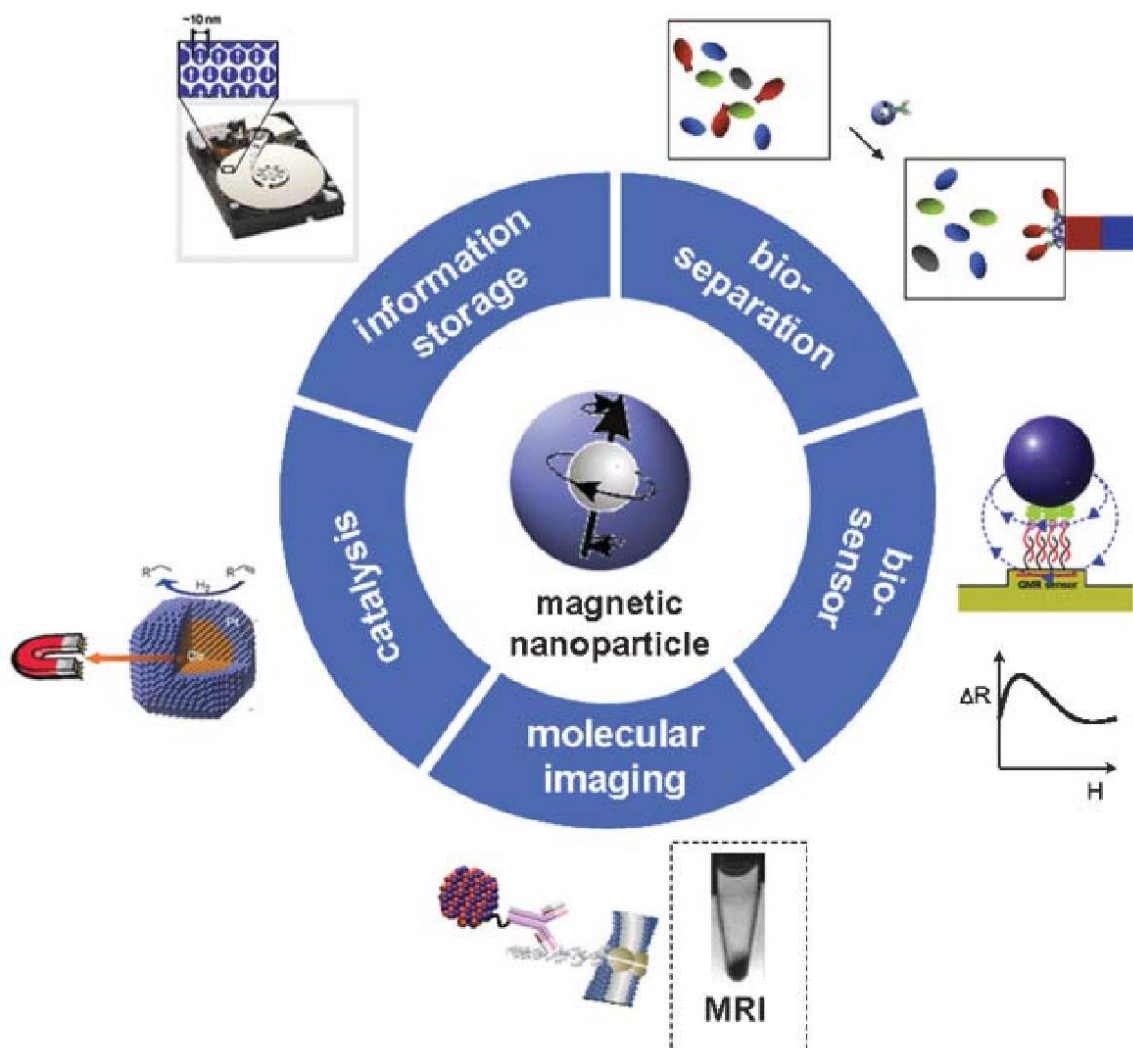
According to the U.S. The National Nanotechnology Initiative, nanotechnology can be understood as the ability to manipulate matter in the range of approximately 1 – 100 nm in order to create materials, devices, as well as systems having essentially new properties and functions because of their small structure (Roco, 2011). In the last years, the integration between nanotechnology and different areas of knowledge such as chemistry, physics, and biology have generated new research fields. For instance, it can be mentioned the nanomedicine area, which offers opportunities to discover new materials, processes and phenomena aiming biomedical field (Gao *et al.*, 2009). The same is also true for every research field. In this sense, the development of materials in the nanoscale range (1 – 100 nm) is essential. However, the manipulation of the matter at this level is not an easy task, i.e. precise control of the atom in order to create a desired nanostructure is extremely difficult. Given the exposed, researchers worldwide have developed several approaches to synthesize mostly inorganic nanoparticles (NPs) having different magnetic, optical and structural properties (Rao *et al.*, 2012). Therefore, it can be produced inorganic NPs such magnetic nanoparticles (MNPs), silica, gold or silver NPs, quantum dots, among others. Although, MNPs have gained much attention in recent years. The possibility to control the transport of the studied system by using a magnetic external field is a great advantage over other NPs

1.1.1 Magnetic Nanoparticles

MNPs have been investigated over decades. Their magnetic and structural properties have attracted many researchers worldwide. As consequence, iron-based MNPs can be synthesized through different methods including co-precipitation (Barreto, A. C. H. *et al.*, 2013), thermal decomposition (Herrera *et al.*, 2013), microwave (Galvão *et al.*, 2014), hydrothermal (Freire *et al.*, 2013), micro-emulsion (Ali *et al.*, 2014), sol-gel (Lemine *et al.*, 2014), among others. As it can be seen, great efforts have been driven toward the selective control of the matter at atom level. Therefore, it is important to recognize advances in the area of the synthetic approaches, but there is still a demand for methodologies to obtain nanostructures of controlled shape and size. Furthermore, it is important to mention MNPs have a wide range of applications such as drug

delivery (Barreto, A. *et al.*, 2013), hyperthermia (Jeun *et al.*, 2014), (bio)sensor (Min and Wenzhong, 2013) and others. Fig. 1.1 displays the general applications of the MNPs.

Figure 1.1. Applications of MNPs in different technological fields. Reproduced from Jun and co-authors with permission of The Royal Chemistry Society.



Source: (Jun *et al.*, 2007)

Although the large applicability, MNPs have gained much attention when used in sensing or biosensing systems. First, the low cost of production is an excellent attractive and the surface properties of the MNPs can be tailored in order to modulate the interaction between NPs and analytes (Latham and Williams, 2008; Reddy *et al.*, 2012). Beyond these advantages, still offer improvements like enhanced sensitivity, low limit of detection, high signal-to-noise ratio, and

shorter time of analysis when compared to strategies based on just NPs (Justino *et al.*, 2013). However, it is important to highlight these improvements can only be achieved by tuning the characteristics of the MNPs. For instance, in order to obtain the best performance, the MNPs must present the superparamagnetic behavior because this makes the response faster even applying low magnetic fields (Netto *et al.*, 2013). Therefore, this additionally support the demand for new protocols to synthesize desired MNPs having adequate morphology and size.

In sensing field, MNPs are usually found integrated with transducer materials (Rocha-Santos, 2014). Thus, the target analyte can be detected through different mechanism involving electrochemical (Li *et al.*, 2010; Yang *et al.*, 2014; Yola *et al.*, 2014), optical (Zamfir *et al.*, 2011; Wang, J. *et al.*, 2013; Agrawal *et al.*, 2014) and piezoelectric (Wan *et al.*, 2010; Zhou *et al.*, 2013). Nevertheless, it is important to highlight there is also a possibility to use the MNPs itself as a probe as well-demonstrated in the literature (Perez *et al.*, 2004; Hao *et al.*, 2010; McNally, 2013). When integrated with a transducer, MNPs can be in the aqueous phase playing the carrier to lead the analyte onto the transducing surface by application of an external magnetic field. Once the surface properties of the MNPs can be easily tuned in order to provide selective interaction with the analyte, this approach is vastly used. Furthermore, magnetite (Fe_3O_4) is, by far, the most used nanostructure as well. This can be explained based on high values found for saturation magnetization (around 60 emu/g (Barreto, A. *et al.*, 2013)) of the magnetically ordered crystalline phase. In addition, the superparamagnetism, an essential requirement for high-performance MNPs in sensing field, is also achieved (Demir *et al.*, 2013). However, it is well-known that Fe_3O_4 is easily oxidized under air, which causes changes in the crystalline phase and consequent loss of the magnetic properties. Since is thermodynamically unstable with respect to hematite ($\alpha\text{-Fe}_2\text{O}_3$) in the presence of oxygen (Tang *et al.*, 2003). Therefore, oxidation resistance MNPs having great saturation magnetization (~ 60 emu/g) needs to be investigated. In this sense, it is important to highlight the MNPs of general formula $\text{M}_{0.5}\text{Zn}_{0.5}\text{Fe}_2\text{O}_4$, where M can be manganese (Mn) or nickel (Ni) due their excellent magnetic properties (Freire *et al.*, 2013), which demonstrates the potential of these kind of nanomaterials in sensing field.

1.1.2 Carbon Quantum Dots

As it can be observed, MNPs are frequently used as a capture probe for the target analyte. Thus, the transducer materials, as well as the detection mechanism play a key role in the detection

approach. In this regard, it is worth to mention the probes based on optical properties. Since the optical methods are simple, fast, sensitive, cost-effective and easily implemented into a high-throughput screening (You *et al.*, 2015). For example, fluorescence spectroscopy, interferometry, reflectance, light scattering and refractive index are some examples of optical devices to be used as a sensor. Among them, fluorescence measurements have to be emphasized given the context of this work, and because the analytical signal related to the fluorescence intensity can be enhanced using a capture probe like MNPs (Rocha-Santos, 2014).

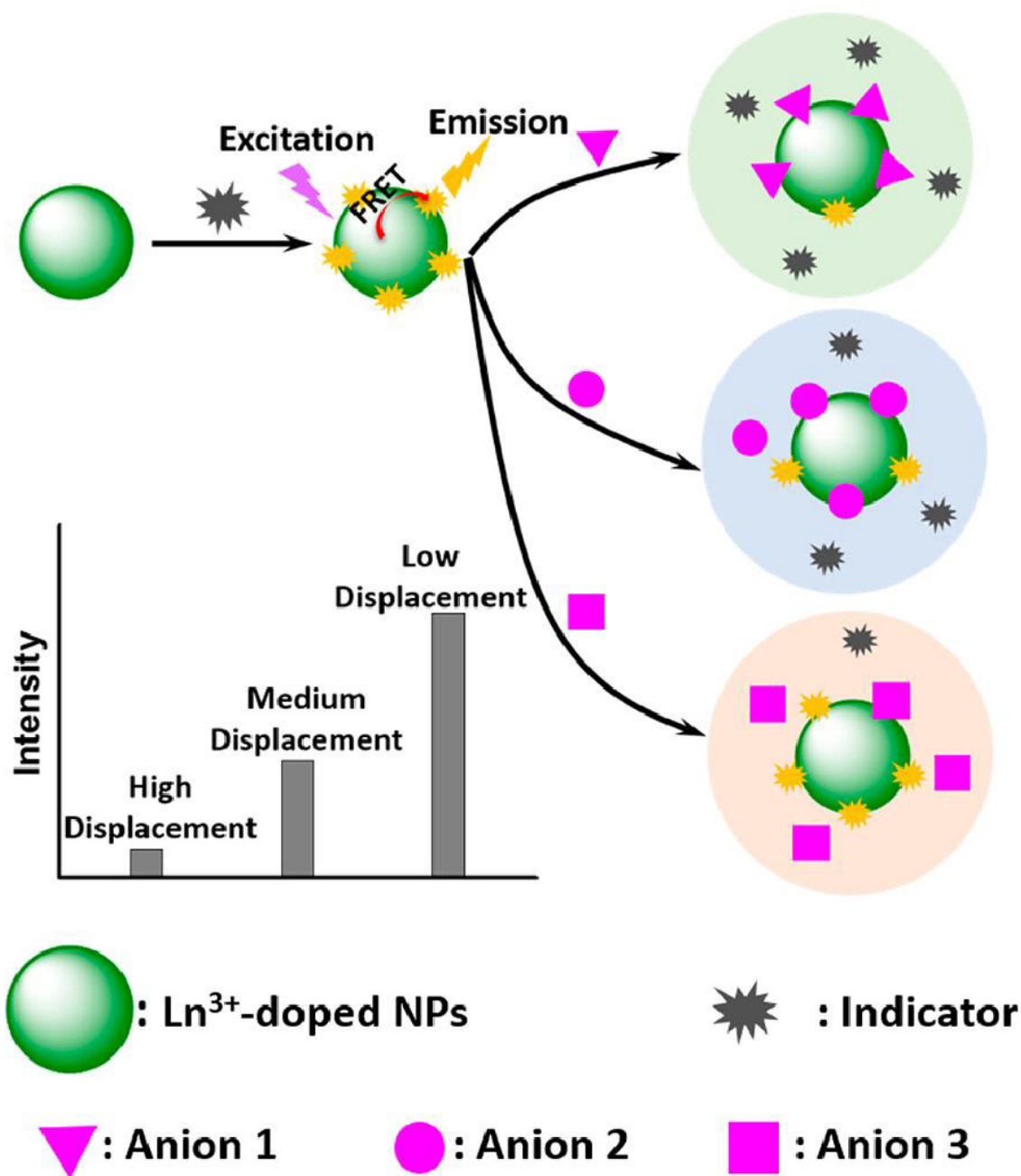
The literature reports several fluorescence probes including inorganic and organic NPs. For inorganic NPs, the semiconductor quantum dots (QDs) have been extensively investigated for optical sensing (Freeman and Willner, 2012). This can be explained based on their unique photophysical properties, versatile surface chemistry and ligand binding ability (Lou *et al.*, 2014). Furthermore, this kind of NPs presents large versatility once the literature reports the possibility of integration in different materials keeping their native luminescence property (Zhao *et al.*, 2014; Yang *et al.*, 2015; Deng *et al.*, 2016). Taken together, QDs seems to be a perfect optical probe, but their composition containing heavy metals such cadmium (Cd) and selenium (Se), for example, is an important drawback. Heavy metals, even at low levels, are well-known to cause some severe problems to the human health. Cardiovascular diseases, cancer mortality, damage to liver, kidneys, and central nervous system, neurological, reproductive are some of them (Hussein *et al.*, 2005; Vázquez-González and Carrillo-Carrion, 2014). Therefore, there is still a growing interest in developing a safe and cheap fluorescent probe for optical sensing. In this context, organic NPs named carbon quantum dots (CQDs) deserve to be highlighted.

In the last years, CQDs have gained much attention due to its good biocompatibility, non-toxicity, resistance to the photobleaching and optical properties (Wang and Hu, 2014). These features place this new carbon-based nanomaterial, accidentally discovered in 2004 (Xu *et al.*, 2004), as a promising candidate to replace the traditional fluorescent materials like the already mentioned QDs. The literature have reported CQDs as a fluorescent probe for many analytes including metal ions (Wang *et al.*, 2014; Guo *et al.*, 2015), which includes heavy metals (Zhang and Chen, 2014; Cui *et al.*, 2015), up to biomolecules (Li *et al.*, 2011; Amjadi *et al.*, 2015; Cai *et al.*, 2015). Specifically, CQDs have showed great potential for protein detection, mostly hemoglobin (Wang, Y. *et al.*, 2013; Barati *et al.*, 2015; Huang *et al.*, 2015; Singh Rana *et al.*, 2016). Once the level of proteins

in the human body are related to the various diseases such as cancer (Madu and Lu, 2010), this is an excellent fact. Although, the number of publications is still low and the real potential of the CQDs as a fluorescent probe targeting protein is still unknown. Therefore, new researches need to be conducted in order to fill this gap of the knowledge.

Moreover, beyond detection, a good probe should also provide identification as well-demonstrated by Vince M. Rotello et al. using fluorescent polymers (Miranda *et al.*, 2007; Bajaj, Miranda, *et al.*, 2010), green-fluorescent protein (Bajaj, Rana, *et al.*, 2010), as well as a chemical “nose” approach (You *et al.*, 2007). Therefore, the sensing strategy involving CQDs should detect and identify the analyte. From the mentioned literature (Barati *et al.*, 2015), the authors have already demonstrated that proteins can directly interact to the CQDs surface generating a fluorescence intensity change. In order to move forward, the sensing strategy should provide the protein identification. Considering the differential sensing approach, which was used by Rotello et al., the challenge is the signal engineering to obtain a distinct fluorescence intensity for each protein. However, it is important to remember more than 20,000 can be found in the Human Serum (De *et al.*, 2009). Given the huge number, the attempt to get a direct and, at the same time, differential sensing seems difficult. To solve this problem, it was developed an differential sensing approach based on the chemistry of the mammalian nose and tongue (Lavigne and Anslyn, 2001). Rather than selectively sensing an analyte, the molecular recognition is found through multiples responses, which generates a characteristic and unique pattern. In this sense, the direct sensing can be applied to obtain one response and the other ones may be obtained using the so-called indicator displacement assay (IDA) (Nguyen and Anslyn, 2006). This entity generates new signals based on competitive binding between IDA and analyte. Fig. 1.2 displays a schematic illustration to clarify how competitive binding can generate new signals to sensitive detection of glyphosate and proteins (Wang *et al.*, 2016).

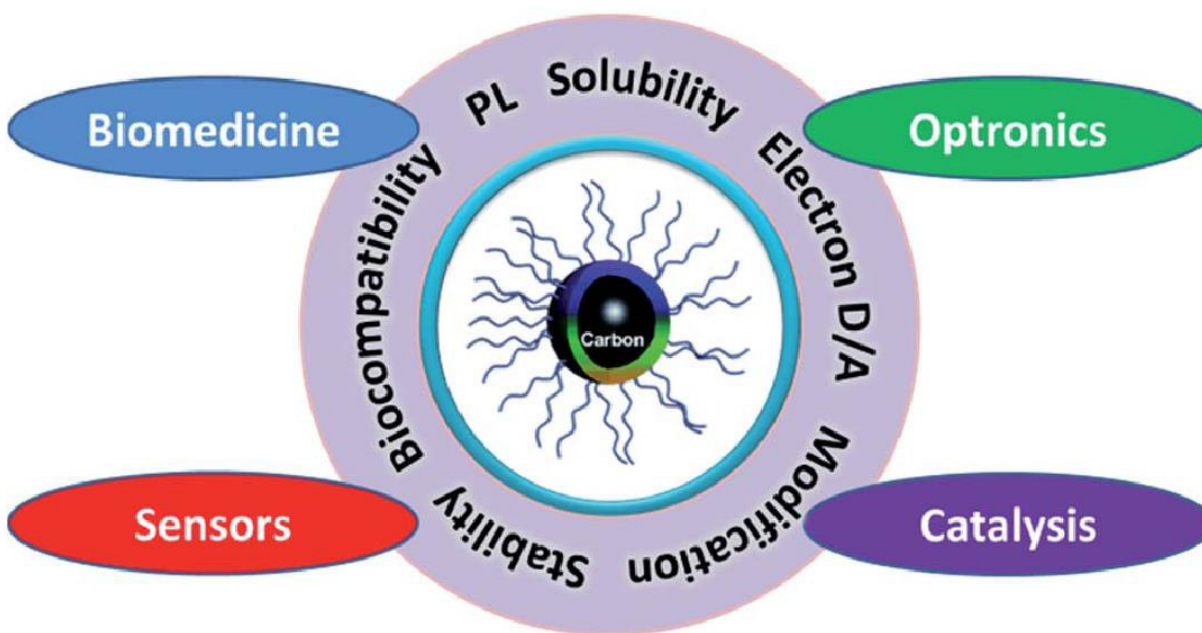
Figure 1.2. Schematic illustration of luminescence modulation via Förster resonance energy transfer (FRET) within the context of pattern recognition based on competitive binding between indicator and anionic analyte on the surface of the lanthanide (Ln^{3+})-doped NPs. Reprinted with permission from Wang and co-authors. Copyright 2016 American Chemical Society



Source: (Wang *et al.*, 2016)

As it can be seen in the Fig. 1.2, the Ln^{3+} -doped NPs were first bound with the indicator. Subsequently, the binding equilibrium is perturbed by adding the analytes represented by triangle (anion 1), circle (anion 2) and square (anion 3). This would lead for a displacement of the indicator. Once the interaction involving each one of the analytes and the system Ln^{3+} -doped NPs is unique, the fluorescence intensity should be found to generate a characteristic signal. Using this concept and by changing the indicator, different signals can be generated for each analyte and their combination would give rise a pattern recognition. Therefore, fluorescent fingerprints related to the analyte could be created, which makes possible to perform the identification utilizing chemometrics tools (Anzenbacher *et al.*, 2010). From the top of our knowledge, a few papers involving CQDs for differential sensing can be found in the literature (Tao *et al.*, 2014). Therefore, this is a gap in the sensing field ready to be explored.

Figure 1.3. Illustration presenting CQDs properties, as well as potential research fields. Reproduced from Wang and Hu with permission of The Royal Chemistry Society.



Source: (Wang and Hu, 2014)

By having such properties, CQDs are expected to have huge applicability. In this regard, Fig. 1.3 shows the properties and some potential research fields based on the publications up to today. Thus, it is important to highlight the utilization of CQDs for biomedicine, sensors, optronics and

catalysis according to the reviews published by Wang et al. (Wang and Hu, 2014). In another review published in the famous journal named Chemical Society Reviews (Impact factor equal to 34.09/2016) by Lim et al. (Lim *et al.*, 2015), the cited research fields were chemical sensing, biosensing, bioimaging, nanomedicine, photocatalysis and electrocatalysis. As expected, CQDs can be applied in many fields. However, the utilization of the CQDs in the educational field must also be considered. For instance, QDs were already used to demonstrate quantum phenomena (light absorption and emission) for undergraduate students (Landry *et al.*, 2014). Therefore, the educational field is an open door to explore it.

1.2 Objectives

1.2.1 General

- To explore the properties of the mixed ferrites of general formula $M_{0.5}Zn_{0.5}Fe_2O_4$ (M=Mn or Ni) and/or carbon quantum dots in order to develop a chemical “nose/tongue” approach for detection and identification of proteins, as well as to develop a safe laboratory experiment to demonstrate quantum phenomena for undergraduate students

1.2.2 Specifics

1.2.2.1 Magnetic Nanoparticles

- To synthesize MNPs of general formula $M_{0.5}Zn_{0.5}Fe_2O_4$ (M=Mn or Ni) under different experimental conditions
- To investigate the structural and magnetic properties of the synthesized MNPs by using powder X-ray diffraction (PXRD), Fourier transform infrared spectroscopy (FT-IR), Mössbauer spectroscopy, vibrating sample magnetometer (VSM) and transmission electron microscopy (TEM)
- To evaluate the effect of experimental conditions on the MNPs characteristics
- To choose the MNPs with highest potential based on structural and magnetic properties.
- To find the optimal condition to synthesize the MNPs in order to obtain a high potential nanomaterial to compound a chemical “nose” approach to detect and identify proteins.

1.2.2.2 Carbon Quantum Dots

- To synthesize NH_2 -rich carbon quantum dots

- To investigate the structural, morphological, surface and optical properties of the synthesized CQDs through X-ray photoelectron spectroscopy (XPS), Fourier transform infrared spectroscopy (FTIR), Transmission electron microscopy (TEM) and absorbance/fluorescence measurements
- To check the potential of the synthesized CQDs as a protein-responsive platform
- To develop a “nose”-based approach to identify the analyte proteins
- To evaluate the potential of the developed “nose”-based approach by testing unknown and serum samples
- To evaluate the utilization of CQDs in the educational field by developing a safe laboratory experiment to demonstrate quantum phenomena

References

- AGRAWAL, S.; PAKNIKAR, K.; BODAS, D. Development of immunosensor using magnetic nanoparticles and circular microchannels in PDMS. **Microelectronic Engineering**, Place Published, v. 115, p. 66-69, 2014. ISSN 0167-9317. Disponível em: < <http://www.sciencedirect.com/science/article/pii/S0167931713006503> >.
- ALI, R. et al. Impacts of Ni–Co substitution on the structural, magnetic and dielectric properties of magnesium nano-ferrites fabricated by micro-emulsion method. **Journal of Alloys and Compounds**, Place Published, v. 584, p. 363-368, 2014. ISSN 0925-8388. Disponível em: < <http://www.sciencedirect.com/science/article/pii/S0925838813019907> >.
- AMJADI, M.; ABOLGHASEMI-FAKHRI, Z.; HALLAJ, T. Carbon dots-silver nanoparticles fluorescence resonance energy transfer system as a novel turn-on fluorescent probe for selective determination of cysteine. **Journal of Photochemistry and Photobiology A: Chemistry**, Place Published, v. 309, p. 8-14, 2015. ISSN 1010-6030. Disponível em: < <http://www.sciencedirect.com/science/article/pii/S1010603015001434> >.
- ANZENBACHER, J. P. et al. A practical approach to optical cross-reactive sensor arrays. **Chemical Society Reviews**, Place Published, v. 39, n. 10, p. 3954-3979, 2010. ISSN 0306-0012. Disponível em: < <http://dx.doi.org/10.1039/B926220M> >.
- BAJAJ, A. et al. Array-Based Sensing of Normal, Cancerous, and Metastatic Cells Using Conjugated Fluorescent Polymers. **Journal of the American Chemical Society**, Place Published, v. 132, n. 3, p. 1018-1022, 2010/01/27 2010. ISSN 0002-7863. Disponível em: < <http://dx.doi.org/10.1021/ja9061272> >.
- BAJAJ, A. et al. Cell surface-based differentiation of cell types and cancer states using a gold nanoparticle-GFP based sensing array. **Chemical Science**, Place Published, v. 1, n. 1, p. 134-138, 2010. ISSN 2041-6520. Disponível em: < <http://dx.doi.org/10.1039/C0SC00165A> >.
- BARATI, A.; SHAMSIPUR, M.; ABDOLLAHI, H. Hemoglobin detection using carbon dots as a fluorescence probe. **Biosensors and Bioelectronics**, Place Published, v. 71, p. 470-475, 2015. ISSN 0956-5663. Disponível em: < <http://www.sciencedirect.com/science/article/pii/S0956566315300749> >.
- BARRETO, A. et al. Magnetic Nanosystem for Cancer Therapy Using Oncocalyxone A, an Antitumour Secondary Metabolite Isolated from a Brazilian Plant. **International Journal of Molecular Sciences**, Place Published, v. 14, n. 9, p. 18269-18283, 2013. ISSN 1422-0067. Disponível em: < <http://www.mdpi.com/1422-0067/14/9/18269> >.
- BARRETO, A. C. H. et al. Grain Size Control of the Magnetic Nanoparticles by Solid State Route Modification. **Journal of Materials Engineering and Performance**, Place Published, v. 22, n. 7, p. 2073-2079, 2013. Disponível em: < <http://dx.doi.org/10.1007/s11665-013-0480-8> >.

CAI, Q.-Y. et al. A rapid fluorescence “switch-on” assay for glutathione detection by using carbon dots–MnO₂ nanocomposites. **Biosensors and Bioelectronics**, Place Published, v. 72, p. 31-36, 2015. ISSN 0956-5663. Disponível em: < <http://www.sciencedirect.com/science/article/pii/S0956566315300774> >.

CUI, X. et al. A fluorescent biosensor based on carbon dots-labeled oligodeoxyribonucleotide and graphene oxide for mercury (II) detection. **Biosensors and Bioelectronics**, Place Published, v. 63, p. 506-512, 2015. ISSN 0956-5663. Disponível em: < <http://www.sciencedirect.com/science/article/pii/S0956566314005880> >.

DE, M. et al. Sensing of proteins in human serum using conjugates of nanoparticles and green fluorescent protein. **Nat Chem**, Place Published, v. 1, n. 6, p. 461-465, 2009. ISSN 1755-4330. Disponível em: < <http://dx.doi.org/10.1038/nchem.334> >.

DEMIR, A.; TOPKAYA, R.; BAYKAL, A. Green synthesis of superparamagnetic Fe₃O₄ nanoparticles with maltose: Its magnetic investigation. **Polyhedron**, Place Published, v. 65, p. 282-287, 2013. ISSN 0277-5387. Disponível em: < <http://www.sciencedirect.com/science/article/pii/S0277538713006049> >.

DENG, J. et al. Enhanced H₂S gas sensing properties of undoped ZnO nanocrystalline films from QDs by low-temperature processing. **Sensors and Actuators B: Chemical**, Place Published, v. 224, p. 153-158, 2016. ISSN 0925-4005. Disponível em: < <http://www.sciencedirect.com/science/article/pii/S0925400515304883> >.

FREEMAN, R.; WILLNER, I. Optical molecular sensing with semiconductor quantum dots (QDs). **Chemical Society Reviews**, Place Published, v. 41, n. 10, p. 4067-4085, 2012. ISSN 0306-0012. Disponível em: < <http://dx.doi.org/10.1039/C2CS15357B> >.

FREIRE, R. M. et al. MZnFe₂O₄ (M = Ni, Mn) cubic superparamagnetic nanoparticles obtained by hydrothermal synthesis. **Journal of Nanoparticle Research C7 - 1616**, Place Published, v. 15, n. 5, p. 1-12, 2013. Disponível em: < <http://dx.doi.org/10.1007/s11051-013-1616-3> >.

GALVÃO, W. S. et al. Cubic superparamagnetic nanoparticles of NiFe₂O₄ via fast microwave heating. **Journal of Nanoparticle Research**, Place Published, v. 16, n. 12, p. 1-10, 2014// 2014. ISSN 1572-896X. Disponível em: < <http://dx.doi.org/10.1007/s11051-014-2803-6> >.

GAO, J.; GU, H.; XU, B. Multifunctional Magnetic Nanoparticles: Design, Synthesis, and Biomedical Applications. **Accounts of Chemical Research**, Place Published, v. 42, n. 8, p. 1097-1107, 2009/08/18 2009. ISSN 0001-4842. Disponível em: < <http://dx.doi.org/10.1021/ar9000026> >.

GUO, Y. et al. Fluorescent carbon nanoparticles for the fluorescent detection of metal ions. **Biosensors and Bioelectronics**, Place Published, v. 63, p. 61-71, 2015. ISSN 0956-5663. Disponível em: < <http://www.sciencedirect.com/science/article/pii/S0956566314005107> >.

HAO, L. et al. Magnetic nanoparticle detection using nano-SQUID sensors. **Journal of Physics D: Applied Physics**, Place Published, v. 43, n. 47, p. 474004, 2010. ISSN 0022-3727. Disponível em: < <http://stacks.iop.org/0022-3727/43/i=47/a=474004> >.

HERRERA, A. P. et al. Influence of aging time of oleate precursor on the magnetic relaxation of cobalt ferrite nanoparticles synthesized by the thermal decomposition method. **Journal of Magnetism and Magnetic Materials**, Place Published, v. 328, p. 41-52, 2013. ISSN 0304-8853. Disponível em: < <http://www.sciencedirect.com/science/article/pii/S0304885312008207> >.

HUANG, S. et al. A carbon dots based fluorescent probe for selective and sensitive detection of hemoglobin. **Sensors and Actuators B: Chemical**, Place Published, v. 221, p. 1215-1222, 2015. ISSN 0925-4005. Disponível em: < <http://www.sciencedirect.com/science/article/pii/S0925400515301568> >.

HUSSEIN, H. et al. Tolerance and uptake of heavy metals by Pseudomonads. **Process Biochemistry**, Place Published, v. 40, n. 2, p. 955-961, 2005. ISSN 1359-5113. Disponível em: < <http://www.sciencedirect.com/science/article/pii/S0032959204001517> >.

JEUN, M. et al. Tailoring Mg_xMn_{1-x}Fe₂O₄ Superparamagnetic Nanoferrites for Magnetic Fluid Hyperthermia Applications. **ACS Applied Materials & Interfaces**, Place Published, v. 6, n. 19, p. 16487-16492, 2014/10/08 2014. ISSN 1944-8244. Disponível em: < <http://dx.doi.org/10.1021/am5057163> >.

JUN, Y.-W.; CHOI, J.-S.; CHEON, J. Heterostructured magnetic nanoparticles: their versatility and high performance capabilities. **Chemical Communications**, Place Published, n. 12, p. 1203-1214, 2007. ISSN 1359-7345. Disponível em: < <http://dx.doi.org/10.1039/B614735F> >.

JUSTINO, C. I. L. et al. Strategies for enhancing the analytical performance of nanomaterial-based sensors. **TRAC Trends in Analytical Chemistry**, Place Published, v. 47, p. 27-36, 2013. ISSN 0165-9936. Disponível em: < <http://www.sciencedirect.com/science/article/pii/S0165993613000678> >.

LANDRY, M. L. et al. Simple Syntheses of CdSe Quantum Dots. **Journal of Chemical Education**, Place Published, v. 91, n. 2, p. 274-279, 2014/02/11 2014. ISSN 0021-9584. Disponível em: < <http://dx.doi.org/10.1021/ed300568e> >.

LATHAM, A. H.; WILLIAMS, M. E. Controlling Transport and Chemical Functionality of Magnetic Nanoparticles. **Accounts of Chemical Research**, Place Published, v. 41, n. 3, p. 411-420, 2008/03/01 2008. ISSN 0001-4842. Disponível em: < <http://dx.doi.org/10.1021/ar700183b> >.

LAVIGNE, J. J.; ANSLYN, E. V. Sensing A Paradigm Shift in the Field of Molecular Recognition: From Selective to Differential Receptors. **Angewandte Chemie International Edition**, Place Published, v. 40, n. 17, p. 3118-3130, 2001. ISSN 1521-3773. Disponível em: < [http://dx.doi.org/10.1002/1521-3773\(20010903\)40:17<3118::AID-ANIE3118>3.0.CO;2-Y](http://dx.doi.org/10.1002/1521-3773(20010903)40:17<3118::AID-ANIE3118>3.0.CO;2-Y) >.

LEMINE, O. M. et al. γ -Fe₂O₃ by sol–gel with large nanoparticles size for magnetic hyperthermia application. **Journal of Alloys and Compounds**, Place Published, v. 607, p. 125-131, 2014. ISSN 0925-8388. Disponível em: < <http://www.sciencedirect.com/science/article/pii/S0925838814007944> >.

LI, H. et al. Nucleic acid detection using carbon nanoparticles as a fluorescent sensing platform. **Chemical Communications**, Place Published, v. 47, n. 3, p. 961-963, 2011. ISSN 1359-7345. Disponível em: < <http://dx.doi.org/10.1039/C0CC04326E> >.

LI, J. et al. An electrochemical immunosensor for carcinoembryonic antigen enhanced by self-assembled nanogold coatings on magnetic particles. **Analytica Chimica Acta**, Place Published, v. 665, n. 1, p. 98-104, 2010. ISSN 0003-2670. Disponível em: < <http://www.sciencedirect.com/science/article/pii/S000326701000303X> >.

LIM, S. Y.; SHEN, W.; GAO, Z. Carbon quantum dots and their applications. **Chemical Society Reviews**, Place Published, v. 44, n. 1, p. 362-381, 2015. ISSN 0306-0012. Disponível em: < <http://dx.doi.org/10.1039/C4CS00269E> >.

LOU, Y. et al. Metal ions optical sensing by semiconductor quantum dots. **Journal of Materials Chemistry C**, Place Published, v. 2, n. 4, p. 595-613, 2014. ISSN 2050-7526. Disponível em: < <http://dx.doi.org/10.1039/C3TC31937G> >.

MADU, C. O.; LU, Y. Novel diagnostic biomarkers for prostate cancer. **Journal of Cancer**, Place Published, v. 1, p. 150-177, 2010. ISSN 1837-9664. Disponível em: < <http://www.ncbi.nlm.nih.gov/pmc/articles/PMC2962426/> >.

MCNALLY, A. Magnetic sensors: Nanoparticles detect infection. **Nat Nano**, Place Published, v. 8, n. 5, p. 315-316, 2013. ISSN 1748-3387. Disponível em: < <http://dx.doi.org/10.1038/nnano.2013.76> >.

MIN, B. U.; WENZHONG, M. Study on core–shell–shell structured nanoparticles with magnetic and luminescent features: Construction, characterization and oxygen-sensing behavior. **Journal of Luminescence**, Place Published, v. 141, n. 0, p. 80-86, 2013. ISSN 0022-2313. Disponível em: < <http://www.sciencedirect.com/science/article/pii/S0022231313001610> >.

MIRANDA, O. R. et al. Array-Based Sensing of Proteins Using Conjugated Polymers. **Journal of the American Chemical Society**, Place Published, v. 129, n. 32, p. 9856-9857, 2007/08/01 2007. ISSN 0002-7863. Disponível em: < <http://dx.doi.org/10.1021/ja0737927> >.

NETTO, C. G. C. M.; TOMA, H. E.; ANDRADE, L. H. Superparamagnetic nanoparticles as versatile carriers and supporting materials for enzymes. **Journal of Molecular Catalysis B: Enzymatic**, Place Published, v. 85–86, p. 71-92, 2013. ISSN 1381-1177. Disponível em: < <http://www.sciencedirect.com/science/article/pii/S138111771200224X> >.

NGUYEN, B. T.; ANSLYN, E. V. Indicator–displacement assays. **Coordination Chemistry Reviews**, Place Published, v. 250, n. 23–24, p. 3118–3127, 2006. ISSN 0010-8545. Disponível em: < <http://www.sciencedirect.com/science/article/pii/S0010854506001147> >.

PEREZ, J. M.; JOSEPHSON, L.; WEISSLEDER, R. Use of Magnetic Nanoparticles as Nanosensors to Probe for Molecular Interactions. **ChemBioChem**, Place Published, v. 5, n. 3, p. 261–264, 2004. ISSN 1439-7633. Disponível em: < <http://dx.doi.org/10.1002/cbic.200300730> >.

RAO, C. N. R. et al. Recent progress in the synthesis of inorganic nanoparticles. **Dalton Transactions**, Place Published, v. 41, n. 17, p. 5089–5120, 2012. ISSN 1477-9226. Disponível em: < <http://dx.doi.org/10.1039/C2DT12266A> >.

REDDY, L. H. et al. Magnetic Nanoparticles: Design and Characterization, Toxicity and Biocompatibility, Pharmaceutical and Biomedical Applications. **Chemical Reviews**, Place Published, v. 112, n. 11, p. 5818–5878, 2012/11/14 2012. ISSN 0009-2665. Disponível em: < <http://dx.doi.org/10.1021/cr300068p> >.

ROCHA-SANTOS, T. A. P. Sensors and biosensors based on magnetic nanoparticles. **TrAC Trends in Analytical Chemistry**, Place Published, v. 62, n. 0, p. 28–36, 2014. ISSN 0165-9936. Disponível em: < <http://www.sciencedirect.com/science/article/pii/S0165993614001617> >.

ROCO, M. C. The long view of nanotechnology development: the National Nanotechnology Initiative at 10 years. **Journal of Nanoparticle Research**, Place Published, v. 13, n. 2, p. 427–445, 2011// 2011. ISSN 1572-896X. Disponível em: < <http://dx.doi.org/10.1007/s11051-010-0192-z> >.

SINGH RANA, P. J.; SINGH, P.; KAR, P. Fluorescence alarming ON-OFF-ON switch derived from biocompatible carbon nanoparticle-hemoglobin-H₂O₂ interaction. **RSC Advances**, Place Published, v. 6, n. 74, p. 70660–70668, 2016. Disponível em: < <http://dx.doi.org/10.1039/C6RA14308C> >.

TANG, J. et al. Magnetite Fe₃O₄ Nanocrystals: Spectroscopic Observation of Aqueous Oxidation Kinetics. **The Journal of Physical Chemistry B**, Place Published, v. 107, n. 30, p. 7501–7506, 2003/07/01 2003. ISSN 1520-6106. Disponível em: < <http://dx.doi.org/10.1021/jp027048e> >.

TAO, Y. et al. Array-Based Sensing of Proteins and Bacteria By Using Multiple Luminescent Nanodots as Fluorescent Probes. **Small**, Place Published, v. 10, n. 18, p. 3667–3671, 2014. ISSN 1613-6829. Disponível em: < <http://dx.doi.org/10.1002/sml.201400661> >.

VÁZQUEZ-GONZÁLEZ, M.; CARRILLO-CARRION, C. Analytical strategies based on quantum dots for heavy metal ions detection. **Journal of Biomedical Optics**, Place Published, v. 19, n. 10, p. 101503–101503, 2014. ISSN 1083-3668. Disponível em: < <http://dx.doi.org/10.1117/1.JBO.19.10.101503> >.

WAN, Y.; ZHANG, D.; HOU, B. Determination of sulphate-reducing bacteria based on vancomycin-functionalised magnetic nanoparticles using a modification-free quartz crystal microbalance. **Biosensors and Bioelectronics**, Place Published, v. 25, n. 7, p. 1847-1850, 2010. ISSN 0956-5663. Disponível em: < <http://www.sciencedirect.com/science/article/pii/S0956566309007064> >.

WANG, F. et al. Graphene quantum dots as a fluorescent sensing platform for highly efficient detection of copper(II) ions. **Sensors and Actuators B: Chemical**, Place Published, v. 190, p. 516-522, 2014. ISSN 0925-4005. Disponível em: < <http://www.sciencedirect.com/science/article/pii/S0925400513010496> >.

WANG, J. et al. Studies of Fe₃O₄/Ag/Au composites for immunoassay based on surface plasmon resonance biosensor. **Colloids and Surfaces B: Biointerfaces**, Place Published, v. 102, p. 165-170, 2013. ISSN 0927-7765. Disponível em: < <http://www.sciencedirect.com/science/article/pii/S0927776512004882> >.

WANG, M. et al. A Supramolecular Sensor Array Using Lanthanide-Doped Nanoparticles for Sensitive Detection of Glyphosate and Proteins. **ACS Applied Materials & Interfaces**, Place Published, v. 8, n. 1, p. 574-581, 2016/01/13 2016. ISSN 1944-8244. Disponível em: < <http://dx.doi.org/10.1021/acsami.5b09607> >.

WANG, Y.; HU, A. Carbon quantum dots: synthesis, properties and applications. **Journal of Materials Chemistry C**, Place Published, v. 2, n. 34, p. 6921-6939, 2014. ISSN 2050-7526. Disponível em: < <http://dx.doi.org/10.1039/C4TC00988F> >.

WANG, Y. et al. Using Graphene Quantum Dots as Photoluminescent Probes for Protein Kinase Sensing. **Analytical Chemistry**, Place Published, v. 85, n. 19, p. 9148-9155, 2013/10/01 2013. ISSN 0003-2700. Disponível em: < <http://dx.doi.org/10.1021/ac401807b> >.

XU, X. et al. Electrophoretic Analysis and Purification of Fluorescent Single-Walled Carbon Nanotube Fragments. **Journal of the American Chemical Society**, Place Published, v. 126, n. 40, p. 12736-12737, 2004/10/01 2004. ISSN 0002-7863. Disponível em: < <http://dx.doi.org/10.1021/ja040082h> >.

YANG, C. et al. rGO quantum dots/ZnO hybrid nanofibers fabricated using electrospun polymer templates and applications in drug screening involving an intracellular H₂O₂ sensor. **Journal of Materials Chemistry B**, Place Published, v. 3, n. 13, p. 2651-2659, 2015. ISSN 2050-750X. Disponível em: < <http://dx.doi.org/10.1039/C4TB02134G> >.

YANG, Z. et al. Potentiometric glucose biosensor based on core-shell Fe₃O₄-enzyme-polypyrrole nanoparticles. **Biosensors and Bioelectronics**, Place Published, v. 51, p. 268-273, 2014. ISSN 0956-5663. Disponível em: < <http://www.sciencedirect.com/science/article/pii/S0956566313005265> >.

YOLA, M. L.; EREN, T.; ATAR, N. A novel and sensitive electrochemical DNA biosensor based on Fe@Au nanoparticles decorated graphene oxide. **Electrochimica Acta**, Place

Published, v. 125, p. 38-47, 2014. ISSN 0013-4686. Disponível em: < <http://www.sciencedirect.com/science/article/pii/S001346861400142X> >.

YOU, C.-C. et al. Detection and identification of proteins using nanoparticle-fluorescent polymer / "chemical nose" sensors. **Nat Nano**, Place Published, v. 2, n. 5, p. 318-323, 2007. ISSN 1748-3387. Disponível em: < <http://dx.doi.org/10.1038/nnano.2007.99> >.

YOU, L.; ZHA, D.; ANSLYN, E. V. Recent Advances in Supramolecular Analytical Chemistry Using Optical Sensing. **Chemical Reviews**, Place Published, v. 115, n. 15, p. 7840-7892, 2015/08/12 2015. ISSN 0009-2665. Disponível em: < <http://dx.doi.org/10.1021/cr5005524> >.

ZAMFIR, L.-G. et al. Highly sensitive label-free immunosensor for ochratoxin A based on functionalized magnetic nanoparticles and EIS/SPR detection. **Sensors and Actuators B: Chemical**, Place Published, v. 159, n. 1, p. 178-184, 2011. ISSN 0925-4005. Disponível em: < <http://www.sciencedirect.com/science/article/pii/S092540051100606X> >.

ZHANG, R.; CHEN, W. Nitrogen-doped carbon quantum dots: Facile synthesis and application as a "turn-off" fluorescent probe for detection of Hg²⁺ ions. **Biosensors and Bioelectronics**, Place Published, v. 55, p. 83-90, 2014. ISSN 0956-5663. Disponível em: < <http://www.sciencedirect.com/science/article/pii/S0956566313008646> >.

ZHAO, D. et al. Metal-organic frameworks (MOFs) combined with ZnO quantum dots as a fluorescent sensing platform for phosphate. **Sensors and Actuators B: Chemical**, Place Published, v. 197, p. 50-57, 2014. ISSN 0925-4005. Disponível em: < <http://www.sciencedirect.com/science/article/pii/S0925400514002184> >.

ZHOU, J. et al. Ultratrace detection of C-reactive protein by a piezoelectric immunosensor based on Fe₃O₄@SiO₂ magnetic capture nanoprobe and HRP-antibody co-immobilized nano gold as signal tags. **Sensors and Actuators B: Chemical**, Place Published, v. 178, p. 494-500, 2013. ISSN 0925-4005. Disponível em: < <http://www.sciencedirect.com/science/article/pii/S0925400513000208> >.

CHAPTER 2

2 EFFECT OF SOLVENT COMPOSITION ON THE STRUCTURAL AND MAGNETIC PROPERTIES OF MNZN FERRITE NANOPARTICLES OBTAINED BY HYDROTHERMAL SYNTHESIS

Abstract

Samples of MnZn ferrites were successfully prepared by hydrothermal syntheses using different compositions of the reactive system $(\text{H}_2\text{O})_{1-x}:(\text{EG})_x$ ($x = 0, 0.2, 0.4, 0.6, 0.8$ and 1.0), where EG= ethylene glycol. The samples were fully investigated by powder X-ray diffraction (PXRD), Fourier transform infrared spectroscopy (FT-IR) for both liquid and solid specimens, Mössbauer spectroscopy, vibrating sample magnetometer (VSM) and transmission electron microscopy (TEM). All the MnZn ferrites presented spinel phase and average particle diameters between 3.1 and 12.1 nm. The increase of the x values results in a decrease in the particle sizes. The FTIR spectra performed in liquid phase showed significant interaction between EG and metallic precursors used in the synthesis. Magnetic features as for instance saturation magnetization (M_s) also decreases upon increasing the x values. In addition, all synthesized samples exhibited a superparamagnetic character at room temperature. The experimental methodology presented in this work is determining to obtain superparamagnetic nanoparticles with controlled size (smaller than 13 nm) and morphology.

Keywords: Magnetic Nanoparticles. MnZn Ferrite. Ethylene glycol. Hydrothermal synthesis.

2.1 Introduction

In the last decades, magnetic materials have been the subject of intensive investigations due to their inherent magnetic properties and applications in electronic devices, such as inductors, AC/DC converters, transformers, noise filters, recording heads and others (Poddar *et al.*, 2005; Zhang *et al.*, 2009). This kind of material also have generated a lot of interest in biomedical applications (Arruebo *et al.*, 2007; Boyer *et al.*, 2010; Barreto, A. N. *et al.*, 2013) for magnetic contrast resonance imaging (MRI), magnetic separation, targeted drug delivery, tissue engineering, cell tracking, bioseparation and magnetic hyperthermia. Thus, the advancement of nanotechnology has brought new strategies and perspectives mainly for medicine (Botelho *et al.*, 2009; Botelho *et al.*, 2010; Gonzaga *et al.*, 2012; Botelho *et al.*, 2013). In this way, Manganese–Zinc ferrites (MnZn) assume special importance due to their chemical composition and crystal structure, with the metal ions distributed among eight tetrahedral (A) and 16 octahedral (B) coordinated sites per unit cell, in which oxygen atoms form a face-centered cubic (FCC) lattice. These characteristics lead to a material with high initial permeability and saturation magnetization, as well as lower eddy current loss compared with alloy cores (Shokrollahi and Janghorban, 2007). Apart from being interesting for electronic devices, MnZn ferrites have been also used for biomedical applications and also potentially promising for MRI, drug delivery and magnetic fluid hyperthermia (Latorre-Esteves *et al.*, 2009).

In order to obtain good magnetic and structural properties, several methodologies were developed to synthesize magnetic nanoparticles (MNP): as for instance microemulsion-based methods (Pérez *et al.*, 1997), sol-gel syntheses (Dai *et al.*, 2005), co-precipitation (Velmurugan *et al.*, 2010; Barreto, A. C. H. *et al.*, 2013) and hydrothermal reactions (Srivastava *et al.*, 2009; Freire *et al.*, 2013). These methods provide MNP with different and tunable shapes (nanospheres, nanorods, etc), size, structural and magnetic properties. Among these methodologies, the hydrothermal approach has been commonly used as a favorable route to synthesize spinel ferrites. This technique allows obtaining a variety of ceramics and offers many advantages over other conventional and non-conventional procedures. The nanoparticles (NP) nucleate directly in the solution leading to materials of high purity and crystallinity (Suchanek and Riman, 2006). Moreover, the rate and uniformity of nucleation and growth can be modeled by thermodynamic variables (temperature, reactant concentrations, various additives and/or solvents etc). The liquid phase allows for parameter changes as diffusion, adsorption, reaction rate and others

(Riman *et al.*, 2002). This improves the size and morphology control of crystallites and significantly reduces the extent of NP aggregation. Then, the choice of the reaction environment (solvent or mixtures) in which the NP will be produced is extremely important. Nevertheless, literature (Yáñez-Vilar *et al.*, 2009; Pérez-Mirabet *et al.*, 2013) reports few studies evaluating the role of different solvents in the synthesis of MNP under solvo/hydrothermal conditions. The majority of papers evaluate how the experimental conditions as temperature (Mozaffari *et al.*, 2010), stirring velocity (Valenzuela *et al.*, 2009) and precipitating agent (Aquino *et al.*, 2002) may affect the particle size and morphology. However, another strategy largely employed by researchers is the use of stabilizing agents such as oleic acid (Zhang *et al.*, 2006) and sodium acetate (Wang *et al.*, 2009), oleylamine (Pérez-Mirabet *et al.*, 2013) and polysaccharides (carboxymethyl cellulose sodium) (Chang *et al.*, 2011).

In the present work, $\text{MnZnFe}_2\text{O}_4$ nanoparticles were prepared under hydro/solvothermal conditions in different solvent compositions of water and/or EG. We show a dependency of the magnetic and structural properties on changes of solvent compositions. Structural, optical and magnetic features of the produced nanoparticles were studied by PXRD, TEM, FTIR, Raman and Mössbauer spectroscopies, and vibrating sample magnetometry.

2.2 Experimental

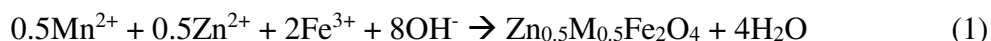
2.2.1 Materials and Methods

All reagents were commercially available, with analytical grade and employed without further purification. The chemical reagents for this work are ferric chloride hexahydrate ($\text{FeCl}_3 \cdot 6\text{H}_2\text{O}$, Dinâmica, 97%) manganese chloride tetrahydrate ($\text{MnCl}_2 \cdot 4\text{H}_2\text{O}$, Vetec, 99%), zinc chloride (ZnCl_2 , Dinâmica, 97%), sodium hydroxide (NaOH , Cinética Química, 97%) and EG ($\text{C}_2\text{H}_6\text{O}_2$, Reagen, P.A.).

2.2.2 Synthesis of $\text{MnZnFe}_2\text{O}_4$ nanoparticles

$\text{MnZnFe}_2\text{O}_4$ nanoparticles were synthesized according to Lee *et al.* (Lee *et al.*, 1999). However, some modifications were performed, as follows. Stoichiometrically required amounts of metallic reagents were dissolved in a beaker under different proportions of $(\text{H}_2\text{O})_{1-x}:(\text{EG})_x$ ($0 \leq x \leq 1$). All of the x values used for the samples' preparation are summarized in Table 2.1. Under vigorous mechanical stirring, it was prepared a mixture

of 1.85 mmol of $\text{MnCl}_2 \cdot 4\text{H}_2\text{O}$, 1.85 mmol of ZnCl_2 and 7.4 mmol of $\text{FeCl}_3 \cdot 6\text{H}_2\text{O}$. NaOH (~37.5 mmol) was added into the mixture in order to precipitate the desired hydroxides. The as obtained slurry was sealed in a teflon-lined stainless-steel autoclave and the crystallization was carried out under autogenously pressure at temperature of 250°C for 0.5 h. The reaction occurring during this process can be summarized as follows:



After this procedure, the autoclave was cooled down to room temperature and the precipitate washed several times with water and methanol. The materials were then dried in air at 100°C for 3h. The resultant MNP was labeled according to the x values, which indicate the amount of EG contained in the solvent.

Table 2.1. x values and label of the samples obtained in this work.

x	Label
0.0	EG0
0.2	$(\text{H}_2\text{O})_{0.8}:(\text{EG})_{0.2}$
0.4	$(\text{H}_2\text{O})_{0.6}:(\text{EG})_{0.4}$
0.6	$(\text{H}_2\text{O})_{0.4}:(\text{EG})_{0.6}$
0.8	$(\text{H}_2\text{O})_{0.2}:(\text{EG})_{0.8}$
1.0	EG1

Source: Author

2.2.3 Stabilization of the metallic precursors from EG

The stabilizing role of EG relatively to the metal chlorides employed in the MnZn ferrite synthesis was tested separately at the same conditions of reagent's concentration and temperature. Each metallic salt was loaded into a 10 mL glass flask containing the system $(\text{H}_2\text{O})_{1-x}:(\text{EG})_x$ in different proportions ($x = 0, 0.2, 0.4, 0.6, 0.8$ and 1.0). After this step, NaOH was added dropwise under continuous magnetic stirring. The products obtained were investigated by Infrared - FT Raman Vertex 70 Bruker equipped with a PIKE MIRacle™ ATR accessory.

2.2.4 Characterization of the MNPs

The structural analysis was made by X-ray powder diffraction (PXRD) patterns of the obtained samples using $\text{CuK}\alpha$ (1.54056 Å) radiation from a Rigaku diffractometer with a Bragg-Brentano geometry in the range of 20-70° angle degrees. The phase identification was made by comparing powder diffractograms with standard patterns from International Centre for Diffraction Data (ICDD). Rietveld refinement procedures (Rietveld, 1967; Maia *et al.*, 2006) were applied to all diffraction patterns using the DBWS 2.25 (Bleicher *et al.*, 2000). The infrared spectra (FTIR) of the samples were carried out on a Perkin-Elmer Fourier transform infrared spectrometer in the range 4000 – 400 cm^{-1} . In recording FTIR spectra, each sample was mixed with potassium bromide (KBr) powder and pressed into pellets. The Mössbauer spectrum was recorded at room temperature (300K) from FAST (ConTec) Mössbauer System spectrometer using transmission geometry. A ^{57}Co radioactive source was used. The data analysis was performed using NORMOS program written by R.A. Brand (distributed by Wissenschaftliche Elektronik GmbH, Germany). Isomer shifts (δ) are referred to $\alpha\text{-Fe}$ at room temperature. Magnetic properties were investigated by a vibrating sample magnetometer (VSM) Mini 5 Tesla from Cryogenic Ltd. The VSM has been previously calibrated using a YIG sphere, and after measuring the mass of each sample the magnetization was given in emu/g. Microstructural studies including evaluation of particle size and morphology were performed on a Jeol JEM-1011 electron microscope operating at 100 kV, equipped with a CCD camera ORIUS 831 from Gatan. Transmission Electron Microscope (TEM) images of the samples were prepared by drop-casting dilute nanocrystal solutions onto carbon coated copper grids. Afterwards, the deposited samples were allowed to complete dry at 60°C for one night before examination.

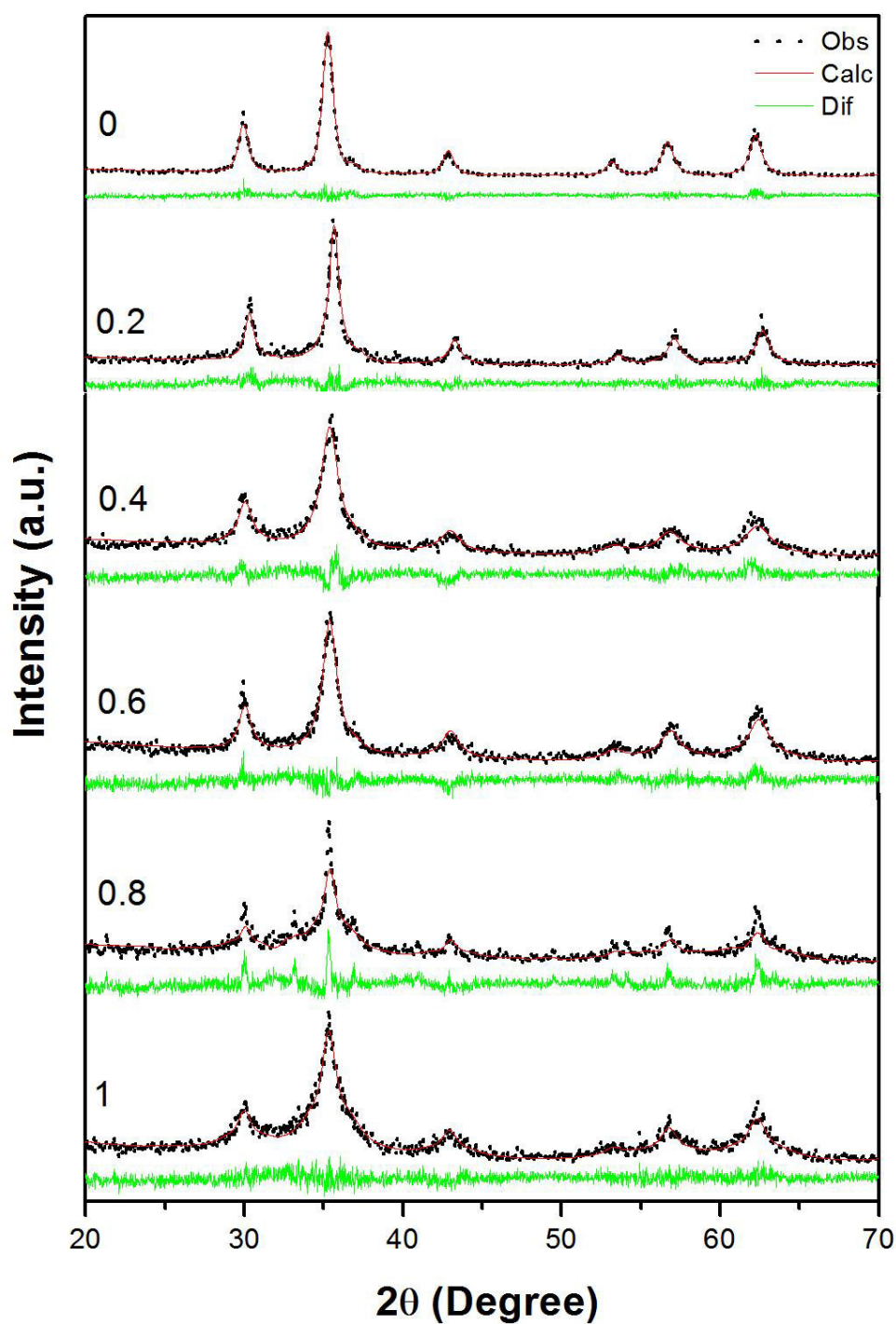
2.3 Results and discussion

2.3.1 X-ray powder diffraction (PXRD)

Fig. 2.1 shows the PXRD patterns for all samples synthesized under different conditions of composition of water and ethylene glycol. Black dots in the figure represent the observed (Obs) data collected from experimental measurements. On the other hand, red lines correspond to calculated (Calc) data obtained from the computational processing performed by the Rietveld method, while the green lines represent the relative difference (Dif) between them. The diffraction peaks can be assigned to the spinel cubic phase

(ICDS, file n° 017-0912) with spatial group O_h^7 . However, the sample with $x=0.8$ ($(H_2O)_{0.2}:(EG)_{0.8}$) exhibits a peak at 33.2° , which indicates the presence of the hematite phase ($\alpha\text{-Fe}_2\text{O}_3$) (ICSD, file n° 071-0469). This phase may be explained by Fe^{3+} migration out of the spinel structure (Paiva *et al.*, 2008). Generally, calcination is a necessary step in the preparation of ferrites by chemical methods (Zhang *et al.*, 2009). Moreover, the calcination temperature plays a key role in the determination of final crystal structure and particle size (Lv *et al.*, 2008). The PXRD results showed that only samples subjected to hydrothermal treatment performed during synthesis exhibit diffraction peaks characteristics of the spinel phase. Thereby, a calcination step was not necessary for all samples synthesized in this work. This highlights the efficiency of the synthesis process furthermore providing particles of small size, since for MnZn ferrites the average crystalline size generally increases by increasing the calcination temperature due to the crystallites coalescence at high temperatures (Raming *et al.*, 2002; Maaz *et al.*, 2007). In addition, the presence of EG may play the role of a complexing agent stabilizing particles's dispersibility in solution their small dimensions. Similar studies in literature corroborates this effect played by polyols (Knetsch and L. Groeneveld, 1973; Caruntu *et al.*, 2002; Poul *et al.*, 2003; Chkoundali *et al.*, 2004).

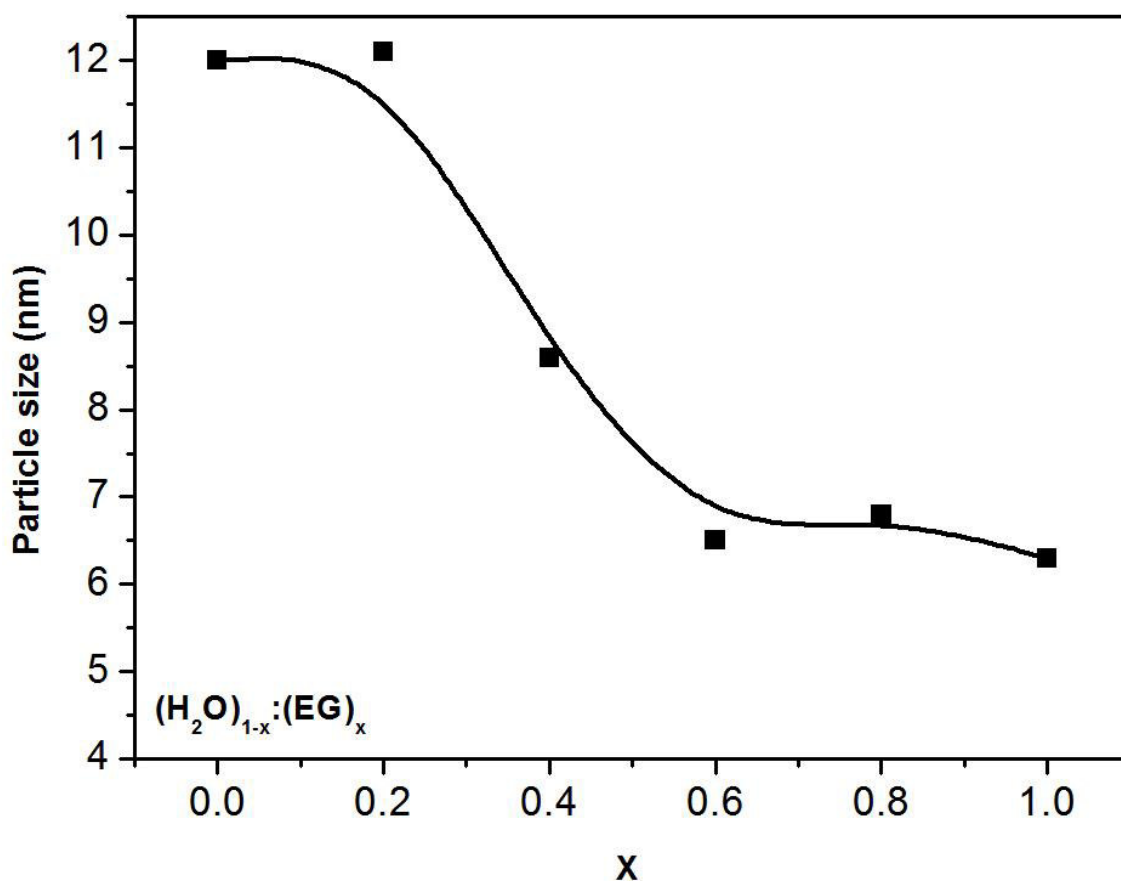
Figure 2.1. XRD for samples of the system $(\text{H}_2\text{O})_{1-x}:(\text{EG})_x$, where x denotes the amount of the EG used to compose the solvent. The corresponding x values are reported in each diffractogram. The black dots reveal the experimental data, while the red line denotes the calculated data. The green line displays the difference between experimental and calculated data.



Source: Author

The average crystallite size was calculated using the Debye-Scherrer equation after accounting for instrumental broadening (Rietveld method) (Velmurugan *et al.*, 2010). These values are plotted as a function of EG fraction (Fig. 2.2). It was possible to observe a decrease in average crystallite sizes when the EG fraction in the reactive domain raises. Interestingly, the size reduction sharply decreases (approximately 30%) as the EG fraction exceeds 0.2. Then after a x value of 0.5, it levels out again due to a less pronounced crystallite size reduction. This trend suggests the existence of a minimum threshold concentration in which EG can stabilize a maximum number of nanoparticles in solution, thus contributing to decrease the average sizes of the samples.

Figure 2.2. Particle size describe in function of the x values, which denotes the amount of the EG used to compose the solvent.



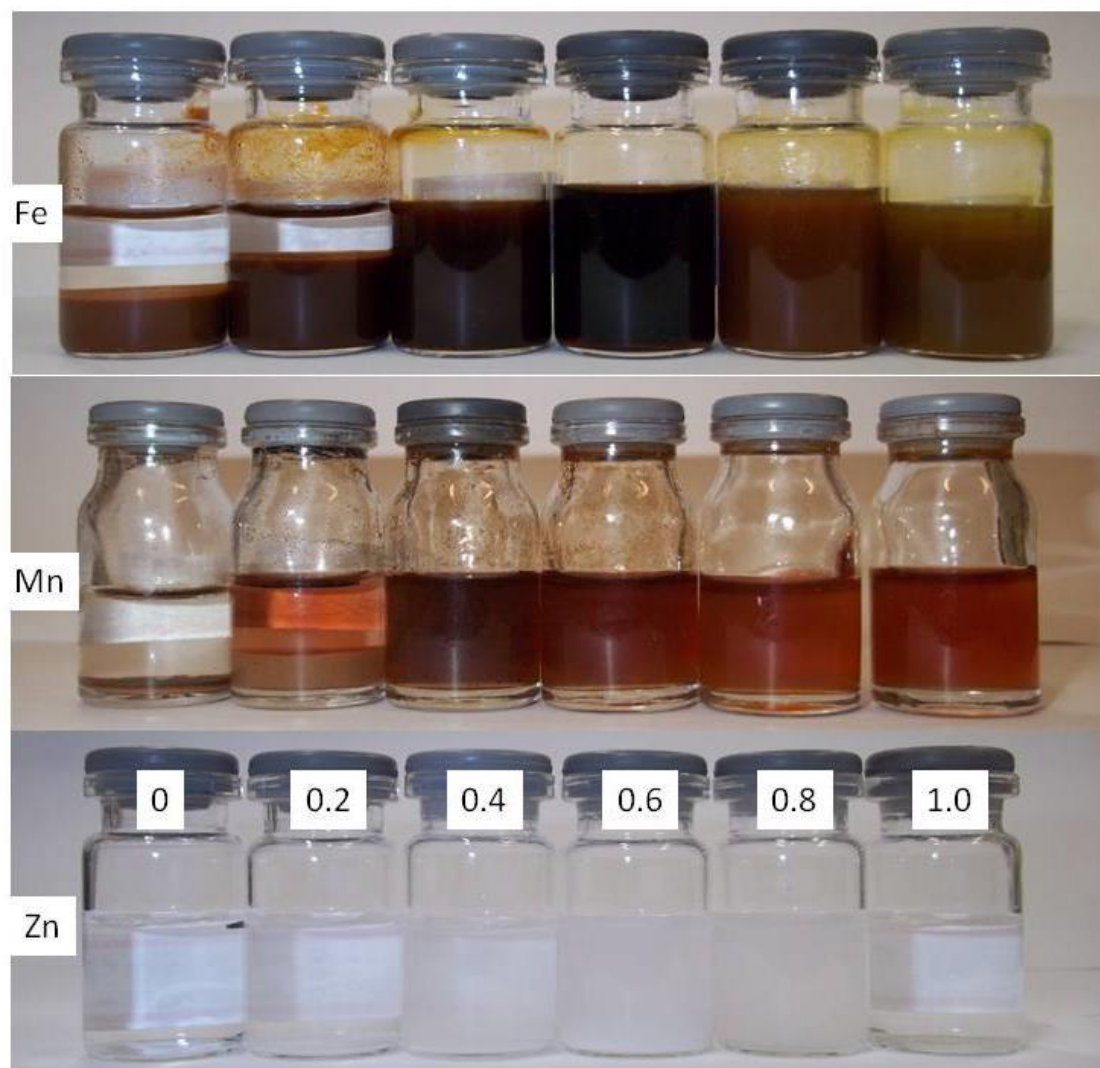
Source: Author

2.3.2 Stability of metallic chlorides with EG

Tests of solubility of the diverse metallic precursors individually dispersed in solutions exhibiting different compositions of water-to-ethylene glycol $((\text{H}_2\text{O})_{1-x}:(\text{EG})_x)$ have been

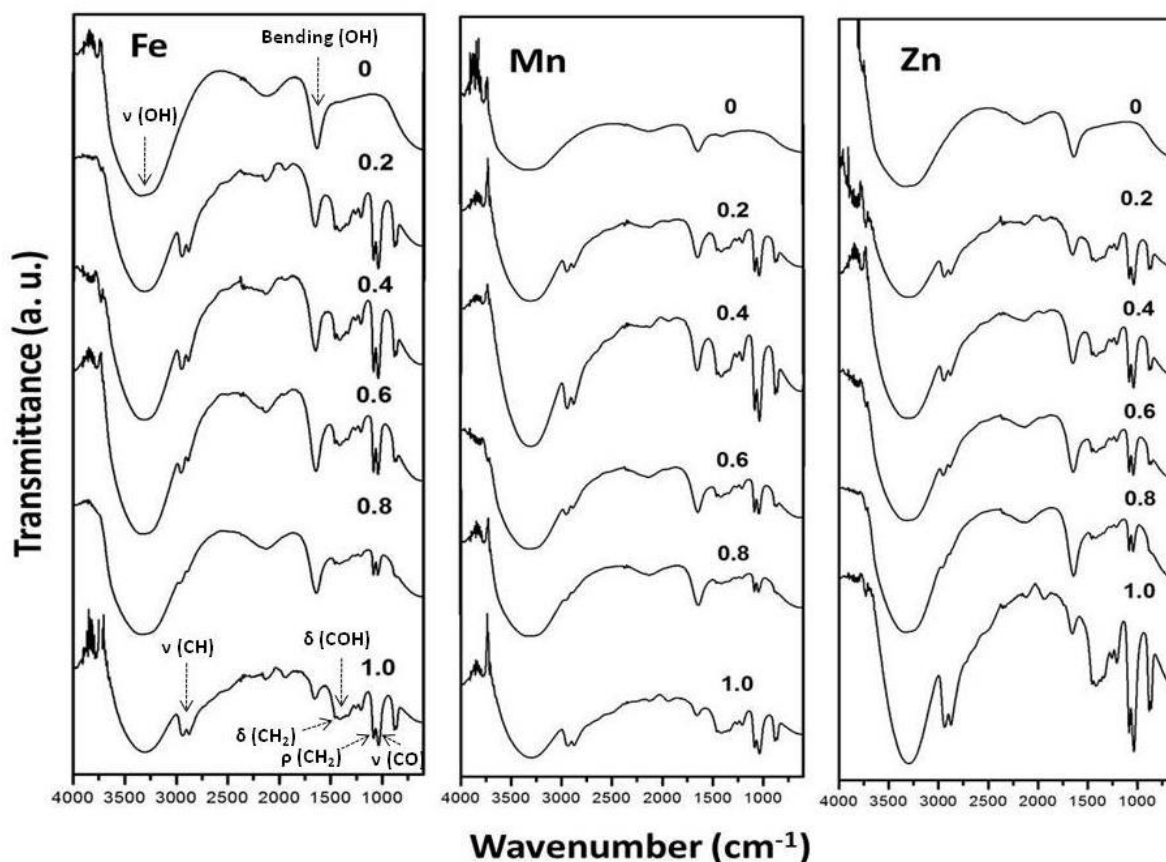
performed. These experiments were carried out in order to investigate the influence of EG on the stability of Mn^{2+} , Zn^{2+} , and Fe^{3+} chlorides in phase solution. Each metallic chloride was solubilized in 5 mL of solvent with different amounts of EG ($x = 0, 0.2, 0.4, 0.6, 0.8, 1.0$). The same solubilizing procedure was applied to anhydrous NaOH which works as precipitating agent of formed nanoparticles in the synthesis. Upon mixing both solutions, possible precipitation can be observed depending on the x values. Fig. 2.3 summarizes the final outcomes. Relatively to Mn and Fe, a solid precipitate was noted in the case of solutions containing 0 or 0.2 of EG fraction. When this concentration was exceeding, it was observed only color changes without any solid precipitation. Differently Zn-based salt did not show any changes of color or precipitate formation as a function of EG fraction. This result confirmed the improved dispersibility of particles in solution due to the increase of EG fraction. Literature reports that EG can behave as a mono or bidentate ligand (Knetsch and L. Groeneveld, 1973). Therefore, to evaluate the interaction of metallic precursors with EG, it was performed FTIR spectra of solutions resultant after adding of the NaOH. Fig. 2.4 shows the spectrum for each test realized with different x values and metallic precursors. It is possible to observe a similarity for all spectra with bands around 3350 and 1640 cm^{-1} for sample with $x = 0$, characteristic of the stretch and bending O-H of water molecules, respectively. However, for the tests performed with $x \neq 0$ the same band clearly shows shift to lower frequencies ($\sim 3300\text{ cm}^{-1}$). This indicates coordination of EG with metallic precursors by oxygen atoms. The bands referring to stretch of CH_2 near 3000 cm^{-1} showed no displacement. It was observed bands in 1082 and 1036 cm^{-1} , which can be attributed to CH_2 rocking vibrations. No splittings were observed and both bands show shift of approximately 10 cm^{-1} to lower frequencies (Miyake, 1959). This evidences the bidentate coordination, but the shape of the spectra in the range $1700 - 1200\text{ cm}^{-1}$ with a series of bands contradicts such a claim (Knetsch and L. Groeneveld, 1973). Since a bending COH was observed also indicating monodentate coordination. Therefore, the results showed in this section indicated a strongly interact of EG with metal chlorides and minimal concentration close to 0.4 for stabilization of the precursors in solution. This may explain the decrease in average crystallite size from that concentration observed in the results of PXRD.

Figure 2.3. Results of the stabilization test for different precursors metallic used in the synthesis. On the left side of each series of tests the relative metalis reported. The x values for the system $(\text{H}_2\text{O})_{1-x}:(\text{EG})_x$ are presented only in the case of Zn series, but can be straightforwardly expanded for Mn and Fe.



Source: Author

Figure 2.4. IR spectra of the tests realized with different x in the system $((\text{H}_2\text{O})_{1-x}:(\text{EG})_x)$ for metallic precursors.

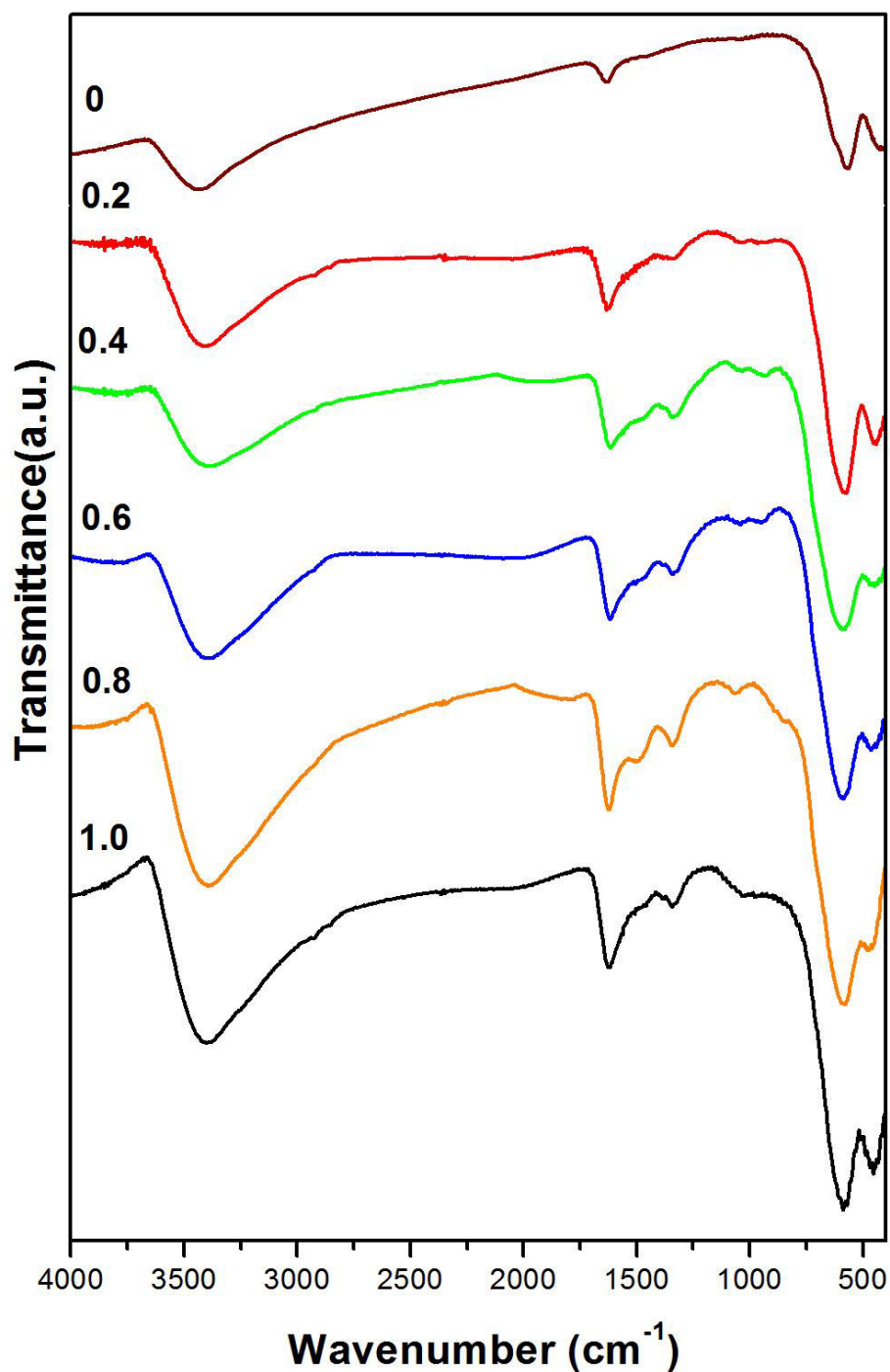


Source: Author

2.3.3 Infrared Spectroscopy

As reported before, it was possible to confirm the presence of spinel phase in all samples from the results of PXRD. According to literature (Shebanova and Lazor, 2003), this phase contains two distinct cationic lattice positions namely tetrahedral and octahedral sites coordinated by oxygen anions. Both sites contribute to the active modes in IR and a theoretical analysis based on the nuclear site group approach (Porto, 1981) predicts four IR-active bands T_{1u} (Gupta *et al.*, 2002). Fig. 2.5 shows the FTIR spectra in the range $4000 - 400 \text{ cm}^{-1}$ for all samples. It can be observed two bands in the range $650 - 400 \text{ cm}^{-1}$ widely observed for ordered spinel ferrites (Ravinder, 1999; Bezerra, 2007). The absorption bands observed in the range $600 - 550 \text{ cm}^{-1}$ and $450 - 385 \text{ cm}^{-1}$ can be attributed to the tetrahedral and octahedral sites, respectively (Barreto *et al.*, 2011; Clemente *et al.*, 2013). It is important to note that in the working range only is possible to observe two modes. These results are in agreement with literature (Thomas and George, 2009; Freire *et al.*, 2012; Freire *et al.*, 2013).

Figure 2.5. FTIR for samples of the system $(\text{H}_2\text{O})_{1-x}:(\text{EG})_x$, where x denotes the amount of the EG used to compose the solvent. The corresponding x values are reported in each spectrum.



Source: Author

The different position of the absorption bands attributed to octahedral and tetrahedral sites gives key indications relatively to the insertion or mobility of cations into network spinel (Dawoud, 2006). The interaction between oxygen and cations strongly affect the

wavelength values observed in Fig. 2.5. According to literature (Amer *et al.*, 2011), bands's frequency are proportional to the force constant (K), which can be calculated using the relation:

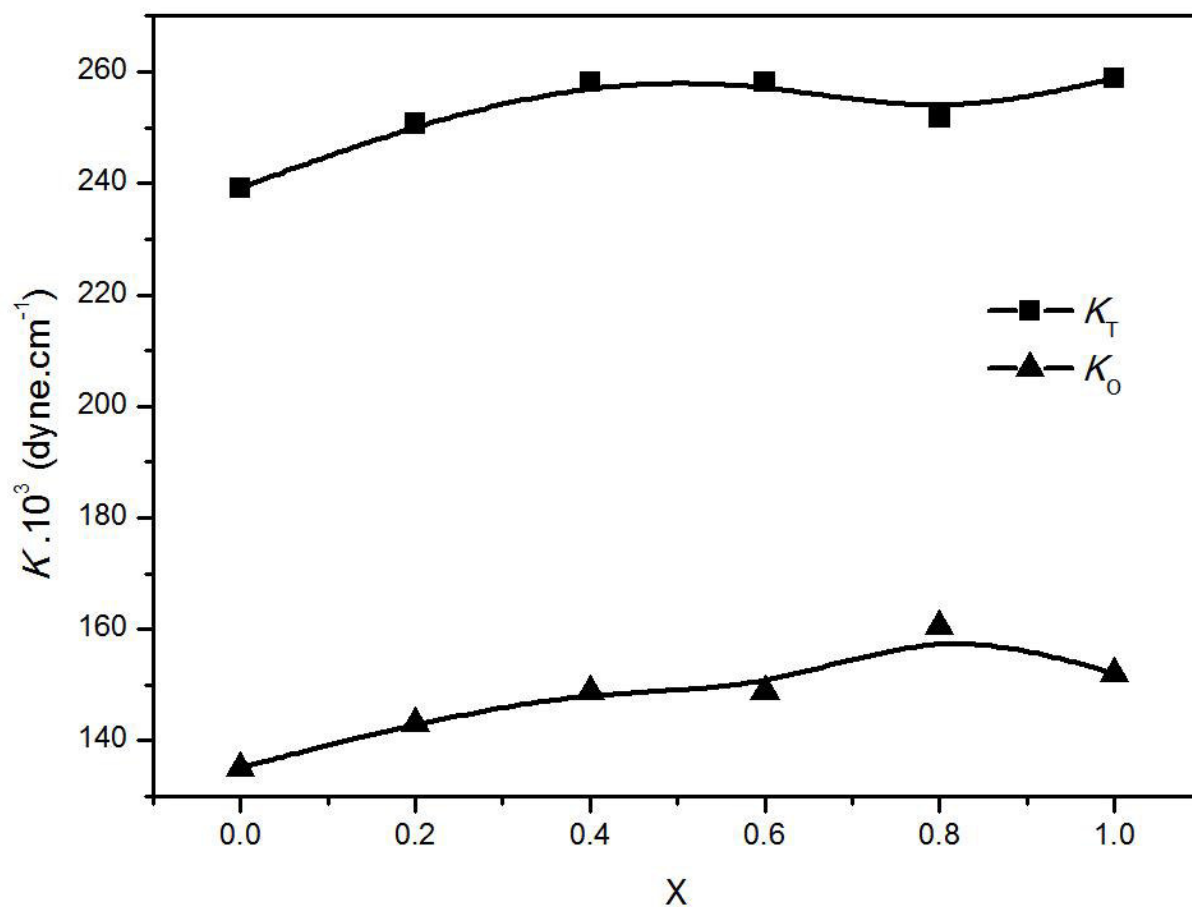
$$\nu = \frac{1}{2\pi} \sqrt{\frac{K}{\mu}} \quad (3)$$

where μ is the reduced mass and ν the frequency. The values of ν_O , ν_T , K_o and K_T for all samples are listed in the Table 2.2, where subscripts O and T means octahedral and tetrahedral, respectively. Fig. 2.6 shows the K values plotted as a function of EG fraction. As a general trend, it was clear that the force constants values increase with EG fraction in the system, which was accompanied by the decrease of the particle size. Literature (Choi *et al.*, 2005) reports that a volume contraction occurs within the nanoparticles due to decrease particle size. This leads to increase in the force constants as a result of the decreases in the interatomic distances. Then, the behavior observed can be assigned to the decrease in metal–oxygen bond lengths at the octahedral and tetrahedral sites. Moreover, K values can be too influenced by method of preparation and porosity (Waldron, 1955; Josyulu and Sobhanadri, 1981; Reddy and Salagram, 1987). The same relation between K values and EG fraction was observed for both sites. This indicates that increase of the EG fraction did not cause the mobility of cations into spinel network. However, the same conclusion cannot be inferred for sample synthesized with $(\text{H}_2\text{O})_{0.2}:(\text{EG})_{0.8}$. It was seen a decrease in K_T values and increase for K_o . These changes can be attributed to the weakening in metal-oxygen bond at the tetrahedral site due to mobility of cations into network spinel. Migrations of cations with small ionic radius from tetrahedral to octahedral sites lead the shifts of K_o towards high values due to increase the metal-oxygen interaction. This may be related to the Fe^{3+} displacement from tetrahedral to octahedral sites. Similar effect was observed for MgZn ferrite (Mohammed *et al.*, 2012). Furthermore, the PXRD results for $(\text{H}_2\text{O})_{0.2}:(\text{EG})_{0.8}$ have shown $\alpha\text{-Fe}_2\text{O}_3$. As previously reported, the presence this phase can be attributed to migration of Fe^{3+} out of the spinel structure (Paiva *et al.*, 2008). This may have generated an energetic imbalance into network spinel contributing to mobility of Fe^{3+} for octahedral sites.

Table 2.2. Values of x , ν_T , ν_O , K_o and K_T for all samples synthesized.

Samples	x	ν (cm^{-1})		$K \cdot 10^3$ (dyne.cm^{-1})	
		ν_T	ν_O	K_T	K_O
EG0	0.0	566.9	419.3	239.2	135.1
(H₂O)_{0.8}:(EG)_{0.2}	0.2	580.3	446.1	250.7	143.2
(H₂O)_{0.6}:(EG)_{0.4}	0.4	591.0	451.4	258.1	148.9
(H₂O)_{0.4}:(EG)_{0.6}	0.6	592.3	450.9	258.1	148.9
(H₂O)_{0.2}:(EG)_{0.8}	0.8	588.4	459.5	251.8	160.5
EG1	1.0	585.6	454.8	258.8	152.0

Source: Author

Figure 2.6. K values for tetrahedral (K_T) and octahedral (K_O) site plotted as a function of x .

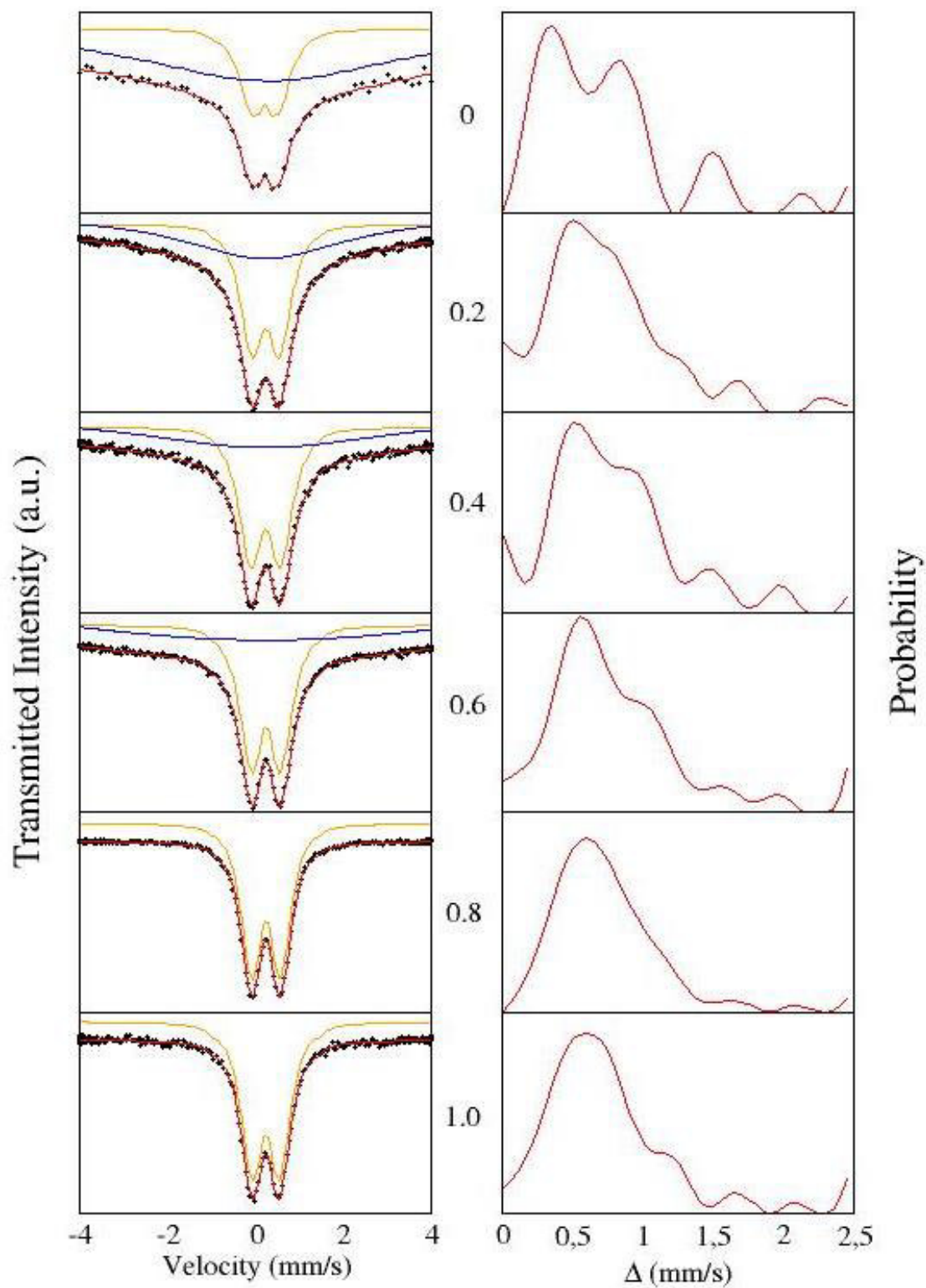
Source: Author

2.3.4 Mössbauer Spectroscopy

Fig. 2.7 shows Mössbauer spectrum at room-temperature of the samples of the $(\text{H}_2\text{O})_{1-x}:(\text{EG})_x$ system. The dots represent the experimental data, while solid lines illustrate least-squares fitting. All synthesized samples presented strong superparamagnetic characteristics due to their particle size (Knobel *et al.*, 2008) which was evidenced by a doublet at the centre of spectra (Wang and Li, 2001; Siddique and Butt, 2010). When the sizes decrease, the thermal energy strongly contributes to the collapse of the magnetic ordering and the superparamagnetic relaxation phenomenon is observed. Furthermore, it is interesting to note that for samples with fraction (x) between 0 and 0.6 it was needed to add sub-spectrum (continuous lines in different colors inside each spectrum) for a better fit to the baseline. This corresponds to different environments at the iron nucleus. As reported above, the doublet (orange line) corresponds to Fe atoms into small particles with superparamagnetic character. It was also found a V-shaped sub-spectrum (blue line). This can be explained by substitution of manganese ions with those of zinc, weakening the magnetic interactions, thus reducing A–B sites coupling pairs (Upadhyay *et al.*, 2003). The said sub-spectrum V-shaped was gradually disappearing with increase EG fraction.

Hyperfine parameters are presented at Table 2.3. The isomer shifts (δ) remained between 0.31–0.34 mm/s. These values can be attributed at high-spin Fe^{3+} state (Dickson and Berry, 1986). The average δ for all samples appears to show no significant variation with EG fraction. Since, this parameter is inherent to oxidation state of the Fe atom. In order to obtain the best fit of the experimental data for quadrupole interaction (Δ), it was performed using a distribution of probable values for this parameter. The resulting distribution graphs are shown beside each sample and the peak of greatest intensity shows the most likely value. Thus, it can be seen that for all samples the Δ has values in the range 0.3 – 0.6 mm/s. The relatively high values of Δ can be assigned to the chemical disorder and the local symmetry reduction in site (Ying *et al.*, 1992; Singhal *et al.*, 2006). Moreover, the broad distribution and the presence of peaks at lower intensities also reflects the high degree of disorder of the structures (Sorescu *et al.*, 2004). Interestingly, these peaks appear to be attenuated with increasing x values. Therefore, a decrease in the degree of disorder of the structure can be observed. However, this effect was better viewed for $x \geq 0.4$ due to stabilization of metallic precursors founded for these values. Thus, clearly the increase of the EG fraction contributes to a structural homogeneity site Fe.

Figure 2.7. Mössbauer spectra (left) and quadrupole (Δ) distribution (right) for samples of the system $(\text{H}_2\text{O})_{1-x}:(\text{EG})_x$, where x denotes the amount of the EG used to compose the solvent. The corresponding x values are reported beside spectrum.



Source: Author

Table 2.3. Hyperfine parameter for samples synthesized in this work.

Samples	Hyperfine Parameters
	δ (mm/s)*
EG0	0.31
(H₂O)_{0.8}:(EG)_{0.2}	0.33
(H₂O)_{0.6}:(EG)_{0.4}	0.33
(H₂O)_{0.4}:(EG)_{0.6}	0.34
(H₂O)_{0.2}:(EG)_{0.8}	0.34
EG1	0.34

*For all the samples, δ measured relative to α -Fe.

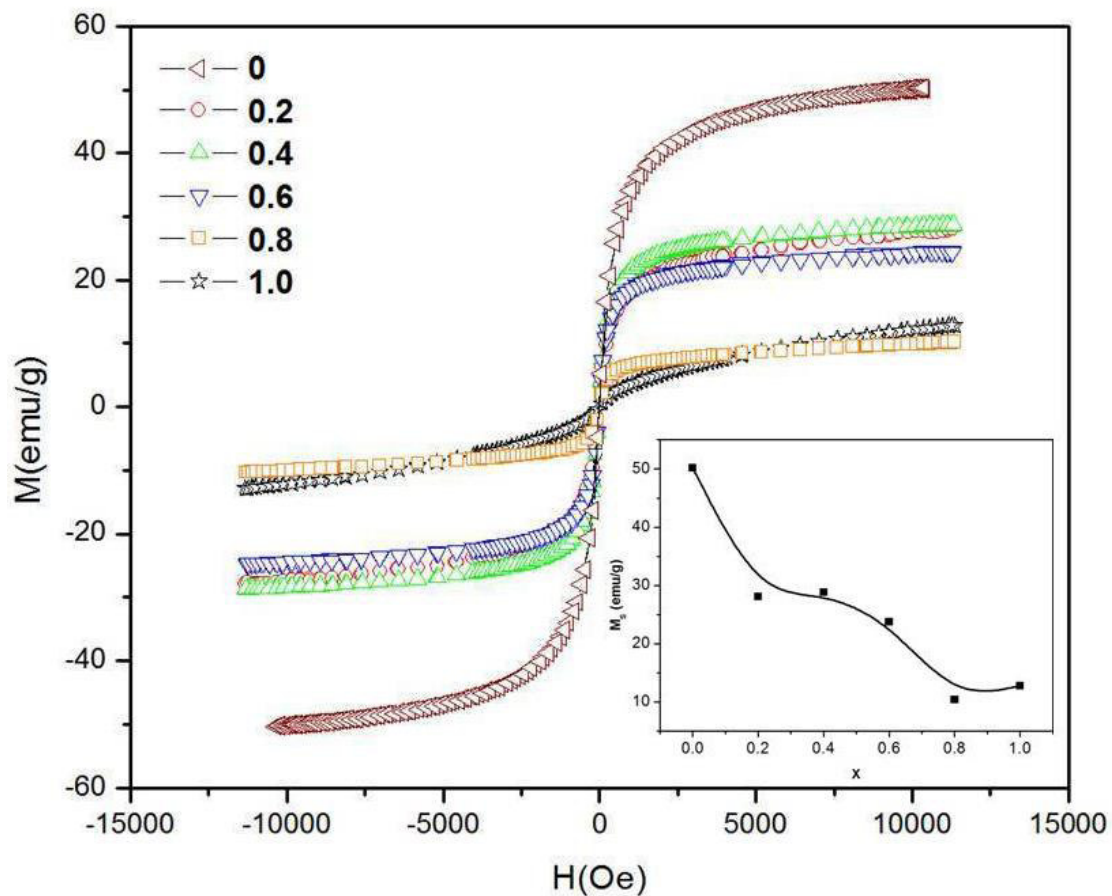
Source: Author

2.3.5 Magnetic Measurements

The magnetic properties of the nanoparticles synthesized in this work were measured as a function of the field and temperature. The results of magnetization curves measured at 300 K are presented in Fig. 2.8. The magnetization curves almost did not present coercivity and remanence at room temperature. This fact points for relaxation superparamagnetic phenomenon (Knobel *et al.*, 2008) in agreement with the results of Mössbauer Spectroscopy. It is also noted a decrease in saturation magnetization (M_s) for increasing values of x . According to the literature (Sato *et al.*, 1987), the decrease to the M_s occurs due to presence of a magnetically inactive layer or non-collinear spin arrangement on surface of the particles (Morrish and Haneda, 1980). Furthermore, this reduction can be attributed to the higher surface to volume ratio arising from small particles being present in these samples. Since the contribution of the nonmagnetic layer located at the surface is greater as the particle size decreases (Sánchez *et al.*, 2002). The inset of Fig. 2.8 shows the isothermal behavior of M_s as a function of the EG fraction (x). It is possible to observe that M_s decreases almost linearly with increasing of the x values. In general, PXRD data show that the particle size follows an inversely proportional relationship with x values. Therefore, the result observed here was expected due to greater contribution of the nonmagnetic layer. However, the sample

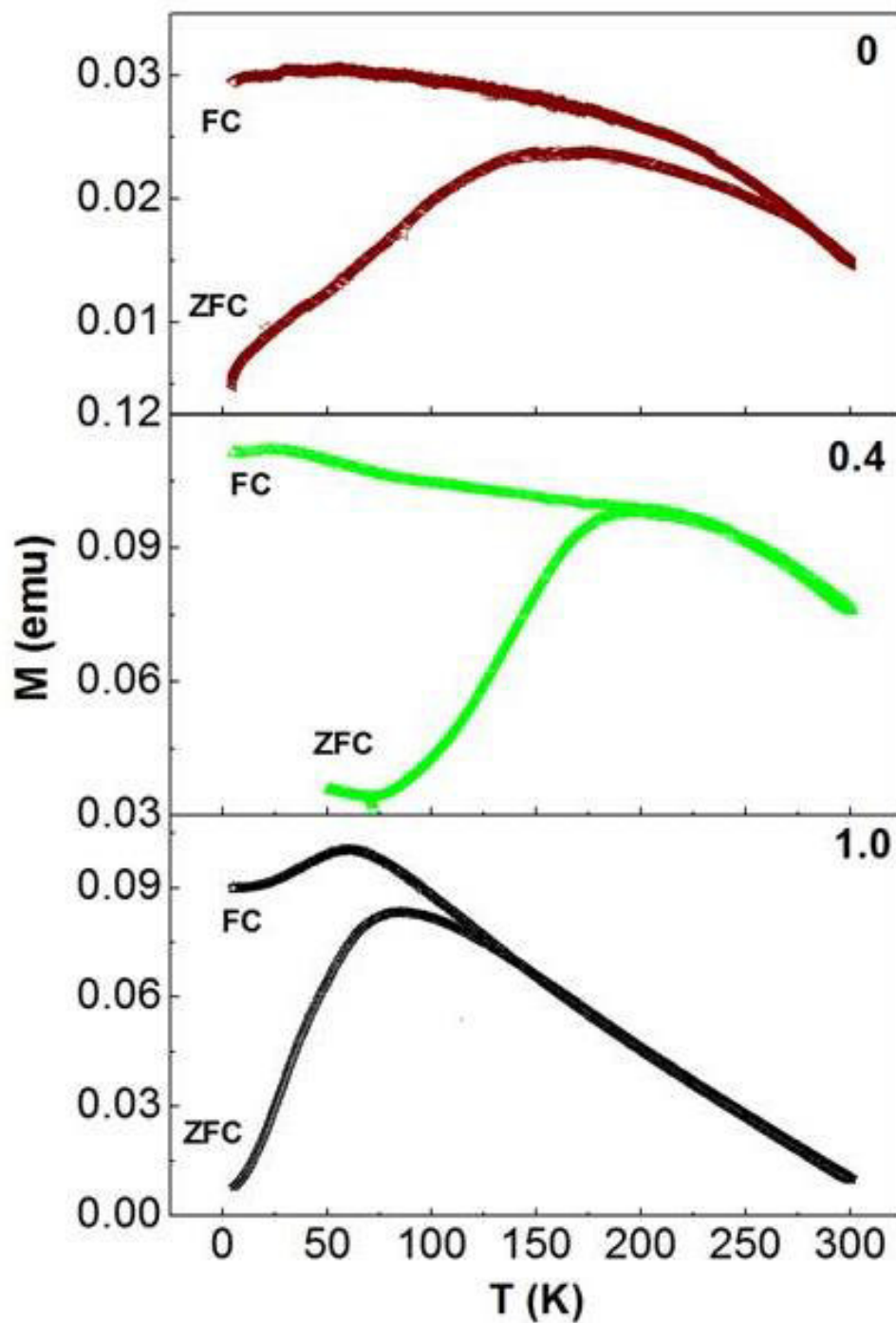
$(\text{H}_2\text{O})_{0.2}:(\text{EG})_{0.8}$ presents abnormality with low M_s value compared with EG1. This can be explained by presence of the $\alpha\text{-Fe}_2\text{O}_3$ (nonmagnetic phase) in the sample $(\text{H}_2\text{O})_{0.2}:(\text{EG})_{0.8}$, as detected by PXRD (Fig. 2.1). Similar results can be found in the literature (Sugimoto, 1999; Laokul *et al.*, 2011; Barreto *et al.*, 2012). Fig. 2.9 shows the zero-field cooled (ZFC)/field cooled (FC) curves measured at a field of 50 Oe for three representative samples, with $x = 0, 0.4$ and 1.0 (selected samples). From these curves it is shown that sample EG1 has a blocking temperature close to 75 K, where there is a maximum in the ZFC curve, and this temperature is where the nanoparticles have a transition from the blocked state to a superparamagnetic state. The blocking temperature is observed to increase for larger nanoparticles (Hassnain Jaffari *et al.*, 2012). The samples with lower EG concentrations have larger values of blocking temperature, as shown in the ZFC-FC curves, in agreement with the results of particle sizes obtained by XRD and TEM images (next section).

Figure 2.8. Magnetic measurements for samples of the system $(\text{H}_2\text{O})_{1-x}:(\text{EG})_x$. Inset reports M_s plotted as a function of the x .



Source: Author

Figure 2.9. Zero field cooled-field cooled curves of samples with $x = 0, 0.4$ and 1.0 .



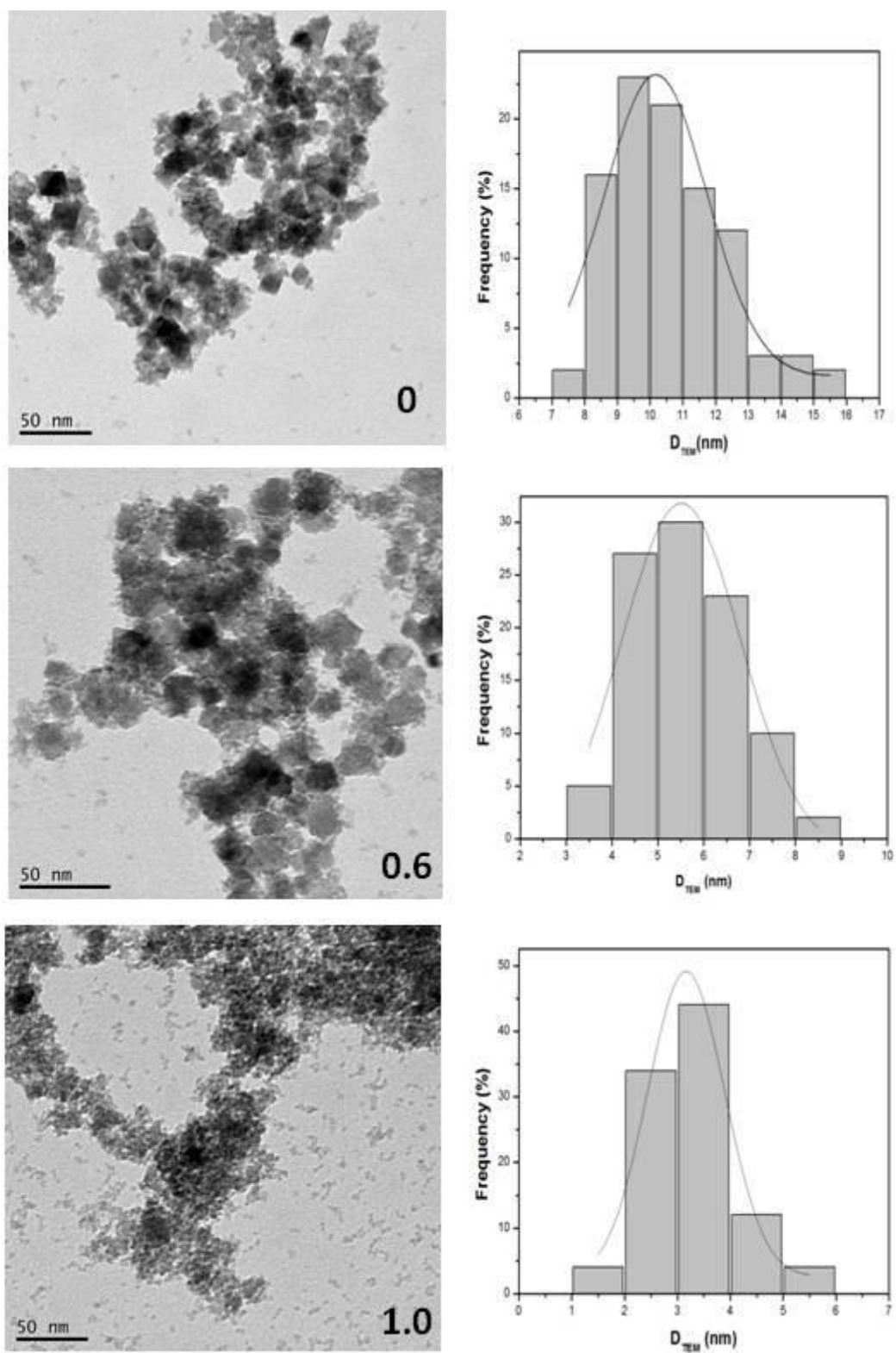
Source: Author

2.3.6 Transmission Electron Microscopy (TEM)

The morphology and particle size of the samples were studied in more detail by TEM analysis, as shown in Fig. 2.10 for the samples EG0, $(\text{H}_2\text{O})_{0.4}:(\text{EG})_{0.6}$ and EG1

respectively. Each TEM picture displays also sample size distribution as determined by analyzing 100 particles randomly selected in different regions of the TEM grid. Specifically, particles with an approximate cubic shape and an average edge length of 12 ± 3 nm were founded for the sample EG0. On the other hand, it is strongly evident from TEM micrographs of the samples $(\text{H}_2\text{O})_{0.4}:(\text{EG})_{0.6}$ and EG1 that the cubic form is not maintained in these cases and the average particle diameter dropped to 5.5 ± 2 and 3.1 ± 2 respectively. This result was in accordance with PXRD data, which showed a decrease of the particle size upon increasing the x values, namely an increment in the content of EG in the reactive environment. Another interesting aspect which draws the attention is represented by the degree of particles aggregation perceptible from TEM investigation. Clearly, the samples $(\text{H}_2\text{O})_{0.4}:(\text{EG})_{0.6}$ and EG1 have a higher degree of particles aggregation than EG0. This can be explained by the fact that a decrease of the particle size entails a larger specific surface area and consequently higher surface energy (Feng *et al.*, 2008). Hence, the samples $(\text{H}_2\text{O})_{0.4}:(\text{EG})_{0.6}$ and EG1 presented a higher number of aggregated particles in the TEM images.

Figure 2.10. TEM micrographs for samples of the system $(\text{H}_2\text{O})_{1-x}:(\text{EG})_x$, where x denotes the amount of the EG used to compose the solvent. The corresponding x values are reported in the image.



Source: Author

2.4 Conclusion

Superparamagnetic MnZn ferrites with high crystallinity and average particle diameter within the range 3.1 to 12.1 nm were synthesized by hydrothermal conditions under different compositions of the system $(\text{H}_2\text{O})_{1-x}:(\text{EG})_x$ ($x=0, 0.2, 0.4, 0.6, 0.8$ and 1.0). PXRD and TEM results showed a decrease in average particle size as a function of the increase of x values. However, this effect becomes more effective for $x \geq 0.4$. In order to explain this, FTIR analysis suggested that EG molecules interact strongly with the original metal precursors ($\text{FeCl}_3 \cdot 6\text{H}_2\text{O}$, $\text{MnCl}_2 \cdot 4\text{H}_2\text{O}$ and ZnCl_2) and images showed in the Fig. 2.3 presented strong stabilization for $x \geq 0.4$. Thus, the solubilization and stabilization of metallic precursors in solution proved to be a factor of great influence on the control of the average particle diameter. Moreover, magnetic properties such as M_s , demonstrated to be strongly dependent on the composition of the reaction environment in the extent that an increase of x values produces a decrease of saturation magnetization. This can be reasonably attributed to a decrease of the particle size. Additionally, the Mössbauer spectroscopy and magnetization measurements showed that all synthesized nanoparticles presented a superparamagnetic behavior at room temperature. Thus, the methodology herein presented has been proved being effective to obtain superparamagnetic nanoparticles with controlled size (smaller than 13 nm).

References

- AMER, M. A. et al. Spectral studies of Co substituted Ni-Zn ferrites. **Journal of Magnetism and Magnetic Materials**, v. 323, n. 11, p. 1445-1452, 2011. Disponível em: < <http://www.sciencedirect.com/science/article/pii/S0304885310009418> >.
- AQUINO, R. et al. Size control of MnFe₂O₄ nanoparticles in electric double layered magnetic fluid synthesis. **Journal of Magnetism and Magnetic Materials**, v. 252, n. 0, p. 23-25, 2002. ISSN 0304-8853. Disponível em: < <http://www.sciencedirect.com/science/article/pii/S0304885302006078> >.
- ARRUEBO, M. et al. Magnetic nanoparticles for drug delivery. **Nano Today**, v. 2, n. 3, p. 22-32, 2007. ISSN 1748-0132. Disponível em: < <http://www.sciencedirect.com/science/article/pii/S1748013207700841> >.
- BARRETO, A. C. H. et al. Grain Size Control of the Magnetic Nanoparticles by Solid State Route Modification. **Journal of Materials Engineering and Performance**, p. 1-7, 2012. Disponível em: < <http://dx.doi.org/10.1007/s11665-013-0480-8> >.
- _____. Grain Size Control of the Magnetic Nanoparticles by Solid State Route Modification. **Journal of Materials Engineering and Performance**, v. 22, n. 7, p. 2073-2079, 2013. Disponível em: < <http://dx.doi.org/10.1007/s11665-013-0480-8> >.
- BARRETO, A. C. H. et al. Magnetic nanoparticles for a new drug delivery system to control quercetin releasing for cancer chemotherapy. **Journal of Nanoparticle Research**, v. 13, n. 12, p. 6545-6553, 2011. Disponível em: < <http://dx.doi.org/10.1007/s11051-011-0559-9> >.
- BARRETO, A. N. et al. Magnetic Nanosystem for Cancer Therapy Using Oncocalyxone A, an Antitumor Secondary Metabolite Isolated from a Brazilian Plant. **International Journal of Molecular Sciences**, v. 14, n. 9, p. 18269-18283, 2013. ISSN 1422-0067. Disponível em: < <http://www.mdpi.com/1422-0067/14/9/18269> >.
- BEZERRA, M. J. O. S. **Síntese e Caracterização da ferrita de MnZn obtida pelo método dos citratos precursores** 2007. Química, Universidade Federal do Rio Grande do Norte, Natal.
- BLEICHER, L.; SASAKI, J. M.; PAIVA SANTOS, C. O. Development of a graphical interface for the Rietveld refinement program DBWS. **Journal of Applied Crystallography**, v. 33, n. 4, p. 1189-1189, 2000. Disponível em: < <http://dx.doi.org/10.1107/S0021889800005410> >.
- BOTELHO, M. A. et al. Protective effect of locally applied carvacrol gel on ligature-induced periodontitis in rats: a tapping mode AFM study. **Phytotherapy Research**, v. 23, n. 10, p. 1439-1448, 2009. Disponível em: < <http://dx.doi.org/10.1002/ptr.2798> >.
- BOTELHO, M. A. et al. Nanotechnology in ligature-induced periodontitis: protective effect of a doxycycline gel with nanoparticles. **Journal of Applied Oral Science**, v. 18, p. 335-342, 2010. ISSN 1678-7757. Disponível em: <

http://www.scielo.br/scielo.php?script=sci_arttext&pid=S1678-77572010000400003&nrm=iso >.

BOTELHO, M. A. et al. Effects of a new testosterone transdermal delivery system, biolipidb2®-testosterone in healthy middle aged men: a confocal raman spectroscopy study. **Journal of Pharmaceutical and Scientific Innovation**, v. 2, n. 2, p. 1-7, 2013.

BOYER, C. et al. The design and utility of polymer-stabilized iron-oxide nanoparticles for nanomedicine applications. **NPG Asia Mater**, v. 2, p. 23-30, 2010. ISSN 1884-4049. Disponível em: < <http://dx.doi.org/10.1038/asiamat.2010.6> >.

CARUNTU, D. et al. Reactivity of 3d Transition Metal Cations in Diethylene Glycol Solutions. Synthesis of Transition Metal Ferrites with the Structure of Discrete Nanoparticles Complexed with Long-Chain Carboxylate Anions. **Inorganic Chemistry**, v. 41, n. 23, p. 6137-6146, 2013/02/08 2002. Disponível em: < <http://dx.doi.org/10.1021/ic025664j> >.

CHANG, P. R. et al. Polysaccharides as stabilizers for the synthesis of magnetic nanoparticles. **Carbohydrate Polymers**, v. 83, n. 2, p. 640-644, 2011. Disponível em: < <http://www.sciencedirect.com/science/article/pii/S0144861710006478> >.

CHKOUNDALI, S. et al. Nickel ferrite nanoparticles: elaboration in polyol medium via hydrolysis, and magnetic properties. **Journal of Physics: Condensed Matter**, v. 16, n. 24, p. 4357, 2004. ISSN 0953-8984. Disponível em: < <http://stacks.iop.org/0953-8984/16/i=24/a=017> >.

CHOI, H. C.; JUNG, Y. M.; KIM, S. B. Size effects in the Raman spectra of TiO₂ nanoparticles. **Vibrational Spectroscopy**, v. 37, n. 1, p. 33-38, 2005. Disponível em: < <http://www.sciencedirect.com/science/article/pii/S0924203104000839> >.

CLEMENTE, C. S. et al. Porphyrin synthesized from cashew nut shell liquid as part of a novel superparamagnetic fluorescence nanosystem. **Journal of Nanoparticle Research C7 - 1739**, v. 15, n. 6, p. 1-10, 2013. Disponível em: < <http://dx.doi.org/10.1007/s11051-013-1739-6> >.

DAI, Z.; MEISER, F.; MOHWALD, H. Nanoengineering of Iron Oxide and Iron Oxide/Silica Hollow Spheres by Sequential Layering Combined with a Sol-gel Process. **Journal of Colloid and Interface Science** v. 288, p. 298 - 300, 2005.

DAWOUD, H. A Structural Study of Cu-Zn Ferrites by Infrared Spectra. **Al-aqsa Journal**, v. 10, p. 247-262, 2006.

DICKSON, D. P. E.; BERRY, F. J. **Mössbauer spectroscopy**. United States of America: Cambridge University Press, 1986.

FENG, B. et al. Synthesis of Fe₃O₄/APTES/PEG diacid functionalized magnetic nanoparticles for MR imaging. **Colloids and Surfaces A: Physicochemical and Engineering Aspects**, v. 328, n. 1-3, p. 52-59, 2008. Disponível em: < <http://www.sciencedirect.com/science/article/pii/S0927775708004184> >.

FREIRE, R. M.; BARRETO, A. C. H.; FECHINE, P. B. A. Nanopartículas Magnéticas: Aplicações terapêuticas no combate ao câncer. **Revista ABM - Metalurgia, Materiais e Mineração**, v. 68, p. 54-56, 2012.

FREIRE, R. M. et al. $MZnFe_2O_4$ (M = Ni, Mn) cubic superparamagnetic nanoparticles obtained by hydrothermal synthesis. **Journal of Nanoparticle Research C7 - 1616**, v. 15, n. 5, p. 1-12, 2013. Disponível em: < <http://dx.doi.org/10.1007/s11051-013-1616-3> >.

GONZAGA, L. W. et al. Nanotechnology in hormone replacement therapy: Safe and efficacy of transdermal estriol and estradiol nanoparticles after 5 Years Follow-Up Study. **Latin American Journal of Pharmacy**, v. 31, n. 03, p. 442-450, 2012. ISSN 0326-2383.

GUPTA, R. et al. Raman study of stoichiometric and Zn-doped Fe_3O_4 . **Physical Review B**, v. 65, n. 10, p. 104430, 2002. Disponível em: < <http://link.aps.org/doi/10.1103/PhysRevB.65.104430> >.

HASSNAIN JAFFARI, G. et al. Effect of particle size distribution on the magnetic properties $g-Fe_2O_3$ nanoparticles. **Materials Science and Engineering: B**, v. 177, n. 12, p. 935-941, 2012. Disponível em: < <http://www.sciencedirect.com/science/article/pii/S0921510712002619> >.

JOSYULU, O. S.; SOBHANADRI, J. The far-infrared spectra of some mixed cobalt zinc and magnesium zinc ferrites. **physica status solidi (a)**, v. 65, n. 2, p. 479-483, 1981. Disponível em: < <http://dx.doi.org/10.1002/pssa.2210650209> >.

KNETSCH, D.; L. GROENEVELD, W. Alcohol as ligands. III. Complexes of Ethylene glycol with some divalent metal halides. **Inorganica Chimica Acta**, v. 7, n. 0, p. 81-87, 1973. Disponível em: < <http://www.sciencedirect.com/science/article/pii/S0020169300947844> >.

KNOBEL, M. et al. Superparamagnetism and Other Magnetic Features in Granular Materials: A Review on Ideal and Real Systems. **Journal of Nanoscience and Nanotechnology**, v. 8, p. 2836–2857, 2008.

LAOKUL, P. et al. Characterization and magnetic properties of nanocrystalline $CuFe_2O_4$, $NiFe_2O_4$, $ZnFe_2O_4$ powders prepared by the Aloe vera extract solution. **Current Applied Physics**, v. 11, n. 1, p. 101-108, 2011. Disponível em: < <http://www.sciencedirect.com/science/article/pii/S1567173910001859> >.

LATORRE-ESTEVEZ, M. et al. Synthesis and characterization of carboxymethyl dextran-coated Mn/Zn ferrite for biomedical applications. **Journal of Magnetism and Magnetic Materials**, v. 321, n. 19, p. 3061-3066, 2009. Disponível em: < <http://www.sciencedirect.com/science/article/pii/S0304885309005253> >.

LEE, J. H. et al. The characteristics of Ni–Zn ferrite powder prepared by the hydrothermal process. **Journal of Materials Science Letters**, v. 18, n. 13, p. 1029-1031, 1999. Disponível em: < <http://dx.doi.org/10.1023/A:1006619409011> >.

LV, W.-Z. et al. XRD studies on the nanosized copper ferrite powders synthesized by sonochemical method. **Journal of Alloys and Compounds**, v. 465, n. 1-2, p. 261-264, 2008. Disponível em: <

<http://www.sciencedirect.com/science/article/pii/S0925838807020014> >.

MAAZ, K. et al. Synthesis and magnetic properties of cobalt ferrite (CoFe₂O₄) nanoparticles prepared by wet chemical route. **Journal of Magnetism and Magnetic Materials**, v. 308, n. 2, p. 289-295, 2007. Disponível em: <

<http://www.sciencedirect.com/science/article/pii/S030488530600895X> >.

MAIA, A. O. G. et al. Synthesis and X-ray structural characterization of NiO nanoparticles obtained through gelatin. **Journal of Non-Crystalline Solids**, v. 352, n. 32-35, p. 3729-3733, 2006. Disponível em: <

<http://www.sciencedirect.com/science/article/pii/S002230930600754X> >.

MIYAKE, A. Infrared spectra of glycols coordinated to metal ions. **Bulletin of the Chemical Society of Japan**, v. 32, p. 1381-1383, 1959.

MOHAMMED, K. A. et al. Infrared and structural studies of Mg_{1-x}Zn_xFe₂O₄ ferrites. **Physica B: Condensed Matter**, v. 407, n. 4, p. 795-804, 2012. Disponível em: <

<http://www.sciencedirect.com/science/article/pii/S0921452611012907> >.

MORRISH, A. H.; HANEDA, K. Non-collinearity as a crystallite-size effect of g-Fe₂O₃ small particles. **J. Phys. Colloques**, v. 41, n. C1, p. C1-171-C1-172, 1980. Disponível em: < <http://dx.doi.org/10.1051/jphyscol:1980147> >.

MOZAFFARI, M. et al. The effect of solution temperature on crystallite size and magnetic properties of Zn substituted Co ferrite nanoparticles. **Journal of Magnetism and Magnetic Materials**, v. 322, n. 4, p. 383-388, 2010. Disponível em: <

<http://www.sciencedirect.com/science/article/pii/S0304885309009482> >.

PAIVA, A. C. L. A. et al. Síntese e caracterização de pós de ferrita Mn-Zn: efeito da substituição do Mn²⁺ pelo Fe²⁺ e da quantidade de H₂O. **Revista Eletrônica de Materiais e Processos**, v. 3.1, p. 25-30, 2008.

PÉREZ-MIRABET, L. et al. One-pot synthesis of stable colloidal solutions of MFe₂O₄ nanoparticles using oleylamine as solvent and stabilizer. **Materials Research Bulletin**, v. 48, n. 3, p. 966-972, 2013. Disponível em: <

<http://www.sciencedirect.com/science/article/pii/S0025540812009282> >.

PÉREZ, J. A. L. et al. Advances in the Preparation of Magnetic Nanoparticles by the Microemulsion Method. **Journal of Physical Chemistry B**, v. 101, p. 8045 - 8047, 1997.

PODDAR, P. et al. Inter-particle interactions and magnetism in manganese-zinc ferrite nanoparticles. **Journal of Magnetism and Magnetic Materials**, v. 288, n. 0, p. 443-451, 2005. Disponível em: <

<http://www.sciencedirect.com/science/article/pii/S0304885304010753> >.

- PORTO, S. Normal Mode Determination in Crystals. **Journal of Raman Spectroscopy**, v. 10, p. 253-290, 1981.
- POUL, L. et al. Synthesis of Inorganic Compounds (Metal, Oxide and Hydroxide) in Polyol Medium: A Versatile Route Related to the Sol-Gel Process. **Journal of Sol-Gel Science and Technology**, v. 26, n. 1-3, p. 261-265, 2003. Disponível em: < <http://dx.doi.org/10.1023/A%3A1020763402390> >.
- RAMING, T. P. et al. The Synthesis and Magnetic Properties of Nanosized Hematite (α-Fe₂O₃) Particles. **Journal of Colloid and Interface Science**, v. 249, n. 2, p. 346-350, 2002. Disponível em: < <http://www.sciencedirect.com/science/article/pii/S0021979701981949> >.
- RAVINDER, D. Far-infrared spectral studies of mixed lithium-zinc ferrites. **Materials Letters**, v. 40, n. 5, p. 205-208, 1999. Disponível em: < <http://www.sciencedirect.com/science/article/pii/S0167577X99000750> >.
- REDDY, P. V.; SALAGRAM, M. The far-infrared spectra of mixed manganese–magnesium ferrites. **physica status solidi (a)**, v. 100, n. 2, p. 639-643, 1987. Disponível em: < <http://dx.doi.org/10.1002/pssa.2211000230> >.
- RIETVELD, H. Line profiles of neutron powder-diffraction peaks for structure refinement. **Acta Crystallographica**, v. 22, n. 1, p. 151-152, 1967. ISSN 0365-110X. Disponível em: < <http://dx.doi.org/10.1107/S0365110X67000234> >.
- RIMAN, R. E. et al. Solution synthesis of hydroxyapatite designer particulates. **Solid State Ionics**, v. 151, n. 1-4, p. 393-402, 2002. Disponível em: < <http://www.sciencedirect.com/science/article/pii/S0167273802005453> >.
- SÁNCHEZ, R. D. et al. Particle size effects on magnetic properties of yttrium iron garnets prepared by a sol-gel method. **Journal of Magnetism and Magnetic Materials**, v. 247, n. 1, p. 92-98, 2002. Disponível em: < <http://www.sciencedirect.com/science/article/pii/S0304885302001701> >.
- SATO, T. et al. Magnetic properties of ultrafine ferrite particles. **Journal of Magnetism and Magnetic Materials**, v. 65, n. 2-3, p. 252-256, 1987. Disponível em: < <http://www.sciencedirect.com/science/article/pii/0304885387900448> >.
- SHEBANOVA, O. N.; LAZOR, P. Raman spectroscopic study of magnetite (FeFe₂O₄): a new assignment for the vibrational spectrum. **Journal of Solid State Chemistry**, v. 174, n. 2, p. 424-430, 2003. Disponível em: < <http://www.sciencedirect.com/science/article/pii/S0022459603002949> >.
- SHOKROLLAHI, H.; JANGHORBAN, K. Influence of additives on the magnetic properties, microstructure and densification of Mn-Zn soft ferrites. **Materials Science and Engineering: B**, v. 141, n. 3, p. 91-107, 2007. Disponível em: < <http://www.sciencedirect.com/science/article/pii/S0921510707002632> >.
- SIDDIQUE, M.; BUTT, N. M. Effect of particle size on degree of inversion in ferrites investigated by Mossbauer spectroscopy. **Physica B: Condensed Matter**, v. 405, n. 19,

p. 4211-4215, 2010. Disponível em: <

<http://www.sciencedirect.com/science/article/pii/S0921452610007003> >.

SINGHAL, S.; BARTHWAL, S. K.; CHANDRA, K. Structural, magnetic and Mossbauer spectral studies of nanosize aluminum substituted nickel zinc ferrites.

Journal of Magnetism and Magnetic Materials, v. 296, n. 2, p. 94-103, 2006.

Disponível em: < <http://www.sciencedirect.com/science/article/pii/S0304885305001113> >.

SORESCU, M. et al. Hydrothermal synthesis and structural characterization of (1-x)a-Fe₂O₃-xSnO₂ nanoparticles. **Journal of Physics and Chemistry of Solids**, v. 65, n. 5, p. 1021-1029, 2004. Disponível em: <

<http://www.sciencedirect.com/science/article/pii/S0022369703004736> >.

SRIVASTAVA, M.; CHAUBEY, S.; OJHA, A. K. Investigation on size dependent structural and magnetic behavior of nickel ferrite nanoparticles prepared by sol-gel and hydrothermal methods. **Materials Chemistry and Physics**, v. 118, n. 1, p. 174-180, 2009. Disponível em: <

<http://www.sciencedirect.com/science/article/pii/S0254058409004246> >.

SUCHANEK, W. L.; RIMAN, R. E. Hydrothermal Synthesis of Advanced Ceramic Powders. **Advances in Science and Technology** v. 45, p. 184-193, 2006.

SUGIMOTO, M. The Past, Present, and Future of Ferrites. **Journal of the American Ceramic Society**, v. 82, n. 2, p. 269-280, 1999. Disponível em: <

<http://dx.doi.org/10.1111/j.1551-2916.1999.tb20058.x> >.

THOMAS, M.; GEORGE, K. C. Infrared and magnetic study of nanophase zinc ferrite. **Indian Journal of Pure & Applied Physics**, v. 47, p. 81-86, 2009.

UPADHYAY, C. et al. Effect of preparation conditions on formation of nanophase Ni-Zn ferrites through hydrothermal technique. **Journal of Magnetism and Magnetic Materials**, v. 260, n. 1, p. 188-194, 2003. Disponível em: <

<http://www.sciencedirect.com/science/article/pii/S0304885302013203> >.

VALENZUELA, R. et al. Influence of stirring velocity on the synthesis of magnetite nanoparticles (Fe₃O₄) by the co-precipitation method. **Journal of Alloys and Compounds**, v. 488, n. 1, p. 227-231, 2009. Disponível em: <

<http://www.sciencedirect.com/science/article/pii/S0925838809016545> >.

VELMURUGAN, K.; VENKATACHALAPATHY, V. S. K.; SENDHILNATHAN, S. Synthesis of nickel zinc iron nanoparticles by coprecipitation technique. **Materials Research**, v. 13, n. 3, p. 299-303, 2010. ISSN 1516-1439. Disponível em: <

http://www.scielo.br/scielo.php?script=sci_arttext&pid=S1516-14392010000300005&nrm=iso >.

WALDRON, R. D. Infrared Spectra of Ferrites. **Physical Review**, v. 99, n. 6, p. 1727-1735, 1955.

WANG, J. et al. Solvothermal synthesis and magnetic properties of size-controlled nickel ferrite nanoparticles. **Journal of Alloys and Compounds**, v. 479, n. 1-2, p. 791-796, 2009. Disponível em: < <http://www.sciencedirect.com/science/article/pii/S0925838809001054> >.

WANG, L.; LI, F. S. Mossbauer study of nanocrystalline Ni-Zn ferrite. **Journal of Magnetism and Magnetic Materials**, v. 223, n. 3, p. 233-237, 2001. Disponível em: < <http://www.sciencedirect.com/science/article/pii/S0304885300013317> >.

YÁÑEZ-VILAR, S. et al. A simple solvothermal synthesis of MFe₂O₄ (M=Mn, Co and Ni) nanoparticles. **Journal of Solid State Chemistry**, v. 182, n. 10, p. 2685-2690, 2009. Disponível em: < <http://www.sciencedirect.com/science/article/pii/S0022459609003491> >.

YING, J. Y. et al. STM/AFM study of grain boundary migration in nanostructured solids. **Materials Letters**, v. 15, n. 3, p. 180-185, 1992. Disponível em: < <http://www.sciencedirect.com/science/article/pii/0167577X92901416> >.

ZHANG, C. F. et al. Effects of cobalt doping on the microstructure and magnetic properties of Mn-Zn ferrites prepared by the co-precipitation method. **Physica B: Condensed Matter**, v. 404, n. 16, p. 2327-2331, 2009. Disponível em: < <http://www.sciencedirect.com/science/article/pii/S0921452609002592> >.

ZHANG, L.; HE, R.; GU, H.-C. Oleic acid coating on the monodisperse magnetite nanoparticles. **Applied Surface Science**, v. 253, n. 5, p. 2611-2617, 2006. Disponível em: < <http://www.sciencedirect.com/science/article/pii/S0169433206007197> >.

CHAPTER 3

3 MORPHOLOGIC AND MAGNETIC PROPERTIES OF SUPERPARAMAGNETIC NiZn FERRITES OBTAINED BY HYDROTHERMAL ROUTE

Abstract

$\text{Ni}_{0.5}\text{Zn}_{0.5}\text{Fe}_2\text{O}_4$ superparamagnetic nanoparticles (NPs) were successfully synthesized using hydrothermal method under different experimental conditions. The influence of the NaOH concentration and hydrothermal reaction time on the magnetic nanoparticles (MNPs) properties were fully investigated by Powder X-ray Diffraction (PXRD), Fourier Transform Infrared Spectroscopy (FT-IR), Mössbauer spectroscopy, Transmission Electron Microscopy (TEM), Vibrating Sample Magnetometer (VSM) and Zero Field-Cooled (ZFC)/Field-Cooled (FC) magnetization curves. The average crystallite size calculated through different methods was found to change (13.1 – 49.2 nm) with increase of NaOH concentration, but remain similar by changing of hydrothermal reaction time (10.7 – 20.3 nm). TEM images showed a square-like structure for MNP3 – 4, while MNP5 – 7 presented shape from truncated hexagonal to quasi-sphere structures. All samples presented ferrimagnetic behavior when analyzed by Mössbauer spectroscopy. However, the magnetic properties through VSM lead to the superparamagnetic regime, since absence of loop hysteresis was observed. The saturation magnetization (M_s) shows itself a parameter largely surface effect-dependent. The thickness (t) of the dead layer calculated considering the core-shell MNPs structure was found to be in the range 1.18 – 2.56 nm. The trend of the t values explain the change on the M_s observed for MNP3 – 7. This shows the predominant effect of the surface effects for the magnetic properties of the MNPs. Further, the results observed in the ZFC/FC curves displayed a different source for the effect of NaOH concentration and hydrothermal reaction time under blocking temperature (T_b) values achieved (103 – 153K) for the samples synthesized in this work.

Keywords: Magnetic materials. Nanostructures. Chemical synthesis. Magnetic properties

3.1 Introduction

Magnetic nanoparticles (MNPs) represent an interesting class of the materials frequently used for the development of the nanotechnology (Naseri and B.Saion, 2012). Their versatility due to intrinsic magnetic properties have been attracted many researchers around the world. Since allow the applications of MNPs on many fields of the knowledge, such as nanomedicine (Dave and Gao, 2009; Barreto, A. *et al.*, 2013), environmental (Tang and Lo, 2013), among others (Latham and Williams, 2008). The most used MNPs for the many applications cited show the spinel – type structure, which can be described as a cubic close-packed arrangement of oxygen atoms with spatial symmetry group O_h^7 ($Fd3m$) (Freire *et al.*, 2013). The general formula is MFe_2O_4 or $MO.Fe_2O_3$, where M is a divalent metal with positive charge (Ni^{2+} , Mn^{2+} , Zn^{2+} , among others) (Kumar *et al.*, 2011). Since the spinel – type structure present octahedral and tetrahedral sites in your network, another general formula can be used to describe the position of the divalent and trivalent cations is the $(A)[B]_2O_4$. Here, the parentheses and brackets indicate the cation in the tetrahedral and octahedral site, respectively.

Although the same structure for materials from spinel class, it is important to emphasize that each application require special characteristics. Thus, the control of MNPs properties is very important. This may be done using different synthetic routes and experimental conditions. Since the physical and chemical MNPs properties are size- and morphology-dependent (Tang *et al.*, 1991). Given this, methodologies including co-precipitation (Barreto, A. C. H. *et al.*, 2013), Sol-Gel (Kumar *et al.*, 2011), microemulsion (Kořak *et al.*, 2004), hydrothermal reaction (Seema *et al.*, 2004), flow injection (Alvarez, 2004) and others were developed to synthesize MNPs. However, it is important to highlights the hydrothermal method owing to the ability to precipitate already crystallized powders directly from solution. It also regulates the rate and uniformity of nucleation, growth and aging represent a great advantage (Suchanek and Riman, 2006). Additionally, the literature (Karaagac *et al.*, 2015) reports that the control of the structural, morphological and magnetic properties can be reached from experimental conditions used during synthesis of the MNPs.

In the present work, $Ni_{0.5}Zn_{0.5}Fe_2O_4$ superparamagnetic NPs were prepared using the hydrothermal method in different experimental conditions. We investigate the influence of the change of the NaOH concentration and hydrothermal reaction time on the

structural, morphologic and magnetic properties of the MNPs. Square, hexagonal and quasi-spheres structures were the morphologies obtained changing the experimental conditions. This can be clearly seen in the TEM micrographs. A shape transition was observed along the hydrothermal reaction time. Assuming the core-shell NPs model, our results suggest that the magnetic properties such as M_s were highly affected by thickness (t) of the dead layer, while T_b values were found to be influenced by magnetically ordered core size and surface disorder. Therefore, this study additionally helps to understand the dependency of the MNPs properties as a function of experimental conditions.

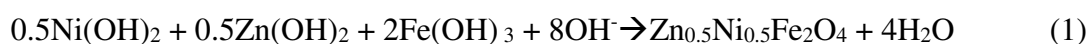
3.2 Materials and Methods

3.2.1 Chemicals

The chemical reagents for this study were glacial acetic acid ($C_2H_4O_2$, Vetec, 99.8%), iron(III) chloride hexahydrate ($FeCl_3 \cdot 6H_2O$, Dinâmica, 97 %), nickel chloride hexahydrate ($NiCl_2 \cdot 6H_2O$, Vetec, 97 %), zinc chloride anhydrous ($ZnCl_2$, Dinâmica, 97 %) and sodium hydroxide (NaOH, Cinética Química, 97 %). All chemicals were used without further purification.

3.2.2 Synthesis of $Ni_{0.5}Zn_{0.5}Fe_2O_4$ MNPs

The MNPs were synthesized using the co-precipitation method following by hydrothermal reaction (Lee *et al.*, 1999; Freire *et al.*, 2013). Firstly, the salt precursors were dissolved at a molar ratio 0.5:0.5:2 (1.85 Ni:1.85 Zn:7.39 mM Fe) using distilled water previously acidified with 50 μ L of acetic acid. Under vigorous mechanical stirring, 10 mL of NaOH was gradually added into the mixture to precipitate the desired hydroxides. In this step, different concentrations (3.0 - 5.2 M) of the NaOH were evaluated in order to understand their influence on the MNPs properties. The resultant solution was carried to a Teflon-lined autoclave to perform the hydrothermal reaction for different times (0.5 - 24h) at 250 °C. The reactions occurring during the synthetic process can be summarized as follows:



Afterward of the hydrothermal reaction performed for respective time, the product resultant was naturally cooled down to the room temperature. The MNPs were filtered

and then exhaustively washed with distilled water and methanol. Finally, the powder was dried in the oven at 100° C for 3 h and stored for characterization. Table 3.1 shows all the conditions used as well as the label for each sample synthesized in this work.

Table 3.1. Label for all the samples as well as the used conditions (NaOH concentration and time).

Samples	[NaOH] (mol.L ⁻¹)	time (h)
MNP1	3.0	0.5
MNP2	3.3	0.5
MNP3	4.5	0.5
MNP4	5.2	0.5
MNP5	3.7	6
MNP6	3.7	12
MNP7	3.7	24

Source: Author

3.2.3 Characterization of MNPs

The PXRD analysis was obtained using CuK α (1.54056 Å) from X-ray powder diffractometer Rigaku with Bragg–Brentano geometry in the angular range of 15–85 (2θ). The phase identification analysis was made by comparing powder diffractograms with standard patterns from International Centre for Diffraction Data. Rietveld refinement procedures (Rietveld, 1967) were applied to all diffraction patterns using the DBWS 2.25 (Bleicher *et al.*, 2000). Fourier Transform Infrared (FTIR) spectrum was carried out on a Perkin–Elmer Spectrometer in the range 4,000–400 cm⁻¹. In recording IR spectra, the samples were mixed with potassium bromide powder and pressed into pellets. The Mössbauer spectra were recorded at room temperature (300 K) from FAST (ConTec) Mössbauer System spectrometer using transmission geometry. A ⁵⁷Co radioactive source was used. The data analysis was performed using NORMOS program written by R. A. Brand (distributed by Wissenschaftliche Elektronik GmbH, Germany). Isomer shifts (δ) are referred as α -Fe at room temperature. The magnetic measurements were obtained using a vibrating sample magnetometer (Cryogenic VSM 5 Tesla system) with a temperature range 5–300 K. The VSM has been previously calibrated using a pure Ni sphere, and after measuring the mass of each sample the magnetization was given in emu/g. The TEM images were obtained at MSC JEOL TEM-2100 200 kV, equipped with

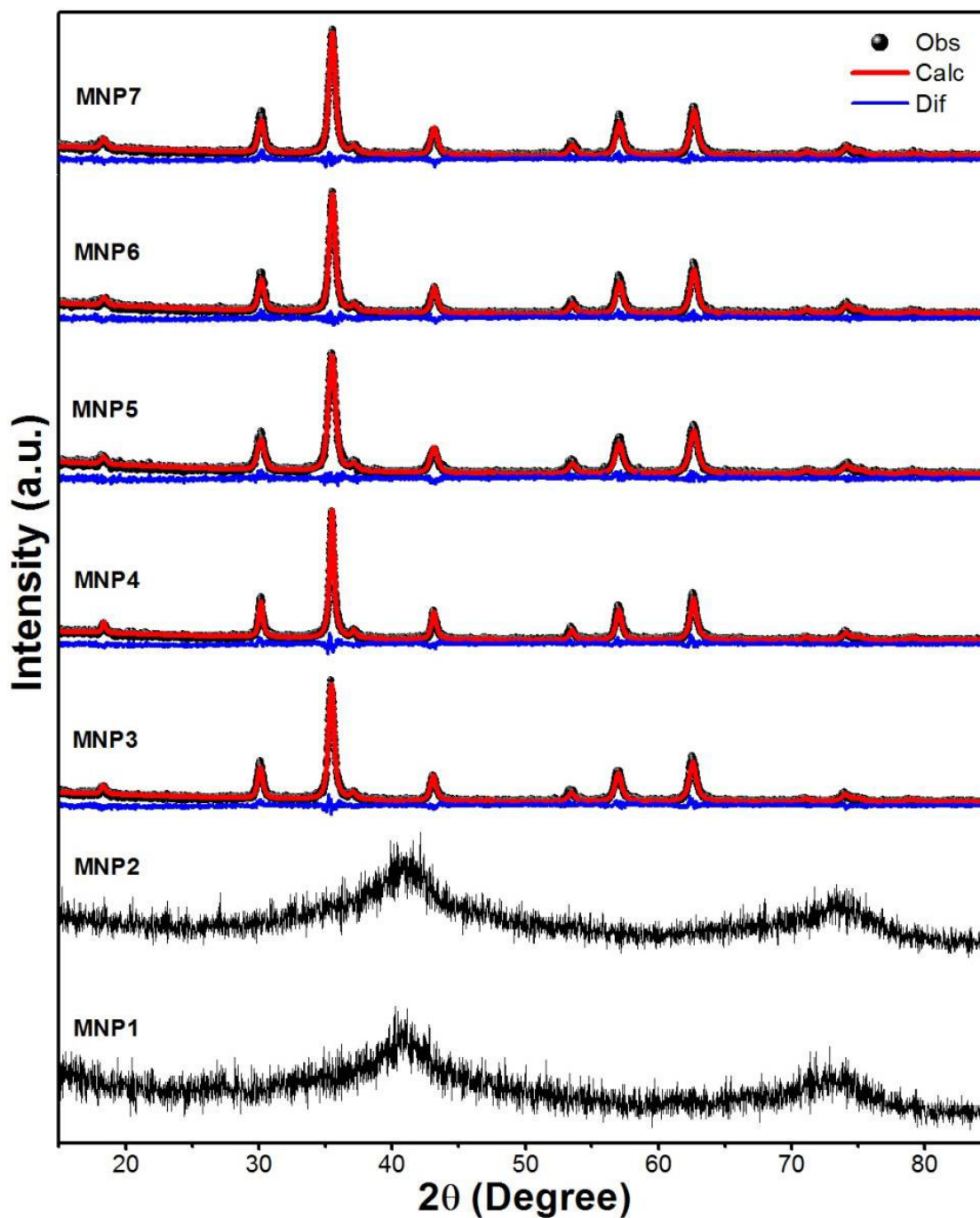
a CCD (TVips– 16MP) and TV (Gatan ES500W) available in LNNano, Campinas, Brazil. TEM samples were dispersed in isopropyl alcohol to which was added in a drop onto carbon-coated copper grids. Afterward, the deposited samples are allowed to completely dry overnight before examination.

3.3 Results and discussion

3.3.1 PXRD

PXRD patterns for all samples synthesized in this work are showed in the Fig. 3.1. It was possible to observe diffraction peaks at 30.1° , 35.4° , 43.1° , 53.4° , 57.0° , 62.5° , 74.1° and 89.7° for samples MNP3 – 7. Clearly, these peaks indicated the formation of the spinel structure without any additional thermal process (calcination, for example) after the hydrothermal reaction performed. For samples MNP1 – 4, the parameter evaluated was the NaOH concentration (Fig. 3.1), while for MNP5 – 7, it was the hydrothermal reaction time. The standard parameters (for example, NaOH concentration for MNP5 – 7) to perform this experimental condition study was based on works previously published in our group (Freire *et al.*, 2013). The absence of peaks was observed for samples MNP1 – 2 owing to the amorphous structure. Thus, the experimental conditions used to synthesize these samples were not enough to get crystalline MNPs. Since the amount of NaOH used was stoichiometrically enough to the crystallization process, explanations related to this were discarded. Thus, amorphous-like structure may be caused by interference of chemical species, which might inhibit the crystallization process. In our case, the impurities of the chemicals or even acetic acid used can be classified as an interfering. Moreover, small NP size can also explain amorphous behavior observed (Karaagac *et al.*, 2015).

Figure 3.1. PXRD patterns for samples MNP1 – 7 as well as the fit made using the Rietveld Method.



Source: Author

Rietveld refinement was performed for samples MNP3 – 7 to obtain data from crystalline structure, such as average crystallite size, microstrain and network parameters (Table 3.2). In addition, this Table also shows the Rwp and S values. These parameters can be utilized to check the good agreement between experimental and calculated data from the

refinement. The values smaller than 20% and 1.3 for Rwp and S, respectively, evidenced the reliability of the refinement performed. One can also observe in Fig. 3.1, that the blue line represents the relative difference between the observed (Obs) and the calculated (Calc) intensity obtained by the Rietveld refinement. Since the samples MNP1 – 2 do not show any diffractions peaks from spinel structure, they are not refined. The crystallite size was obtained from refinement data using the Scherrer and Willinasom-Hall (WH) equations (Barreto, A. C. H. *et al.*, 2013). For samples MNP3 – 4, it was possible to observe an increase of the size as a function of the NaOH concentration. The relationship involving NaOH concentration and size can be explained by the interaction between the nucleation (formation of crystallization center) and the NP growth processes (Aquino *et al.*, 2002). The crystal growth is more efficient at high concentration due to the displaced of the equilibrium towards hydrolysis and condensation reactions. Growth prevails against the nucleation, which leads to a small number of large particles. On the other hand, small concentration leads to a metastable equilibrium state and an inefficient deprotonation of intermediate structures (Equations 1, 2, 3 and some dimers rising from polymerization reaction) can be observed. This favors a rapid nucleation to form a large number of small NPs (Ribeiro, 2008). Furthermore, the rapid growth can lead to the poor formation of crystals. Clearly, this was evidenced by microstrain (ε) values found for the samples MNP3 and MNP4 (0.212 and 0.276, respectively). The effect from higher heterogeneity with the increase of NaOH concentration can also be seen on the crystallite size values calculated using the WH equation. It was observed differences when compared to the values found using Scherrer and WH equations. Moreover, the network parameters showed a descending behavior with increase of the NaOH concentration: 8.3901 and 8.3881 Å for 4.5 mol.L⁻¹ (MNP3) and 5.2 mol.L⁻¹ (MNP4), respectively. This may be attributed to the cationic mobility between the tetrahedral and octahedral sites. The defects evidenced by high ε values might influence the network parameter and magnetic properties of the MNPs.

For samples MNP5 – 7, no regular behavior was observed for network parameter values. However, it was found smaller changes in the crystallite size (13.3 – 20.0 nm) when compared to the samples MNP3 (15.8 nm) and MNP4 (49.2 nm). As mentioned before, the large range found for samples MNP3 – 4 was due to the interference caused by large ε values (0.212 and 0.276, respectively). The ε values found for the samples MNP5 – 7 were 0.127, 0.127 and 0.142, respectively. These smaller values can explain the short

range observed. Therefore, it is important to emphasize that the changes in ε values from the samples under NaOH concentration were bigger than ones synthesized as a function of the reaction time. This is directly related with the predominant crystal growth under experimental conditions performed where the equilibrium is shifted towards hydrolysis and condensation reactions. Fast crystal growth is observed and the defects increase causing large ε values (Zhao *et al.*, 2008). In other words, the nucleation process is predominant for the samples synthesized under time change and a slowly crystal growth occur. Thus, the defects should be smaller, as observed in this work.

Table 3.2. Values of average crystallite size (D), microstrain (ε), network parameter, Rwp and S for the samples that showed spinel phase.

Samples	D_s (nm)	D_{WH} (nm)	ε (%)	Network Parameter (Å)	Rwp (%)	S
MNP3	15.8	27.9	0.212	8.3901	15.27	1.14
MNP4	18.8	49.2	0.276	8.3881	15.86	1.17
MNP5	13.3	16.8	0.127	8.3805	15.65	1.14
MNP6	15.5	20.3	0.127	8.3843	16.71	1.19
MNP7	15.8	20.0	0.142	8.3805	15.71	1.16

D_s and D_{WH} values were calculated based on Scherrer and Williamsom-Hall equations, respectively.

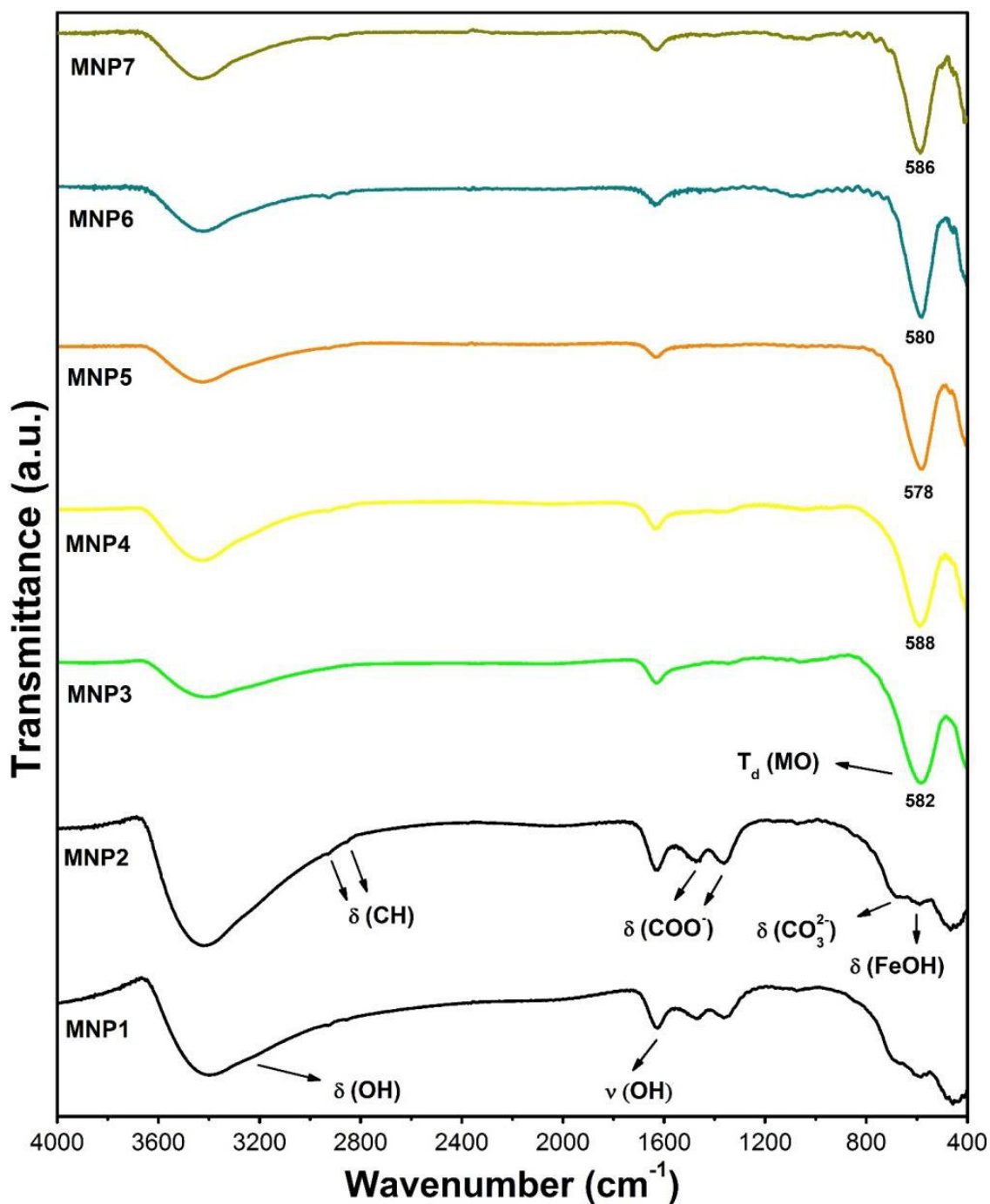
Source: Author

3.3.2 FTIR measurements

Fig. 3.2 shows the FTIR spectra of the samples. According to the literature (Amer *et al.*, 2011), five normal modes ($5T_{1u}$) can be observed from infrared lattice vibration. In the studied range ($4000 - 400 \text{ cm}^{-1}$), only two modes related to octahedral and tetrahedral sites can be seen below 700 cm^{-1} . No bands related to spinel phase were observed for samples MNP1 – 2, which is in agreement with PXRD data. The presence of bands at 3500 and 1500 cm^{-1} can be attributed to the stretch and bend vibrations of O-H group, respectively. For both MNP1 – 2, a band observed at 592 cm^{-1} is characteristic of Fe-OH stretching (Kim *et al.*, 2007). Clearly, these results suggest the presence of intermediate species. Interestingly, bands related to the C-O and C-H species adsorbed on the surface of the MNPs were found for both MNP1 – 2. A band around 690 cm^{-1} can be assigned to the CO_3^{2-} , while bands observed in the range $1500 - 1300 \text{ cm}^{-1}$ are correlated to the COO^-

(Yu and Liu, 2006). It was also possible to observe the presence of bands at 2921 and 2855 cm^{-1} . These bands can be attributed to the vibrations of C-H stretch from alkane species. These results evidence acetate ions adsorbed on the surface of the MNP1 – 2. As such bands were found only for samples which show amorphous structure, it fair to infer that the acetate ions on the surface of the MNPs act as a protecting agent. Therefore, their presence retarded the particle growth during the hydrothermal reaction inhibiting crystallization process. Similar results were observed by Nagase et al. (Nagase *et al.*, 1997). In their work, the authors conclude that the acetic acid was highly able to suppress the crystallization process. So, the same effect was observed in this work.

Figure 3.2. FT-IR for samples MNP1 - 7.



Source: Author

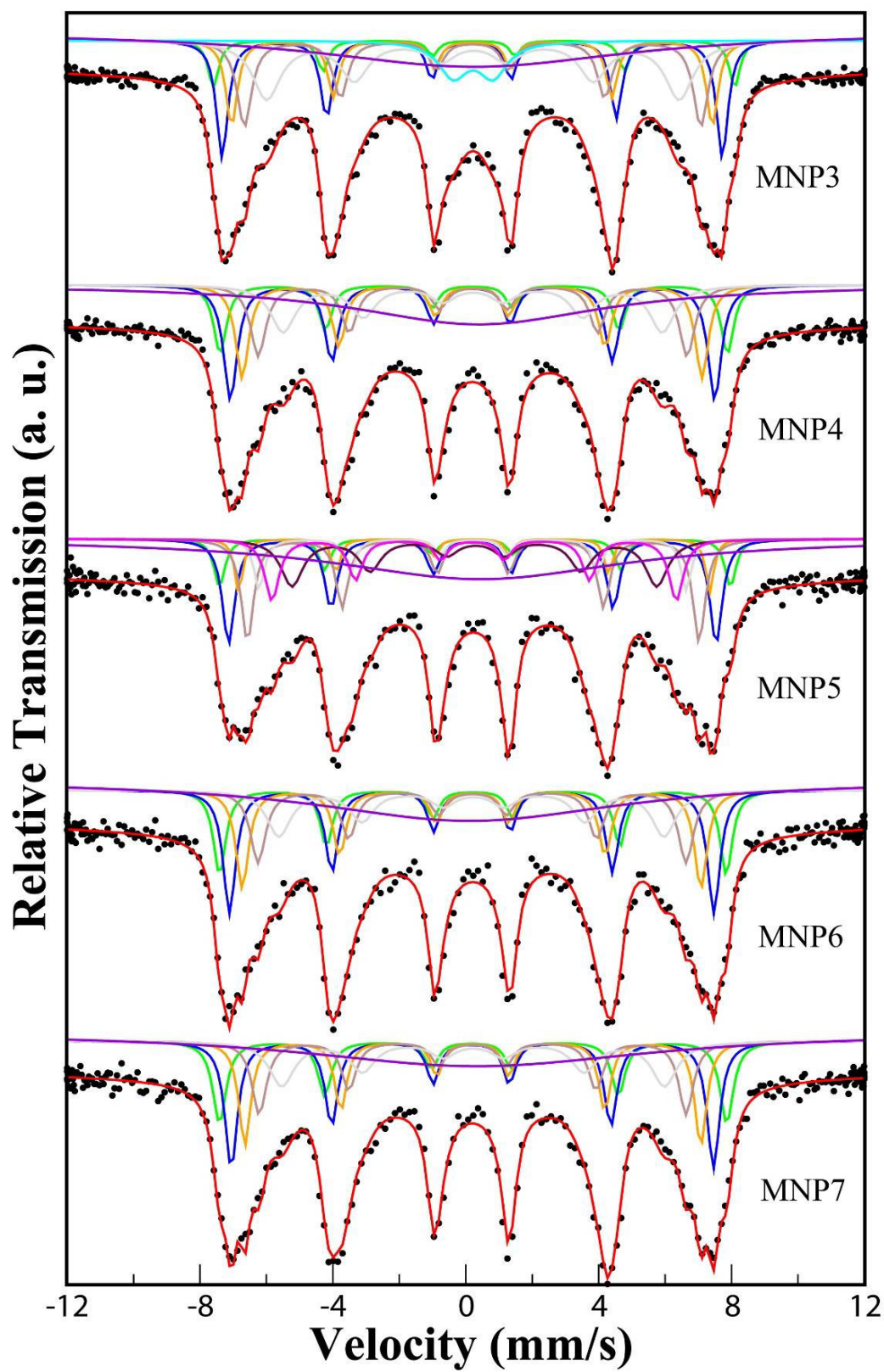
For samples MNP3 – 7, bands related with spinel phase were clearly found. The band in the range 576 – 586 cm^{-1} can be attributed to the tetrahedral site (symmetry T_d) from spinel structure (Maaz *et al.*, 2010). The slight discrepancy observed for wavenumber is due to cationic mobility under different experimental conditions (Sharma *et al.*, 2007). However, it seems that the experimental conditions studied in this work did not show

much influence on the cationic mobility. Another band near to 400 cm^{-1} can be attributed to the “octahedral” site (symmetry D_{3d}) (Freire *et al.*, 2014). The bands at 3500 and 1500 cm^{-1} can be attributed O-H stretch and bend from hydroxyls groups attached on the MNPs surface, respectively. However, it is important to notice that water adsorbed on surface can also contributed for these bands (Kandasamy *et al.*, 2010).

3.3.3 ^{57}Fe Mössbauer Spectroscopy

Fig. 3.3 shows the typical Mössbauer spectra for samples MNP3–7 recorded at room temperature. The experimental data points are represented by the black dots, while the solid red line coincides with least-square fitting. Solid lines with different colors denotes the adjust performed. Many sub-spectra (blue, green, yellow, pink and cyan) were found. Thus, it is possible to infer that iron is located in sites with different magnetic neighborhoods. A central doublet peak was observed only for sample MNP3. This can be attributed for superparamagnetic behavior arises from collapse of the magnetic ordering due to small particle size (Knobel *et al.*, 2008; Malik *et al.*, 2010). On the other hand, a paramagnetic doublet can also appear due to interaction between Fe^{3+} and non-magnetic Zn^{2+} ions (Naik *et al.*, 2014). For all samples, a single peak was found. This V-shaped peak may be assigned to the reduction of the magneto crystalline anisotropy or insertion of zinc in the spinel structure, which reduce the magnetic interactions between sites by decreasing the A–B coupling pairs (Upadhyay *et al.*, 2003). In order to obtain a satisfactory fit to describe the ferromagnetic nature of the samples, a high number of sextet patterns were required. This can be explained by the variety of cations in the sample (Zn^{2+} , Ni^{2+} and Fe^{3+}) as well as their preference for site occupation. It well known that ZnFe_2O_4 is a normal spinel structure in which Zn^{2+} (diamagnetic) has high preference for tetrahedral sites (Lazarević *et al.*, 2014). On the other hand, NiFe_2O_4 is an inverse spinel structure where Ni^{2+} (paramagnetic) occupy octahedral positions (Ivanov *et al.*, 2010). Therefore, the random distribution of the diamagnetic (Zn^{2+}) and paramagnetic (Ni^{2+} and Fe^{3+}) cations lead for many different magnetic neighborhoods. This explains the many sub-spectra necessary to obtain an acceptable fit model for tetrahedral A-site and octahedral B-site. Another plausible explanation for the multi-sextet fit is the presence of canted spins as suggested by Yafet and Kittel (Yafet and Kittel, 1952).

Figure 3.3. Mössbauer spectrum for MNP3 - 7.



Source: Author

The hyperfine parameters obtained are showed in the Table 3.3. The range of isomer shift (δ) values found (0.29 – 0.39 mm/s) indicate high-spin Fe^{3+} state (Naik *et al.*, 2014). The δ is a parameter related with the electrostatic interaction between s-electron with finite probability to be found close to the nucleus and your charge distribution. In other words, the change is this parameter can be interpreted as the difference in the Fe^{3+} –O– Fe^{3+} inter-nuclear separation normally larger for octahedral B-site ions as compared to that for tetrahedral A-site ions (Heiba *et al.*, 2014). Therefore, the larger overlapping of orbitals of Fe^{3+} and O^{2-} ions found for the tetrahedral A-sites will result in a higher covalency and hence smaller δ values. The δ values obtained in this work shown no appreciable changes under different experimental conditions. For the quadrupole interaction (Δ), the most of the values were observed in the range from -0.06 to 0.06 mm/s. This shows a weak influence of the experimental conditions in the Δ parameter. However, a doublet with Δ equal to 1.20 mm/s was found only for MNP3. Non-zero Δ denote the presence of electric field gradient (EFG) arising from chemical disorder in the spinel structure (Kumar *et al.*, 2008). Thus, the large local symmetry reduction in site was observed for MNP3. Moreover, the existence of Fe^{2+} in the spinel structure may also increase the value of Δ (Amer *et al.*, 2014). In addition to the hyperfine parameters discussed, the hyperfine magnetic field (B_{HF}) and percentage area can be used to assign the sub-spectrum to a specific configuration (octahedral B-site or tetrahedral A-site). Based on these parameters, the assignment for each sub-spectrum fitted can be seen in the Table 3.3.

Table 3.3. Mössbauer parameters for MNP3 – 7 samples.

Samples	Sites	Hyperfine parameters			Area (%)
		δ (mm/s)	Δ (mm/s)	B_{HF} (T)	
MNP3	A ₀	0.29	0.02	46.7	15.0
	A ₁	0.30	-0.02	44.9	11.0
	A ₂	0.31	0.00	42.6	14.0
	B ₀	0.35	0.00	48.6	5.60
	B ₁	0.34	-0.03	38.5	18.0
	B ₂	0.33	1.20	-	5.60
	B ₃	0.36	-	-	30.8
MNP4	A ₀	0.31	0.02	45.2	18.5

	A ₁	0.30	-0.02	42.9	14.5
	B ₀	0.33	-0.02	40.0	13.0
	B ₁	0.33	0.04	47.3	10.5
	B ₂	0.32	-0.01	35.4	13.7
	B ₃	0.50	-	-	29.8
MNP5	A ₀	0.30	0.00	45.5	14.6
	A ₁	0.33	0.06	44.0	4.8
	A ₂	0.33	-0.01	42.0	14.2
	A ₃	0.34	-0.04	39.8	5.9
	B ₀	0.39	-0.03	34.0	11.5
	B ₁	0.34	0.05	37.7	9.8
	B ₂	0.54	-	-	33.3
	B ₃	0.35	0.06	47.7	5.9
MNP6	A ₀	0.22	-	-	35.0
	A ₁	0.29	-0.01	45.2	14.6
	B ₀	0.30	-0.02	42.8	4.8
	B ₁	0.31	-0.02	39.9	11.9
	B ₂	0.32	-0.06	35.9	11.8
	B ₃	0.34	0.00	47.3	11.2
MNP7	A ₀	0.29	0.03	45.0	17.5
	A ₁	0.32	0.01	42.5	39.8
	A ₂	0.31	0.01	39.8	11.6
	B ₀	0.33	-0.01	35.7	12.0
	B ₁	0.31	0.04	47.3	11.9
	B ₂	0.43	-	-	33.4

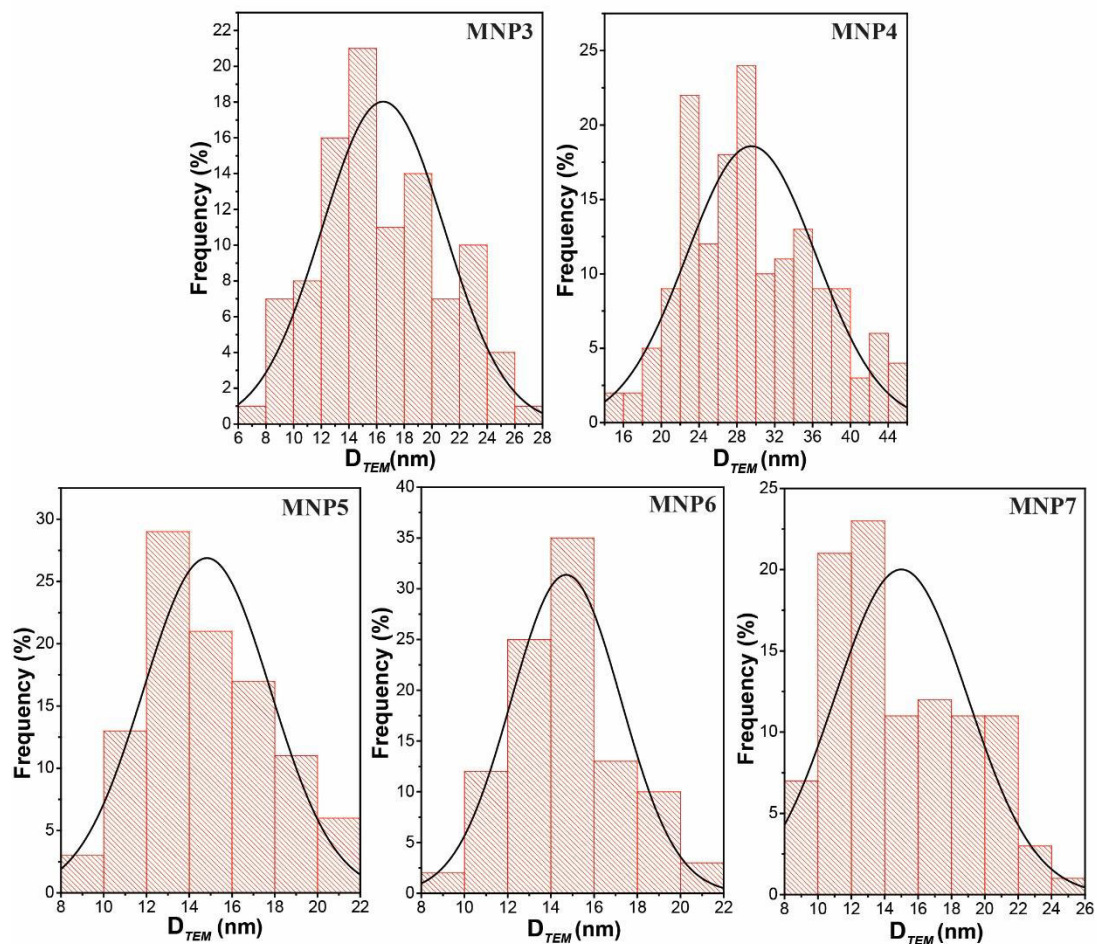
Source: Author

3.3.4 TEM

The size distribution graph for MNP3 – 7 are shown in the Fig. 3.4. The average crystallite size from low-magnification TEM micrographs (D_{TEM}) was estimated using 100 MNPs

randomly chosen. A normal distribution was utilized to fit the data. The D_{TEM} values found for MNP3 – 7 were 16.4 ± 4.4 , 29.5 ± 6.8 , 14.8 ± 2.9 , 14.7 ± 2.5 and 14.9 ± 3.9 , respectively. The results are in good agreement to the PXRD data for MNP3 and MNP5 - 7. The sample MNP4 showed high difference due to the high values for ε , which indicates the poor crystal growth. Thus, this observed discrepancy was expected. Furthermore, this sample showed the higher standard deviation as well as a wide size distribution.

Figure 3.4. Size distribution graph for MNP3 – 7. The black solid line denotes the distribution curve made using a normal distribution to fit the data.

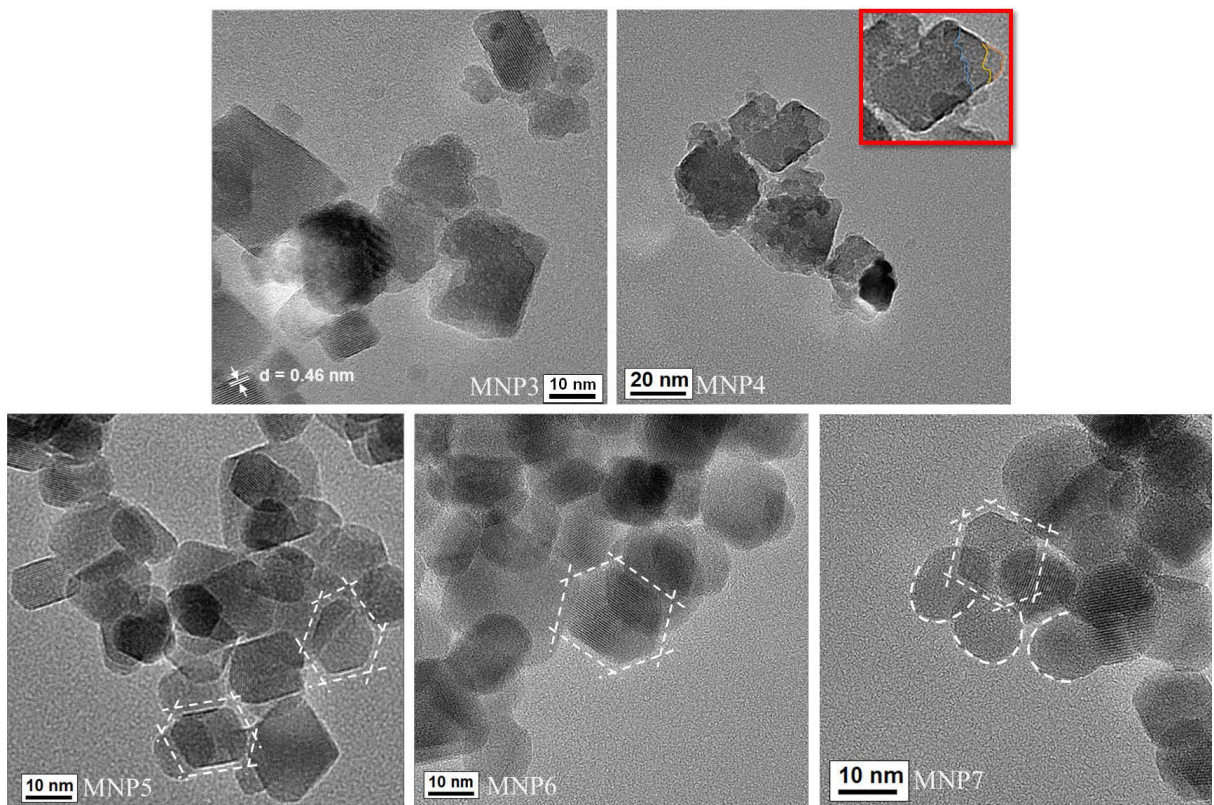


Source: Author

In order to deepen further our study, the morphological evaluation was carried out based on high-magnification TEM images shown in the Fig. 3.5. The shape of the samples studied was found to be different due to hydrothermal treatment time. It was possible to observe square-like structures for MNP3 and 4 samples. Agglomerates can also be seen

on the MNPs. This is very clear for MNP4 and shows the effect of NaOH concentration changes on the crystal growth. Under higher NaOH concentrations, the crystal growth is poor owing to the shifted equilibrium towards hydrolysis and condensation and the crystal growth prevails against the crystal nucleation. Therefore, the fast growth leads to bigger and imperfect crystallites, as observed for MNP4 in the Fig. 3.5. This is in good agreement with ϵ value found for that sample through PXRD data. Interestingly, some imperfections visualized might help to evidence the mechanism of the crystal growth. A careful analysis of MNP4 micrograph clearly reveal a self-assembly of the plates as highlighted in the inset Figure. This indicates a preferential crystal growth in the x, y plane. Further, the interplanar spacing observed on bottom left side of the square-like structures for MNP3 (Fig. 3.5) was measured and the value achieved was 0.46 nm. According to the literature (Sue *et al.*, 2011), this value can be assigned to the (111) plane of the spinel structure. It is well-known in the literature that square-like shape can be obtained when the crystal growth rate along the $\langle 111 \rangle$ is faster than $\langle 100 \rangle$ directions (Wu *et al.*, 2014). Generally, shape-control is achieved by using molecules such as oleic acid to preferentially binding to the $\{100\}$ planes, which increase the speed of the crystal growth along $\langle 111 \rangle$ directions. Therefore, some organic molecules can act as a crystal growth rate controller tuning the shape of the MNPs obtained. Another approach to control the morphology is the utilization of templates formed from surfactants to physically reach the desired shape (Liu *et al.*, 2010). In our study, the synthesis of the MNPs were performed with no organic molecules or surfactants to control the shape. In this sense, it is worth to infer that the hydroxyl species (OH^-) from the NaOH, may play as a crystal growth rate controller by preferred binding to the $\{100\}$ planes under the hydrothermal used conditions. This is the reason behind the formation of obtained square-like structure. Additionally, the imperfections highlighted for MNP4 (self-assembly of square-like plates) in the inset Figure can be explained by the lack of enough building blocks to grow the crystal along $\langle 111 \rangle$ directions. As a result, the imperfections are formed.

Figure 3.5. High magnification TEM images for samples MNP3 – 7.



Source: Author

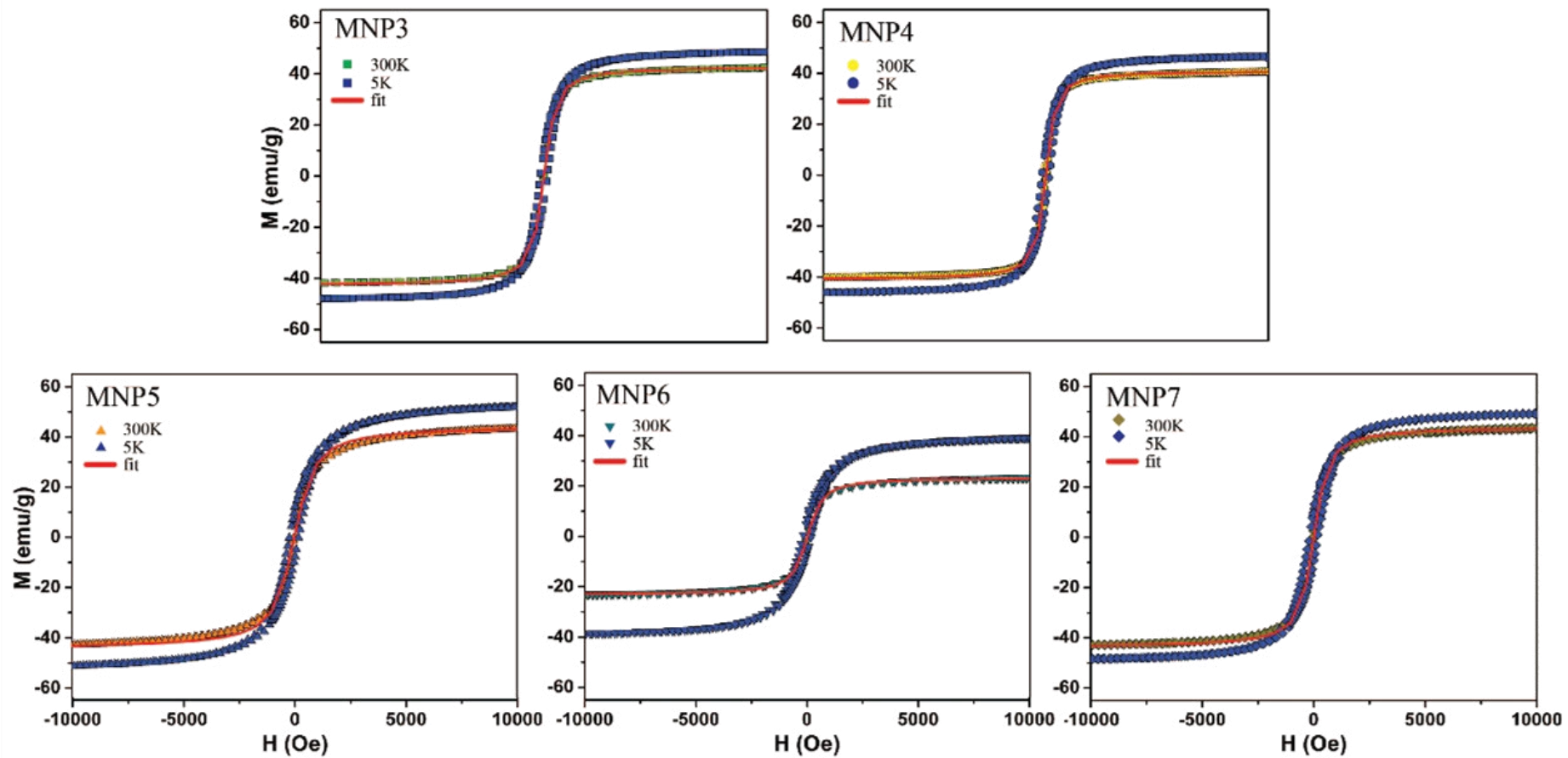
For samples MNP5 – 7, the hydrothermal reaction time seems to have a different effect under the shape of these MNPs. Unlike square-like morphology, a truncated hexagonal-and/or quasi-sphere-like structures were found. Initially, it is possible to observe a truncated hexagonal-like structure for the sample MNP5. Basically, this structure might arise from deformation of the square-like structure and following by the appearance of new edges. For MNP6, a well-defined and truncated hexagonal-structures were observed. Finally, the hexagonal-structure was also observed for the sample MNP7, but quasi-sphere-like structures were also obtained. This last shape may indicate a formation of a large number of the edges, which makes the MNPs seems like a sphere.

3.3.5 Magnetic measurements

Fig. 3.6 displays the magnetization measures at 300 and 5K for MNP3 – 7. The solid red line represent the fit performed using the Langevin function. Negligible hysteresis can be observed for the measurements at 300K, i. e., both remanence and coercivity nearly zero for all samples. This evidence a superparamagnetic nature of the samples (Srinivas *et al.*, 2015). Interestingly, the Mössbauer spectroscopy showed the ferromagnetic behavior.

This difference is due to the relaxation time of the samples (τ_{MNP}) as well as the measuring time (τ_m) (Knobel *et al.*, 2008). Usually, the measure time for VSM and Mössbauer spectroscopy are 100 and 10^{-8} s, respectively. For magnetization measures performed in this work, the τ_m is much bigger than τ_{MNP} . Thus, the sample had enough time to reach the thermodynamically equilibrium and the superparamagnetic behavior was observed. In this case, τ_m is smaller than τ_{MNP} for the Mössbauer spectroscopy and the relaxation process is very slow compared to measure time. An ordered magnetic system can be achieved and the MNPs are in the so-called blocked regime. Therefore, the ferromagnetic nature can be observed. Unlike the measurements observed at 300K, the magnetic loop at 5K for all samples showed the presence of hysteresis. This fact can be explained by effects of thermal fluctuations of the blocked moment across the anisotropy barrier, which cause the increase of the coercivity at low temperatures (Maaz *et al.*, 2010). Further, the magnetization also showed strong temperature dependence. The M_s values for all samples were observed to increase by decreasing the temperature. The reason for this behavior is the presence of huge amount of superparamagnetic structures (Sharma *et al.*, 2007).

Figure 3.6. Magnetization curves at 300 and 5K for MNP3 – 7.



Source: Author

The superparamagnetic loops found for the samples at 300K were well-described using the Langevin function. The average crystallite size can be easily correlated with the magnetic properties of the MNPs using this function (Knobel *et al.*, 2008; Freire *et al.*, 2013; Güner *et al.*, 2014; Baykal *et al.*, 2015). Thus, the average crystallite size obtained via Langevin fit (D_L) for MNP3 – 7 were 13.1, 14.4, 10.7, 14.6 and 12.1 nm, respectively. Moreover, parameters such as saturation magnetization (M_s) can also be obtained from the performed fit. The values found for this parameter were 43.0, 41.2, 44.6, 23.5 and 44.1 emu/g for MNP3 – 7, respectively. For MNP3 – 4, slight decrease of the M_s ($M_s(\Delta) = -1.8$ emu/g) values was observed for the samples synthesized under NaOH changed concentration (MNP3 (4.5 mol.L⁻¹) and MNP4 (5.2 mol.L⁻¹)). On the other hand, random behavior of M_s values was observed for MNP5 – 7. The magnetic properties of MNPs can be correlated with several factors, such as composition, crystallite size and surface effects, among others. In this case, the composition is the same for all the samples. Therefore, the factors with strongest effect should be the crystallite size and surface effects. No matter the technique used to evaluate the crystallite size, it was possible to observe the increase of this parameter along the increase of NaOH concentration. Thus, M_s should be expected to increase. However, the M_s values found for MNP3 – 4 displays a decrease. This highly indicates a strong influence from surface effect. The literature (Pereira *et al.*, 2012) reports the use of NaOH as precipitant agent can lead for higher degree of surface disorder compared to alkanolamine bases. Thus, the decrease of M_s may be explained by increase of magnitude of the uncompensated spins on the surface. For MNP5 – 7, the crystallite size remained similar for all techniques, but a decrease of M_s value can be found only for MNP6. Again, the surface effects are playing essential role for the magnetic properties of this sample. According to the literature (Jovic *et al.*, 2012), the magnetic properties of the MNPs can be explained using a core-shell model. In this case, a core compose by ordered spins would interact with a magnetically disordered shell (“dead” layer). Thus, the surface effects could strongly influence on the magnetic properties of the MNPs. This phenomenon is being observed in this work. In order to deepen further our study, the thickness (t) of the “dead” layer can be achieved using the following expression,

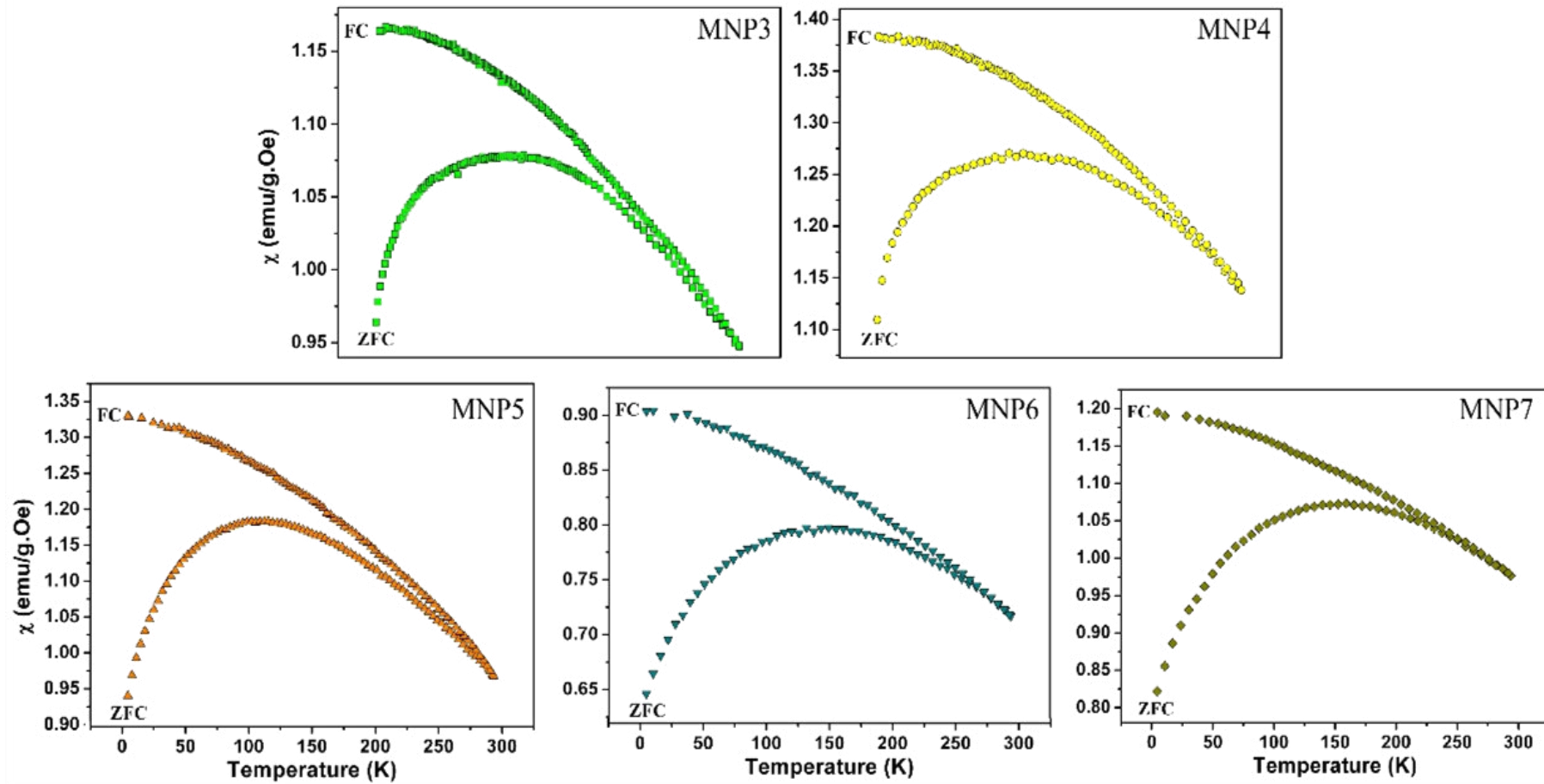
$$M_s(d) = M_s^{Bulk} \left(1 - \frac{6t}{d}\right) \quad (5)$$

where d is the average crystallite size, $M_s(d)$ is the magnetization saturation related to the MNPs d and M_s^{Bulk} is the magnetization saturation for the bulk. Assuming D_{TEM} and M_s^{Bulk} equal 86 emu/g (Sreeja *et al.*, 2009), the t values were 1.30, 2.56, 1.18, 1.78 and 1.20 nm for MNP3 – 7, respectively. Particularly for MNP4, it was found a very impressive value. Usually, the values found in the literature (Jovic *et al.*, 2012; Pereira *et al.*, 2012) are smaller. The core-shell model considers a spherical self-assembly. Thus, shape considerations might explain this discrepancy. Since absence of spheres were observed in the TEM micrographs for MNP4. However, it is important to highlight that the t values perfectly explain the change of observed M_s values. For MNP3 – 4, the increase of t displayed strongly affect the M_s . This agrees to the poor crystal growth with the increase of NaOH concentration. On the other hand, t values for MNP5 – 7 were found to follow a random behavior along the hydrothermal reaction time. This might be related to the shape transition observed through TEM images, which can affect the surface of the MNPs.

Additionally, it is well-known that the superparamagnetic behavior observed is strongly related through critical diameter (D_C) considering a spherical particle model (Sánchez *et al.*, 2002). MNPs with crystallite size smaller than D_C exhibit superparamagnetic relaxation. On the other hand, MNPs with crystallite size bigger than D_C shows ferromagnetic behavior, where the spins are in the so-called blocked regime. According to the literature (Caizer and Stefanescu, 2002), the D_C value for Ni-Zn Ferrite is 21.62 nm. Thus, blocked regime should be expected for MNP4. Since crystallite size values bigger than D_C assuming D_{WH} or D_{TEM} . Interestingly, all samples synthesized displayed superparamagnetic character according to VSM data. This highly suggest that the D_L or D_S values should be the more accurately parameter to evaluate the MNPs regime. The probably reason for this can be found in the fundamental concepts about the techniques employed to calculate the crystallite size. D_S considers only the crystalline portion of the MNPs. Therefore, the size calculated should be near to the magnetically ordered core. D_{WH} can be affected by defects on the surface, which can cause large deviation as

observed for MNP4. The size observed by TEM exhibited some difference compared to D_s due to consider both crystalline and amorphous portion. D_L was very precise to evaluate the MNPs regime. The Langevin function consider an ideal system where the MNPs are non-interacting and spherical (Knobel *et al.*, 2008). Since the TEM images for MNP5 – 7 showed a shape transition from truncated hexagonal-like to quasi-sphere structures, some deviation should be expected. Surprisingly, the parameters obtained using the fit was found to have good agreement. This shows how reliable the Langevin function can be.

Figure 3.7. ZFC/FC measurements for MNP3 – 7.



Source: Author

The zero field-cooled (ZFC)/field-cooled (FC) curves at an applied field of 500 kOe for MNP3 – 7 are shown in the Fig. 3.7. From these experiments, it is possible to know the blocking temperature (T_B). The temperature found can be correlated to the MNPs characteristics by the Stoner–Wohlfarth relation (Knobel *et al.*, 2008),

$$T_B = \frac{K_{eff} V_0}{25K_B} \quad (6)$$

where K_{eff} is the average value of the magnetic anisotropy constant, V_0 is volume of the MNPs and K_B is the Boltzmann's constant. Clearly, a broad distribution of the ZFC curve for each sample can be seen and the maximum could be denoted as the blocking temperature (T_B). However, it is important to remember the wide profile found for the ZFC curve can be understood as a distribution of different T_B for various NPs crystallite sizes. Therefore, the maximum observed denote a mean. In this sense, a better way to represent this parameter is T_B^m . For the samples synthesized in this work, the values found for T_B^m were 105, 121, 103, 137 and 153 K for MNP3 – 7, respectively. From the equation 6, these values can be correlated with MNPs characteristics. Thus, it is possible to see that both increase of NaOH concentration and hydrothermal reaction time led for bigger T_B^m values. Although the effect seems to be similar, the source for the two set of samples may be different. For MNP3 – 4, an increase of the crystallite size was observed by increasing NaOH concentration. Thus, the T_B^m values found for these samples can be easily explained by the increase of V_0 . By contrast, a pretty similar crystallite size was achieved for MNP5 – 7, which indicates a negligible contribution of V_0 . In this way, K_{eff} should have a large contribution for the increase of the T_B^m along the hydrothermal reaction time. This can be related to the shape transition observed in the TEM images for MNP5 – 7. The change of morphology would increase K_{eff} leading for higher T_B^m values. Additionally, thermomagnetic irreversibility for each sample was observed from the temperature where the ZFC and FC curves superimpose. According to the literature (Sharma *et al.*, 2007), this behavior is characteristic to the superparamagnetic regime of the NPs synthesized as well as spin-glass (SG)-like states.

3.4 Conclusion

The structural, morphological and magnetic properties of $\text{Ni}_{0.5}\text{Zn}_{0.5}\text{Fe}_2\text{O}_4$ have been investigated under different experimental conditions. The average crystallite size calculated through different methods was found to be in the range 10.7 – 49.2 nm. Clearly, the increase of the NaOH concentration leads to bigger crystallite size. However, this crystallite presented an uncompleted growth along x, y plane, which cause defects on the self-assembly structure. This fact was evidenced by ε values calculated from PXRD data and TEM micrographs for MNP3 – 4. In contrast, the hydrothermal reaction time plays a different role. The average crystallite size values found for MNP5 – 7 were nearly equal. The morphology of the crystallites was observed to change from truncated hexagonal to quasi-sphere structures. Our results strongly suggest the Scherrer equation and the Langevin function are the best techniques to evaluate the MNPs regime. The M_s for MNP3 – 7 can be observed in the range 23.5 – 44.6 emu/g. The core-shell NPs model was used to explain the change in this parameter. It was possible to observe that the increase of the NaOH concentration increases surface disorder, which led to the smaller M_s values. On the other hand, the hydrothermal reaction time displayed an irrelevant effect on the M_s . ZFC/FC curves were also studied in order to know the effects of NaOH concentration and hydrothermal reaction time on the T_B values. The behavior of this parameter for each set of samples seems to have a different source. The increase of V_0 along the increase of NaOH concentration explains the T_B values achieved for MNP3 – 4. However, the surface effects played an essential role for the T_B values of the MNP5 – 7, which may be associated with the shape transition observed through TEM micrographs.

References

- ALVAREZ, G. S. **Synthesis, characterisation and applications of iron oxide nanoparticles**. 2004. 67 (degree of Doctor in Technology). KTH, Superseded Departments, Materials Science and Engineering, Stockholm University, Stockholm.
- AMER, M. A. et al. Characterization and spectral studies of Co³⁺-doped Cd_{0.4}Mn_{0.6}Fe₂O₄ ferrites. **Ceramics International**, v. 40, n. 1, Part A, p. 241-248, 2014. ISSN 0272-8842. Disponível em: < <http://www.sciencedirect.com/science/article/pii/S0272884213006469> >.
- AMER, M. A. et al. Spectral studies of Co substituted Ni–Zn ferrites. **Journal of Magnetism and Magnetic Materials**, v. 323, n. 11, p. 1445-1452, 2011. ISSN 0304-8853. Disponível em: < <http://www.sciencedirect.com/science/article/pii/S0304885310009418> >.
- AQUINO, R. et al. Size control of MnFe₂O₄ nanoparticles in electric double layered magnetic fluid synthesis. **Journal of Magnetism and Magnetic Materials**, v. 252, n. 0, p. 23-25, 2002. ISSN 0304-8853. Disponível em: < <http://www.sciencedirect.com/science/article/pii/S0304885302006078> >.
- BARRETO, A. et al. Magnetic Nanosystem for Cancer Therapy Using Oncocalyxone A, an Antitumour Secondary Metabolite Isolated from a Brazilian Plant. **International Journal of Molecular Sciences**, v. 14, n. 9, p. 18269-18283, 2013. ISSN 1422-0067. Disponível em: < <http://www.mdpi.com/1422-0067/14/9/18269> >.
- BARRETO, A. C. H. et al. Grain Size Control of the Magnetic Nanoparticles by Solid State Route Modification. **Journal of Materials Engineering and Performance**, v. 22, n. 7, p. 2073-2079, 2013. Disponível em: < <http://dx.doi.org/10.1007/s11665-013-0480-8> >.
- BAYKAL, A.; GÜNER, S.; DEMIR, A. Synthesis and magneto-optical properties of triethylene glycol stabilized Mn_{1-x}Zn_xFe₂O₄ nanoparticles. **Journal of Alloys and Compounds**, v. 619, n. 0, p. 5-11, 2015. ISSN 0925-8388. Disponível em: < <http://www.sciencedirect.com/science/article/pii/S0925838814021124> >.
- BLEICHER, L.; SASAKI, J. M.; PAIVA SANTOS, C. O. Development of a graphical interface for the Rietveld refinement program DBWS. **Journal of Applied Crystallography**, v. 33, n. 4, p. 1189, 2000. ISSN 0021-8898. Disponível em: < <http://dx.doi.org/10.1107/S0021889800005410> >.
- CAIZER, C.; STEFANESCU, M. Magnetic characterization of nanocrystalline Ni–Zn ferrite powder prepared by the glyoxylate precursor method. **Journal of Physics D: Applied Physics**, v. 35, n. 23, p. 3035, 2002. ISSN 0022-3727. Disponível em: < <http://stacks.iop.org/0022-3727/35/i=23/a=301> >.
- DAVE, S. R.; GAO, X. Monodisperse magnetic nanoparticles for biodetection, imaging, and drug delivery: a versatile and evolving technology. **Wiley Interdisciplinary Reviews: Nanomedicine and Nanobiotechnology**, v. 1, n. 6, p. 583-609, 2009. ISSN 1939-0041. Disponível em: < <http://dx.doi.org/10.1002/wnan.51> >.

FREIRE, R. M. et al. Effect of solvent composition on the structural and magnetic properties of MnZn ferrite nanoparticles obtained by hydrothermal synthesis. **Microfluidics and Nanofluidics**, v. 17, n. 1, p. 233-244, 2014/07/01 2014. ISSN 1613-4982. Disponível em: < <http://dx.doi.org/10.1007/s10404-013-1290-x> >.

FREIRE, R. M. et al. MZnFe₂O₄ (M = Ni, Mn) cubic superparamagnetic nanoparticles obtained by hydrothermal synthesis. **Journal of Nanoparticle Research**, v. 15, n. 5, p. 1-12, 2013// 2013. ISSN 1572-896X. Disponível em: < <http://dx.doi.org/10.1007/s11051-013-1616-3> >.

GÜNER, S. et al. Magneto-optical properties of Cu_{1-x}Zn_xFe₂O₄ nanoparticles. **Superlattices and Microstructures**, v. 74, n. 0, p. 184-197, 2014. ISSN 0749-6036. Disponível em: < <http://www.sciencedirect.com/science/article/pii/S0749603614002274> >.

HEIBA, Z. K. et al. Cation distribution and dielectric properties of nanocrystalline gallium substituted nickel ferrite. **Journal of Alloys and Compounds**, v. 586, n. 0, p. 773-781, 2014. ISSN 0925-8388. Disponível em: < <http://www.sciencedirect.com/science/article/pii/S0925838813025528> >.

IVANOV, V. G. et al. Short-range **B**-site ordering in the inverse spinel ferrite NiFe₂O₄. **Physical Review B**, v. 82, n. 2, p. 024104, 2010. Disponível em: < <http://link.aps.org/doi/10.1103/PhysRevB.82.024104> >.

JOVIC, N. et al. Magnetic Properties of Lithium Ferrite Nanoparticles with a Core/Shell Structure. **Current Nanoscience**, v. 8, n. 5, p. 651-658, 2012. Disponível em: < <http://www.ingentaconnect.com/content/ben/cnano/2012/00000008/00000005/art00002> >.

KANDASAMY, V.; VELLAIYAPPAN SANGLI KARUPPANAN, V.; SECHASSALOM, S. Synthesis of nickel zinc iron nanoparticles by coprecipitation technique. **Materials Research**, v. 13, n. 3, 2010. ISSN 1516-1439. Disponível em: < <http://dx.doi.org/10.1590/S1516-14392010000300005> >.

KARAAGAC, O.; BILIR, B.; KOCKAR, H. Superparamagnetic Cobalt Ferrite Nanoparticles: Effect of Temperature and Base Concentration. **Journal of Superconductivity and Novel Magnetism**, v. 28, n. 3, p. 1021-1027, 2015/03/01 2015. ISSN 1557-1939. Disponível em: < <http://dx.doi.org/10.1007/s10948-014-2798-3> >.

KIM, S.-G. et al. Low-Temperature Crystallization of Barium Ferrite Nanoparticles by a Sodium Citrate-Aided Synthetic Process. **The Journal of Physical Chemistry C**, v. 111, n. 28, p. 10175-10180, 2007/07/01 2007. ISSN 1932-7447. Disponível em: < <http://dx.doi.org/10.1021/jp068249b> >.

KNOBEL, M. et al. Superparamagnetism and Other Magnetic Features in Granular Materials: A Review on Ideal and Real Systems. **Journal of Nanoscience and Nanotechnology**, v. 8, n. 6, p. 2836-2857, 2008. Disponível em: < <http://www.ingentaconnect.com/content/asp/jnn/2008/00000008/00000006/art00009> >.

<http://dx.doi.org/10.1166/jnn.2008.017> >.

KOŠAK, A. et al. Preparation of MnZn-ferrite with microemulsion technique. **Journal of the European Ceramic Society**, v. 24, n. 6, p. 959-962, 2004. ISSN 0955-2219. Disponível em: < <http://www.sciencedirect.com/science/article/pii/S0955221903005247> >.

KUMAR, P.; MISHRA, P.; SAHU, S. K. Synthesis of Ni-Zn Ferrites Using Low Temperature Sol-Gel Process. **International Journal of Scientific & Engineering Research**, v. 2, n. 8, 2011 ISSN 2229-5518.

KUMAR, S. et al. Mössbauer studies of $\text{Co}_{0.5}\text{Cd}_x\text{Fe}_{2.5-x}\text{O}_4$ ($0.0 \leq x \leq 0.5$) ferrite. **Physica B: Condensed Matter**, v. 403, n. 19–20, p. 3604-3607, 2008. ISSN 0921-4526. Disponível em: < <http://www.sciencedirect.com/science/article/pii/S0921452608002573> >.

LATHAM, A. H.; WILLIAMS, M. E. Controlling Transport and Chemical Functionality of Magnetic Nanoparticles. **Accounts of Chemical Research**, v. 41, n. 3, p. 411-420, 2008/03/01 2008. ISSN 0001-4842. Disponível em: < <http://dx.doi.org/10.1021/ar700183b> >.

LAZAREVIĆ, Z. Ž. et al. Characterization of partially inverse spinel ZnFe_2O_4 with high saturation magnetization synthesized via soft mechanochemically assisted route. **Journal of Physics and Chemistry of Solids**, v. 75, n. 7, p. 869-877, 2014. ISSN 0022-3697. Disponível em: < <http://www.sciencedirect.com/science/article/pii/S0022369714000584> >.

LEE, J. H. et al. The characteristics of Ni–Zn ferrite powder prepared by the hydrothermal process. **Journal of Materials Science Letters**, v. 18, n. 13, p. 1029-1031, 1999// 1999. ISSN 1573-4811. Disponível em: < <http://dx.doi.org/10.1023/A:1006619409011> >.

LIU, J. et al. Cerium Vanadate Nanorod Arrays from Ionic Chelator-Mediated Self-Assembly. **Angewandte Chemie International Edition**, v. 49, n. 20, p. 3492-3495, 2010. ISSN 1521-3773. Disponível em: < <http://dx.doi.org/10.1002/anie.201000783> >.

MAAZ, K. et al. Temperature dependent coercivity and magnetization of nickel ferrite nanoparticles. **Journal of Magnetism and Magnetic Materials**, v. 322, n. 15, p. 2199-2202, 2010. ISSN 0304-8853. Disponível em: < <http://www.sciencedirect.com/science/article/pii/S0304885310000764> >.

MALIK, R. et al. Mössbauer and magnetic studies in nickel ferrite nanoparticles: Effect of size distribution. **Journal of Magnetism and Magnetic Materials**, v. 322, n. 23, p. 3742-3747, 2010. ISSN 0304-8853. Disponível em: < <http://www.sciencedirect.com/science/article/pii/S030488531000483X> >.

NAGASE, T.; SAKANE, K.; WADA, H. Effect of Acids on Crystallization of Lithium Borate Films. **Journal of Sol-Gel Science and Technology**, v. 8, n. 1-3, p. 431-435, 1997/01/01 1997. ISSN 0928-0707. Disponível em: < <http://dx.doi.org/10.1023/A%3A1026413202998> >.

NAIK, P. P. et al. Gamma radiation roused lattice contraction effects investigated by Mössbauer spectroscopy in nanoparticle Mn–Zn ferrite. **Radiation Physics and Chemistry**, v. 102, n. 0, p. 147-152, 2014. ISSN 0969-806X. Disponível em: < <http://www.sciencedirect.com/science/article/pii/S0969806X14001741> >.

NASERI, M. G.; B.SAION, E. **Advances in Crystallization Processes**. InTech, 2012. 648 ISBN 978-953-51-0581-7. Disponível em: < <http://www.intechopen.com/books/advances-in-crystallization-processes/crystallization-in-spinel-ferritenanoparticles> >.

PEREIRA, C. et al. Superparamagnetic MFe₂O₄ (M = Fe, Co, Mn) Nanoparticles: Tuning the Particle Size and Magnetic Properties through a Novel One-Step Coprecipitation Route. **Chemistry of Materials**, v. 24, n. 8, p. 1496-1504, 2012/04/24 2012. ISSN 0897-4756. Disponível em: < <http://dx.doi.org/10.1021/cm300301c> >.

RIBEIRO, T. G. D. **Síntese e caracterização de nanopartículas magnéticas de óxidos mistos de MnFe₂O₄ recobertas com quitosana. Estudos da influência da dopagem com Gd³⁺ nas propriedades estruturais e magnéticas**. 2008. (master). Instituto de Pesquisas Energéticas e Nucleares, Univerdade de São Paulo, São Paulo.

RIETVELD, H. Line profiles of neutron powder-diffraction peaks for structure refinement. **Acta Crystallographica**, v. 22, n. 1, p. 151-152, 1967. ISSN 0365-110X. Disponível em: < <http://dx.doi.org/10.1107/S0365110X67000234> >.

SÁNCHEZ, R. D. et al. Particle size effects on magnetic properties of yttrium iron garnets prepared by a sol–gel method. **Journal of Magnetism and Magnetic Materials**, v. 247, n. 1, p. 92-98, 2002. ISSN 0304-8853. Disponível em: < <http://www.sciencedirect.com/science/article/pii/S0304885302001701> >.

SEEMA, V. et al. Synthesis of nanosized MgFe₂O₄ powders by microwave hydrothermal method. **Mater Lett**, v. 58, n. 6, p. 1092-1095, 2004. ISSN 0167-577X. Disponível em: < http://pubget.com/paper/pgtmp_dc48850bd65cbfe851e15d0da5835969/synthesis-of-nanosized-mgfe2o4powders-by-microwave-hydrothermal-method <http://www.sciencedirect.com/science/article/pii/S0167577X03007018> >.

SHARMA, S. K. et al. Magnetic study of Mg_{0.95}Mn_{0.05}Fe₂O₄ ferrite nanoparticles. **Solid State Communications**, v. 141, n. 4, p. 203-208, 2007. ISSN 0038-1098. Disponível em: < <http://www.sciencedirect.com/science/article/pii/S0038109806009367> >.

SREEJA, V. et al. Magnetic and Mössbauer spectroscopic studies of NiZn ferrite nanoparticles synthesized by a combustion method. In: GAJBHIYE, N. S. e DATE, S. K. (Ed.). **ICAME 2007**: Springer Berlin Heidelberg, 2009. cap. 32, p.271-279. ISBN 978-3-540-87122-4.

SRINIVAS, C. et al. Effect of Ni²⁺ substitution on structural and magnetic properties of Ni–Zn ferrite nanoparticles. **Journal of Magnetism and Magnetic Materials**, v. 382,

n. 0, p. 15-19, 2015. ISSN 0304-8853. Disponível em: <
<http://www.sciencedirect.com/science/article/pii/S0304885315000104>>.

SUCHANEK, W. L.; RIMAN, R. E. Hydrothermal Synthesis of Advanced Ceramic Powders. **Advances in Science and Technology**, v. 45, p. 184-193, 2006.

SUE, K. et al. Continuous Hydrothermal Synthesis of Nickel Ferrite Nanoparticles Using a Central Collision-Type Micromixer: Effects of Temperature, Residence Time, Metal Salt Molality, and NaOH Addition on Conversion, Particle Size, and Crystal Phase. **Industrial & Engineering Chemistry Research**, v. 50, n. 16, p. 9625-9631, 2011/08/17 2011. ISSN 0888-5885. Disponível em: <
<http://dx.doi.org/10.1021/ie200036m>>.

TANG, S. C. N.; LO, I. M. C. Magnetic nanoparticles: Essential factors for sustainable environmental applications. **Water Research**, v. 47, n. 8, p. 2613-2632, 2013. ISSN 0043-1354. Disponível em: <
<http://www.sciencedirect.com/science/article/pii/S0043135413001437>>.

TANG, Z. X. et al. Size-dependent magnetic properties of manganese ferrite fine particles. **Journal of Applied Physics**, v. 69, n. 8, p. 5279-5281, 1991. Disponível em: <
<http://scitation.aip.org/content/aip/journal/jap/69/8/10.1063/1.348048>>.

UPADHYAY, C. et al. Effect of preparation conditions on formation of nanophase Ni–Zn ferrites through hydrothermal technique. **Journal of Magnetism and Magnetic Materials**, v. 260, n. 1–2, p. 188-194, 2003. ISSN 0304-8853. Disponível em: <
<http://www.sciencedirect.com/science/article/pii/S0304885302013203>>.

WU, L. et al. Monolayer Assembly of Ferrimagnetic $\text{Co}_x\text{Fe}_{3-x}\text{O}_4$ Nanocubes for Magnetic Recording. **Nano Letters**, v. 14, n. 6, p. 3395-3399, 2014/06/11 2014. ISSN 1530-6984. Disponível em: <
<http://dx.doi.org/10.1021/nl500904a>>.

YAFET, Y.; KITTEL, C. Antiferromagnetic Arrangements in Ferrites. **Physical Review**, v. 87, n. 2, p. 290-294, 1952. Disponível em: <
<http://link.aps.org/doi/10.1103/PhysRev.87.290>>.

YU, H.-F.; LIU, P.-C. Effects of pH and calcination temperatures on the formation of citrate-derived hexagonal barium ferrite particles. **Journal of Alloys and Compounds**, v. 416, n. 1–2, p. 222-227, 2006. ISSN 0925-8388. Disponível em: <
<http://www.sciencedirect.com/science/article/pii/S0925838805013381>>.

ZHAO, Y.; QIU, Z.; HUANG, J. Preparation and Analysis of Fe_3O_4 Magnetic Nanoparticles Used as Targeted-drug Carriers. **Chinese Journal of Chemical Engineering**, v. 16, n. 3, p. 451-455, 2008. ISSN 1004-9541. Disponível em: <
<http://www.sciencedirect.com/science/article/pii/S1004954108601044>>.

CHAPTER 4

4 NH₂-RICH CARBON QUANTUM DOTS: A POWERFUL PROTEIN-RESPONSIVE PROBE

Abstract

In this chapter, we synthesized a branched-polyethylenimine (BPEI) functionalized Carbon Quantum Dots (CQDs) and studied their potential as a sensor for different proteins (Hemoglobin, Myoglobin, α -Amylase, Cytochrome C, Bovine Serum Albumin, Human Serum Albumin, Acid Phosphatase and Alkaline Phosphatase). The positively charged CQDs (CQDs.BPEI) were fully investigated using Infrared spectroscopy (IR), X-ray photoelectron spectroscopy (XPS) and Transmission electron microscopic (TEM). The fluorescent properties were also studied. It was possible to observe 2 nm excitation-independent CQDs with graphitic core. The capping performed with BPEI was observed through IR and XPS. For instance, XPS study displayed a large amount of amine groups, which evidences the surface functionalization. These new fluorescent carbon-based nanoparticles were found to be a powerful protein-responsive platform. Since it was able to detect eight different proteins even using concentrations in the range as low as from 5 to 40 nM. In order to provide a better understanding about how to interface CQDs with proteins, fluorescence titrations were performed at different temperatures (298 and 310K). These experiments displayed the fluorescence quenching is related to the collisional mechanism. It was also possible to infer the fluorescence quench comes from the amino acid residues on the surface of the analyte proteins. CQDs-BPEI were found to ΔG were achieved. The values of ΔH and ΔS indicates the CQDs-BPEI were not able to interact with the hydrophobic portion of the proteins. Therefore, a fluorescent probe that strongly interact with these amino acid residues can improve the limit detection. This would provide early diagnoses of diseases related with abnormal levels of proteins like cancer, for example.

Keywords: Carbon quantum dots. Proteins. Interaction. Detection

4.1 Introduction

Carbon quantum dots (CQDs) are a new class of fluorescent nanomaterials. These nanoparticles basically are made from carbon and have been gaining much attention due to excellent properties (Lim *et al.*, 2015), since their accidental discovery by Xu *et al.* (Xu *et al.*, 2004) in 2004. Good solubility, high quantum yield and resistance to photobleaching are some of these wonderful characteristics (Wang and Hu, 2014). Relevant biological properties, such as low toxicity as well as biocompatibility can also be mentioned (Liu *et al.*, 2013). Therefore, CQDs have been exploited by many researchers worldwide. As a consequence, a wide range of applications including sensing (Esteves Da Silva and Gonçalves, 2011), imaging (Yang *et al.*, 2009), nanomedicine (Huang *et al.*, 2012), photocatalysis (Li *et al.*, 2010), among others, have been emerging. However, it is important to highlight the application involving CQDs for sensing purpose. Since a huge number of recent publications can be found in this field. By exploiting fluorescent properties of CQDs in the sensing field, a broad variety of different analytes like heavy metals (Guo *et al.*, 2013; Guo *et al.*, 2015), organic pollutant (Bu *et al.*, 2014), drugs (Niu and Gao, 2014), among other can be detected.

In the last years, CQDs have been exploited to sense molecules inside biological systems (cells, for example (Yu *et al.*, 2013)) in order to detect diseases in early stages. This would increase the chance of cure of the patient. In this sense, the detection of proteins is very important. Since these biomolecules can serve as a biomarker related to diseases such as cancer, for example (Daniels *et al.*, 2004). Thus, a real-time analytical protein detection is strongly desired to facilitate medical diagnosis. Most approaches to analyze proteins are high-resolution two-dimensional polyacrylamide gel electrophoresis (2D-PAGE), mass spectroscopy, enzyme-linked immunosorbent assay (ELISA), among other (Gygi *et al.*, 1999; Haab, 2006). In general, the current methods to detect proteins are time-consuming requiring specific, complicated and demand expense instrumentation and expertise. Many of the methodologies mentioned are not adaptable to routine analysis. Despite the great effort, new strategies to monitor protein levels remain a big issue in medical diagnosis.

In this regard, some publications have demonstrated that proteins can be detected using CQDs (Yan *et al.*, 2014; Huang *et al.*, 2015; Qian, Z. *et al.*, 2015; Qian, Z. S. *et al.*, 2015). However, the full potential of CQDs for protein sensing is still unknown. From the top of

our knowledge, only a few papers involving these new fluorescent carbon-based NPs and proteins can be found in the literature. Therefore, a better understanding about the interaction between CQDs and protein as well as to be able to modulate them, it is essential to do the detection approach. Further, this knowledge may provide a powerful and cheap protein-responsive probe. In this study, we synthesized NH₂-rich CQDs and their potential as a sensor for different metallic and non-metallic proteins was evaluated. The morphological, surface and optical properties of the CQDs.BPEI were fully investigated. Additionally, the interaction between CQDs.BPEI and eight different proteins (four metallic and four non-metallic) have been analyzed. It was found the proteins tested could quench the intrinsic fluorescence of CQDs via collisional mechanism. The CQDs synthesized in this work were capable to detect the some of the proteins evaluated (hemoglobin, for example) even using concentrations as low as 5 nM. Therefore, CDs-BPEI system shows great potential for protein sensing.

4.2 Materials and Methods

4.2.1 Materials

The chemicals used in this study were citric acid anhydrous (CA, C₆H₈O₇, 99.5%, Aldrich), polyethylenimine, ethylenediamine branched (BPEI, H(NHCH₂CH₂)_nNH₂, Average Mw of 800, Aldrich), sodium phosphate monobasic (NaH₂PO₄·H₂O) and dibasic (Na₂HPO₄). The analyte proteins, bovine serum albumin (BSA), human serum albumin (HSA), acid phosphatase (PhosA, from potato) and alkaline phosphatase (PhosB, from bovine intestinal mucosa), Hemoglobin (Hem, from human), Myoglobin (Myo, from equine heart), α -Amylase (α -Am, from *Bacillus licheniformis*) and cytochrome c (Cyt.c, from equine heart), were all purchased from Sigma-Aldrich and used as received. The dialysis membrane tubing cut-off in the range 0.5–1.0 kDa was supplied by Spectrum Laboratories.

4.2.2 Synthesis of CQDs.BPEI

Positively charge CQDs were synthesized according to a known procedure (Dong, Shao, *et al.*, 2012). However, some modifications were applied in order to perform the capping using BPEI. Briefly, 2g of CA were weighted and transferred to a 20 mL glass vial. Then 1g of BPEI was added and the mixture was heated at 180°C for 30 min. Afterwards, milli-Q water (resistivity of 18.2 M Ω ·cm) was added to extract the CQDs.BPEI and the final

solution was purified through dialysis membrane (0.5 – 1.0 kDa) for 24 h. Finally, the solution was lyophilized to obtain the powder. This was kept in the fridge at 4°C for further application and characterization.

4.2.3 Characterization of CQDs.BPEI

The absorbance and fluorescent measurements were recorded using a fluorescence microplate reader (Molecular Devices SpectraMax M5). FTIR spectrum was carried out on an ALPHA FT-IR Spectrometer in the range of 4,000 – 400 cm^{-1} . XPS analysis were performed on a Physical Electronics Quantum 2000 spectrometer using a monochromatic Al $K\alpha$ excitation at a spot size of 10 mm with pass energy of 46.95 eV. To confirm the size and shape of carbon dots, transmission electron microscope (TEM) samples were prepared by a drop-casting method. Briefly, a drop of the CQDs solution (5 μL) was placed onto a 300-mesh nickel grid coated with Formvar film and allowed to dry overnight in room temperature, then measured the sample by using a JEOL 200FX TEM. The concentration of CQDs.BPEI in solution was obtained building up a calibration curve (concentration x absorbance). The knowledge of the amount of CQDs.BPEI in solutions obtained upon lyophilization allowed to know the concentration (mass/volume) of stock solution. Subsequently, dilutions were performed as well as absorbance measurements.

4.2.4 Detection Experiments

Initially, a stock solution of CQDs.BPEI was prepared in phosphate buffer (PB, 5 mM, pH 7.4). The absorbance of this solution at 350 nm was measured and the concentration of CQDs was precisely obtained based on the calibration curve. Afterwards, a stock solution of each analyte protein was also prepared in PB for the sensing experiments. The concentration of these solutions were acquired by absorbance measurements at 280 nm (A_{280}). Unlike CQDs.BPEI, the concentration of proteins (C) were calculated using Beer-Lambert law ($C = A_{280}/(\epsilon_{280} \cdot l)$), where ϵ_{280} and l are molar absorbtivity at 280 nm and path length of the cuvette in which the sample is contained, respectively. For the initial detection experiments, 200 μL of the CQDs.BPEI solution (2 $\mu\text{g} \cdot \text{mL}^{-1}$) was loaded into a well on a 96-well plate (300 mL Whatman black bottom microplate). The fluorescence intensity value at 445 nm was measured with excitation at 350 nm. This value was considered the initial intensity (I_0). Subsequently, 10 μL of protein solution with adequate concentration was added in order to obtain 40 nM in the well. After 1 min, the

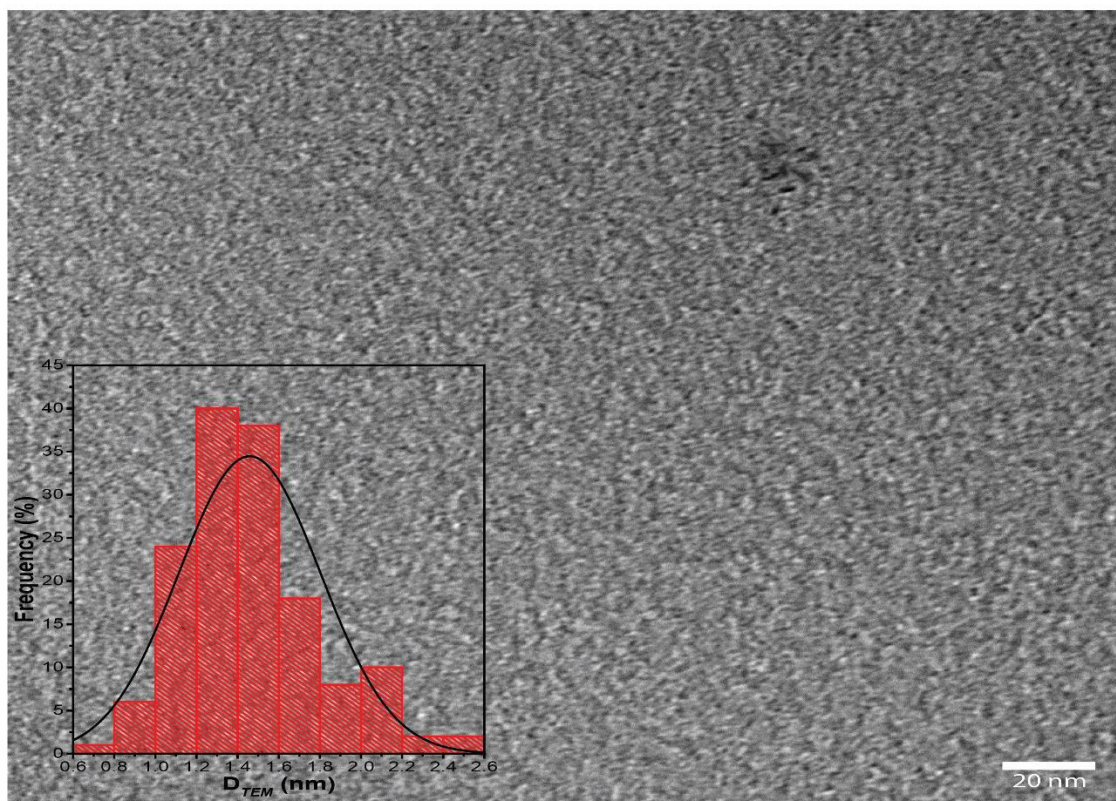
fluorescence intensity was recorded again (I). The value found for I/I_0 ratio was the response investigated. For all proteins evaluated, the procedure was the same and the process was repeated three times for each protein. For the fluorescence titration studies, the protein concentration in the well was adjusted to obtain values in the range 5 – 40 nM. The same procedure described above was applied to get the fluorescence response. Therefore, the fluorescence response was recorded as a function of the analyte protein concentrations. In order to further investigate the fluorescence quenching, the titration experiments were performed at 298 and 310 K. All experiments described until here were carried out in PB.

4.3 Results and discussion

4.3.1 CQDs Characterization

Fig. 4.1 shows the TEM image as well as the distribution size graph (inset) for CQDs.BPEI ($2 \mu\text{g.mL}^{-1}$). This graph was built by measuring 150 particles randomly chosen. The average nanoparticle size was estimated using a normal distribution. It can be observed that CQDs.BPEI presented good uniformity and monodispersity. Since a narrow distribution and no agglomerates can be observed, respectively. The value for average nanoparticle size was 1.45 ± 0.34 nm. Similar results can be achieved in the literature (Chen *et al.*, 2013; Ding *et al.*, 2013; Hui *et al.*, 2014).

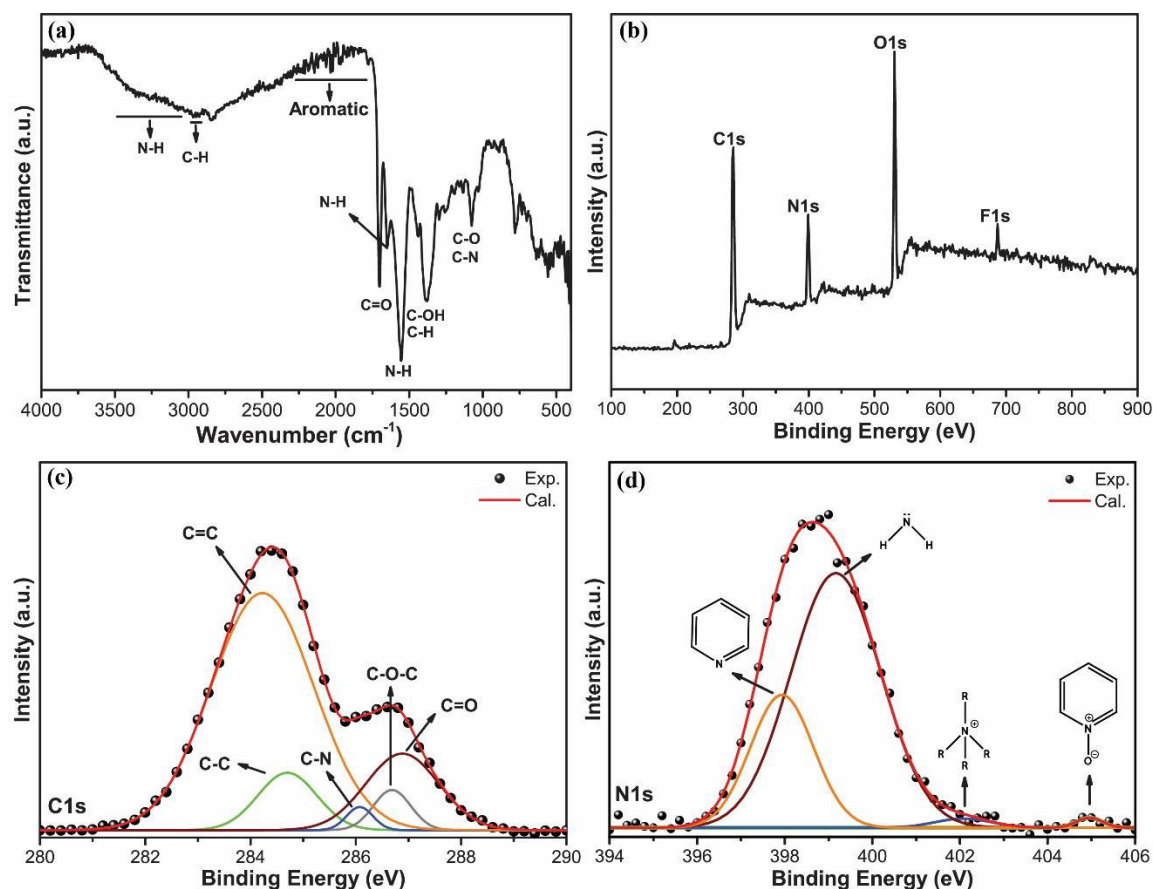
Figure 4.1. TEM image of CQDs.BPEI. Inset: distribution size graph based on the measurements of 150 particles randomly chosen.



Source: Author

FTIR and XPS were performed in order to know the surface chemistry (functional groups and elemental states) of the CQDs.BPEI. The FTIR spectrum of the CQDs.BPEI, recorded at room temperature, is displayed in the Fig. 4.1(a). Absorption bands arising from carboxyl (C=O/COOH) and hydroxyl (-OH) groups were observed at 1702 and 1378 cm^{-1} , respectively. In the range of 1700 – 2000 cm^{-1} , it appeared many weak bands, which reflects the substitution pattern of the benzene ring: presence of aromatic rings in the structure of the CD.BPEI. The absorption bands from N-related groups were also observed. Clearly, there is a broad band above 3000 cm^{-1} , which it can be assigned to the N-H stretching of primary amines. Around 1600 cm^{-1} , N-H bends from primary and secondary amines can be seen. Further, C-N stretching bands from aliphatic amines were observed in the range of 1200 – 1020 cm^{-1} .

Figure 4.2. Surface properties of CQDs.BPEI. (a) FT-IR spectrum of CQDs.BPEI. XPS analysis (c) Survey scan, (d) C1s analysis and (e) N1s analysis.

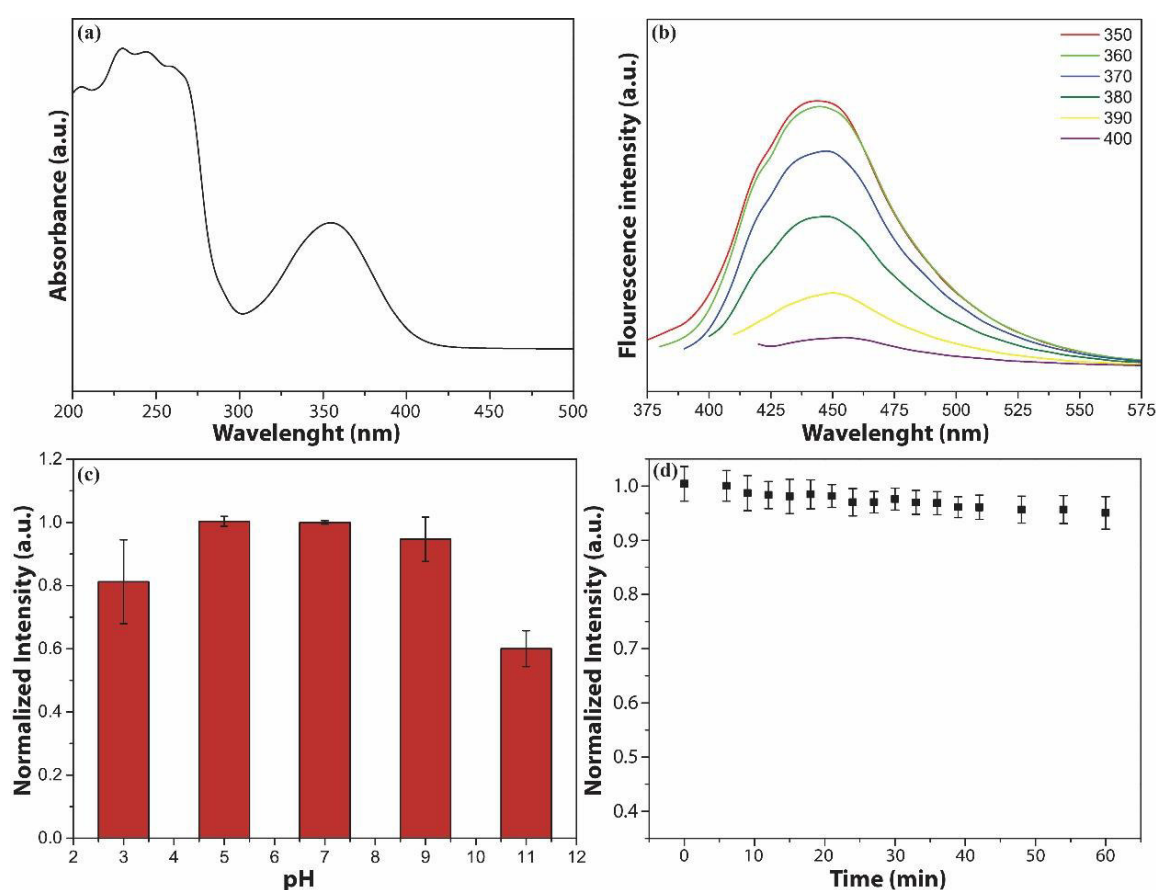


Source: Author

Fig. 4.2(b) shows the XPS survey scan of the studied system. Clearly, the spectrum reveals peaks at 286, 399, 530 and 687 eV, which it can be attributed to the C, N, O and F species, respectively (Jankovsky *et al.*, 2014; Gong *et al.*, 2015). This result assigns the N content on the surface of the synthesized CQDs. Therefore, the capping performed was confirmed. On the other hand, the unexpected peak related to the F displayed the presence of the impurities. In order to deepen further our study, the detailed spectra for C and N are showed in the Fig. 4.2(c) and (d), respectively. In the Fig. 4.2(c), five different components were identified. The C1s spectrum displays predominant sp^2 and sp^3 graphitic C peaks at 284.2 (C=C) and 284.7 (C-C) eV, respectively (Wei *et al.*, 2014; Zhang *et al.*, 2014). It was also possible to see peaks from C-N, C-O-C and C=O at 286.0, 286.6 and 286.8 eV, respectively (Li *et al.*, 2012). Once again, the N content was confirmed on the surface of the system. Beyond, the other observed groups show the evidence of the presence of oxygen on the structure, which is plausible. Since the citric

acid was used as a carbon source to synthesized the CQDs. Fig. 4.2(d) shows the N1s spectrum, where four components can be found. The predominant intensities were observed for the peaks assigned to the pyridinic and amine (-NH₃) species at 397.3 and 399.1 eV, respectively (Barinov *et al.*, 2009; Usachov *et al.*, 2011; Qu *et al.*, 2014). Further, a comparative study of these peaks revealed a huge amount of the -NH₃ groups on the surface, since the peak at 399.1 eV showed the highest intensity. Groups amine highly substituted and NO_x species were also evidenced at 402.0 and 404.eV, respectively (Pylypenko *et al.*, 2011). Both results found through XPS and FTIR are in good agreement.

Figure 4.3. Optical properties of CQDs.BPEI. (a) UV/Vis absorption spectra of CQDs.BPEI. (b) The excitation-wavelength independent fluorescence spectra of CQDs.BPEI. (c) Fluorescence intensity as function of pH values and (d) Photobleaching experiment: fluorescence intensity recorded during 60 min at room temperature.



Source: Author

In order to investigate the optical properties of the CQDs.BPEI, UV-Vis absorption and fluorescence spectroscopy were performed. The UV-Vis spectrum is displayed in the Fig.

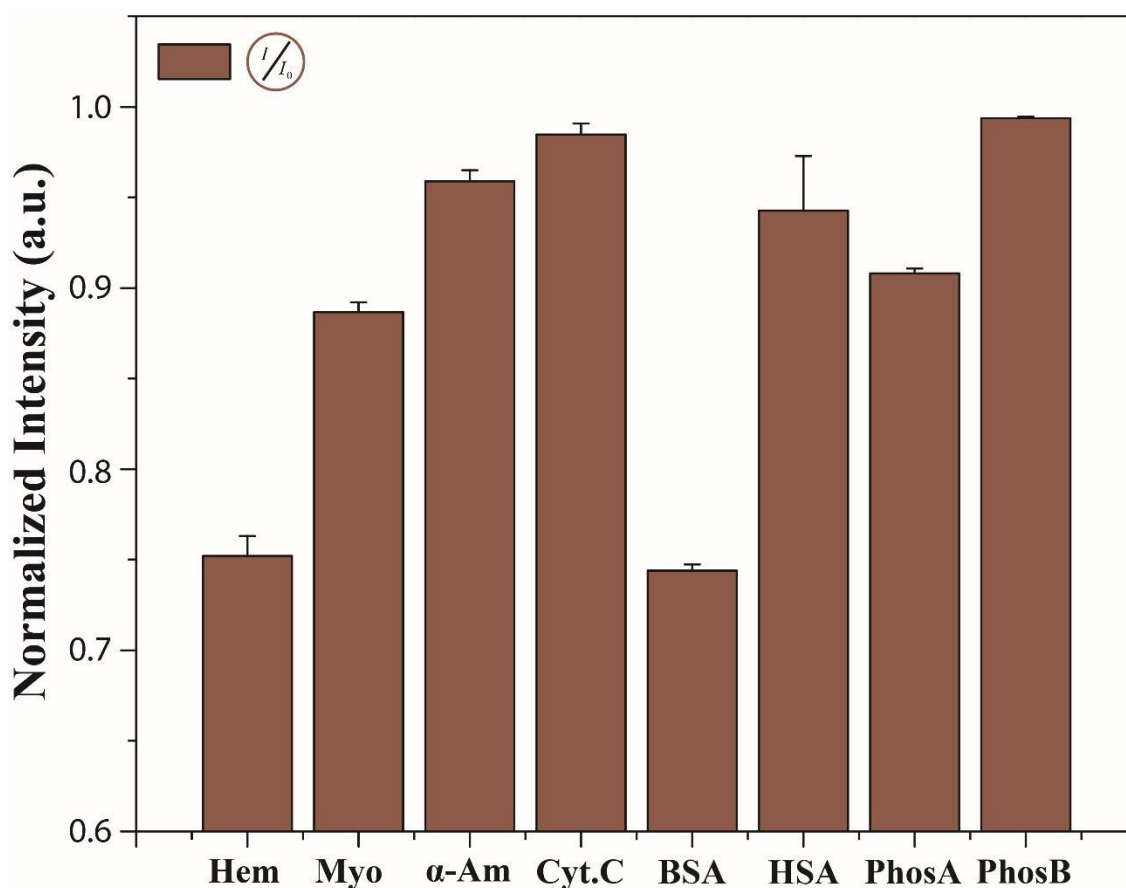
4.3(a). A typical band centered at 230 nm can be found. According to the literature, this band is attributed to the π - π^* transition of aromatic sp^2 domains (Pan *et al.*, 2010). It was also observed a band at ca. 270 nm, which denotes the n - π^* transition coming from C-O bond (Thema *et al.*, 2013). Another strong and symmetrical absorption band at ca. 350 nm was observed. This notably band is attributed to the contributions of the surface groups. Since the CQDs synthesized in this work were passivated with a NH_2 -rich polymer. Furthermore, the NH_2 group are expected to be an electron-donating, which it may improve the functionalization degree, as well as the electron transitions. This additionally explains the very strong and symmetrical absorption band evidencing the high amount of NH_2 groups on the surface (Li *et al.*, 2014). In agreement with this discussion, the emission should also be affected by the passivation. In this regard, the Fig. 4.3(b) present the fluorescent spectra recorded for CQDs.BPEI at different excitations wavelength (350, 360, 370, 380, 390 and 400 nm). Clearly, the CQDs synthesized in this work was found to be excitation-independent. The emission bands were no longer shifted by changing the excitation wavelength. Therefore, an absence of surface states between HOMO and LUMO can be inferred, which leads to a single transition mode. Considering that NH_2 groups have contribution for the electron structure of CQDs.BPEI, this behavior confirms a large amount of these species on the surface and it shows how homogeneous the passivation process happened. In addition, the Fig. 4.3(c) and (d) displays the fluorescence intensity as a function of pH and time, respectively. The intensity was statically constant in a solution of pH in the range 5 – 9. However, high or low values of pH decreased the intensity. No relevant photobleaching was observed during the 60 min.

4.3.2 Detection of proteins using CQDs.BPEI

Once all detection experiments were performed in PB, the first test was naturally to check if the metallic cations present in the PB composition would be able to quench the fluorescence intensity of the CQDs.BPEI. This might be true based on the various papers in the literature exploiting CQDs as a metal sensor (Dong, Wang, *et al.*, 2012; Wang *et al.*, 2014; Cui *et al.*, 2015; Guo *et al.*, 2015). This initial test is very important due to the fluorescence quench will be used as an evidence for the detection of the proteins. Thus, if something in the PB composition are able to quench the fluorescence intensity of the CQDs.BPEI, this would lead us for a false positive result. A simple test was performed and it was possible to observe that PB components displayed no quenching effects on the fluorescence intensity of the CQDs.BPEI. In addition, this result is further supported

based on literature (Dong, Wang, *et al.*, 2012). Afterwards, the potential of the CQDs.BPEI as a protein-responsive fluorescent probe was tested by evaluating eight different proteins. In this regard, four metallic (Hem, Myo, α -Am and Cyt.C) and four non-metallic (BSA, HSA, PhosA and PhosB) proteins were chosen. Fig. 4.4 presents the fluorescence response (I/I_0) of the CQDs.BPEI upon addition of the proteins. Clearly, each protein was capable to quench the fluorescence intensity even using a concentration as low as 40 nM. This shows the high potential of the CQDs.BPEI as a protein-responsive sensor.

Figure 4.4. Fluorescence response of the CQDs.BPEI upon addition of protein at 40 nM (concentration in the well).

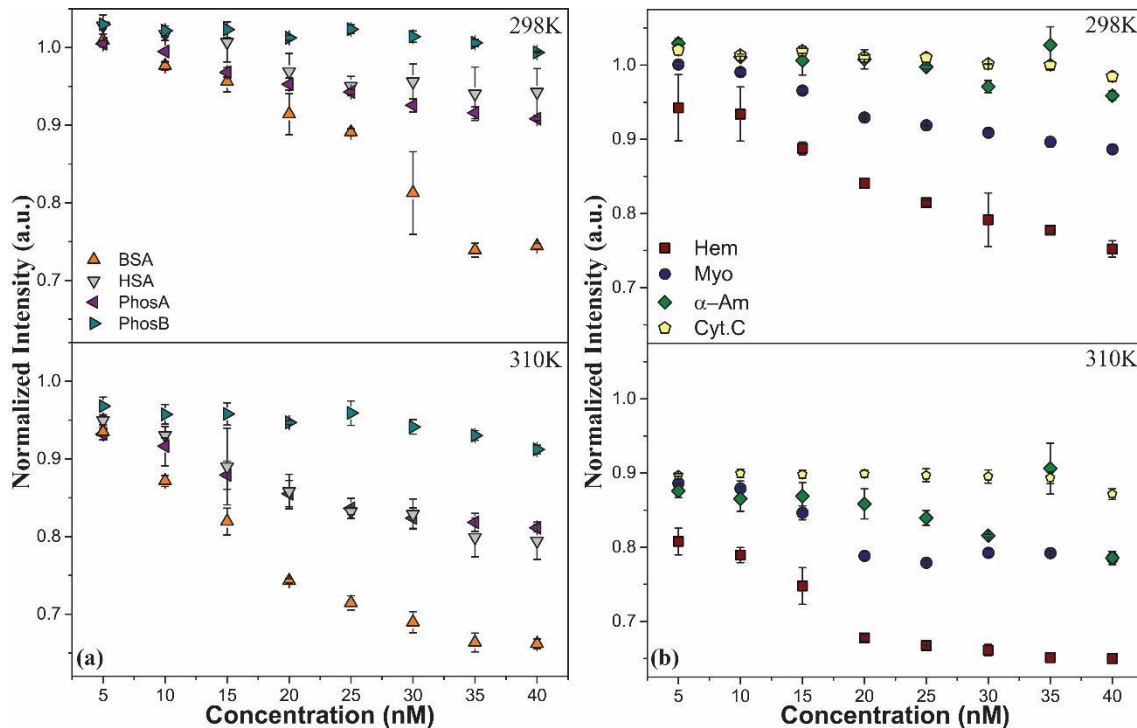


Source: Author

Beyond detection, it is also important to know the type of interaction between CQDs.BPEI and proteins. Therefore, the Fig. 4.5(a) and (b) display the titrations at 298 and 310K for non-metallic and metallic proteins, respectively. By observing the plots (

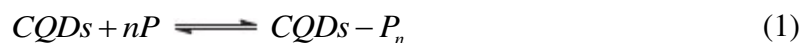
I/I_0 vs protein concentration) at 298K, it was possible to see a deviation of linearity at high protein concentration. This indicates the presence of both collisional (dynamic) and binding-related (static) quenching mechanism (Barbero *et al.*, 2009). However, in order to discriminate between one another, the titrations were also performed at 310 K. As a consequence of the increase of the temperature, the quenching efficiency was higher for all proteins evaluated. According to the literature (Van De Weert and Stella, 2011), the increase of the temperature should increase the quenching efficiency for collisional mechanism, while the opposite way should be expected for binding-related quenching. Therefore, the results found in the Fig. 4.5(b) and (c) can be explained by the increase of the collisions along increasing of the temperature, which leads to higher quenching efficiency. Moreover, the deviation of the linearity observed in the titration experiments may be explained based on a protein structural view. Similar results can be found when the fluorophore is not able to interact with the hydrophobic interior of the protein (Lakowicz, 2006). As a result, the fluorescence quench comes from the tryptophan residues on the surface of the system. In this sense, it is plausible to infer that CQDs.BPEI were not able to penetrate into the hydrophobic domain of the protein. Therefore, the decrease of the fluorescence intensity from CQDs.BPEI may be explained based on surface interactions between the CQDs and amino acids residues.

Figure 4.5. Fluorescence titration performed at 298 and 310K for non-metallic (a) and metallic (b) proteins.



Source: Author

In order to deepen further our study, the fluorescence titrations were mathematically described. Since a dynamic quench mechanism was found, there is no chemical bond between CQDs and the proteins tested. Although, the decrease of the fluorescence intensity of the CQDs comes from interactions involving binding sites on the protein. The number of these binding sites is very important to describe the quenching efficiency. Therefore, we first assumed the following equation to describe the interaction between CQDs and proteins:



where $CQDs$, P (protein) and $CQDs - P_n$ are the concentration of the chemical species. To keep the calculation simple, we considered a number n of proteins interacting with one CQD. So, the quenching-related constant (K_Q) can be found by:

$$K_Q = \frac{(CQDs - P_n)}{(CQDs) \cdot (P)^n} \quad (2)$$

However, the law of mass action gives

$$(CQDs) = (CQDs)_0 - (CQDs - P_n) \quad (3)$$

where $(CQDs)_0$ is the initial concentration of the CQDs. By replacing the equation 3 in 2, we obtained

$$K_Q = \frac{(CQDs - P_n)}{[(CQDs)_0 - (CQDs - P_n)] \cdot (P)^n} \quad (4)$$

Doing all the math, we finally got the equation 5 displayed below:

$$K_Q = \frac{1}{(P)^n} \cdot \left(\frac{(CQDs - P_n)}{(CQDs)_0} - 1 \right) \quad (5)$$

The terms $(CQDs)_0$ and $(CQDs - P_n)$ can be related to the I_0 and I , respectively. Therefore, the equation 5 turn into

$$K_Q = \frac{1}{(P)^n} \cdot \left(\frac{I}{I_0} - 1 \right) \quad (6)$$

By rearranging the equation 6, we finally obtained the equation to analyze the fluorescence titration experiments showed below:

$$\frac{I}{I_0} = 1 + K_Q \cdot (P)^n \quad (7)$$

The equation 7 can be interpreted as a modification of the Stern-Volmer relationship (Barbero *et al.*, 2009). Some publications in the literature consider the coefficient n as a number of binding sites between the involved entities (Chen *et al.*, 2008; Tansakul *et al.*, 2010; Lin *et al.*, 2012; Chaturvedi *et al.*, 2015). However, it is important to highlight a critical review wrote by Marco van de Weert and Lorenzo Stella (Van De Weert and Stella, 2011). They reported a comparative study using BSA and 1-Anilino-8-naphthalenesulfonic acid hemi-magnesium salt hydrate (ANS). By using a modified Stern-Volmer relationship, a fit of the data gives $n = 1.14$, while another study (Togashi and Ryder, 2007) of the same system utilizing more complex approach yields 5 binding sites. Therefore, the coefficient n , as usual assumed in the Stern-Volmer equation, may be lower than the real number of the binding sites. That is why, in this work, we consider n as a number of proteins interacting with one CQDs.

In addition to K_D and n , Gibbs energy change (ΔG), Enthalpy change (ΔH) and Entropy change (ΔS) were also calculated in order to elucidate the type of interaction between CQDs and the different proteins. Since the literature (Leckband, 2000; Huang *et al.*, 2015) reveals the binding process to macromolecules may include hydrophobic, van der Waals, hydrogen bonds and/or electrostatic interactions. Thus, ΔG was calculated using the following equation:

$$\Delta G = -RT \ln K \quad (8)$$

ΔH was calculated through Van't Hoff equation:

$$\ln \frac{K_2}{K_1} = \frac{\Delta H}{R} \cdot \left(\frac{1}{T_1} - \frac{1}{T_2} \right) \quad (9)$$

While ΔS was obtained by using

$$\Delta G = \Delta H - T \cdot \Delta S \quad (10)$$

The value of R (gas constant) adopted for all calculations was $8.314 \text{ J}\cdot\text{mol}^{-1}\cdot\text{K}^{-1}$. Using this whole set of data including values of K_D , n , ΔG , ΔH and ΔS , it was possible to perform a complete investigation about magnitude and type of interaction as well as the number of binding sites between CQDs and proteins. The values found for each parameter cited are summarized in the Table 4.1 for all non-metallic proteins.

Table 4.1. Values of K_Q , n , ΔG , ΔH and ΔS found for non-metallic proteins.

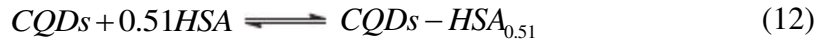
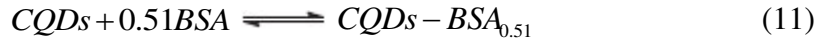
Protein	T (K)	K_Q	n	ΔG (kJ.mol ⁻¹)	ΔH (kJ.mol ⁻¹)	ΔS (J.mol ⁻¹ .K ⁻¹)
BSA	298	49.0·10 ⁴	1.72	-32.4	261.8	987.5
	310	293.0·10 ⁵	0.68	-44.3		
HSA	298	-	-	-	-	-
	310	169.1·10 ⁵	0.68	-42.8		
PhosA	298	94.0·10 ⁴	1.26	-34.0	220.4	854.2
	310	294.6·10 ⁵	0.51	-44.3		
PhosB	298	-	-	-	-	-
	310	111.7·10 ⁵	0.51	-41.8		

Source: Author

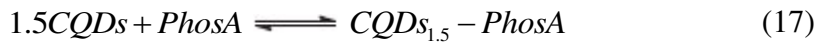
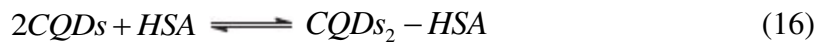
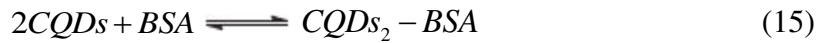
For all non-metallic proteins, it was possible to observe the increase of K_Q along the increase of the temperature. The difference going from K_Q^{298} to K_Q^{310} is one order higher. Thus, raising the temperature of the experiment makes the interaction between CQDs.BPEI and proteins stronger. This also confirms the quenching mechanism occurs through dynamic process and it displays the endothermic character of the interaction. Under the same conditions, different proteins have different ways to interact. This is demonstrated by the different values of K_Q . However, some of the proteins chosen to perform this work are similar. For instance, BSA and HSA are both albumin proteins. Therefore, the behavior of the proteins pairs BSA/HSA and PhosA/PhosB are expected to be similar. Once it cannot be observed taking K_Q values, this may indicate different type of aminoacids residues on the protein surface interacting to CQDs.BPEI.

The expected similarity was observed by analyzing the n coefficient. The values for this parameter were found to be equal for the proteins pairs at 310 K. For BSA/HSA, 0.68 is observed, while 0.51 was the achieved value for PhosA/PhosB. At this moment, it is

important to remember the assumption made for n in this work, where n is considered as a number of proteins interacting with one CQDs. Therefore, we can write the following chemical equations:



These chemical equations denoted the stoichiometry of the “reaction” at 310 K. However, if the number of binding sites is the goal of this part of the treatment, we need to assume CQDs interacting with one protein. In this sense, the equations 11 and 12 have to be multiplied by 2, while equations 13 and 14 by 1.5, approximately. So, the mentioned equations can be re-written to obtain



Upon multiplication, the equations 15, 16, 17 and 18 display how many CQDs can be related to one protein. Therefore, it is possible to extract the number of binding sites. For BSA and HSA, 2 CQDs were found to interact with one protein. Therefore, it can be inferred 2 equivalent binding sites. For PhosA and PhosB, the relationship found was 1.5 CQDs for one protein. As we cannot assume 0.5 CQDs interacting, this result may indicate 2 non-equivalent binding sites, where one of them is stronger. Therefore, n coefficient might be an indicative of the force intensity of the binding site, since it is no sense consider half binding site. Furthermore, n values were found to decrease by increasing of the temperature. For instance, the BSA coefficients decrease from 1.72 at 298K to 0.68 at 310K. As it can be seen, the relationship between n and the number of binding sites is inversely proportional. Thus, smaller n values are expected to generate

higher number of binding sites. This easily explain the increase of the quenching efficiency observed when the temperature was raised from 298 to 310 K. By increasing the number of the binding sites, the number of the collisions between CQDs and proteins will also increase. Consequently, the quenching efficiency is higher.

As mentioned, the thermodynamic parameters can be used to further describe the interaction between CQDs.BPEI and proteins. In this sense, the negative values of ΔG observed in the range of -32.4 – -44.3 KJ/mol for all non-metallic proteins indicates the binding process occurs spontaneously. According to the literature (Ross and Subramanian, 1981), the positive values of ΔH and ΔS indicates a hydrophobic association between the ligand and biological macromolecules, such as proteins. Therefore, this evidences the hydrophobic interaction predominantly acting in the binding process. Since the surface of CQDs.BPEI is highly polar, this seems to be weird and even no sense at first time. However, it is necessary to understand what is the meaning for the hydrophobic association mentioned by Ross and Subramanian (Ross and Subramanian, 1981). In their work, it was assumed the protein association process to happen through two steps. The first one represents the approximation process between ligand and protein. In this step, the isolated species starts to move towards each other. When the distance between the hydrated species is smaller enough, there is an interpenetration of H₂O layers from the species and this is what is called hydrophobic association.

To further understand, the association process through hydrophobic interaction means that non polar amino acid side chains residues (previously accessible to solvent in the isolated specie) become buried as long as the interpenetration process is deeper. Therefore, the hydrophobic association denotes the reorganization of the H₂O molecules around the species upon approximation. In this first step of the protein association process, the thermodynamic parameters are expected to satisfy $\Delta G < 0$, $\Delta H > 0$ and $\Delta S > 0$. The second step of the association denotes the formation of the complex between ligand and protein. Unlike the first step, the immobilization of the ligand on the protein is more extensive. Moreover, intermolecular interaction such as hydrogen bonds and/or van der Waals forces are expected to be found. The thermodynamic parameters for the second step have to satisfy $\Delta G < 0$, $\Delta H < 0$ and $\Delta S < 0$. Clearly, the first step is what is occurring between CQDs.BPEI and the non-metallic proteins evaluated. Taken together, the thermodynamic view points the interaction to be highly spontaneous occurring through hydrophobic forces. Additionally, the non-polar residues buried during the

interpenetration process are blocked for CQDs.BPEI. Thus, we can further support our assumption that CQDs.BPEI were not able to penetrate the hydrophobic interior of the proteins, which it may explain the deviation of the linearity observed at the fluorescence titration experiments.

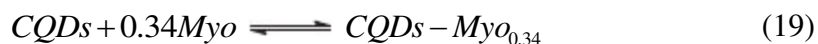
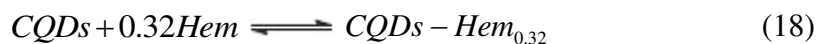
The fluorescence titrations were also performed for metallic proteins. Table 4.2 shows the values of K_Q , n , ΔG , ΔH and ΔS for this group of studied proteins. For K_Q , the values were found to increase from 298 to 310K, which it evidences the endothermic character of the binding process. Once again, the difference between K_Q^{298} and K_Q^{310} is one order. As a result, it was possible to achieve a value of $141.8 \cdot 10^4$ (K_Q^{298}) and $109.9 \cdot 10^5$ (K_Q^{310}) for Hem. Another interesting fact to analysis is the magnitude of the K_Q^{298} values for the different metallic proteins. For Myo, the K_Q^{298} is equal to $174.0 \cdot 10^4$ M^{-1} , which is higher than the value of K_Q^{298} for Hem. It is well-known that Hem and Myo are compounded by heme groups. However, the number of the heme groups in the composition of each protein tested is different. It can be observed Hem containing four heme groups, while Myo is compound by only one of these groups. Therefore, the K_Q^{298} values found for each protein may indicates the heme groups are not interacting with CQDs.BPEI. Since the value of K_Q^{298} for Hem was smaller. If the heme groups would be interacting, the higher number of these groups in the composition of the Hem would increase the K_Q^{298} values.

Table 4.2. Values of K_Q , n , ΔG , ΔH and ΔS found for metallic proteins.

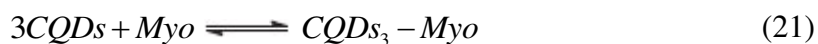
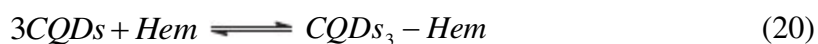
Protein	T (K)	K_Q	n	ΔG (kJ.mol ⁻¹)	ΔH (kJ.mol ⁻¹)	ΔS (J.mol ⁻¹ .K ⁻¹)
Hem	298	$141.8 \cdot 10^4$	0.78	-40.7	131.0	567.7
	310	$109.9 \cdot 10^5$	0.32	-47.7		
Myo	298	$174.0 \cdot 10^4$	1.15	-35.6	192.5	765.6
	310	$352.5 \cdot 10^5$	0.34	-44.7		

Source: Author

The n coefficient was also found to decrease along the increase of the temperature. From the n values at 310K, it was allowed to write the following chemical equations:



Once our goal is to achieve the number of binding sites on the surface of the protein. For this propose, it can be consider a variable number of CQDs interacting with one protein. Thus, it was multiplied the equations 18 and 19 by 3, approximately, and the equations can re-write as follow:



Both Hem and Myo displayed three possible binding sites, which shows the similarity of the interaction between the two proteins and CQDs.BPEI. This further support the heme groups as a non-interacting unit. The thermodynamics parameters were also calculated for Hem and Myo in order to describe the interaction between these proteins and CQDs.BPEI. ΔG values (in the range of -35.6 – - 47.7 KJ/mol) also show a spontaneous binding process. The ΔH and ΔS results for Hem and Myo were found to be bigger than 0, which evidence support the interaction mainly occurring via hydrophobic forces.

Comparing the thermodynamic parameters calculated for all tested proteins, the negative values found for ΔG are similar. This can be easily seen looking at the values in the Tables 4.1 and 4.2. On the other hand, the values of ΔH and ΔS are different in magnitude by observing metallic and non-metallic proteins, which was unexpected. In this sense, it is important to mention the negative ΔH and ΔS values increase in magnitude along increase of the polarizability of the π electron charge cloud (Ross and Subramanian, 1981). The polarizability is considered as a term to describe how easy the electron cloud can distort, giving a dipolar charge distribution. Generally, atoms containing a huge number of electrons and show higher polarizability than atoms with small amount of electrons. As the electron distribution as well as atom size are parallel parameters (directly proportional relationship), the polarizability and the atom mass can be easily related. Given together, the results of ΔH and ΔS may be linked to the protein

molecular weight (M_w). In this sense, the Table 4.3 displays the values of M_w for all tested proteins in this work.

Table 4.3. Values of M_w of the analyte proteins targeted.

Type	Proteins	M_w (kDa)
Non-metallic	BSA	66.3
	HSA	69.4
	PhosA	110
	PhosB	140
Metallic	Hem	64.5
	Myo	17.0
	α -Am	50.0
	Cyt.C	12.3

Source: (Miranda *et al.*, 2007)

Using the values of M_w displayed in the Table 4.3, it is possible to observe a random behavior along the results of ΔH and ΔS in the Tables 4.1 and 4.2. For example, values of M_w for BSA and PhosA are 66.3 and 110 kDa, respectively. Thus, it was expected greater values of ΔH and ΔS for PhosA. However, this was not observed looking at the results for the thermodynamic mentioned parameters. Both ΔH and ΔS values for BSA were found to be larger than the values achieved for PhosA. For metallic proteins, the observed behavior was the same. Since Hem, with much larger value of M_w (64.5 kDa), showed ΔH and ΔS smaller values than the results observed for Myo, a protein with M_w equal to 17.0 kDa. Given these surprisingly results, it may be possible the thermodynamic parameters are not linked to the properties of the whole protein. If this is not true, it should be expected the values of ΔH and ΔS to increase in magnitude when a protein with larger value of M_w is compared to another with smaller M_w . So, it is

plausible to infer the properties of the binding site have a predominant effect under values of ΔH and ΔS .

The explanation for the thermodynamic studied parameters may be supported on the mass of the amino acids residues interacting to the CQDs.BPEI. Since the polarizability of the π electron charge cloud may behavior affecting by the local properties of the binding site. Once we cannot assure what are the amino acids residues involved at the formation of *CQDs – P* , an even deeper investigation about the interaction between CQDs.BPEI and proteins needs to be done.

Finally, it is important to highlight the great potential of the CQDs.BPEI as a platform to also identify the analyte proteins through a chemical nose-based strategy (Le *et al.*, 2013). Usually, the terms ‘nose’ or ‘tongue’ are used to describe sensing studies using electrodes (Bunz and Rotello, 2010). However, the same ‘nose’ approach can be applied for optical properties where the material gives a fluorescent signal (Rana *et al.*, 2015; Peveler *et al.*, 2016). Using this approach, the analyte can easily be recognized by having distinct interactions with the sensor used platform, which it will generate a specific fluorescent pattern from each analyte. Obviously, the different signals come from distinct interactions. Once in this study, we have demonstrated different interactions occurring between the analyte proteins and CQDs.BPEI, it may be possible to use our fluorescent NPs to compound a nose-based strategy to perform the identification of proteins. This becomes even more clear by looking at the results presented in the Fig. 4.4. Each protein gives a distinct fluorescent signal, which clearly evidences the great potential of the CQDs.BPEI as a protein-responsive platform to perform identification beyond detection.

4.4 Conclusion

In conclusion, we have successfully synthesized ~1.5 nm NH_2 -rich CQDs via easy methodology involving the partial decomposition of citric acid and BPEI. The capping containing NH_2 groups was confirmed by XPS analysis as well as FTIR measurements. Structural features like a graphene/graphitic core were also evidenced by characterization techniques. The great potential of the CQDs.BPEI have been demonstrated for detection of the eight different proteins including metallic and non-metallic kinds. This is clearly demonstrated by detection of some proteins such as Hem, for example, by using values of concentrations as low as 5 nM. The investigation through the fluorescence titrations at distinct temperatures (298 and 310K) gives spontaneous interaction between CQDs.BPEI

and all proteins targeted, since the values of ΔG were found to be negative. Values of ΔH and ΔS were also calculated. For both non-metallic and metallic proteins, below zero values can be found, which indicates the interaction at the binding sites occurring via hydrophobic forces. As long as the non-polar amino acid residues become buried in the structure of the protein, this type of interaction evidences CQDs.BPEI were not able to penetrate in the hydrophobic domain of the protein. In this sense, we conclude a variation of the surface properties in order to make the CQDs able to interact with the non-polar amino acids residues would decrease the limit detection. This would improve the early diagnosis of the diseases like cancer, for example. In addition, the distinct fluorescent signal of each protein demonstrated the high potential of the CQDs.BPEI to perform the identification of the proteins. Given together, the results obtained in this work place our fluorescent carbon-based NPs as a powerful protein-responsive platform.

References

BARBERO, N. et al. A study of the interaction between fluorescein sodium salt and bovine serum albumin by steady-state fluorescence. **Dyes and Pigments**, v. 80, n. 3, p. 307-313, 2009. ISSN 0143-7208. Disponível em: < <http://www.sciencedirect.com/science/article/pii/S0143720808001228> >.

BARINOV, A. et al. Initial Stages of Oxidation on Graphitic Surfaces: Photoemission Study and Density Functional Theory Calculations. **The Journal of Physical Chemistry C**, v. 113, n. 21, p. 9009-9013, 2009/05/28 2009. ISSN 1932-7447. Disponível em: < <http://dx.doi.org/10.1021/jp902051d> >.

BU, D. et al. An immunosensor designed for polybrominated biphenyl detection based on fluorescence resonance energy transfer (FRET) between carbon dots and gold nanoparticles. **Sensors and Actuators B: Chemical**, v. 195, p. 540-548, 2014. ISSN 0925-4005. Disponível em: < <http://www.sciencedirect.com/science/article/pii/S0925400514000963> >.

BUNZ, U. H. F.; ROTELLO, V. M. Gold Nanoparticle–Fluorophore Complexes: Sensitive and Discerning “Noses” for Biosystems Sensing. **Angewandte Chemie International Edition**, v. 49, n. 19, p. 3268-3279, 2010. ISSN 1521-3773. Disponível em: < <http://dx.doi.org/10.1002/anie.200906928> >.

CHATURVEDI, S. K. et al. Elucidating the interaction of limonene with bovine serum albumin: a multi-technique approach. **Molecular BioSystems**, v. 11, n. 1, p. 307-316, 2015. ISSN 1742-206X. Disponível em: < <http://dx.doi.org/10.1039/C4MB00548A> >.

CHEN, B. et al. Large scale synthesis of photoluminescent carbon nanodots and their application for bioimaging. **Nanoscale**, v. 5, n. 5, p. 1967-1971, 2013. ISSN 2040-3364. Disponível em: < <http://dx.doi.org/10.1039/C2NR32675B> >.

CHEN, W. et al. Water-Soluble Off–On Spin-Labeled Quantum-Dots Conjugate. **Small**, v. 4, n. 6, p. 759-764, 2008. ISSN 1613-6829. Disponível em: < <http://dx.doi.org/10.1002/smll.200700788> >.

CUI, X. et al. A fluorescent biosensor based on carbon dots-labeled oligodeoxyribonucleotide and graphene oxide for mercury (II) detection. **Biosensors and Bioelectronics**, v. 63, p. 506-512, 2015. ISSN 0956-5663. Disponível em: < <http://www.sciencedirect.com/science/article/pii/S0956566314005880> >.

DANIELS, M. J. et al. Abnormal Cytokinesis in Cells Deficient in the Breast Cancer Susceptibility Protein BRCA2. **Science**, v. 306, n. 5697, p. 876-879, 2004. Disponível em: < <http://science.sciencemag.org/content/306/5697/876.abstract> >.

DING, H. et al. Luminescent carbon quantum dots and their application in cell imaging. **New Journal of Chemistry**, v. 37, n. 8, p. 2515-2520, 2013. ISSN 1144-0546. Disponível em: < <http://dx.doi.org/10.1039/C3NJ00366C> >.

DONG, Y. et al. Blue luminescent graphene quantum dots and graphene oxide prepared by tuning the carbonization degree of citric acid. **Carbon**, v. 50, n. 12, p.

- 4738-4743, 2012. ISSN 0008-6223. Disponível em: < <http://www.sciencedirect.com/science/article/pii/S0008622312005088> >.
- DONG, Y. et al. Polyamine-Functionalized Carbon Quantum Dots as Fluorescent Probes for Selective and Sensitive Detection of Copper Ions. **Analytical Chemistry**, v. 84, n. 14, p. 6220-6224, 2012/07/17 2012. ISSN 0003-2700. Disponível em: < <http://dx.doi.org/10.1021/ac3012126> >.
- ESTEVEZ DA SILVA, J. C. G.; GONÇALVES, H. M. R. Analytical and bioanalytical applications of carbon dots. **TrAC Trends in Analytical Chemistry**, v. 30, n. 8, p. 1327-1336, 2011. ISSN 0165-9936. Disponível em: < <http://www.sciencedirect.com/science/article/pii/S0165993611001567> >.
- GONG, X. et al. Facile synthesis of nitrogen-doped carbon dots for Fe³⁺ sensing and cellular imaging. **Analytica Chimica Acta**, v. 861, p. 74-84, 2015. ISSN 0003-2670. Disponível em: < <http://www.sciencedirect.com/science/article/pii/S0003267014014834> >.
- GUO, Y. et al. Hydrothermal synthesis of highly fluorescent carbon nanoparticles from sodium citrate and their use for the detection of mercury ions. **Carbon**, v. 52, p. 583-589, 2013. ISSN 0008-6223. Disponível em: < <http://www.sciencedirect.com/science/article/pii/S000862231200841X> >.
- GUO, Y. et al. Fluorescent carbon nanoparticles for the fluorescent detection of metal ions. **Biosensors and Bioelectronics**, v. 63, p. 61-71, 2015. ISSN 0956-5663. Disponível em: < <http://www.sciencedirect.com/science/article/pii/S0956566314005107> >.
- GYGI, S. P. et al. Quantitative analysis of complex protein mixtures using isotope-coded affinity tags. **Nat Biotech**, v. 17, n. 10, p. 994-999, 1999. ISSN 1087-0156. Disponível em: < <http://dx.doi.org/10.1038/13690> >.
- HAAB, B. B. Applications of antibody array platforms. **Current Opinion in Biotechnology**, v. 17, n. 4, p. 415-421, 2006. ISSN 0958-1669. Disponível em: < <http://www.sciencedirect.com/science/article/pii/S0958166906000978> >.
- HUANG, P. et al. Light-Triggered Theranostics Based on Photosensitizer-Conjugated Carbon Dots for Simultaneous Enhanced-Fluorescence Imaging and Photodynamic Therapy. **Advanced Materials**, v. 24, n. 37, p. 5104-5110, 2012. ISSN 1521-4095. Disponível em: < <http://dx.doi.org/10.1002/adma.201200650> >.
- HUANG, S. et al. Study on the molecular interaction of graphene quantum dots with human serum albumin: Combined spectroscopic and electrochemical approaches. **Journal of Hazardous Materials**, v. 285, p. 18-26, 2015. ISSN 0304-3894. Disponível em: < <http://www.sciencedirect.com/science/article/pii/S0304389414009261> >.
- HUI, D. et al. Nitrogen-doped carbon dots derived from polyvinyl pyrrolidone and their multicolor cell imaging. **Nanotechnology**, v. 25, n. 20, p. 205604, 2014. ISSN 0957-4484. Disponível em: < <http://stacks.iop.org/0957-4484/25/i=20/a=205604> >.

- JANKOVSKY, O. et al. Water-soluble highly fluorinated graphite oxide. **RSC Advances**, v. 4, n. 3, p. 1378-1387, 2014. Disponível em: < <http://dx.doi.org/10.1039/C3RA45183F> >.
- LAKOWICZ, J. R. **Principles of fluorescence spectroscopy**. 3rd. New York: Springer-Verlag, 2006.
- LE, N. D. B.; RANA, S.; ROTELLO, V. M. Chemical Nose Sensors – an Alternative Strategy for Cancer Diagnosis. **Expert review of molecular diagnostics**, v. 13, n. 2, p. 111-113, 2013. ISSN 1473-7159 1744-8352. Disponível em: < <http://www.ncbi.nlm.nih.gov/pmc/articles/PMC4067236/> >.
- LECKBAND, D. Measuring the Forces that Control Protein Interactions. **Annual Review of Biophysics and Biomolecular Structure**, v. 29, n. 1, p. 1-26, 2000. Disponível em: < <http://www.annualreviews.org/doi/abs/10.1146/annurev.biophys.29.1.1> >.
- LI, H. et al. Water-Soluble Fluorescent Carbon Quantum Dots and Photocatalyst Design. **Angewandte Chemie International Edition**, v. 49, n. 26, p. 4430-4434, 2010. ISSN 1521-3773. Disponível em: < <http://dx.doi.org/10.1002/anie.200906154> >.
- LI, X. et al. Engineering surface states of carbon dots to achieve controllable luminescence for solid-luminescent composites and sensitive Be²⁺ detection. **Scientific Reports**, v. 4, p. 4976, 2014. Disponível em: < <http://dx.doi.org/10.1038/srep04976> >.
- LI, Y. et al. Nitrogen-Doped Graphene Quantum Dots with Oxygen-Rich Functional Groups. **Journal of the American Chemical Society**, v. 134, n. 1, p. 15-18, 2012/01/11 2012. ISSN 0002-7863. Disponível em: < <http://dx.doi.org/10.1021/ja206030c> >.
- LIM, S. Y.; SHEN, W.; GAO, Z. Carbon quantum dots and their applications. **Chemical Society Reviews**, v. 44, n. 1, p. 362-381, 2015. ISSN 0306-0012. Disponível em: < <http://dx.doi.org/10.1039/C4CS00269E> >.
- LIN, F. et al. Electron transfer quenching by nitroxide radicals of the fluorescence of carbon dots. **Journal of Materials Chemistry**, v. 22, n. 23, p. 11801-11807, 2012. ISSN 0959-9428. Disponível em: < <http://dx.doi.org/10.1039/C2JM31191G> >.
- LIU, Q. et al. Strong Two-Photon-Induced Fluorescence from Photostable, Biocompatible Nitrogen-Doped Graphene Quantum Dots for Cellular and Deep-Tissue Imaging. **Nano Letters**, v. 13, n. 6, p. 2436-2441, 2013/06/12 2013. ISSN 1530-6984. Disponível em: < <http://dx.doi.org/10.1021/nl400368v> >.
- MIRANDA, O. R. et al. Array-Based Sensing of Proteins Using Conjugated Polymers. **Journal of the American Chemical Society**, v. 129, n. 32, p. 9856-9857, 2007/08/01 2007. ISSN 0002-7863. Disponível em: < <http://dx.doi.org/10.1021/ja0737927> >.
- NIU, J.; GAO, H. Synthesis and drug detection performance of nitrogen-doped carbon dots. **Journal of Luminescence**, v. 149, p. 159-162, 2014. ISSN 0022-2313.

Disponível em: < <http://www.sciencedirect.com/science/article/pii/S0022231314000295> >.

PAN, D. et al. Hydrothermal Route for Cutting Graphene Sheets into Blue-Luminescent Graphene Quantum Dots. **Advanced Materials**, v. 22, n. 6, p. 734-738, 2010. ISSN 1521-4095. Disponível em: < <http://dx.doi.org/10.1002/adma.200902825> >.

PEVELER, W. J. et al. Multichannel Detection and Differentiation of Explosives with a Quantum Dot Array. **ACS Nano**, v. 10, n. 1, p. 1139-1146, 2016/01/26 2016. ISSN 1936-0851. Disponível em: < <http://dx.doi.org/10.1021/acsnano.5b06433> >.

PYLYPENKO, S. et al. Tuning Carbon-Based Fuel Cell Catalyst Support Structures via Nitrogen Functionalization. I. Investigation of Structural and Compositional Modification of Highly Oriented Pyrolytic Graphite Model Catalyst Supports as a Function of Nitrogen Implantation Dose. **The Journal of Physical Chemistry C**, v. 115, n. 28, p. 13667-13675, 2011/07/21 2011. ISSN 1932-7447. Disponível em: < <http://dx.doi.org/10.1021/jp1122344> >.

QIAN, Z. et al. Carbon Quantum Dots-Based Recyclable Real-Time Fluorescence Assay for Alkaline Phosphatase with Adenosine Triphosphate as Substrate. **Analytical Chemistry**, v. 87, n. 5, p. 2966-2973, 2015/03/03 2015. ISSN 0003-2700. Disponível em: < <http://dx.doi.org/10.1021/ac504519b> >.

QIAN, Z. S. et al. A real-time fluorescent assay for the detection of alkaline phosphatase activity based on carbon quantum dots. **Biosensors and Bioelectronics**, v. 68, p. 675-680, 2015. ISSN 0956-5663. Disponível em: < <http://www.sciencedirect.com/science/article/pii/S0956566315000858> >.

QU, D. et al. Formation mechanism and optimization of highly luminescent N-doped graphene quantum dots. **Scientific Reports**, v. 4, p. 5294, 2014. Disponível em: < <http://dx.doi.org/10.1038/srep05294> >.

RANA, S. et al. A Multichannel Biosensor for Rapid Determination of Cell Surface Glycomic Signatures. **ACS Central Science**, v. 1, n. 4, p. 191-197, 2015/07/22 2015. ISSN 2374-7943. Disponível em: < <http://dx.doi.org/10.1021/acscentsci.5b00126> >.

ROSS, P. D.; SUBRAMANIAN, S. Thermodynamics of protein association reactions: forces contributing to stability. **Biochemistry**, v. 20, n. 11, p. 3096-3102, 1981/05/01 1981. ISSN 0006-2960. Disponível em: < <http://dx.doi.org/10.1021/bi00514a017> >.

TANSAKUL, C. et al. Distance-Dependent Fluorescence Quenching and Binding of CdSe Quantum Dots by Functionalized Nitroxide Radicals. **The Journal of Physical Chemistry C**, v. 114, n. 17, p. 7793-7805, 2010/05/06 2010. ISSN 1932-7447. Disponível em: < <http://dx.doi.org/10.1021/jp1005023> >.

THEMA, F. T. et al. Synthesis and Characterization of Graphene Thin Films by Chemical Reduction of Exfoliated and Intercalated Graphite Oxide. **Journal of Chemistry**, v. 2013, p. 6, 2013. Disponível em: < <http://dx.doi.org/10.1155/2013/150536> >.

TOGASHI, D. M.; RYDER, A. G. A Fluorescence Analysis of ANS Bound to Bovine Serum Albumin: Binding Properties Revisited by Using Energy Transfer. **Journal of Fluorescence**, v. 18, n. 2, p. 519-526, 2007. ISSN 1573-4994. Disponível em: < <http://dx.doi.org/10.1007/s10895-007-0294-x> >.

USACHOV, D. et al. Nitrogen-Doped Graphene: Efficient Growth, Structure, and Electronic Properties. **Nano Letters**, v. 11, n. 12, p. 5401-5407, 2011/12/14 2011. ISSN 1530-6984. Disponível em: < <http://dx.doi.org/10.1021/nl2031037> >.

VAN DE WEERT, M.; STELLA, L. Fluorescence quenching and ligand binding: A critical discussion of a popular methodology. **Journal of Molecular Structure**, v. 998, n. 1-3, p. 144-150, 2011. ISSN 0022-2860. Disponível em: < <http://www.sciencedirect.com/science/article/pii/S002228601100398X> >.

WANG, F. et al. Graphene quantum dots as a fluorescent sensing platform for highly efficient detection of copper(II) ions. **Sensors and Actuators B: Chemical**, v. 190, p. 516-522, 2014. ISSN 0925-4005. Disponível em: < <http://www.sciencedirect.com/science/article/pii/S0925400513010496> >.

WANG, Y.; HU, A. Carbon quantum dots: synthesis, properties and applications. **Journal of Materials Chemistry C**, v. 2, n. 34, p. 6921-6939, 2014. ISSN 2050-7526. Disponível em: < <http://dx.doi.org/10.1039/C4TC00988F> >.

WEI, W. et al. Non-Enzymatic-Browning-Reaction: A Versatile Route for Production of Nitrogen-Doped Carbon Dots with Tunable Multicolor Luminescent Display. **Scientific Reports**, v. 4, p. 3564, 2014. Disponível em: < <http://dx.doi.org/10.1038/srep03564> >.

XU, X. et al. Electrophoretic Analysis and Purification of Fluorescent Single-Walled Carbon Nanotube Fragments. **Journal of the American Chemical Society**, v. 126, n. 40, p. 12736-12737, 2004/10/01 2004. ISSN 0002-7863. Disponível em: < <http://dx.doi.org/10.1021/ja040082h> >.

YAN, Z.; YU, Y.; CHEN, J. An Examination of the Interaction of Carbon Quantum Dots with Bovine Serum Albumin by Ultraviolet-Visible and Fluorescence Spectrophotometer. **Advanced Science Focus**, v. 2, n. 1, p. 92-95, 2014. Disponível em: < <http://www.ingentaconnect.com/content/asp/asfo/2014/00000002/00000001/art00017> <http://dx.doi.org/10.1166/asfo.2014.1077> >.

YANG, S.-T. et al. Carbon Dots for Optical Imaging in Vivo. **Journal of the American Chemical Society**, v. 131, n. 32, p. 11308-11309, 2009/08/19 2009. ISSN 0002-7863. Disponível em: < <http://dx.doi.org/10.1021/ja904843x> >.

YU, C. et al. Carbon-dot-based ratiometric fluorescent sensor for detecting hydrogen sulfide in aqueous media and inside live cells. **Chemical Communications**, v. 49, n. 4, p. 403-405, 2013. ISSN 1359-7345. Disponível em: < <http://dx.doi.org/10.1039/C2CC37329G> >.

ZHANG, H. et al. Hydrothermal Transformation of Dried Grass into Graphitic Carbon-Based High Performance Electrocatalyst for Oxygen Reduction Reaction. **Small**, v. 10, n. 16, p. 3371-3378, 2014. ISSN 1613-6829. Disponível em: <
<http://dx.doi.org/10.1002/sml.201400781> >.

CHAPTER 5

5 DEVELOPMENT OF “NOSE”-BASED STRATEGY TO IDENTIFY PROTEINS USING NH₂-RICH CQDs

Abstract

A fast and cheap methodology to detect abnormal level of proteins in human serum is still challenging researchers worldwide. Here, we developed two “nose”-based methodologies to identify proteins. Using materials as cheap as the metal ion Cu²⁺, the chelating agent ethylenediaminetetraacetic Acid (EDTA) and carbon quantum dots (CQDs), our one or two “nose”-based approaches were able to correctly discriminate six proteins in 5 mM phosphate buffer (PB, pH 7.4). The accuracy was higher than 92% according to the Jackknifed classification matrix. Although, the one-plate methodology was capable to keep the level of identification being faster than the two-plate method. Therefore, the one-plate “nose” was further tested in phosphate buffered saline (PBS, pH 7.4) and a random set of unknown samples was also performed. The identification accuracy of the unknowns was 90% with all misclassification between albumin proteins (BSA and HSA). Human serum sensing was also performed. Since this study is far demanding than the same one in PB or PBS. In this sense, it was spiked sufficient amount of proteins in order to obtain a variation of as low as 40 nM in the well. The one-plate methodology was not able to correctly identify the most of the proteins, but the accuracy for acid phosphatase (PhosA) 100% for the unknowns. Therefore, the methodology used in this work may work as an excellent prognostic indicator for prostate cancer and Gaucher’s disease.

Keywords: Proteins. Carbon quantum dots. Identification. “Nose”-based methodology

5.1 Introduction

Proteins are some of the important biomacromolecules involved in all biological events. Their localization, expression level and physiological functions (molecular recognition, enzymatic activities, ion transport, signal transduction etc.) are precisely regulated for the whole human body (Yoshii *et al.*, 2014; Kubota and Hamachi, 2015). The presence of abnormal levels of protein is a sign of some diseases (Slamon *et al.*, 1989; Daniels *et al.*, 2004). For example, acid phosphatase (PhosA) is an important serum biomarker for cancer prostate (Madu and Lu, 2010) and Gaucher's disease (Robinson and Glew, 1980). Thus, a fast and convenient detection of this protein imbalance is essential to provide early diagnosis to achieve the patient cure. At present, some examples of methods to detect proteins include high-resolution two-dimensional polyacrylamide gel electrophoresis (2D-PAGE), mass spectroscopy and enzyme-linked immunosorbent assay (ELISA), among others (Gygi *et al.*, 1999; Haab, 2006). Despite the great effort, protein detection remains a big issue in medical diagnosis. The current methods are still time-consuming requiring specific, complicated and expensive instrumentation and expertise. Therefore, a real-time analytical protein sensing is strongly desired.

The development of sensing approaches involving fluorescence has been proved to be a powerful technique to detect trace of analytes (Dai *et al.*, 2014). Easy operation and simple instrumentation are some of the advantages shown for that optical technique. In this regard, strategies such as fluorescence quenching (Wang *et al.*, 2014) and indicator displacement (Tao *et al.*, 2014) have been developed. Among these approaches, it is important to highlight the fluorescence quenching, where the interaction between the fluorescent probe and the analyte occurs directly. This characteristic may become the detection system more sensitive. Many fluorescent probes including green fluorescent protein (GFP) (Bajaj, Rana, *et al.*, 2010), fluorescent polymers (Woodka *et al.*, 2010), quantum dots (QDs) (Lou *et al.*, 2014) and CQDs (Yu *et al.*, 2013) have been used for chemical sensing. However, CQDs have gained much attention in the past decade due to their excellent properties, such as high quantum yield, biocompatibility, ecofriendly, resistance to photobleaching, and good stability (Sun *et al.*, 2013; Ding *et al.*, 2014).

In these last years, the researcher's effort has highly focused on the analytical applications of CQDs involving their fluorescent properties (Dong *et al.*, 2012). For example, the detection of metals was exhaustively investigated (Tan *et al.*, 2014; Cui *et al.*, 2015; Guo

et al., 2015) and other analytes such as melamine (Dai *et al.*, 2014), glucose (Shi *et al.*, 2011), trinitrotoluene (TNT) (Zhang *et al.*, 2015) and protein (Wang *et al.*, 2013) were also detected using fluorescent properties of CQDs. However, just a few papers aiming protein detection using CQDs can be found in the literature up to now. Therefore, this current study reports the synthesis and application of NH₂-rich CQDs as an excellent protein responsive probe. In this sense, we evaluated eight different proteins (four metallic and four non-metallic) against the fluorescence intensity from CQDs.BPEI. We also developed a chemical “nose” approach to identify proteins combining CQDs, Cu²⁺ and Ethylenediaminetetraacetic Acid (EDTA). Using these components, our “nose”-based strategy was able to generate characteristic fluorescence patterns with high accuracy in PBS. In order to identify the proteins, LDA was used to successfully ascribe the fluorescence patterns. Furthermore, human serum sensing was also performed and PhosA was correctly identified even spiking a variation of 40 nM in the well. This may place our methodology as a powerful prognostic indicator for prostate cancer and Guacher’s disease.

5.2 Materials and Methods

5.2.1 Materials

The chemicals used in this study were citric acid anhydrous (C₆H₈O₇, 99.5%, Aldrich), polyethylenimine, ethylenediamine branched (BPEI) (H(NHCH₂CH₂)_nNH₂, Average Mw of 800 g/mol, Aldrich), sodium phosphate monobasic (NaH₂PO₄·H₂O), sodium phosphate dibasic (Na₂HPO₄), potassium chloride (KCl, 99.0-100.5%, Mallinckrodt), calcium chloride anhydrous (CaCl₂, 96.0%, Fisher), cadmium nitrate (Cd(NO₃)₂ · 4H₂O, 99.0%, Fluka), cobalt (II) chloride (CoCl₂ · 6H₂O), copper acetate (Cu(OOCCH₃)₂ · H₂O, 98.0+%, Alfa Aesar), iron (II) chloride (FeCl₂ · xH₂O, 99.0%, Alfa Aesar), manganese chloride (MnCl₂ · 4H₂O), zinc chloride (ZnCl₂, Fisher), iron (III) nitrate (Fe(NO₃)₃ · 9H₂O, 99.9%, Acros Organics), Ethylenediaminetetraacetic Acid (EDTA, C₁₀H₁₆N₂O₈) and phosphate buffered saline (PBS, pH 7.4, Invitrogen). The analyte proteins, bovine serum albumin (BSA), human serum albumin (HSA), acid phosphatase (PhosA, from potato) and alkaline phosphatase (PhosB, from bovine intestinal mucosa), Hemoglobin (Hem, from human), Myoglobin (Myo, from equine heart), α-Amylase (α-Am, from *Bacillus licheniformis*) and cytochrome c (Cyt.c, from equine heart), were all

purchased from Sigma-Aldrich and used as received. The dialysis membrane tubing cut-off in the range 0.5 – 1.0 kDa was supplied by Spectrum Laboratories.

5.2.2 Sensing Experiments

Initially, a stock solution of CQDs.BPEI was prepared in phosphate buffer (5 mM, pH 7.4). The absorbance of this solution at 350 nm was measured and the concentration of CQDs was precisely regulated for $2 \mu\text{g}\cdot\text{mL}^{-1}$ using the calibration curve. Afterwards, stock solutions of KCl, CaCl₂, Cd(NO₃)₂ · 4H₂O, CoCl₂ · 6H₂O, (Cu(OOCCH₃)₂ · H₂O, FeCl₂ · xH₂O, MnCl₂ · 4H₂O, ZnCl₂ and Fe(NO₃)₃ were prepared in milli-Q water. For the initial detection experiments, 200 μL of the CQDs.BPEI solution ($2\mu\text{g}\cdot\text{mL}^{-1}$) was loaded into a well on a 96-well plate (300 mL Whatman black bottom microplate). The fluorescence intensity value at 445 nm was measured with excitation at 350 nm. The obtained value was considered the initial intensity (I_0). Subsequently, 10 μL of metallic precursor solution with adequate concentration was added in order to obtain 250 μM in the well. After 1 min, the fluorescence intensity was recorded again (I). The value found for I/I_0 ratio was the investigated response. The procedure was the same and the process was repeated three times for each metallic precursor. Then, the metal ion that displays the best quenching efficiency was chosen to compose the strategy. A titration study with this metal was also required aiming to improve the ration between CQDs.BPEI and the chosen metal cation. For this purpose, the metal ion concentration in the well was adjusted to obtain values in the range of 0.05 – 10 μM . The same procedure described above was applied to get the fluorescence response as a function of the metal ion concentrations. EDTA stock solution was also prepared. In this case, the desired concentration in the well for this chemical was 1 mM.

After setting up all the conditions, two “nose”-based strategies were developed involving one or two 96-well plate. The two-plates methodology was initially performed in PB 5 mM (pH 7.4). Thus, 200 μL of solution CQDs.BPEI $2 \mu\text{g}\cdot\text{mL}^{-1}$ were loaded into a well on the first 96-well plate and the fluorescence intensity was recorded (I_0) at 445 nm using 350 nm as excitation. Subsequently, 10 μL of the analyte protein solution was added (40 nM in the well) and the fluorescence intensity was acquired again (I^1) after 1 min. The ratio (I^1/I_0) was the investigated response. Unlike the first plate, at the second 96-well

plate containing CQDs.BPEI $2 \mu\text{g.mL}^{-1}$, $10 \mu\text{L}$ of the metal ion solution was added (appropriate concentration based on fluorescence titration) and the fluorescence intensity was acquired again (I^1) after 1 min. Subsequently, $10 \mu\text{L}$ of the analyte protein solution was added (40 nM in the well) and the fluorescence intensity was obtained (I^2). In this case, the ratio I^2/I^1 was the evaluated response. Next, $10 \mu\text{L}$ of EDTA solution with adequate concentration was added in order to obtain 1 mM in the well. The fluorescence intensity was acquired again (I^3) and the ratio I^3/I^2 was interpreted as the last investigated response.

The one-plate methodology was first tested in PB 5 mM (pH 7.4). In this regard, $200 \mu\text{L}$ of CQDs.BPEI solution $2 \mu\text{g.mL}^{-1}$ was once more placed into a well on a 96-well plate. Using excitation at 350 nm , the fluorescence intensity at 445 nm was recorded (I_0). Subsequently, $10 \mu\text{L}$ of the analyte protein solution was added (40 nM in the well) and the fluorescence intensity was acquired again (I^1) after 1 min. The ratio (I^1/I_0) was the first response. Next, $10 \mu\text{L}$ of the solution containing the metal ion chosen was added and the fluorescence intensity was obtained (I^2). Therefore, a ratio (I^2/I^1) was considered the second response. Finally, $10 \mu\text{L}$ of EDTA solution was added into the well (final concentration 1 mM). The fluorescence intensity was recorded again (I^3) and the ratio (I^3/I^2) was interpreted as the third response. This process was repeated six times for all analyte proteins, which generates a 3 binding events x 8 proteins x 6 replicates training data matrix. The full raw data set was then processed using LDA in SYSTAT (version 11.0). A set of random unknown samples (41 samples) were identified using similar procedures. The methodology describes was also tested in PBS (pH 7.4) to further evaluate the “nose”-based strategy developed in high saline environmental.

The human serum sensing was also performed. In this study, fluorescence titrations involving CQDs.BPEI, the metal ion chosen and/or human serum were initially required in order to improve the sensing conditions. The procedure applied was the same used before. The “nose”-based strategy was employed in different concentrations of human serum stock solutions (0.1 , 0.5 and $1\%(V/V)$). We spiked sufficient amount of analyte proteins into these solutions to obtain a variation of 40 nM in the well. Then, the

fluorescence responses were acquired and processed using the same procedure described before for the “nose”-based approach. A random unknown set (48 samples) was also identified using LDA analysis.

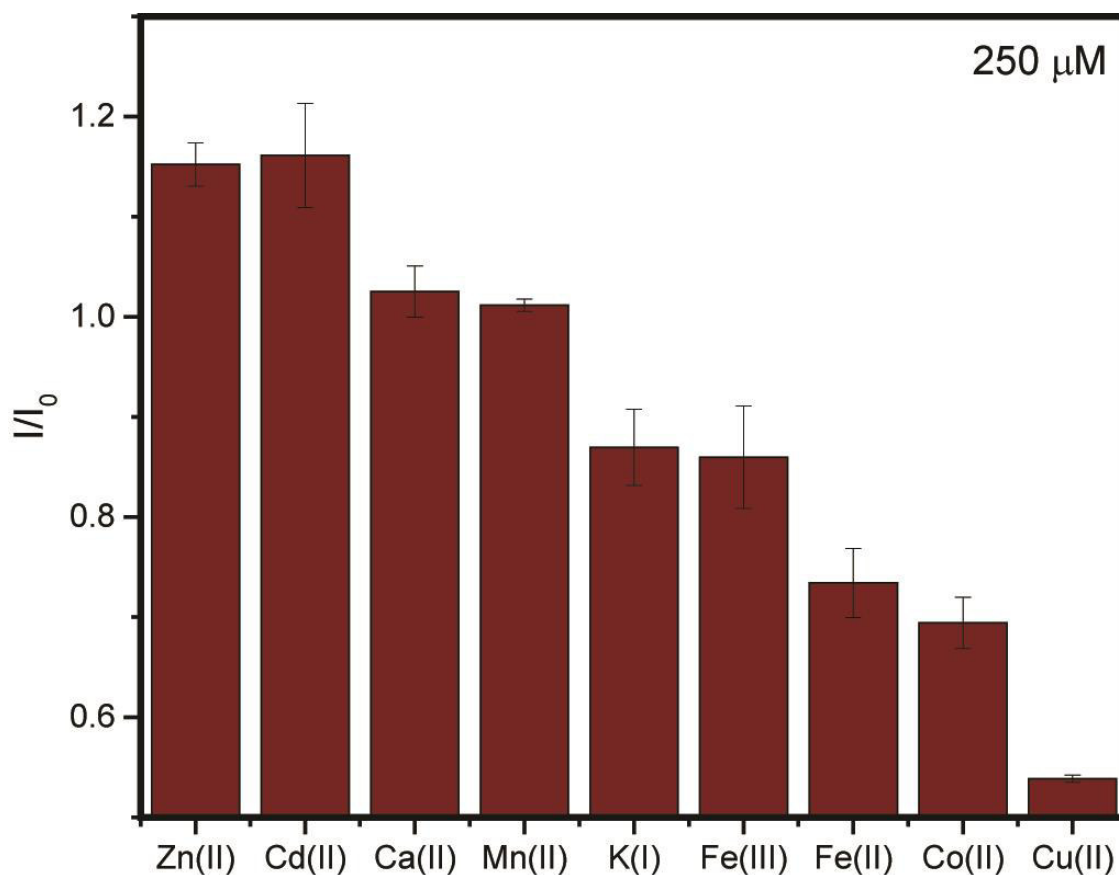
5.3 Results and discussion

5.3.1 Chemical nose/tongue approach

Based on the previous results, the CQDs.BPEI were found to be a powerful protein-responsive platform. Although, beyond detection, a probe should also identify the analyte (Miranda *et al.*, 2007; You *et al.*, 2007; Bajaj, Miranda, *et al.*, 2010; Rana *et al.*, 2015; Yuan *et al.*, 2015; Peveler *et al.*, 2016). In this sense, a strategy based on chemical nose/tongue approach (Röck *et al.*, 2008; Le *et al.*, 2013) can be used to perform the identification of proteins. This is further supported by taking a look at the results obtained in the chapter 4. Each protein evaluated had a unique response, which may indicate a possibility of direct transduction. However, it is well-known a “nose”-based methodology should provide multiple binding events to build a recognition pattern for each analyte using chemometric tools (Wright and Anslyn, 2006). Moreover, it is important to mention the receptors does not need to have specificity. Further, different interactions between receptor and analyte plays a key role for discrimination. Therefore, in this study, our “nose”-sensor was developed to attempt the maximum differentiation by using materials as cheap as CQDs, metallic cations and EDTA.

Naturally, the first receptor was the CQDs.BPEI itself. In order to obtain multivalent interactions, other two steps were added to the procedure. However, before expose the additional steps, it is important to highlight carbon nanoparticles as an excellent fluorescent probe for metal ions (Guo *et al.*, 2015). Aligned to this, proteins can also interact with metallic cations as reported for many researchers (Berg, 1986; Berg, 1990; Jackson *et al.*, 2001). Furthermore, the protein matrix affects the metal-binding site interaction in different ways (Dudev and Lim, 2014). This place the metal ions as an excellent candidate to compose a “nose”-based strategy. Since a unique interaction should be expected between proteins and metallic cations. Therefore, the fluorescence intensity of CQDs.BPEI was evaluated against 250 μM of various metal ions (K^+ , Ca^{2+} , Cd^{2+} , Co^{2+} , Cu^{2+} , Fe^{2+} , Mn^{2+} , Zn^{2+} and Fe^{3+}). The results are displayed in the Fig. 5.1.

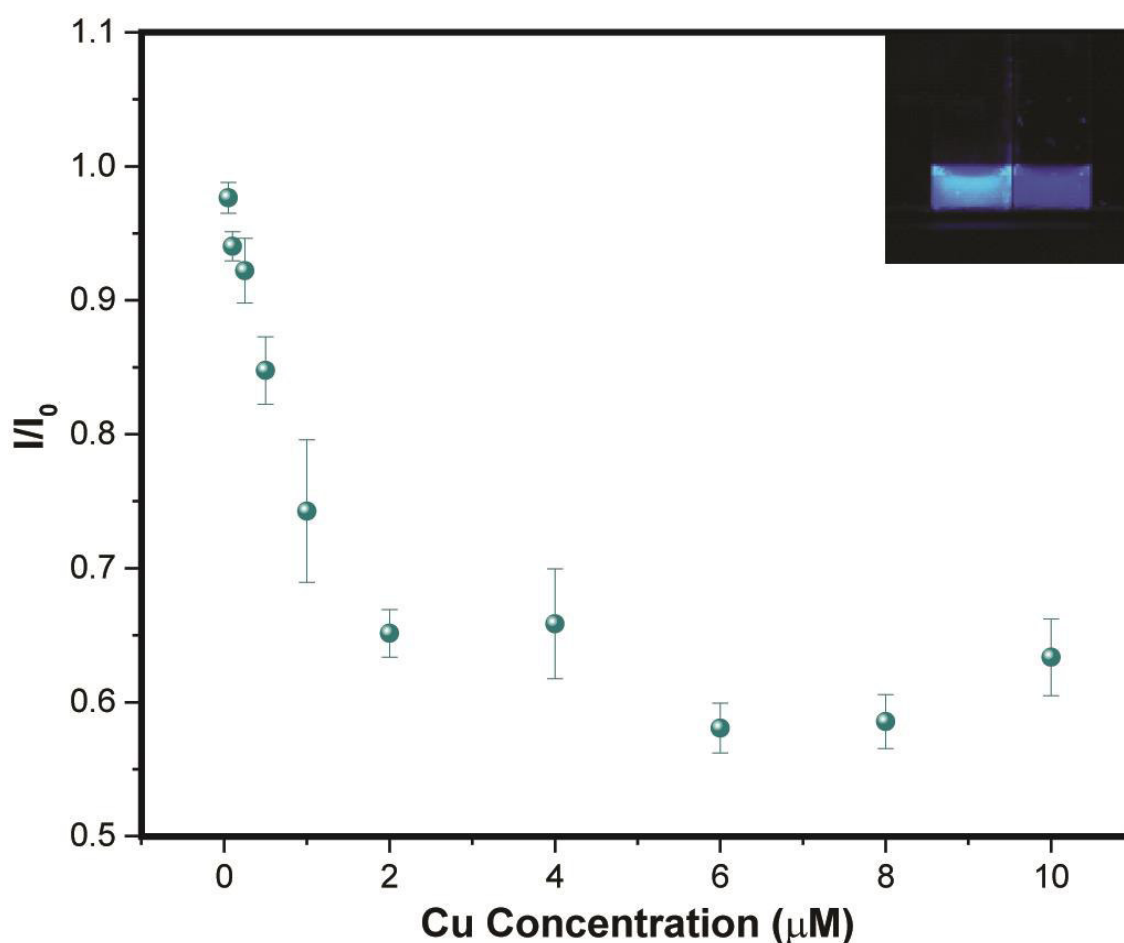
Figure 5.1. Normalized fluorescence intensity of the CQDs.BPEI ($2 \mu\text{g}\cdot\text{mL}^{-1}$) against $250 \mu\text{M}$ of several metal ions in PB 5 mM (pH 7.4).



Source: Author

Clearly, the best quenching efficiency was obtained by using Cu^{2+} . Once CQDs.BPEI have a NH_2 -rich surface, it should be expected the complex cupric amine to be formed. In this regard, the high quenching efficiency may be resulted from the inner effect related to the absorptions of the mentioned complex. In the last years, some publications (Dong *et al.*, 2012; Sun *et al.*, 2013) involving NH_2 functionalized CQDs have demonstrated their great potential for copper detection. Thus, Cu^{2+} was the metallic cation chosen to obtain a second differential binding event by interacting with protein and CQDs.BPEI causing a fluorescence displacement. In this sense, the concentration of Cu^{2+} was investigated through fluorescence titration, as is shown in Fig. 5.2.

Figure 5.2. Fluorescence titration performed at 298 K for Cu^{2+} .

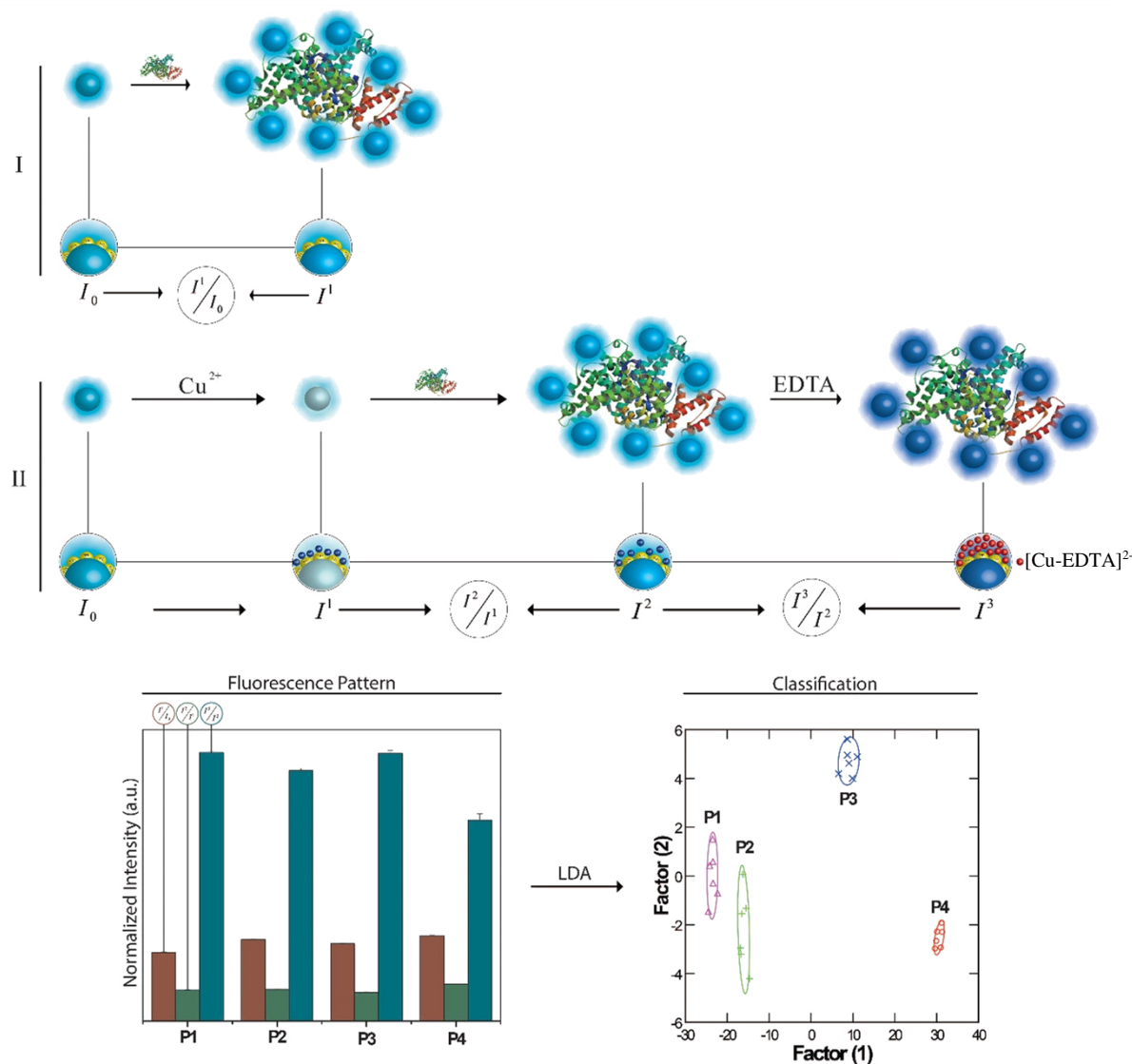


Source: Author

Based on this experiment, 1 μM of Cu^{2+} was the chosen concentration. Since the fluorescence intensity may decrease or increase after interaction with protein or CQDs.BPEI. As a metal ion was used to build a “nose”-based strategy, another multivalent interaction can easily be obtained by using a chelating agent. In this regard, EDTA can provide a selective binding forming a complex. In our case, the formed complex is $[\text{Cu-EDTA}]^{2-}$, a negatively charged specie, which it makes a third discriminant event. Moreover, the literature (Ribou *et al.*, 1999; Ke *et al.*, 2000) report EDTA can also interact with proteins. This may additionally contribute for discrimination between the events.

Once all the multiple binding events were set up, the two-plate methodology was initially tested in PB 5 mM (pH 7.4). Fig. 5.3 shows a schematic picture illustrating the two-plate “nose”-based methodology.

Figure 5.3. Schematic picture illustrating the two-plate “nose”-based strategy developed in this work. I and II denote two different 96-well plates. As it can be seen, the plate I was used to obtain the first discrimination event. The second and third interactional events were obtained in the plate II.



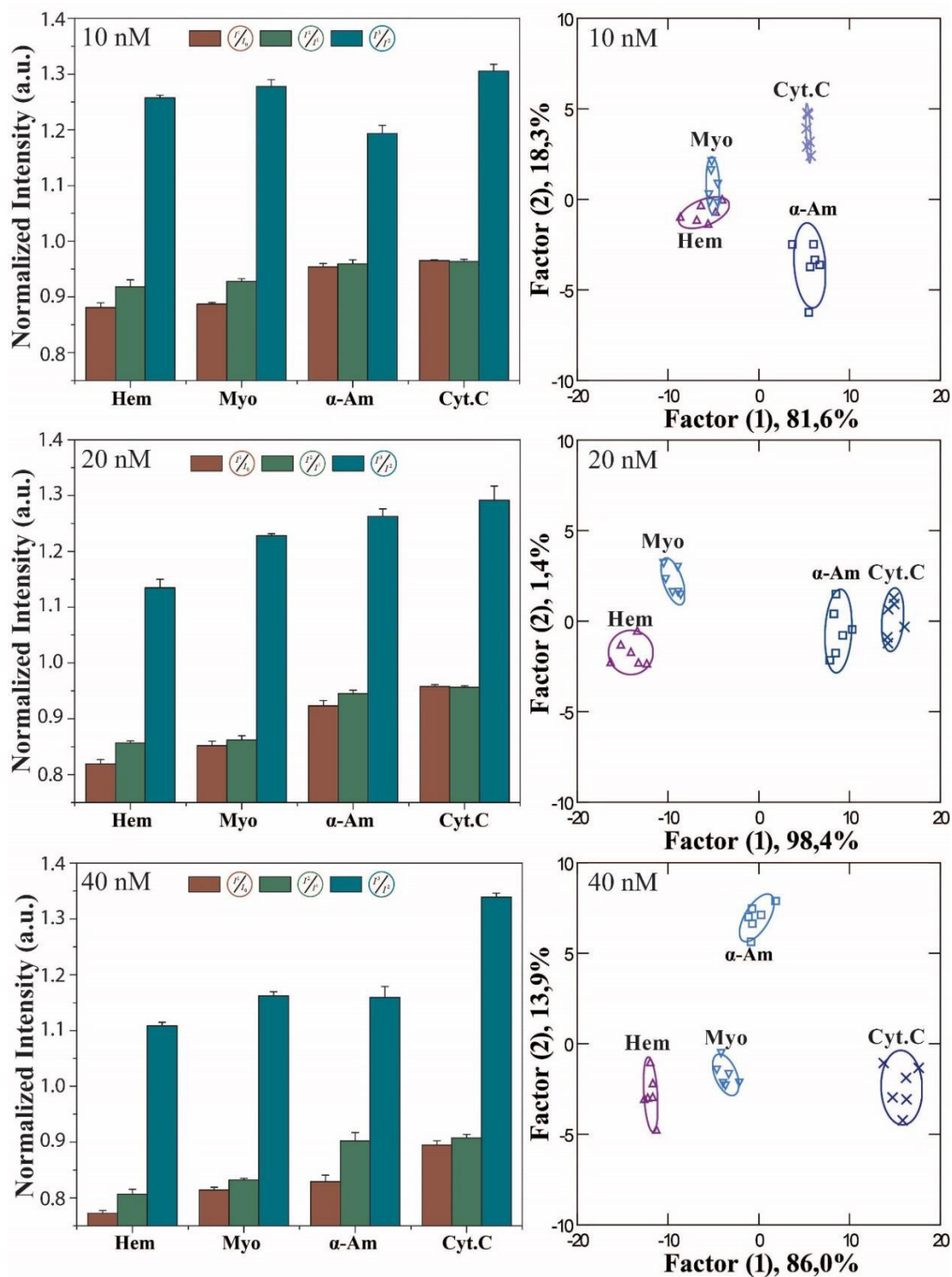
Source: Author

Using this “nose”-based approach, the first discriminant event is based on the straightforward interaction between CQDs.BPEI and proteins. For the second interactional event, $1 \mu\text{M}$ of Cu^{2+} was added to the well in a 96-well plate containing $200 \mu\text{L}$ of CQDs.BPEI $2 \mu\text{g}\cdot\text{mL}^{-1}$. This would change the surface properties of the CQDs.BPEI compared to the naked surface, since the complex cupric amine shows positive charge $+2$, which is different from just NH_2 group. On the other hand, as mentioned before, the third discriminant event was based on the addition of EDTA in order to selectively link

with Cu^{2+} forming a negatively charged complex ($[\text{Cu-EDTA}]^{2-}$). The cited complex on the surface of the CQDs.BPEI should give us totally different interactions. In order to evaluate the discrimination power of the multiple interactional events proposed, the sensing experiments were performed and the Fig. 5.4 displays the fluorescence responses investigated as well as the LDA plot for all metallic proteins at different concentrations (10, 20 and 40 nM). As it can be seen, the fluorescence responses investigated resulted in different patterns for each protein.

Moreover, it is possible to infer the differentiation between the multiple interactional events increasing as a function of the protein concentrations. Clearly, this can be observed in the fluorescence patterns of Hem and α -Am. Fig. 5.4 also shows the LDA plots at 10, 20 and 40 nM supporting the discrimination power of the two-plate “nose”-based methodology, since the clusters were found to be separated from each other. However, overlap between the clusters from Hem and Myo at 10 nM was observed. This indicates a concentration as low as 10 nM was not enough to provide good differentiation for these proteins. However, it is important to mention the similarity between Hem and Myo, where these two proteins show heme groups in their structures. Therefore, 20 nM should be the smallest concentration to be used in order to obtain an enough separation to perform the identification of Hem and Myo. For other proteins evaluated (α -Am and Cyt.C), 10 nM seems to be a concentration more than enough to perform the identification. Since the clusters were well separated. Furthermore, position of the clusters coming from the metallic proteins was also interesting. Clearly, proteins with heme groups (Hem and Myo) were additionally identified even using 10 nM. This evidences the great potential of the two-plate “nose”-based strategy developed in this work.

Figure 5.4. Detection of metallic proteins in PB 5 mM (pH 7.4). (left) Fluorescence response pattern of the proteins evaluated. Each value of average as well as standard deviation was calculated based on 6 replicates. (right) Canonical score plot for the fluorescence patterns as obtained from LDA clustering process.

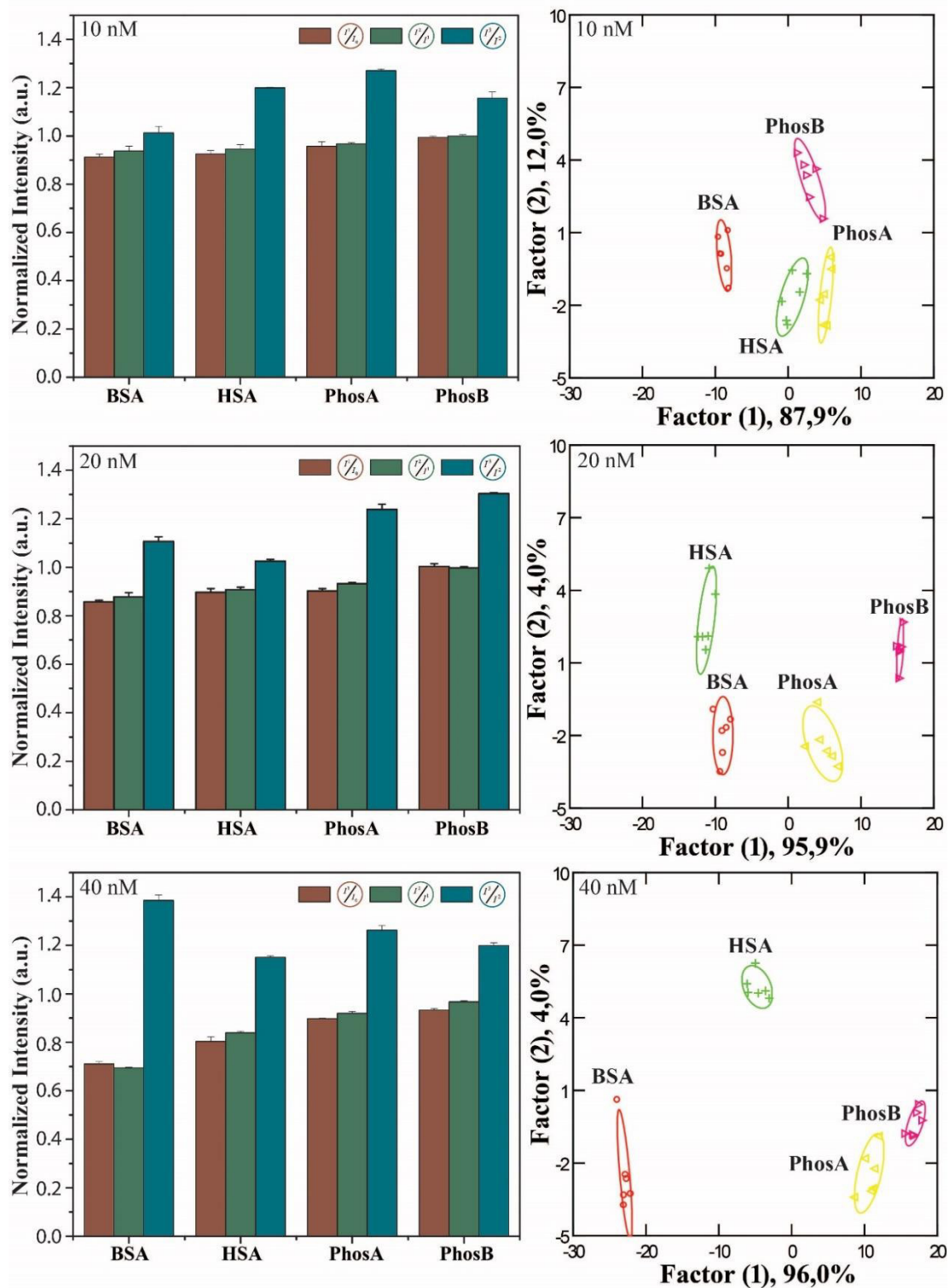


Source: Author

The same identification process was performed for non-metallic proteins. The fluorescence response pattern as well as the LDA plots at 10, 20 and 40 nM are displayed in the Fig. 5.5. One more time, the multiple interactional events provided unique fluorescence patterns for all concentration tested. By increasing this parameter, it was possible to observe bigger differentiation between the discriminant events, which allows the identification process. The clusters from BSA, HSA, PhosA and PhosB were found to be separated even performing the classification process at 10 nM. Increasing the concentration, the clusters can be seen even more distant from each other, indicating a better differentiation between the non-metallic proteins. Once 10 nM was a concentration low enough to provide good separation between the clusters, these results of LDA plots for 20 and 40 nM should be expected. The bigger amount of proteins in the environmental allows the improve the magnitude of the interactions involving proteins and CQDs.BPEI. In order to understand this, it is important to remember the collisional process as the quenching mechanism was demonstrated in the chapter 4. Therefore, this kind mechanism is assumed no matter the discriminant event studied. In this sense, if the amount of the biomacromolecules are bigger, the probability of the collision happens is also bigger. Therefore, the number of collisions between proteins and CQDs.BPEI is expected to increase as long as the concentration is greater in the environmental. Thus, the discriminant events should provide a better discrimination increasing the protein concentrations.

The position of the clusters observed for each concentration is also interesting. Clearly, the albumin (BSA and HSA) and phosphatase (PhosA and PhosB) proteins can be further identified. Since the clusters from the sub-group of proteins are well separated in the LDA plots. For all concentrations, the clusters from BSA and HSA can be find at the left side of the plot, while PhosA and PhosB clusters are at the right side. Therefore, the two-plate methodology can easily classify the type of the protein using concentrations in the range from 10 to 40 nM. This further supports the excellent potential of the “nose”-based strategy developed in this study. Since similar results were found for metallic proteins.

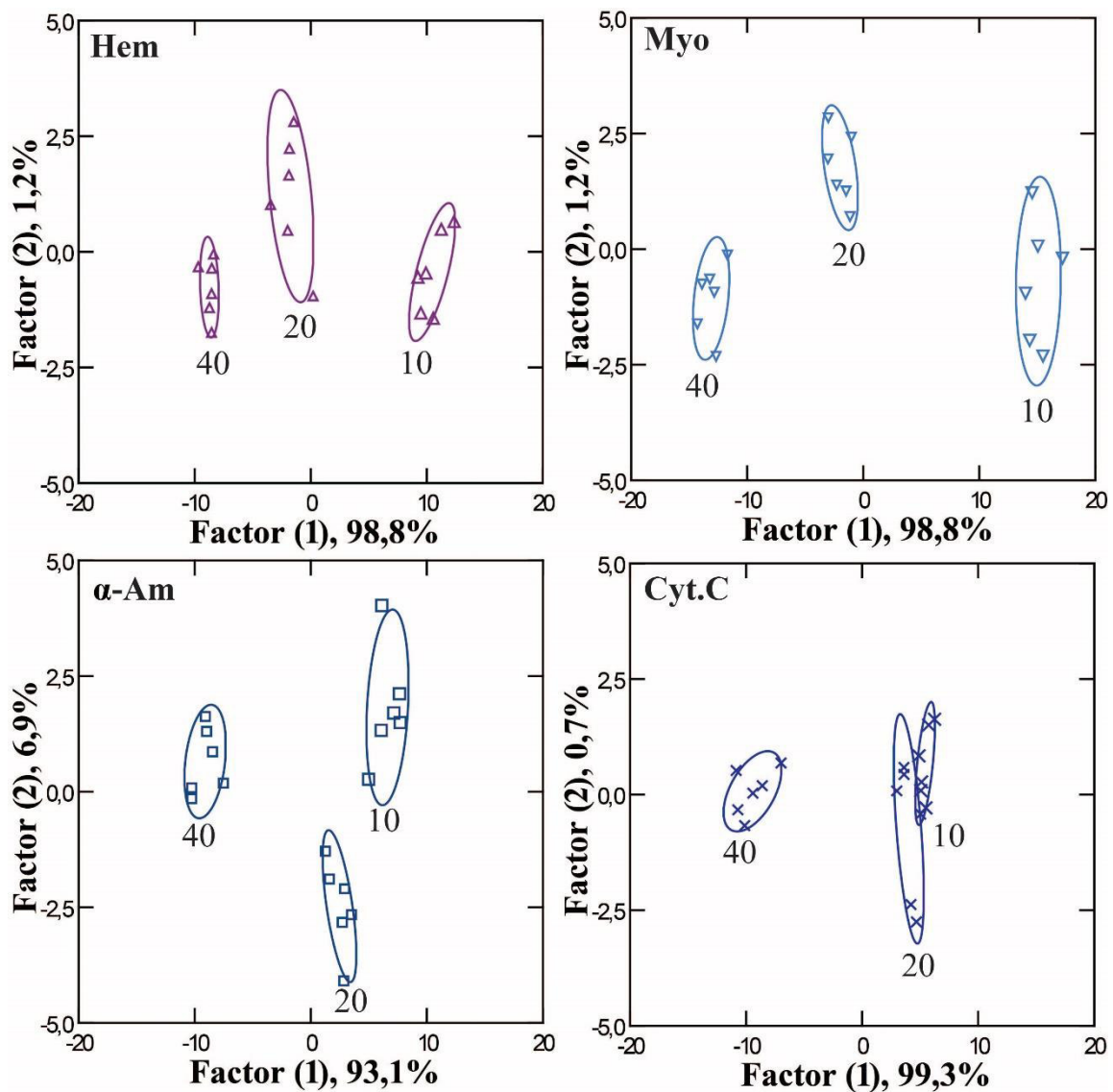
Figure 5.5. Detection of non-metallic proteins in PB 5 mM (pH 7.4). (left) Fluorescence response pattern of the proteins evaluated. Each value of average as well as standard deviation was calculated based on 6 replicates. (right) Canonical score plot for the fluorescence patterns as obtained from LDA clustering process.



Source: Author

Once the classification of the proteins worked out, the clustering process was also carried to classify the different concentration of each protein. Therefore, beyond the identification of the protein, the two-plate methodology was now being evaluated in order to identify the concentrations. In this regard, Fig. 5.6 and 5.7 present the LDA plots for metallic and non-metallic proteins, respectively.

Figure 5.6. LDA plots for metallic proteins using the concentration as a parameter to be classified.

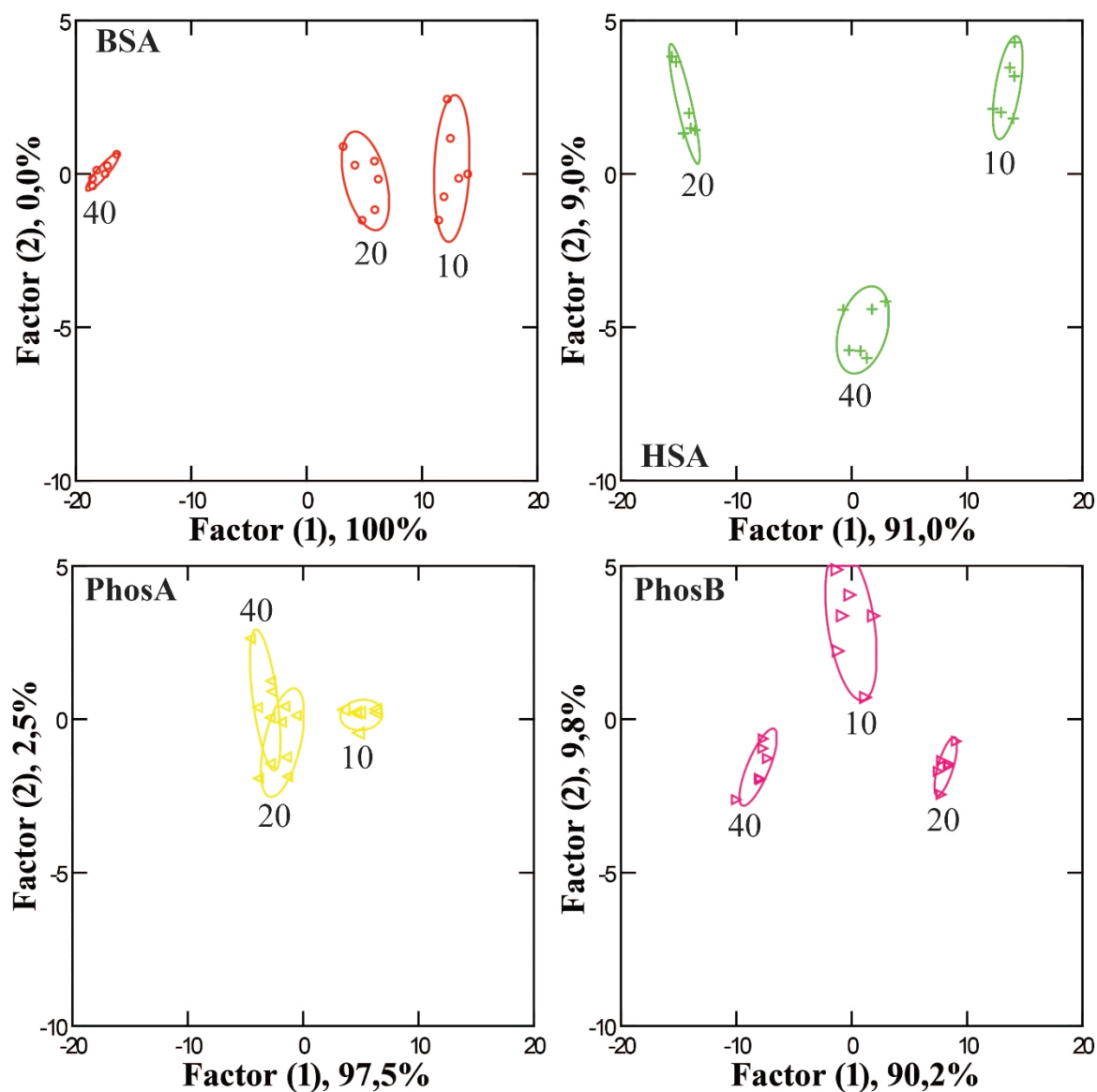


Source: Author

In the Fig. 5.6, the level of the metallic proteins in the well was easily identified. Once again, Hem and Myo had a similar behavior where the clusters for the tested concentrations can be observed almost at the same positions. Although, Myo seems to

have a better identification. Since their clusters can be observed more separated compared to the clusters from Hem. This may indicate metallic proteins containing similar groups should be well identified when the molecular mass is lower (see Table 4.3 in the chapter 4). Therefore, it is plausible to assume the relatively harder identification achieved for Hem might be explained based on steric effects, which it can difficult the interaction. As a consequence, poor classification was achieved for different Hem concentrations. The only protein (Cyt.C) could not be well identified. It was due to the weak interaction demonstrated by using the fluorescence titration experiment.

Figure 5.7. Canonical score plots for non-metallic proteins using the concentration as a parameter to be classified.

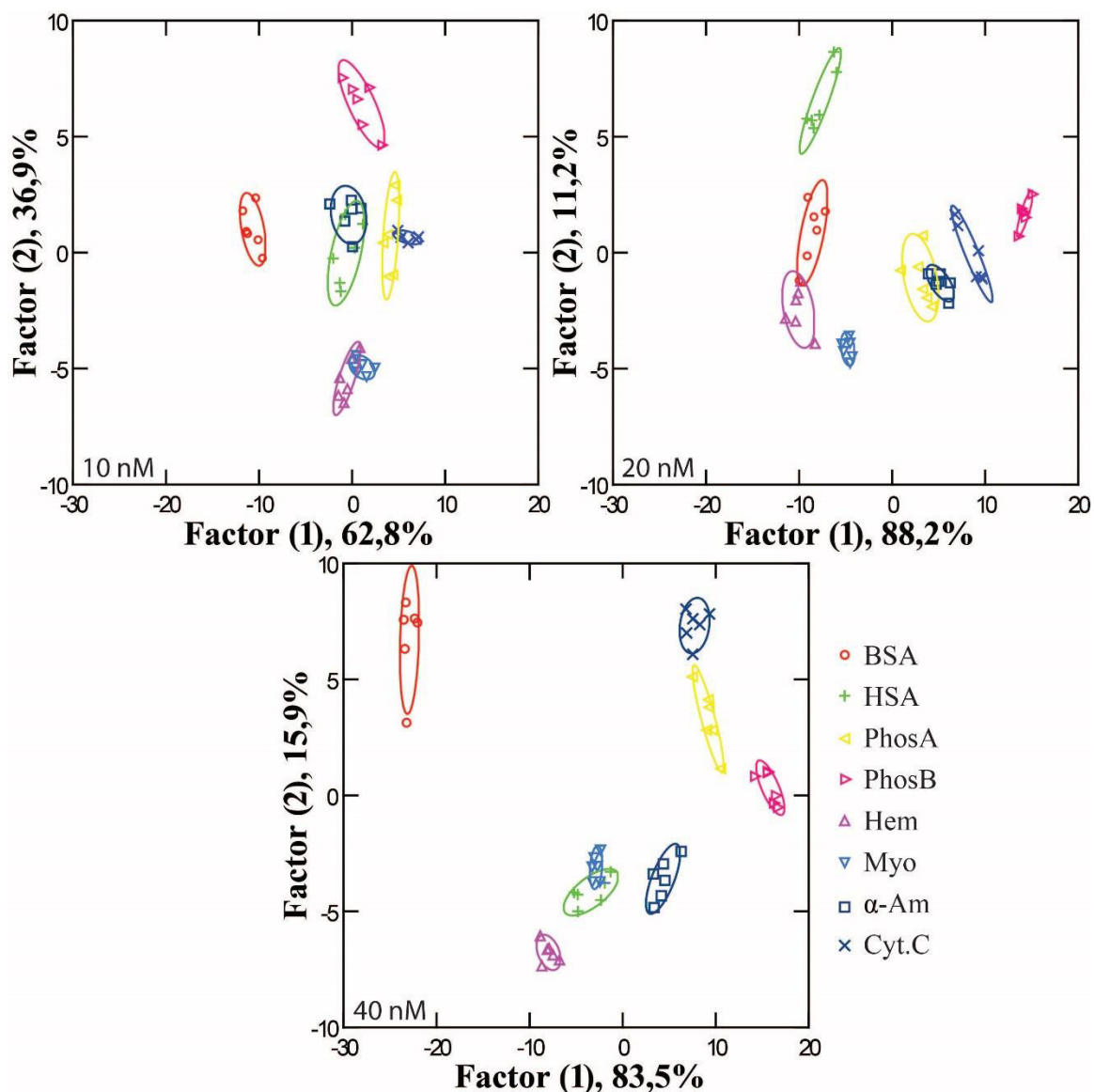


Source: Author

Fig. 5.7 displays the results of the clustering process to classify the concentrations of the non-metallic proteins. It was possible to check clusters well separated from each other for BSA, HSA and PhosB. Surprisingly, PhosA did not present a good separation. Thus, a poor identification of the different concentrations can be observed. This is very strange given the higher value of high quenching constant (K_Q) found in the chapter 4 (see Table 4.1). For instance, at 298 K, K_Q^{298} was found to be equal to $94.0 \cdot 10^4 \text{ M}^{-1}$, while K_Q^{298} for BSA was $49.0 \cdot 10^4 \text{ M}^{-1}$. Therefore, the value for PhosA is almost twice the value found for BSA and the better identification for BSA seems no sense. However, it is interesting to notice that overlap in PhosA profile can be observed to happen between the concentration values of 20 and 40 nM. One more time, this is strange because according to the previous results, higher concentrations should provide a better classification. Once 10 nM was the best identified concentration, the discriminant events at 20 and 40 nM should be saturated, which it makes the classification process more difficult. This explains the observed results.

Taking all results from metallic and non-metallic proteins until now, it is plausible to assume the two-plate methodology should be able to identify the proteins as well as their concentration at the same time. Thus, the results present the excellent potential of the “nose”-based strategy developed. Besides this, a methodology always needs to be evaluated in order to check their whole potential. In this sense, the two-plate method was now tested against the full database, i.e. the eight proteins at 10, 20 and 40 nM. Fig. 5.8 shows the LDA results by carrying the clustering process using all tested proteins. As it can be seen, the clusters were observed to be more separated as long as the increase of the protein concentration. Therefore, the number of overlaps decreases from 10 to 40 nM, which leads for a better identification. This is further supported based on Jackknifed classification matrix (Anzenbacher *et al.*, 2010) for each concentration evaluated. Since the values of accuracy were found to be 83, 94 and 92% for 10, 20 and 40 nM proteins, respectively. Considering the full database (48 samples), the number of misclassification cases for each concentration was approximately 8 (10 nM), 3 (20 nM) and 4 (40 nM). These numbers of cases are not huge, but it may indicate the limit of the potential for the two-plate methodology. Since the increase of the protein concentration did not positively affect the accuracy.

Figure 5.8. Canonical score plots classifying eight proteins at different concentrations (10, 20 and 40 nM).

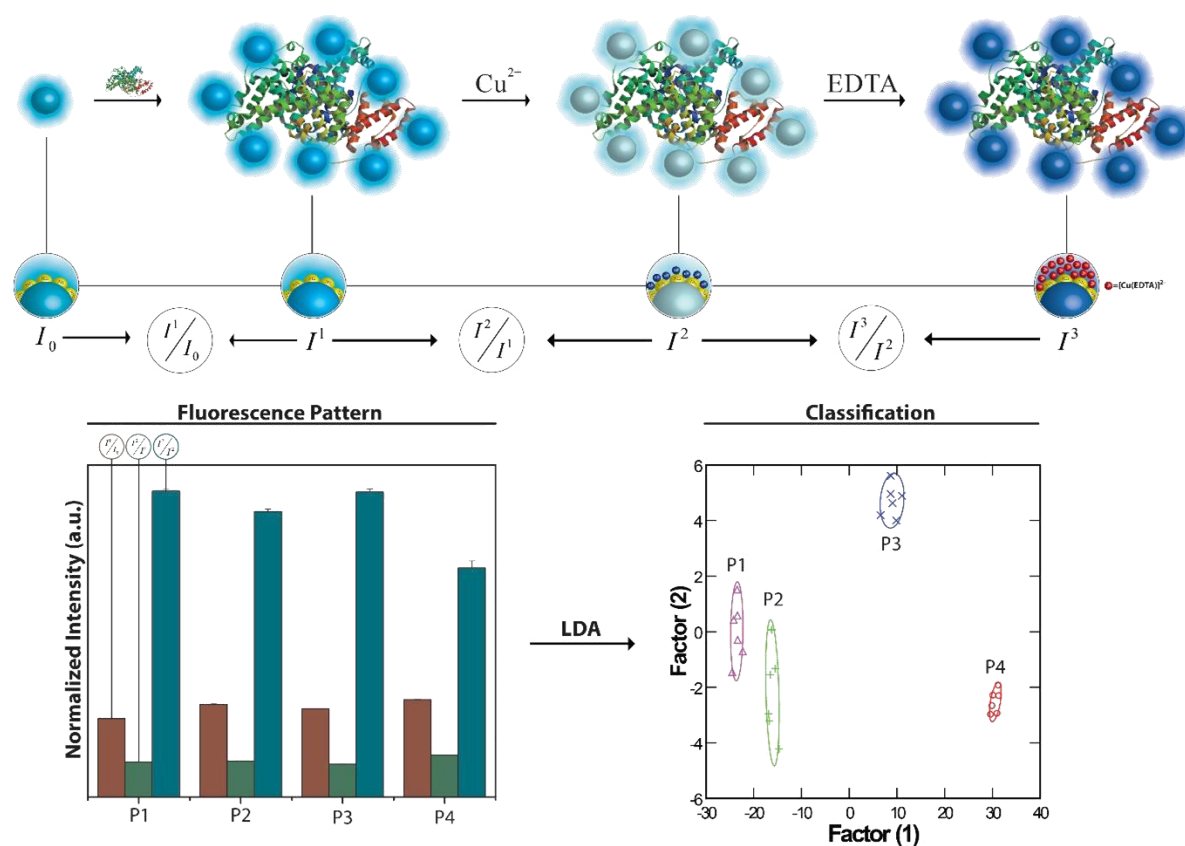


Source: Author

The misclassification observed for the two-plate methodology did not decrease by increasing of the protein concentrations. As mentioned, this evidences about the discrimination events do not have the ability to correctly identify all samples. In this sense, modifications in the methodology needs to be done. The developed method must also be faster. In this sense, the use of two 96-well plate to obtain three discriminant events takes too much time. Moreover, the price is still a parameter to be considered. Therefore, the modifications should become the “nose”-based methodology more robust, faster and cheaper. Regarding all these considerations, it was performed an easy and

simple modification at the second discriminant event. Instead addition of the Cu^{2+} in the well containing only CQDs.BPEI, this metal ion was considered to be putted into the well after the addition of the protein at the first discriminant event. Using this new set, the first, second and third discriminant event can be obtained utilizing only one 96-well plate. This allows a faster “nose”-based methodology and the ability of classification/identification should also change. This may occur due to the addition of the Cu^{2+} onto the system *CQDs.BPEI* – *P* forces a different interactional event. Since the metal ion has the possibility of interact with protein or CQDs.BPEI. In this way, the affinity of each protein with Cu^{2+} can also contribute for the discriminant events, which it might increase the accuracy. Fig. 5.9 presents a schematic illustration that explains the one-plate “nose”-based methodology.

Figure 5.9. Schematic picture illustrating the one-plate “nose”-based strategy developed in this work.

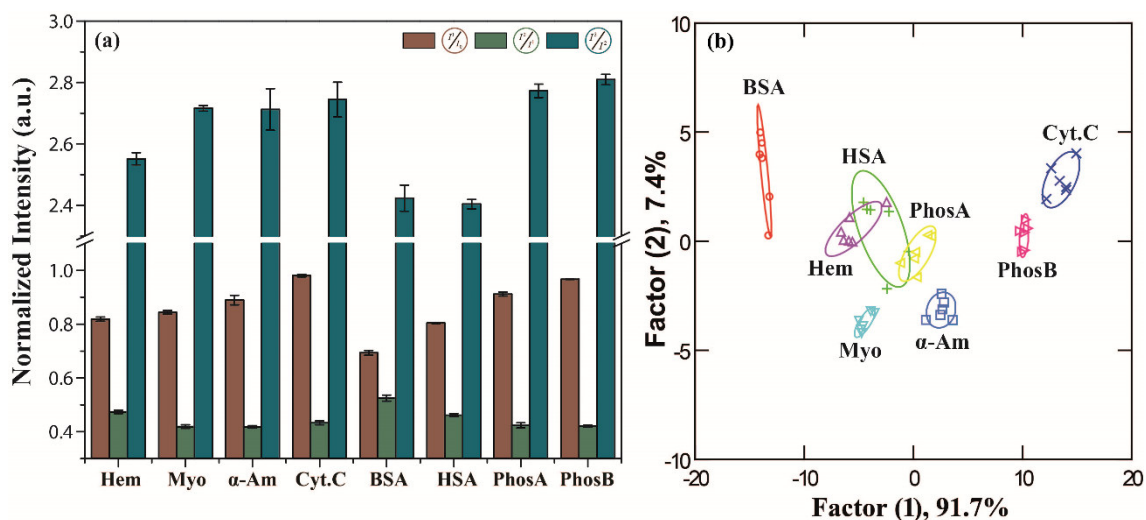


Source: Author

In order to keep the discrimination as hard as possible, all sensing experiments were performed using the eight proteins from now on. Moreover, the concentration of these analytes was also fixed to be 40 nM. The modified one-plate methodology was first tested

in PB 5 mM (pH 7.4). As it can be seen in the Fig. 5.10(a), the fluorescence pattern obtained using the modified methodology seems to have good identification. Each discriminant event resulted in such a different and unique response. However, this can only be checked doing the clustering process through LDA. In this sense, the fluorescence obtained fingerprints using the one-plate methodology were analyzed and Fig. 5.10(b) shows the LDA plot. Clearly, the modified method was able to classify five different proteins at 40 nM. Since the clusters can be observed separated from each other. By contrast, HSA, Hem and PhosA clusters were found to be overlapped. Given this result, it seems the modifications performed at the two-plate methodology did not work out. Although, according to the Jackknifed matrix classification, all misclassification cases occurred between HAS and Hem, which results in 92% accuracy.

Figure 5.10. Detection of eight different proteins in PB 5 mM (pH 7.4). (a) Fluorescence response pattern of the proteins evaluated. Each value of average as well as standard deviation was calculated based on 6 replicates. (b) Canonical score plot for the fluorescence patterns as obtained from LDA utilizing the two most significant factors.



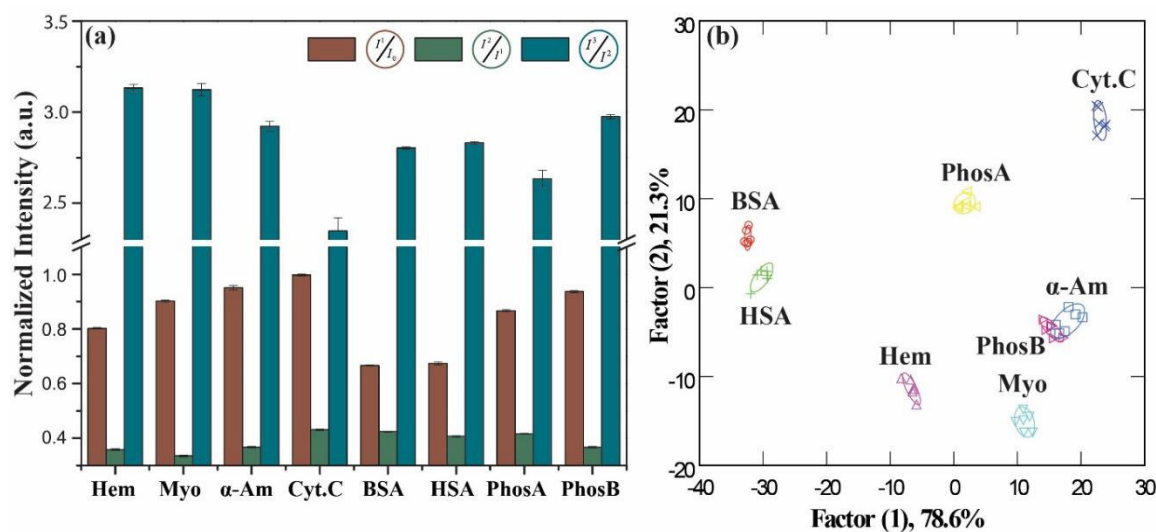
Source: Author

Based on the results presented in the Fig. 5.10 and the accuracy values, the one-plate “nose”-based strategy kept the same level of classification being faster compared to the two-plate methodology. Given this, the ability of the one-plate methodology to identify proteins was further investigated in PBS. Thus, the Fig. 5.11(a) and (b) displays the fluorescence change of the multiples interactional events and canonical score plot obtained by LDA for eight evaluated proteins. The fluorescence pattern presented in the

Fig. 5.11(a) was found to be reproducible and characteristic for each protein. LDA was also employed as a chemometric tool to maximize the differentiation of the fluorescence response (Jurs *et al.*, 2000). By analyzing the full set of data (3 binding events x 8 proteins x 6 replicates), two canonical factors (78.3 and 21.6%) were generated. These two were used to build up the LDA plot as it can be seen in the Fig. 5.11(b). Clearly, the one-plate “nose”-based strategy developed in this work can successfully discriminate six analyte proteins. Since the clustering process resulted into six nonoverlapping groups (95% level confidence). These results evidence the ability of our sensor toward protein differentiation. This also evidences the high saline environmental did not negatively affects the discrimination power. Actually, the clusters were found to be less scattered, which shows a better classification.

Until now, the results about accuracy were all based on the Jackknifed classification matrix, but, in order to further validate the identification efficiency, a random set of unknowns containing seven different proteins chosen from training set was analyzed. It is important to mention the number of unknowns was one more than the perfect classification because the methodology needs to be tested using a situation a little complex. It was observed 90% (37 out of 42) accuracy for randomized set. All misclassified unknowns were between albumin proteins (BSA and HSA). Besides the lower level of accuracy compared to the number obtained using Jackknifed metric classification, 90% can be considered as an improvement. This is supported based on the fact of all misclassification cases were observed to be between BSA and HSA. These proteins are very similar and it should be expected great difficult to correctly perform the identification in high saline environmental.

Figure 5.11. Detection of eight different proteins in PBS. (a) Fluorescence response pattern of the proteins evaluated. Each value of average as well as standard deviation was calculated based on 6 replicates. (b) Canonical score plot for the fluorescence patterns as obtained from LDA utilizing the two most significant factors.

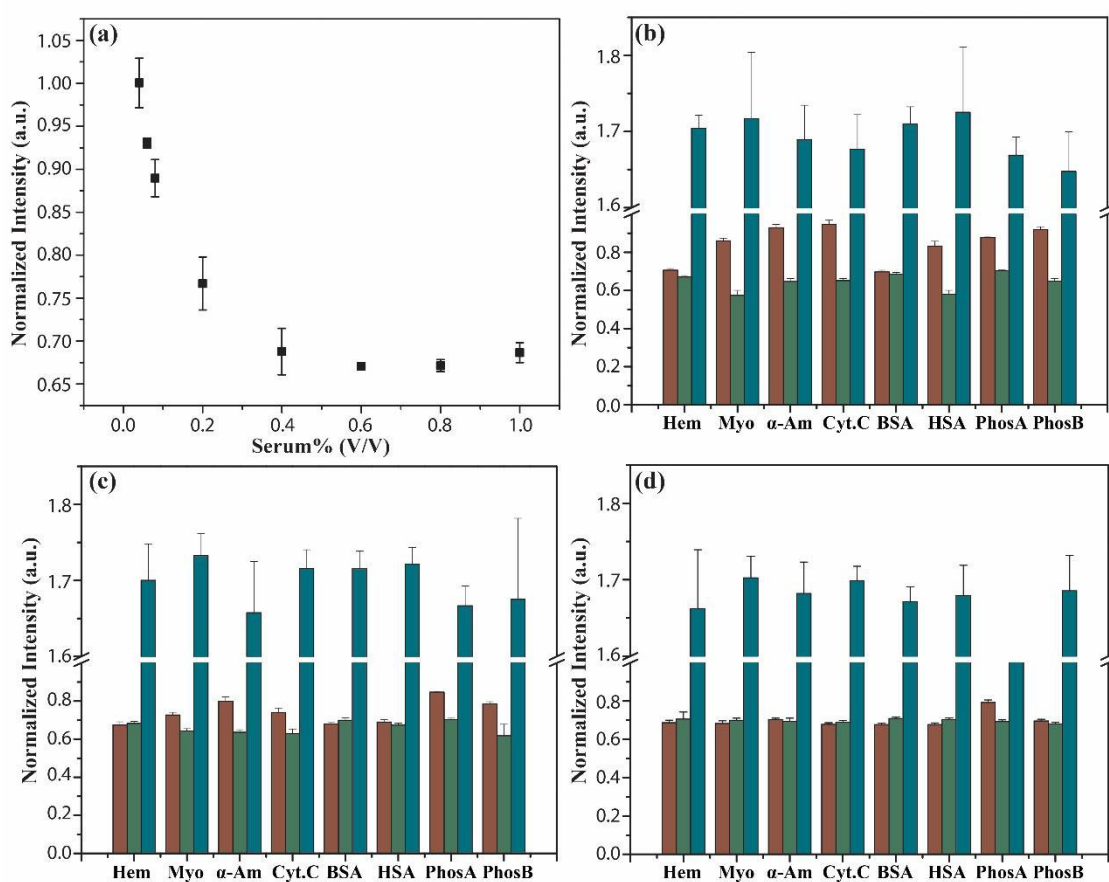


Source: Author

After successful detection and identification of proteins in PBS, the next step of this study was the protein sensing in human serum. Taking into account the complexity of this mixture (~1 mM of protein content), a sensing design in order to detect proteins in human serum is a far more difficult than in PBS. Therefore, human serum sensing would give us an idea about the real potential of our “nose”-based strategy. In this regard, it was initially performed the fluorescence titration with human serum in order to know in which concentration it should be possible to identify the spiked proteins. As it can be seen in the Fig. 5.12(a), the titration data evidences a complete saturation of the CQDs.BPEI fluorescence quenching after 0.4% (V/V) of human serum. This may indicate it should not be possible to successfully perform the identification for concentrations above 0.4% (V/V). In order to investigate this, sensing experiments using 0.1, 0.5 and 1% (V/V) of human serum concentrations were performed (Fig. 5.12(b), (c) and (d), respectively). Notably, the fluorescence pattern from each protein changed towards lack of identity, which did not allow the differentiation. Therefore, the capacity of protein discrimination of the “nose”-based methodology used in this work decrease as long as the concentration of human serum increases. The results found can be easily explained based on complexity of human serum content (more than 20,000 different proteins) (Adkins *et al.*, 2002). Once human serum is added, the interaction between CQDs.BPEI and protein analyte was

drastically modified due to competitive binding. This cause the lack of fluorescence characteristic pattern observed for low human serum concentrations. Interestingly, our sensor was able to identify PhosA even with CQDs.BPEI fluorescence quenching completely saturated (1% (V/V) of human serum).

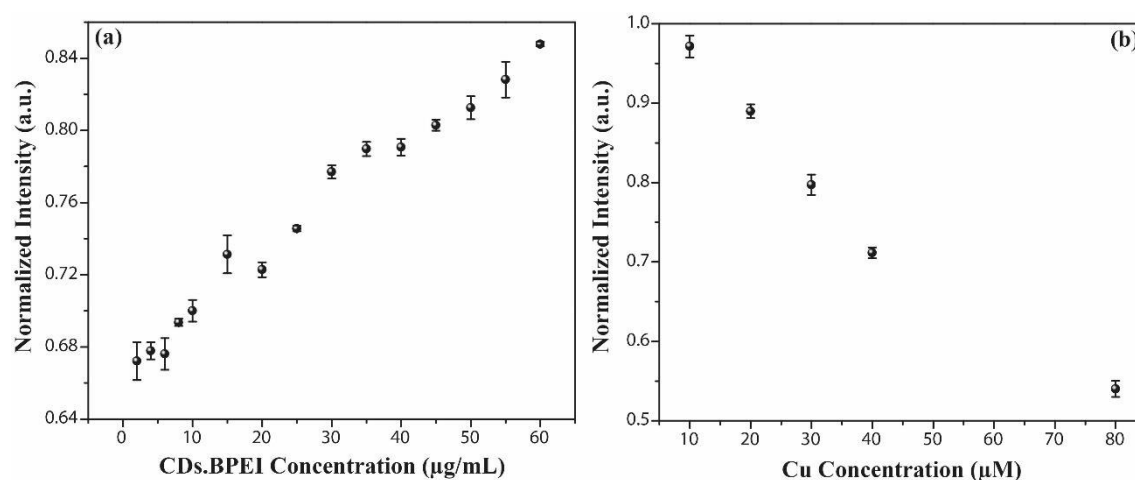
Figure 5.12. (a) Fluorescence titration performed at 298 K using different human serum concentrations. Fluorescence response pattern obtained spiking the proteins tested in 0.1 (b), 0.5 (c) and 1% (V/V) (d) human serum concentrations. Each value of average as well as standard deviation was calculated based on 6 replicates.



Source: Author

Using the conditions displayed for serum sensing, a lack of discrimination was gradually observed. Therefore, we try to optimize the conditions of our methodology in order to obtain a better discrimination in 1% (V/V) of human serum. In this sense, we first adjust the concentration of CQDs.BPEI to provide sufficient response to check the fluorescence changes. Since the amount of CQDs.BPEI needed to be modified, a new fluorescence titration with Cu^{2+} was also required. Both experiments are showed in the Fig. 5.13.

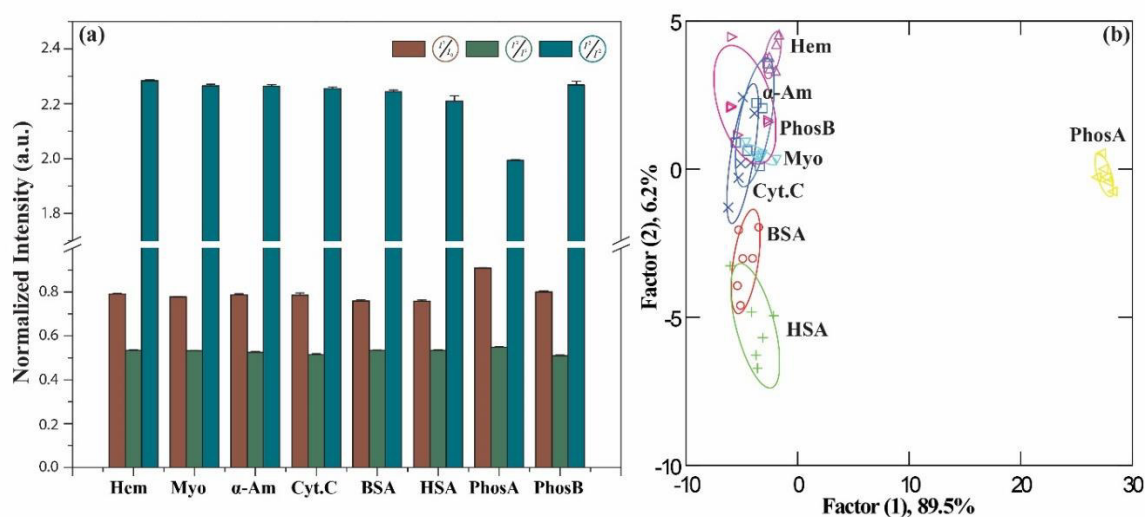
Figure 5.13. Optimization of the conditions for the one-plate methodology in 1% (V/V) human serum. (a) Improvement of the amount of CQDs.BPEI and (b) Cu^{2+} fluorescence titration performed at 298 K.



Source: Author

The new chosen CQDs.BPEI concentration was 40 µg/mL. Again, this amount would give us free CQDs to obtain enough fluorescence response. For Cu^{2+} concentration, the titration data displays no saturation even using 80 µM. Moreover, we hypothesize a better way to get more differentiation between the proteins should be at high concentration of metal ions. Using the cited condition, Cu^{2+} would interact with all the proteins instead CQDs. Therefore, the quenching efficiency would give us the discrimination between the analyte proteins. Taken together, the chosen Cu^{2+} concentration was 80 µM. Finally, the EDTA concentration was remained the same. Since it was already used a huge amount of this chelating agent. The fluorescence response obtained from the sensing experiment utilizing the optimized conditions are presented in the Fig. 5.14(a). As it can be seen, a lack of identity for the most of the analyte proteins was still observed. Once again, PhosA was the only protein that displays a characteristic pattern. This is also confirmed by looking at the LDA plot in the Fig. 5.14(b). Since only PhosA was correctly classified. Therefore, the optimization of the conditions shows no effects on the differentiation capacity. This indicates that improvements need to be made in order to obtain a better protein discrimination.

Figure 5.14. Detection of eight different proteins spiked in human serum 1% (V/V) using the optimized conditions. (a) Fluorescence response pattern acquired for the proteins tested. Each value of average as well as standard deviation was calculated based on 6 replicates. (b) Canonical score plot for the fluorescence patterns as obtained from LDA utilizing the two most significant factors.



Source: Author

On the other hand, the ability to detect abnormal levels of PhosA is very interesting. In the human body, PhosA is considered an important serum marker for many diseases including prostate cancer and Gaucher's disease, for example (Bull *et al.*, 2002; Qian *et al.*, 2015). Thus, a fast, cheap and robust sensing strategy to detect this protein is highly desired. In this sense, we tested our “nose”-based methodology against a random unknown set (48 samples) involving all evaluated proteins. All PhosA samples were correctly identified affording 100% accuracy. Therefore, this result proof the detection efficiency of our approach, which might point the sensing methodology used in this work as a powerful prognostic indicator for the diseases mentioned before.

5.4 Conclusion

In conclusion, we were able to develop a fast and potent “nose”-based approach to differentiate the tested proteins. For one or two-plate sensing methodology, the discrimination relies on the selective interaction of Cu^{2+} with proteins and/or CQDs.BPEI as well as EDTA. The strategies used in this work successfully identify the analyte proteins, but the one-plate methodology was found to keep the level of identification

being faster than the two-plate method. To further investigate the ability of the one-plate sensing to identify proteins, it was performed the study in high saline environmental (PBS). It was possible to correctly classify six different proteins according to the Jackknifed matrix classification. However, in order to deepen our investigation, a random unknown set of samples containing 42 samples was carried out and 90% accuracy (37 out of 42) was found. However, it is important to highlight all 10% misclassified was between BSA and HSA. Both are very similar albumin proteins. In the human serum sensing (0.1, 0.5 and 1% (V/V)), our approach was not able to discriminate most of the evaluated proteins. Only PhosA could be correctly identified. To recover the differentiation capacity, we try to optimize the conditions as well as to modify the “nose”-based strategy. However, PhosA was still the unique protein successfully identified. This result was further validate using a randomly set of unknowns, where all PhosA samples were correctly identified affording 100% accuracy. Taken together, these results place our one-plate methodology as an excellent prognostic indicator for prostate cancer and Gaucher’s disease.

References

ADKINS, J. N. et al. Toward a Human Blood Serum Proteome: Analysis By Multidimensional Separation Coupled With Mass Spectrometry. **Molecular & Cellular Proteomics**, v. 1, n. 12, p. 947-955, December 1, 2002 2002. Disponível em: < <http://www.mcponline.org/content/1/12/947.abstract> >.

ANZENBACHER, J. P. et al. A practical approach to optical cross-reactive sensor arrays. **Chemical Society Reviews**, v. 39, n. 10, p. 3954-3979, 2010. ISSN 0306-0012. Disponível em: < <http://dx.doi.org/10.1039/B926220M> >.

BAJAJ, A. et al. Array-Based Sensing of Normal, Cancerous, and Metastatic Cells Using Conjugated Fluorescent Polymers. **Journal of the American Chemical Society**, v. 132, n. 3, p. 1018-1022, 2010/01/27 2010. ISSN 0002-7863. Disponível em: < <http://dx.doi.org/10.1021/ja9061272> >.

BAJAJ, A. et al. Cell surface-based differentiation of cell types and cancer states using a gold nanoparticle-GFP based sensing array. **Chemical Science**, v. 1, n. 1, p. 134-138, 2010. ISSN 2041-6520. Disponível em: < <http://dx.doi.org/10.1039/C0SC00165A> >.

BERG, J. M. Potential metal-binding domains in nucleic acid binding proteins. **Science**, v. 232, n. 4749, p. 485-487, 1986. Disponível em: < <http://science.sciencemag.org/content/232/4749/485.abstract> >.

BERG, J. M. Zinc fingers and other metal-binding domains. Elements for interactions between macromolecules. **Journal of Biological Chemistry**, v. 265, n. 12, p. 6513-6, April 25, 1990 1990. Disponível em: < <http://www.jbc.org/content/265/12/6513.short> >.

BULL, H. et al. Acid phosphatases. **Molecular Pathology**, v. 55, n. 2, p. 65-72, April 1, 2002 2002. Disponível em: < <http://mp.bmj.com/content/55/2/65.abstract> >.

CUI, X. et al. A fluorescent biosensor based on carbon dots-labeled oligodeoxyribonucleotide and graphene oxide for mercury (II) detection. **Biosensors and Bioelectronics**, v. 63, p. 506-512, 2015. ISSN 0956-5663. Disponível em: < <http://www.sciencedirect.com/science/article/pii/S0956566314005880> >.

DAI, H. et al. A carbon dot based biosensor for melamine detection by fluorescence resonance energy transfer. **Sensors and Actuators B: Chemical**, v. 202, p. 201-208, 2014. ISSN 0925-4005. Disponível em: < <http://www.sciencedirect.com/science/article/pii/S0925400514005875> >.

DANIELS, M. J. et al. Abnormal Cytokinesis in Cells Deficient in the Breast Cancer Susceptibility Protein BRCA2. **Science**, v. 306, n. 5697, p. 876-879, 2004. Disponível em: < <http://science.sciencemag.org/content/306/5697/876.abstract> >.

DING, C.; ZHU, A.; TIAN, Y. Functional Surface Engineering of C-Dots for Fluorescent Biosensing and in Vivo Bioimaging. **Accounts of Chemical Research**, v. 47, n. 1, p. 20-30, 2014/01/21 2014. ISSN 0001-4842. Disponível em: < <http://dx.doi.org/10.1021/ar400023s> >.

DONG, Y. et al. Polyamine-Functionalized Carbon Quantum Dots as Fluorescent Probes for Selective and Sensitive Detection of Copper Ions. **Analytical Chemistry**, v. 84, n. 14, p. 6220-6224, 2012/07/17 2012. ISSN 0003-2700. Disponível em: < <http://dx.doi.org/10.1021/ac3012126> >.

DUDEV, T.; LIM, C. Competition among Metal Ions for Protein Binding Sites: Determinants of Metal Ion Selectivity in Proteins. **Chemical Reviews**, v. 114, n. 1, p. 538-556, 2014/01/08 2014. ISSN 0009-2665. Disponível em: < <http://dx.doi.org/10.1021/cr4004665> >.

GUO, Y. et al. Fluorescent carbon nanoparticles for the fluorescent detection of metal ions. **Biosensors and Bioelectronics**, v. 63, p. 61-71, 2015. ISSN 0956-5663. Disponível em: < <http://www.sciencedirect.com/science/article/pii/S0956566314005107> >.

GYGI, S. P. et al. Quantitative analysis of complex protein mixtures using isotope-coded affinity tags. **Nat Biotech**, v. 17, n. 10, p. 994-999, 1999. ISSN 1087-0156. Disponível em: < <http://dx.doi.org/10.1038/13690> >.

HAAB, B. B. Applications of antibody array platforms. **Current Opinion in Biotechnology**, v. 17, n. 4, p. 415-421, 2006. ISSN 0958-1669. Disponível em: < <http://www.sciencedirect.com/science/article/pii/S0958166906000978> >.

JACKSON, G. S. et al. Location and properties of metal-binding sites on the human prion protein. **Proceedings of the National Academy of Sciences**, v. 98, n. 15, p. 8531-8535, July 17, 2001 2001. Disponível em: < <http://www.pnas.org/content/98/15/8531.abstract> >.

JURS, P. C.; BAKKEN, G. A.; MCCLELLAND, H. E. Computational Methods for the Analysis of Chemical Sensor Array Data from Volatile Analytes. **Chemical Reviews**, v. 100, n. 7, p. 2649-2678, 2000/07/01 2000. ISSN 0009-2665. Disponível em: < <http://dx.doi.org/10.1021/cr9800964> >.

KE, J. et al. Quantitative liquid chromatographic–tandem mass spectrometric determination of reserpine in FVB/N mouse plasma using a “chelating” agent (disodium EDTA) for releasing protein-bound analytes during 96-well liquid–liquid extraction. **Journal of Chromatography B: Biomedical Sciences and Applications**, v. 742, n. 2, p. 369-380, 2000. ISSN 0378-4347. Disponível em: < <http://www.sciencedirect.com/science/article/pii/S0378434700001869> >.

KUBOTA, R.; HAMACHI, I. Protein recognition using synthetic small-molecular binders toward optical protein sensing in vitro and in live cells. **Chemical Society Reviews**, v. 44, n. 13, p. 4454-4471, 2015. ISSN 0306-0012. Disponível em: < <http://dx.doi.org/10.1039/C4CS00381K> >.

LE, N. D. B.; RANA, S.; ROTELLO, V. M. Chemical nose sensors: an alternative strategy for cancer diagnosis. **Expert Review of Molecular Diagnostics**, v. 13, n. 2, p. 111-113, 2013/03/01 2013. ISSN 1473-7159. Disponível em: < <http://dx.doi.org/10.1586/erm.12.143> >.

LOU, Y. et al. Metal ions optical sensing by semiconductor quantum dots. **Journal of Materials Chemistry C**, v. 2, n. 4, p. 595-613, 2014. ISSN 2050-7526. Disponível em: < <http://dx.doi.org/10.1039/C3TC31937G> >.

MADU, C. O.; LU, Y. Novel diagnostic biomarkers for prostate cancer. **Journal of Cancer**, v. 1, p. 150-177, 2010.

MIRANDA, O. R. et al. Array-Based Sensing of Proteins Using Conjugated Polymers. **Journal of the American Chemical Society**, v. 129, n. 32, p. 9856-9857, 2007/08/01 2007. ISSN 0002-7863. Disponível em: < <http://dx.doi.org/10.1021/ja0737927> >.

PEVELER, W. J. et al. Multichannel Detection and Differentiation of Explosives with a Quantum Dot Array. **ACS Nano**, v. 10, n. 1, p. 1139-1146, 2016/01/26 2016. ISSN 1936-0851. Disponível em: < <http://dx.doi.org/10.1021/acsnano.5b06433> >.

QIAN, Z. et al. Reversible Fluorescent Nanoswitch Based on Carbon Quantum Dots Nanoassembly for Real-Time Acid Phosphatase Activity Monitoring. **Analytical Chemistry**, v. 87, n. 14, p. 7332-7339, 2015/07/21 2015. ISSN 0003-2700. Disponível em: < <http://dx.doi.org/10.1021/acs.analchem.5b01488> >.

RANA, S. et al. A Multichannel Biosensor for Rapid Determination of Cell Surface Glycomic Signatures. **ACS Central Science**, v. 1, n. 4, p. 191-197, 2015/07/22 2015. ISSN 2374-7943. Disponível em: < <http://dx.doi.org/10.1021/acscentsci.5b00126> >.

RIBOU, A. C. et al. Interaction of a protein, BSA, and a fluorescent probe, Mag-Indo-1, influence of EDTA and calcium on the equilibrium. **Biophysical Chemistry**, v. 81, n. 3, p. 179-189, 1999. ISSN 0301-4622. Disponível em: < <http://www.sciencedirect.com/science/article/pii/S0301462299000897> >.

ROBINSON, D. B.; GLEW, R. H. Acid phosphatase in Gaucher's disease. **Clinical Chemistry**, v. 26, n. 3, p. 371-82, March 1, 1980 1980. Disponível em: < <http://www.clinchem.org/content/26/3/371.abstract> >.

RÖCK, F.; BARSAN, N.; WEIMAR, U. Electronic Nose: Current Status and Future Trends. **Chemical Reviews**, v. 108, n. 2, p. 705-725, 2008/02/01 2008. ISSN 0009-2665. Disponível em: < <http://dx.doi.org/10.1021/cr068121q> >.

SHI, W. et al. Carbon nanodots as peroxidase mimetics and their applications to glucose detection. **Chemical Communications**, v. 47, n. 23, p. 6695-6697, 2011. ISSN 1359-7345. Disponível em: < <http://dx.doi.org/10.1039/C1CC11943E> >.

SLAMON, D. J. et al. Studies of the HER-2/neu proto-oncogene in human breast and ovarian cancer. **Science**, v. 244, n. 4905, p. 707-712, 1989. Disponível em: < <http://science.sciencemag.org/content/244/4905/707.abstract> >.

SUN, H. et al. Highly Photoluminescent Amino-Functionalized Graphene Quantum Dots Used for Sensing Copper Ions. **Chemistry – A European Journal**, v. 19, n. 40, p. 13362-13368, 2013. ISSN 1521-3765. Disponível em: < <http://dx.doi.org/10.1002/chem.201302268> >.

TAN, X. W. et al. Carbon dots production via pyrolysis of sago waste as potential probe for metal ions sensing. **Journal of Analytical and Applied Pyrolysis**, v. 105, p. 157-165, 2014. ISSN 0165-2370. Disponível em: < <http://www.sciencedirect.com/science/article/pii/S0165237013002398> >.

TAO, Y. et al. Array-Based Sensing of Proteins and Bacteria By Using Multiple Luminescent Nanodots as Fluorescent Probes. **Small**, v. 10, n. 18, p. 3667-3671, 2014. ISSN 1613-6829. Disponível em: < <http://dx.doi.org/10.1002/sml.201400661> >.

WANG, F. et al. Graphene quantum dots as a fluorescent sensing platform for highly efficient detection of copper(II) ions. **Sensors and Actuators B: Chemical**, v. 190, p. 516-522, 2014. ISSN 0925-4005. Disponível em: < <http://www.sciencedirect.com/science/article/pii/S0925400513010496> >.

WANG, Y. et al. Using Graphene Quantum Dots as Photoluminescent Probes for Protein Kinase Sensing. **Analytical Chemistry**, v. 85, n. 19, p. 9148-9155, 2013/10/01 2013. ISSN 0003-2700. Disponível em: < <http://dx.doi.org/10.1021/ac401807b> >.

WOODKA, M. D.; SCHNEE, V. P.; POLCHA, M. P. Fluorescent Polymer Sensor Array for Detection and Discrimination of Explosives in Water. **Analytical Chemistry**, v. 82, n. 23, p. 9917-9924, 2010/12/01 2010. ISSN 0003-2700. Disponível em: < <http://dx.doi.org/10.1021/ac102504t> >.

WRIGHT, A. T.; ANSLYN, E. V. Differential receptor arrays and assays for solution-based molecular recognition. **Chemical Society Reviews**, v. 35, n. 1, p. 14-28, 2006. ISSN 0306-0012. Disponível em: < <http://dx.doi.org/10.1039/B505518K> >.

YOSHII, T. et al. Intracellular Protein-Responsive Supramolecules: Protein Sensing and In-Cell Construction of Inhibitor Assay System. **Journal of the American Chemical Society**, v. 136, n. 47, p. 16635-16642, 2014/11/26 2014. ISSN 0002-7863. Disponível em: < <http://dx.doi.org/10.1021/ja508955y> >.

YOU, C.-C. et al. Detection and identification of proteins using nanoparticle-fluorescent polymer /chemical nose/ sensors. **Nat Nano**, v. 2, n. 5, p. 318-323, 2007. ISSN 1748-3387. Disponível em: < <http://dx.doi.org/10.1038/nnano.2007.99> >.

YU, C. et al. Carbon-dot-based ratiometric fluorescent sensor for detecting hydrogen sulfide in aqueous media and inside live cells. **Chemical Communications**, v. 49, n. 4, p. 403-405, 2013. ISSN 1359-7345. Disponível em: < <http://dx.doi.org/10.1039/C2CC37329G> >.

YUAN, Z. et al. Fluorescent Gold Nanodots Based Sensor Array for Proteins Discrimination. **Analytical Chemistry**, v. 87, n. 8, p. 4253-4259, 2015/04/21 2015. ISSN 0003-2700. Disponível em: < <http://dx.doi.org/10.1021/ac5045302> >.

ZHANG, L. et al. Simple and Sensitive Fluorescent and Electrochemical Trinitrotoluene Sensors Based on Aqueous Carbon Dots. **Analytical Chemistry**, v. 87, n. 4, p. 2033-2036, 2015/02/17 2015. ISSN 0003-2700. Disponível em: < <http://dx.doi.org/10.1021/ac5043686> >.

CHAPTER 6

6 CARBON QUANTUM DOTS: A SAFE TOOL TO LEARN ABOUT QUANTUM PHENOMENON IN NANOMATERIALS

Abstract

In this chapter, a lab experiment to demonstrate quantum phenomena was developed using carbon quantum dots (CQDs), a new carbon-based fluorescent nanomaterial. Over 70 students from biotechnology, pharmacy, engineers and geology courses have successfully performed the developed lab experiment, which is divided into three blocks taking no longer than 90 minutes. By following an easy and totally safe procedure, the students were able to synthesize CQDs, as well as to visualize the quantum phenomena related to the light scattering, absorption and emission. Additionally, the observed wavelength-dependent behavior may be used to deeply study quantum confinement effects. Therefore, CQDs can be a powerful and versatile tool to learn about quantum phenomena in nanomaterials.

Keywords: Upper-Division Undergraduate. Laboratory Instruction. Hands-On Learning / Manipulatives. Synthesis. Quantum Chemistry

6.1 Background

About a decade ago, Xu et al. (Xu *et al.*, 2004) accidentally discovered a new luminescent nanoparticles (NPs) basically made from carbon: the carbon quantum dots (CQDs). Since then, the growing interest in the use of this nanomaterial has been emerging. In the last years, CQDs have attracted great attention because their excellent fluorescent and biological properties. For instance, CQDs show biocompatibility, a required characteristic for application in nanomedicine (Fowley *et al.*, 2012). The fluorescence intensity aligned to the nanoscale size makes CQDs useful for imaging (Hui *et al.*, 2014). As a consequence of these wonderful characteristics, a huge amount of publications exploring CQDs in different fields can be found in the literature (Sun *et al.*, 2006; Yang *et al.*, 2009; Lim *et al.*, 2015). However, the potential of CQDs in the educational field is still unknown given the low number of investigations (Vaz *et al.*, 2015). In this sense, it is important to highlight the optical properties (absorption/emission) of CQDs. Many papers report that the emission can be excitation-dependent (Pan, Zhang, Li, Wu, *et al.*, 2010; Sahu *et al.*, 2012; Hu *et al.*, 2015; Pan *et al.*, 2015) or independent (Dong *et al.*, 2013; Hou, J. *et al.*, 2015; Wen and Yin, 2016). As a mechanism of the luminescence of CQDs may involve surface traps and quantum effects (Yang *et al.*, 2011; Li, H. *et al.*, 2012; Li *et al.*, 2014), CQDs may serve as an excellent candidate to demonstrate quantum-related phenomenon for students, which may place these new NPs as a valuable learning tool.

Beyond CQDs, semiconductor nanocrystal quantum dots (QDs) such as CdSe can also be considered a powerful education tool (Landry *et al.*, 2014). Their size-dependent optical properties are perfect to allow students to visualize applications of quantum chemistry. However, the composition of QDs including heavy metals is a huge drawback. This may pose danger for the students. Since these types of metals are a serious source of pollution in the biosphere, which significantly affects the ecological quality of the environment (Tuzen *et al.*, 2006; Cui *et al.*, 2015). Furthermore, the effects of heavy metals on human health have been extensively investigated. It is well-known an exposure to these metals can contribute for a broad spectrum of carcinogenic, mutagenic and/or toxicological effects (Lim *et al.*, 2008; Fu and Wang, 2011; Mehta *et al.*, 2016). In this regard, Cd has been classified as a potential human carcinogen metal by U.S. Environmental Protection Agency. Moreover, it can cause kidney dysfunction or even death when at high levels concentration in the human body (Nordberg *et al.*, 2009; Arain

et al., 2014). Another negative factor is the methodology employed to synthesize the QDs. The students have to deal with dangerous chemicals, including sodium borohydride (NaBH_4), for example (Mir *et al.*, 2016). Furthermore, it is important to remember heavy metal residues are also generated after the QDs synthesis. Given the number of students who has to perform the procedure, this is a huge issue. Taken together, the use of QDs in a lab experiment to show students quantum phenomena is not totally safe. Furthermore, it is important to highlight the demand towards development of laboratory experiences for students (Hofstein and Lunetta, 2004; Elliott *et al.*, 2008). Aligned to this, the chemistry laboratory is an ideal place for learning. Since help to develop problem solving skills and make abstract ideas tangible (Galloway *et al.*, 2016).

In this regard, imagine a lab experiment developed to demonstrate quantum phenomena using inexpensive and safe chemicals. This may be possible with CQDs. Besides new, the literature already reported many methods to synthesize these luminescent NPs. It can be cited electrochemical (Hou, Y. *et al.*, 2015), combustion (Dong, Wang, *et al.*, 2012), hydrothermal (Pan, Zhang, Li e Wu, 2010), microwave (Li, L.-L. *et al.*, 2012), ultrasound (Costas-Mora *et al.*, 2014), among others. However, it is important to highlight the synthesis of CQDs through combustion. Since simple, safe and cheap chemicals, as well as relatively low temperatures can be employed to synthesize these NPs. For instance, Dong *et al.* (Dong, Shao, *et al.*, 2012) have easily synthesized CQDs via pyrolysis of citric acid at 180°C . Commercial products like milk (Wang and Zhou, 2014), gelatin (Liang *et al.*, 2013) and Nescafe[®] (Jiang *et al.*, 2014) can play as a carbon source in order to obtain CQDs. Another sources such as hair fiber (Sun *et al.*, 2013), orange (Sahu *et al.*, 2012) or banana (De and Karak, 2013) juice or even sugars (Liu *et al.*, 2011; Chen *et al.*, 2013) are also reported in the literature. As it can be seen, all “chemicals” cited here are cheap and easy to find, which further places the CQDs as a safe and potential nanomaterial to compound a lab experiment for students.

6.2 Overview

In this paper, we have performed an easy, cheap and simple lab experiment to demonstrate quantum phenomena in nanomaterials by using CQDs. The preparation method of this nanomaterial is totally safe for students. No dangerous chemicals are used. Basically, the students will perform the partial decomposition of the citric acid in order to obtain the

CQDs. The experiment took no longer than 90 min and the students were allowed to observe absorbance/emission phenomena, as well as the light scattering. The classroom experience allowed us to find out how attractive was the experiment. The work also includes a lab experiment proposed in order to explore the whole potential of the CQDs demonstration classroom, which can serve as a guide for the experiment execution.

6.3 Experimental Design

6.3.1 Chemicals and Materials required

The chemical utilized in this study was only citric acid anhydrous ($C_6H_8O_7$, 99.5%, Vetec). This chemical was used as received. In order to perform the procedure, the following materials were required:

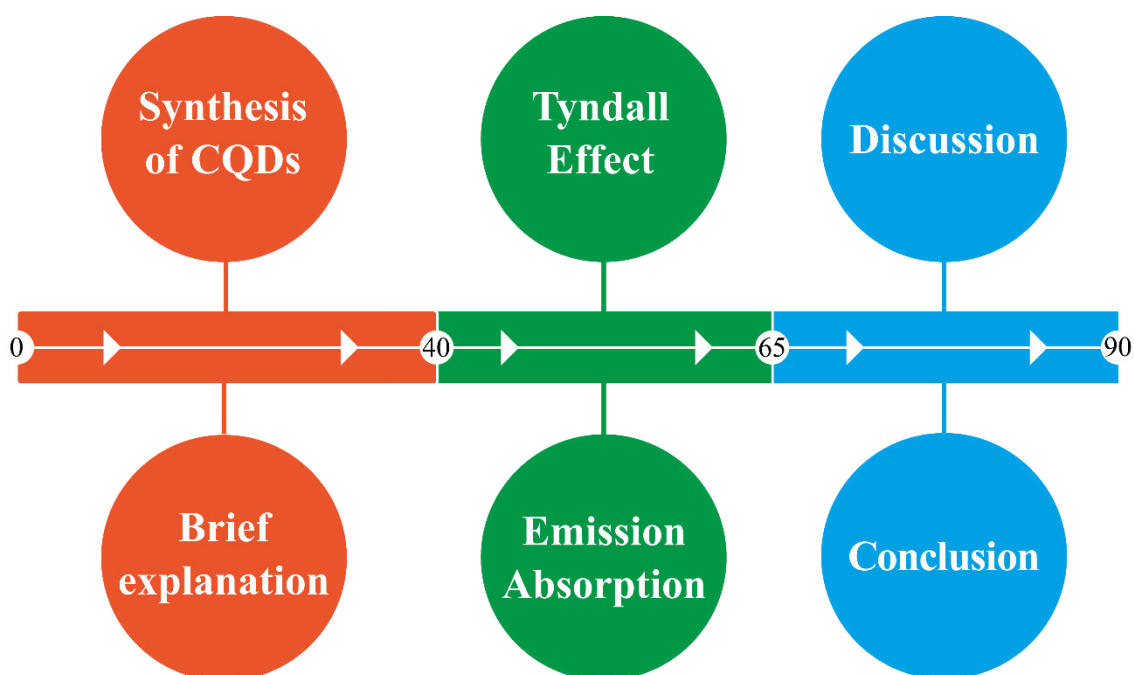
- 50 mL beaker
- muffle furnace
- 3 in 1 Laser Light Pointer
- cuvette
- UV-Vis Spectrophotometer

6.3.2 Procedure

Initially, 500 mg of citric acid anhydrous was weighted in a 50 mL beaker. Subsequently, the beaker containing the citric acid was leaded for a muffle furnace Linn Elektro Therm, which it was previously heated at 180°C. Right after put the beaker, the students set up a timer for 30 min. During this time, the instructor briefly explained some quantum phenomenon-related points (absorption, emission, fluorescence and phosphorescence) as well as the Tyndall effect. After this time, the beaker was carefully removed and allowed to reach the room temperature naturally. Then, 20 mL of distilled water was added in order to disperse the CQDs. Next, a red Laser was positioned to goes through the solution to check the presence of the CQDs using the Tyndall effect. Comparatively, the same procedure was also evaluated using only the solvent (distillated water). Afterwards, the solution was exposed to the short-wavelength ultraviolet lamp to observe the emission coming from the synthesized nanomaterials. Then, an aliquot of 1 mL of CQDs dispersion

was first diluted (1:50) and transferred to a glass cuvette (1 cm) and the absorption spectrum (300 – 600 nm) was recorded at room temperature in a Spectrophometer model UV-1800 from Shimadzu equipped with deuterium and tungsten lamp. In order to perform the experiments related to the Tyndall effect and emission, a 3 in 1 Laser light pointer (red Laser wavelength in the range 630 – 650 nm, ultraviolet light and white LED) was used. Instructor and student notes are available in the support information. A schematic picture illustrating the timeline of the lab experiment proposed is displayed in the Fig. 6.1.

Figure 6.1. Course of time for the lab experiment proposed in this work. The experiment was divided into three blocks. The first block takes 40 min, while the second and third 25 min each. This is also represented by orange, green and blue colors, respectively. The words inside the circles are the point what was done in each block.



Source: Author

6.3.3 Safety

Since it is not used dangerous chemicals, only standard laboratory safety precautions must be followed. Therefore, protective clothing, appropriate gloves and goggles were worn to carry out any part of the procedure. It is also important to highlight the biocompatibility of the CQDs vastly reported in the literature (Yang *et al.*, 2009; Li *et al.*,

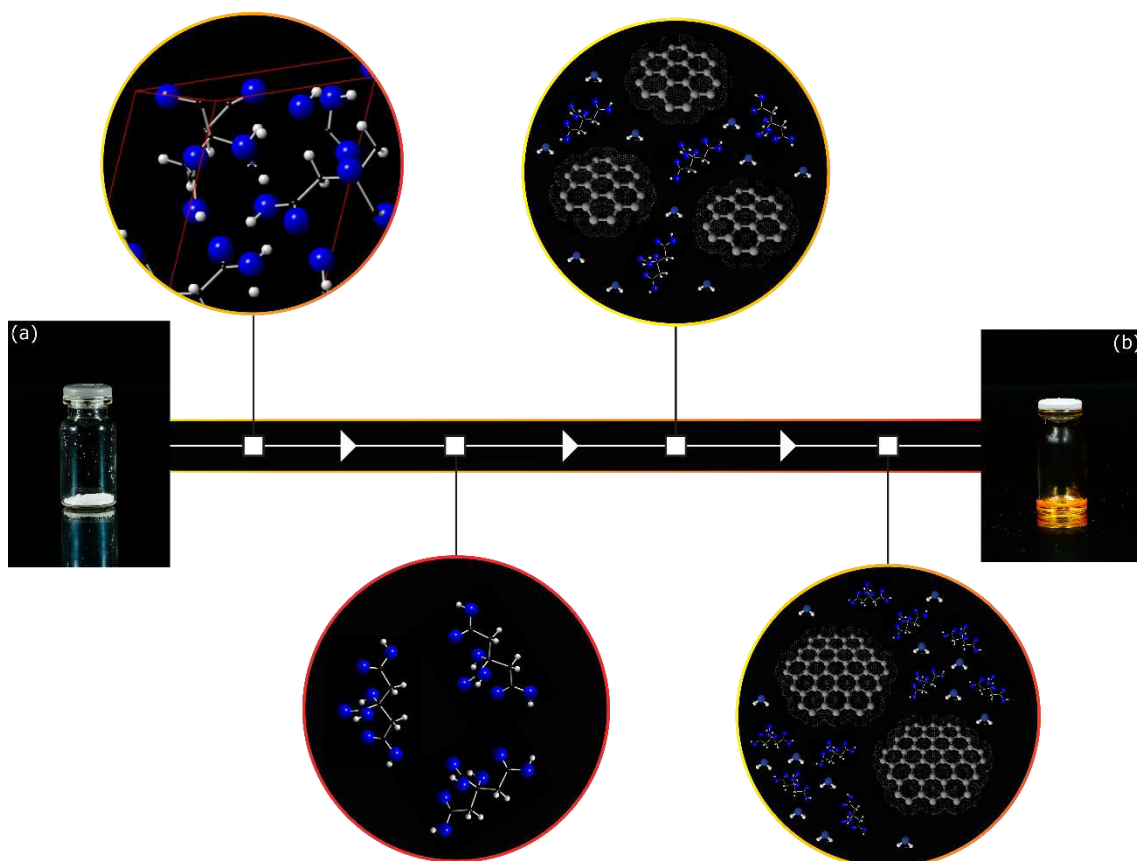
2010; Liu *et al.*, 2013). Thus, the nanomaterial used poses no danger for the students. This further makes the lab experiment proposed in this work additionally safe.

6.4 Results

6.4.1 Synthesis of CQDs

75 undergraduate students from geology, biotechnology, engineers and pharmacy have successfully obtained CQDs (Fig. 6.2) in the lab class. Fig. 6.2(a) shows the starting material (citric acid) inside a 10 mL glass vial under white light. Once this material has a crystalline structure, following the pathway to synthesize CQDs, the initial circle (first white square) presents a part of the citric acid unit cell built using crystal structure data from the Cambridge Structural Database (CSD – number 635772). The software utilized to visualize the cell unit was the CrystalMaker[®], version 2.5.1. Following the white arrows, the temperature is increased and it is expected that citric acid begins to melt at 153°C. Thus, the circle related to the second white square denotes citric acid molecules in a liquid state. As long as the temperature is raised up to 180°C an incomplete thermal decomposition proceeds. In this chemical reaction, the mechanism of the formation of the CQDs involves the condensation of citric acid molecules into sp^2 domains. This is illustrated at circle linked to the third white square. Beyond, water molecules from condensation reactions and citric acid molecules are still present. The software ChemSketch, version for students, was used to build the water molecules. Afterwards, it is expected these sp^2 nucleus formed to perform crosslinking and stacking as the reaction proceeds (Wang *et al.*, 2015). Therefore, the circle linked to the fourth white square shows large sp^2 domains, as well as water and citric acid molecules. Both entities presented at the circles related to the third and fourth white square are expected to have –OH and –COOH groups on the surface. Since the carbon source used to synthesize the CQDs was the citric acid. These chemical functions were hidden in the illustration. Finally, Fig. 6.2(b) shows the as-synthesized CQDs under white light. Clearly, an orange compound can be seen.

Fig. 6.2. Schematic illustration of the thermal decomposition process to obtain CQDs. The pictures (a) and (b) displays citric acid inside 10 mL glass vial before and after the thermal process, respectively. The gray, blue and white balls denote the elements carbon, oxygen and hydrogen, respectively.



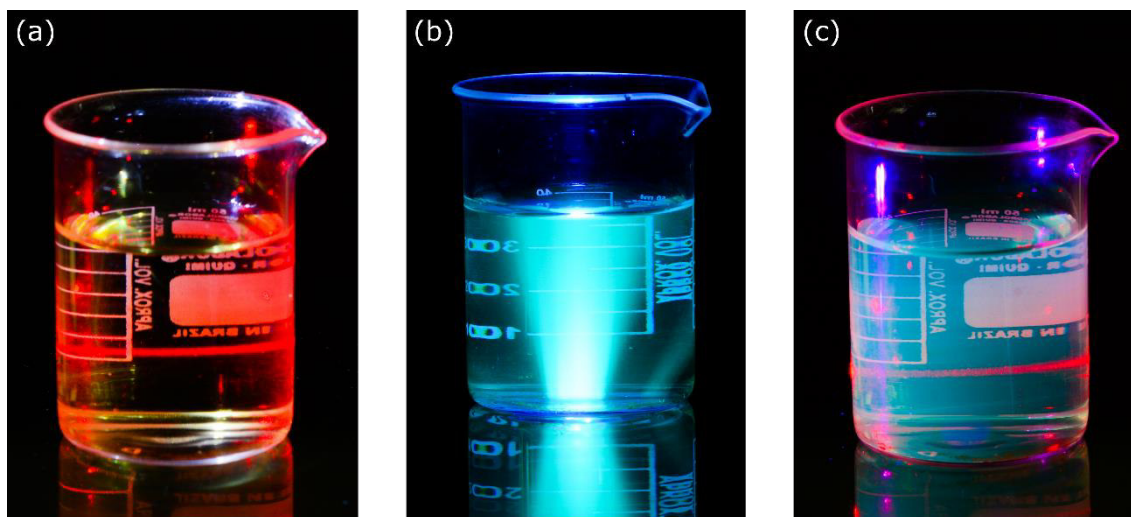
Source: Author

6.4.2 Tyndall Effect and Emission

Once the CQDs were synthesized and cooled down naturally, the next step of the lab experiment proposed in this work was to check the Tyndall effect and emission. For this purpose, the whole amount of the CQDs was first dispersed in distilled water. Then, in order to check the presence or absence of nanomaterials, the red Laser was pointed to the colloidal dispersion. The students could see the red Laser going through the liquid (Fig. 6.3(a)). Therefore, it was plausible to infer the CQDs were suspended in the liquid. Since the studied system was able to scatter the electromagnetic wave in all directions. For comparison, a beaker containing only distilled water was also unilaterally illuminated

using the red Laser. In this experiment, absence of red Laser was observed in the liquid. Therefore, the students confirmed the presence of the nanomaterials through Tyndall effect. Furthermore, Fig. 6.3(a) also displays a colloidal dispersion containing the CQDs under white light. Except by Tyndall effect, no additional quantum phenomenon can be observed in this condition.

Figure 6.3. Demonstration of quantum phenomenon related to the emission and scattering of the light. (a) Front side view of the light scattering result of the red Laser going through the dispersion colloidal containing the CQDs synthesized. (b) Spontaneous blue emission of the dispersion colloidal while is illuminated from down side using the 3 in 1 Laser light pointer. (c) Both spontaneous emission and light scattering of the red Laser. In this case, the 3 in 1 pointer was positioned at the left side of the recipient.



Source: Author

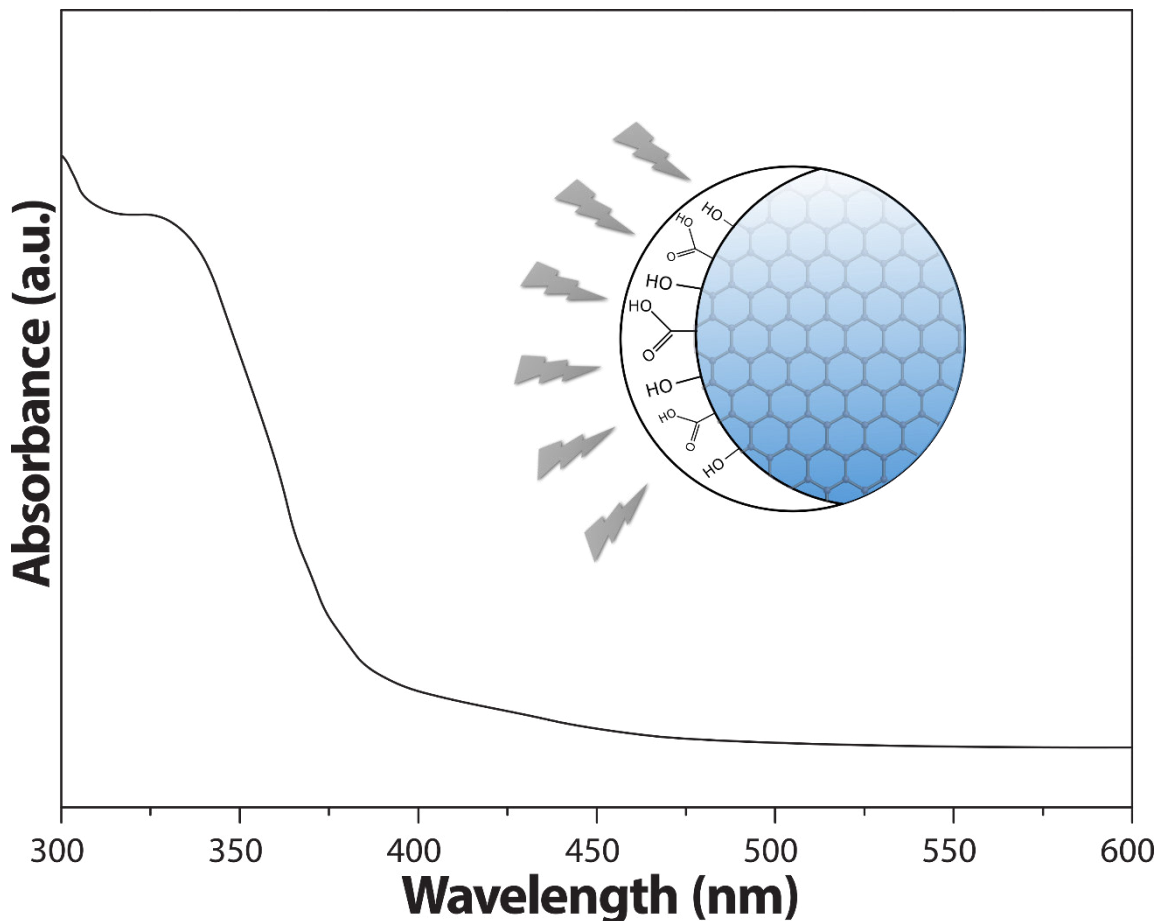
Upon demonstration of the light scattering, the ultraviolet lamp of the 3 in 1 Laser light pointer was positioned in order to go through the colloidal dispersion and a blue light could be seen by students. Spontaneous emission of radiation from a photoexcited species can be specifically considered photoluminescence (Verhoeven, 1996; Braslavsky, 2009). Therefore, the blue light coming out from the colloidal dispersion containing CQDs (Fig. 6.3(b)) may lead the students to considerate this quantum phenomenon. However, it can be further classified as fluorescence or phosphorescence. Traditionally, lifetime is used as a classification parameter to identify the types of photoluminescence from a phenomenological point of view. In this regard, a short-lived luminescence is considered

fluorescence, while a long-lived is phosphorescence. Thus, the luminescence would end as long as there is no irradiation if the substance presents fluorescence. For phosphorescence, the luminescence is still observed a little longer even after the irradiation of the substance is discontinued. Considering the photochemistry mechanism, the classification of luminescence is based on the nature of the electronically excited states. A radiative decay happening between states of the same multiplicity is called fluorescence. According to the spin selection rules, this transition is allowed. Therefore, the transition is fast and the half-lives are found to be around nanoseconds (Berezin and Achilefu, 2010). By contrast, microseconds can be achieved for phosphorescence half-lives, which occurs due to the transition is spin-forbidden. Moreover, the radiative decay typically involves triplet and singlet states. Therefore, a change in spin multiplicity is observed for phosphorescence. Fig. 6.3(c) shows both fluorescence and Tyndall effect in order to further demonstrate of the quantum phenomena.

6.4.3 Absorption Spectra

Once the emission as well as the scatter of the light was demonstrated, the next quantum phenomenon to be studied was the absorption. In this way, an aliquot of 1 mL of the colloidal dispersion containing the CQDs was placed in a glass cuvette. This “*special*” recipient was taken to the spectrophotometer, where the UV-Vis absorption spectrum was recorded. Fig. 6.4 displays the result of this measure. Clearly, there is a very broad absorption band in the range of 300 – 450 nm presenting a maximum around 325 nm. According to the previous studies (Qu *et al.*, 2013; Zhu *et al.*, 2015), this is a typical profile for CQDs where the absorption band observed around 325 nm can be attributed to the $n-\pi^*$ transition coming from C-O bonds. Usually, bands below 300 nm can be related to the $\pi-\pi^*$ transition of aromatic domains (Pan, Zhang, Li e Wu, 2010; Thema *et al.*, 2013). Given the results, the quantum phenomenon of light absorption was easily demonstrated for the students using the proposed nanomaterials.

Figure 6.4. UV-Vis absorption spectrum recorded at room temperature. The illustration inside the graph denotes the irradiation of CQDs presenting –OH and –COOH groups on the surface, as well as the sp^2 domains in the core.



Source: Author

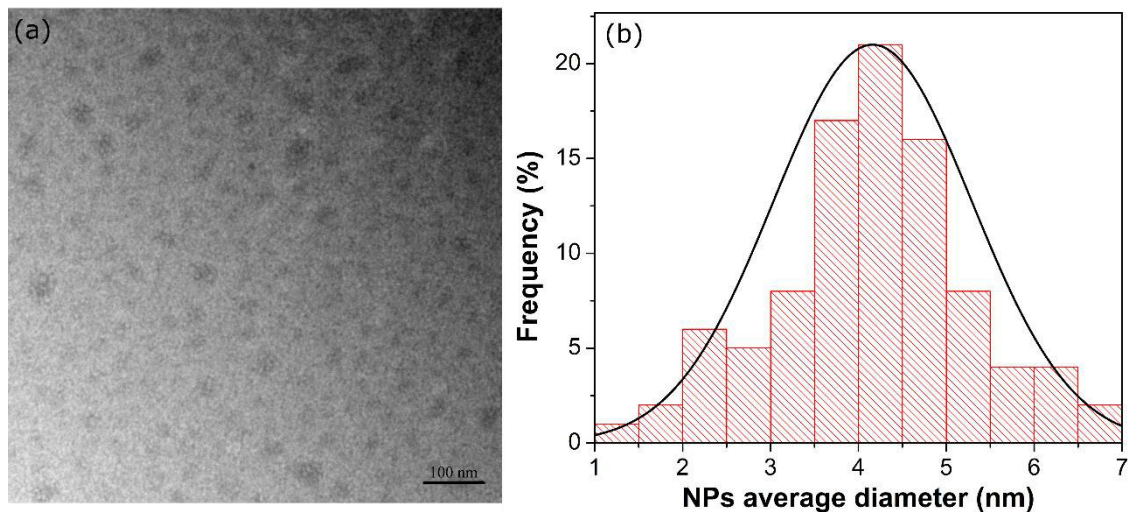
6.5 Discussion

The demonstration of quantum phenomenon is not an easy task to be performed in a simple lab experiment. The chemicals used to synthesize the nanomaterials are frequently an issue. For instance, QDs seems to be the perfect material to allow students visualize absorption/emission of the light, as well demonstrated by Landry *et al.* (Landry *et al.*, 2014). However, it is still danger for students to deal with heavy metals like Cd. For the lab experiment performed in this work, only citric acid was used as a carbon source in order to synthesize the CQDs. According to the U.S. Food and Drug Administration (Fda, 2015), this acid is classified as a food additive representing no danger for humans. Therefore, following lab standard precautions to perform the procedure described, the

students are expected to be totally safe. Taken together, the use of CQDs as a tool to demonstrate quantum phenomena for students is totally supported. Moreover, it is important to mention these nanomaterials were accidentally discovered (Xu *et al.*, 2004), and which may help the students to understand the chemistry as a building science.

Once the use of CQDs were justified, a simple lab experiment involving absorption, emission and scattering of the light was built and applied for 75 undergraduate students from different courses (biotechnology, pharmacy, engineers and geology). In this sense, the students received a support material (Student version), which can be found in the support information. Similarly, an “instructor version” including instructions is also available. The lab experiment in this work begins with the students performing an easy and simple procedure to synthesize the CQDs. During this initial step, the instructor also displayed the basic theory about nanomaterials and the quantum phenomena involved in the experiments. Taken together, this represents the first block of the experiment. The second block started with the students carrying out CQDs to observe the light scattering as well as the photoluminescence phenomena. Thus, the product after the thermolysis (see Fig. 6.2(b)) was suspended in 20 mL distilled water. As a consequence, a pale yellow liquid system was obtained. The light scattering through Tyndall effect was first demonstrated. In this sense, the red Laser of the 3 in 1 pointer was positioned to pass through the liquid in order to check the presence of the nanomaterials into the colloidal dispersion. The red Laser was observed to go through the liquid system in the lab experiment, which confirms the presence of the CQDs. In addition, the experiment can be helpful to classify this liquid system as a colloidal dispersion where the NPs size should be in the range 1 – 1000 nm (Shen *et al.*, 2016). To further support our consideration, it was also performed TEM for CQDs synthesized. TEM image displayed in the Fig. 6.5(a) reveals particles with average diameter of 4.1 ± 1.1 nm according to the size distribution graph (see Fig. 6.5(b)). This confirms both presences of the CQDs into the solution as well as the NPs size in the range of colloidal dispersion.

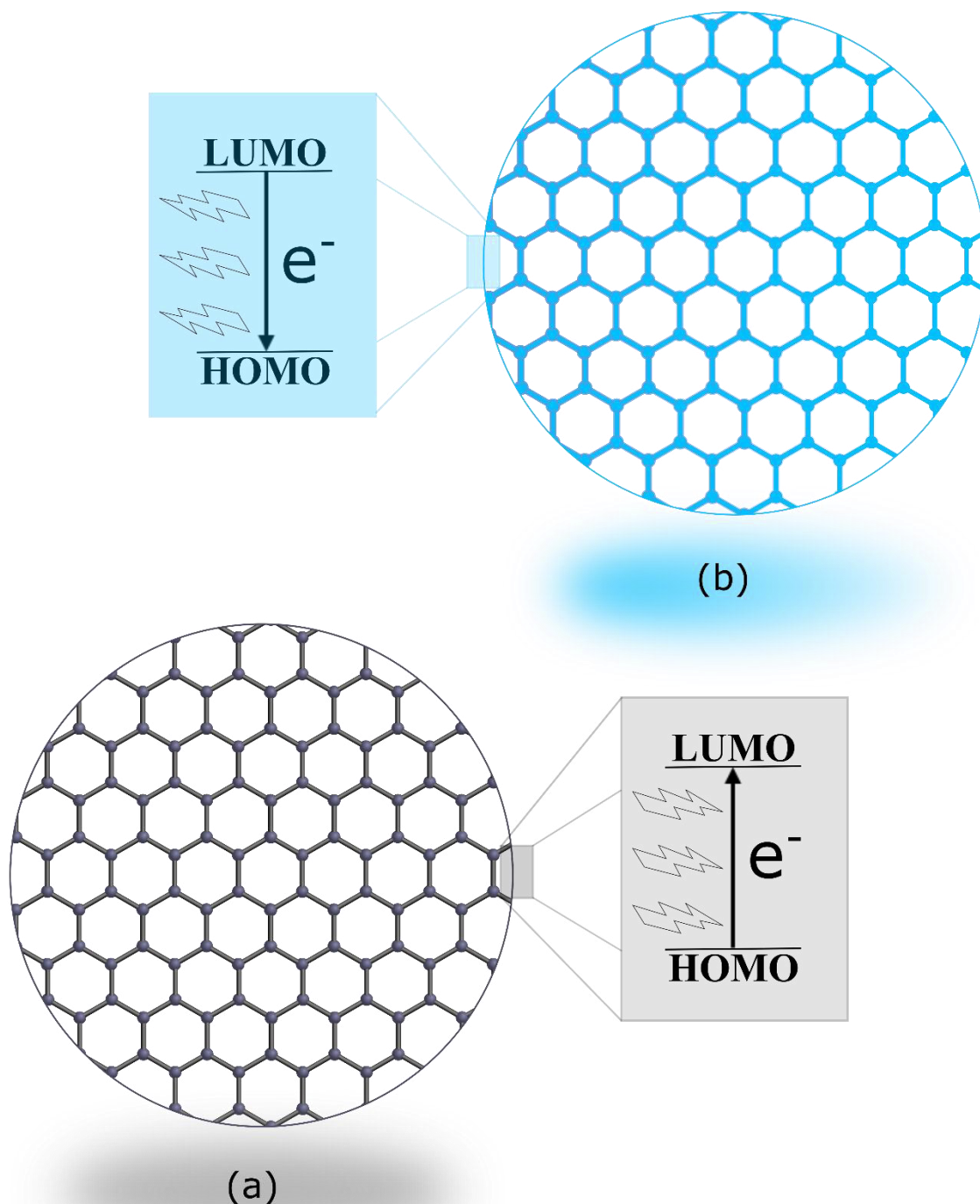
Figure 6.5. (a) TEM micrograph of the synthesized CQDs. (b) Distribution size graph built using over 90 NPs randomly selected.



Source: Author

Afterwards, the UV lamp of the 3 in 1 red Laser pointer was positioned to go through the liquid. A blue light coming out from the solution could be observed by the students, which demonstrated the emission of light from nanomaterials (Fig. 6.3(b)). As luminescent carbon-based NPs, CQDs are able to emit radiation during exposure to the short-wavelength UV lamp. Therefore, considering a basic mechanism (Fig. 6.6), it can be mentioned the electrons in CQDs were first excited from an orbital in the ground state (HOMO) to a high energy orbital (LUMO) through the absorption of the radiation. Next, the de-excitation proceeds and the electrons should return to the ground state. During this process, spontaneous emission of radiation can be observed as a way to discard the excess of the energy to stabilize the quantum system. Besides this basic chemistry, the instructor may briefly cite other photoluminescence mechanisms considering the CQDs. Since it is still an issue for researchers worldwide due to many possibilities of mechanism related to the band gap transitions between π -domains or defects on the surface of CQDs (Zhu *et al.*, 2012; Wang *et al.*, 2014; Ding *et al.*, 2016). The fact of the photoluminescence mechanism remains unclear can further lead the students to realize chemistry as a building science.

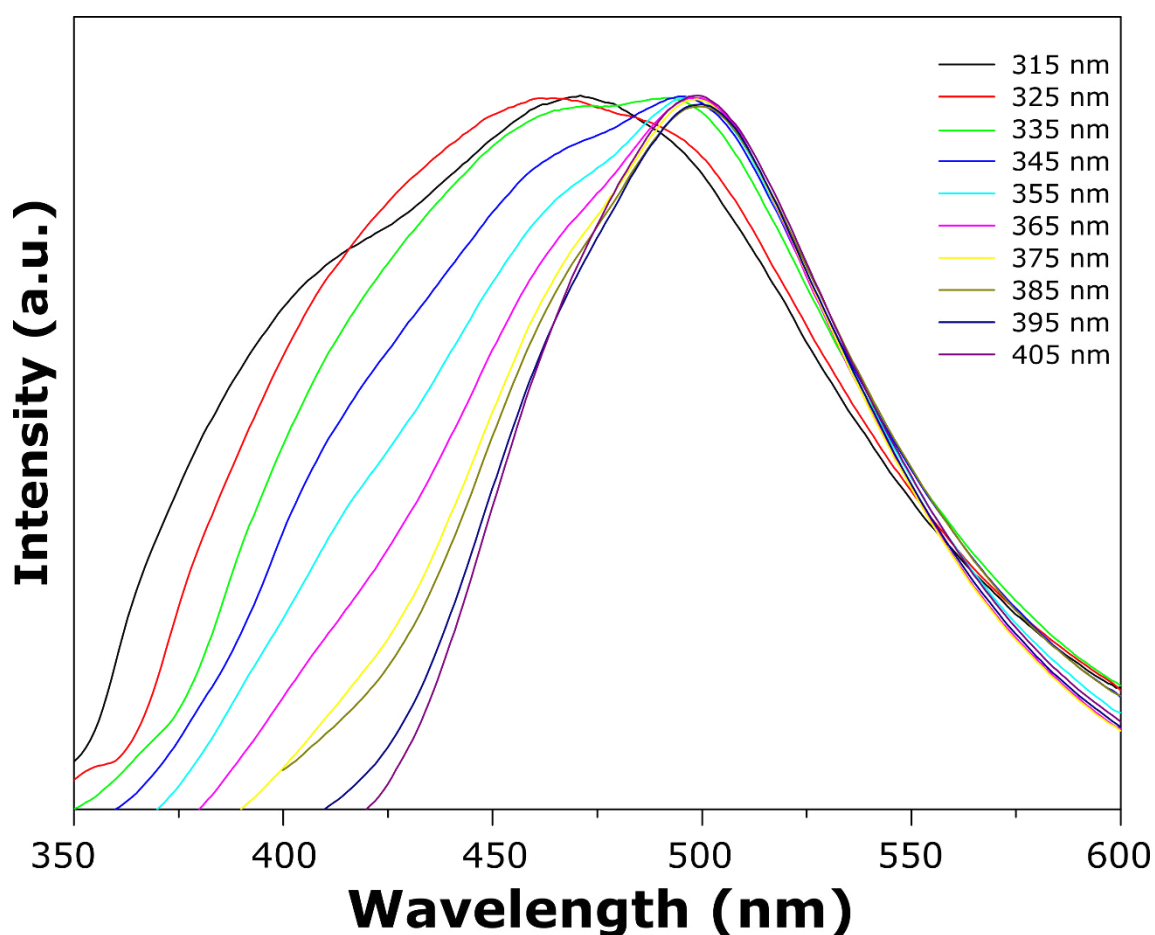
Figure 6.6. Schematic illustration representing the basic mechanism to describe photoluminescence. Once the absorption process (a) does not present spontaneous emission, the excitation of the electron (e^-) is colorless. By contrast, blue light can be seen as a result of the de-excitation process, i.e. emission process (b).



Source: Author

It is important to highlight the lab experiment performed in this work was built based on undergraduate lab with no equipment to check the fluorescence intensity. Obviously, the presence of fluorimeter in the undergraduate chemistry laboratory allows the students to visualize the emission under different excitation wavelength, for example. Fig. 6.7 shows the as-synthesized CQDs fluorescence intensity recorded using excitation wavelengths in the range of 315 – 405 nm. As it can be seen, a wavelength-dependent behavior was found. According to the literature, this may be related to the NPs size(Gan *et al.*, 2016) and/or energy traps created by surface groups(Dang *et al.*, 2016). Thus, the quantum confinement effect may be deeply studied and the students experience would be improved.

Figure 6.7. Normalized fluorescence intensity of the as-synthesized CQDs recorded at room temperature from 350 to 600 nm using different excitations wavelengths (315 – 405 nm).



Source: Author

Finally, the absorption of the light was demonstrated using a UV-Vis spectrophotometer. For this purpose, an aliquot of the diluted colloidal dispersion (1:50) was added into a glass cuvette and the UV-Vis spectrum was recorded at room temperature. A broad absorption band at 325 nm was observed and ascribed to the $n-\pi^*$ transition coming from surface groups on the CQDs(Qu *et al.*, 2013). However, the instructor may also lead the attention of the students for the high absorbance below 325 nm. It seems to have other groups in the CQDs also capable to absorb the light. Therefore, the students can realize how different groups interact to the light, even observing at one single nanoparticle.

6.6 Conclusion

A simple, robust, cheap and easy lab experiment to demonstrate quantum phenomena was performed in this work. Since the citric acid and CQDs are non-toxic materials, the instructors as well as the students only have to observe standard laboratory precautions. In this sense, 75 students from biotechnology, pharmacy, engineers and geology courses have carried out the procedure in an undergraduate chemistry laboratory with no danger. Therefore, the demonstration of the quantum phenomena including the light emission, scattering and absorption were successfully achieved. Once the procedure was completed by the students, the discussion begun and it was possible to find out how attractive was the experience. At first, the lab experiment flow seems to be sequentially strange with emission, scattering and finally absorption. However, our choice to initially perform the light emission and then, the scattering, was because the visual effect provided by these experiments. This kept the attention of the students, which it is very important to demonstrate the quantum mentioned phenomena. At the end of the lab experiment, the feedback of the students was positive. Moreover, materials including citric acid and the 3 in 1 pointer were used to compound the lab experiment in order to keep the lab experiment as cheap as possible. Therefore, even chemistry laboratories observing lack of equipment can demonstrate the quantum phenomena for their undergraduate students. However, it is important to highlight the quantum phenomenon may be deeply studied using CQDs if the chemistry laboratory has a fluorimeter, for instance. Therefore, CQDs can play as a powerful tool to demonstrate quantum phenomena.

6.7 Supporting data

6.7.1 Student Version

1. PRE-LABORATORY

- 1.1 What are nanoparticles?
- 1.2 What are the main types of electromagnetic radiation and which wavelengths associated with it?
- 1.3 How is the process of electronic transition in an atom?
- 1.4 What is absorbance?
- 1.5 What is emission? What is the difference between fluorescence and phosphorescence?
- 1.6 What are Carbon Quantum Dots? Why are they considered luminescent nanoparticles?
- 1.7 What would be a colloidal suspension?
- 1.8 What is meant by Tyndall effect?

2. OBJECTIVE

To demonstrate quantum phenomena through luminescent nanomaterials, studying their properties and applications. Identify colloidal suspensions by Tyndall effect.

3. INTRODUCTION

Materials with size in the interval of nanometers ($1 \text{ nm} = 10^{-9}$ meters) in at least one dimension have gained significant importance in the late twentieth century, leading to the emergence and consolidation of a whole field of knowledge, today recognized as "Nanoscience and Nanotechnology" ¹. Several applications can be explored, such as in the electronics area, pharmaceutical and biotechnology ^{2,3}. A new and interesting class of nanomaterials is called carbon quantum dots (CQDs). CQDs constitute a type of nanomaterial presenting size less than 10 nm and are attractive for emitting strong luminescence, which can be dependent on the excitation-wavelength ⁴. To understand the properties of CQDs, it is important to know the quantum processes of absorption and emission of light. The light can be defined as an electromagnetic radiation with wave characteristics ⁵. Thus, it is remarkable to observe a length (λ) and a wave frequency (ν) the light radiation. The wavelength can be defined as the distance between peaks or dips of a wave, while ν is associated with the number of complete λ s passing a given point per second. These greatness have an inverse proportional relationship, represented in equation (I), where c is the speed of light in vacuum ($2,99 \cdot 10^8 \text{ m.s}^{-1}$).

$$\nu \cdot \lambda = c \quad (\text{I})$$

In 1900, a physicist named Max Planck proposed that energy (E) could be released or absorbed in discrete amounts. Thus, he considered that E could be associated to the ν multiplied by a constant (h), later known as Planck's constant, with a value of $6.63 \cdot 10^{-34}$ J.s. Mathematically,

$$E = h \cdot \nu \quad (\text{II})$$

Relating the equations (I) and (II), it is possible to find the equation (III), by which it is possible to calculate E of electromagnetic radiation as a function of λ . Figure 1 shows the different types of electromagnetic radiation, as well as their distribution in the electromagnetic spectrum.

$$E = \frac{h.c}{\lambda} \quad (\text{III})$$

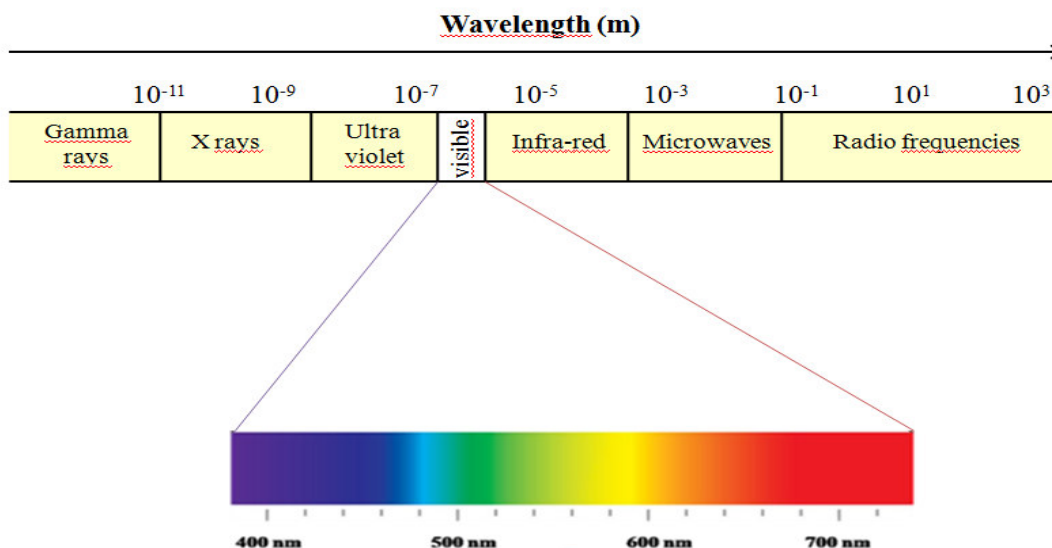


Figure 1. Wavelengths (λ) of electromagnetic radiation characteristic of various regions of the electromagnetic spectrum.

The electromagnetic irradiation can interact to the matter. For instance, the absorption process. When light is absorbed by a sample like nanoparticles, the radiant energy of the beam decreases. This can be observed calculating the transmittance (T). Mathematically, T can be calculated through equation IV.

$$T = \frac{P}{P_0} \quad (\text{IV})$$

Where P is the radiant energy and P_0 is the monochromatic energy. From the relationship presented in equation IV, it is possible to calculate the absorbance (A) of an analyte using the following equation:

$$A = -\log T = \log \frac{P_0}{P} \quad (\text{V})$$

It is well-known A is directly proportional to the concentration ($[x]$) of the chemical entities that absorb light, as well as light pathway ⁶. Further, the molar absorptivity (ϵ , $M^{-1}.cm^{-1}$) must also be considered. These parameters are associated in the Beer-Lambert Law, which is displayed in Equation VI.

$$A = \epsilon.[x].l \quad (\text{VI})$$

On the other hand, the luminescence is defined as the emission of light as a consequence of an electronic transition where the electrons must discard energy to return to the ground state level. However, it is important to mention a process of light absorption of radiation needs to occur in order to excite the electron ⁷. However, the chemical entity cannot

remain in this high level state. Since it is thermodynamically unstable. Thus, the de-excitation process is carried out discarding the absorbed energy in the light form ⁸. These processes of absorption and emission are diagrammed in Figure 2.

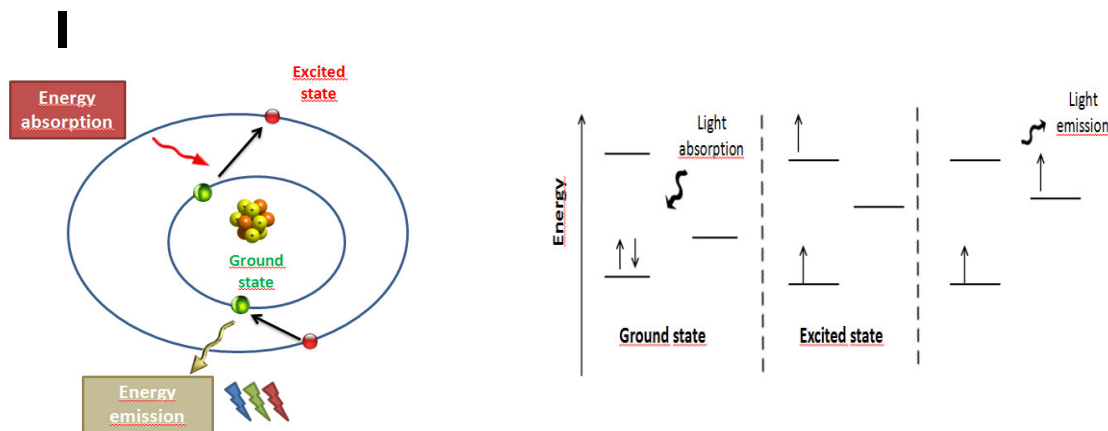


Figure 2. Schematic illustration of the electronic transition in an atom.

It is noteworthy that the emission can occur in two ways called fluorescence or phosphorescence. For fluorescence, there is a spontaneous emission of light when the chemical entity is photoexcited. This type of quantum phenomenon can be described as short-live. Since removed the irradiation source, no more emission can be seen. On the other hand, the phosphorescence is a long-live phenomenon. Emission can be still observed even after the removal of the irradiation source. Moreover, this type of quantum phenomenon implies a change of multiplicity between the ground and high state levels. According to the literature ⁹, the fluorescence emission features short lifetime of luminescence ($<10^{-5}$ s), while the phosphorescence has a lifetime of several seconds after the irradiation.

Beyond absorption and emission, some nanomaterials can also scatter the light. This is easily checked performing optical phenomenon known as Tyndall effect. Some types of nanoparticles, when disperses in water, can originate colloidal dispersion. Accordingly, the science of colloids is related to the study of systems in which at least one component of the mixture has a dimension in the range 1 to 1000 nm ¹⁰. In these dimensions, the particles in the colloid can act as a discontinuity in the medium. As a consequence of the interaction between light and particles, electromagnetic wave is found to be scattered, which is caused by change in their direction. This is well-known as Tyndall effect.

4. EXPERIMENTAL PROCEDURE

- 4.1. Weigh 500 mg of anhydrous citric acid, P.A. ($C_6H_8O_7$). Take notes about the raw product (appearance, texture etc.).
- 4.2 Transfer the citric acid for a 50 mL beaker.
- 4.3 Lead the beaker containing the citric acid for a muffle furnace pre-heated at 180 °C and wait for 30 minutes.
- 4.4 Upon 30 minutes, remove the beaker from the muffle furnace and naturally cool down. Take notes about the final product (appearance, texture etc.).
- 4.5 Disperse the final product in 20 ml of distilled water;

4.6 Using the 3 in 1 pointer, point the red Laser to goes though the liquid. Repeat the same procedure using a beaker containing only water. Take notes summarizing what happened.

4.7 Again, using the 3 in 1 pointer, turn on the UV light and point to goes through the liquid. Take notes summarizing what happened.

4.8 Dilute the colloidal dispersion in the ratio 1:50;

4.9 Take an aliquot of the dispersion containing the CQDs and add into a glass cuvette. Subsequently, lead the cuvette to the spectrophotometer to measure the absorbance;

5 RESULTS

Use the following questions to summarize the results:

5.1. What was the appearance of the final product upon the thermal process carried out in the muffle furnace?

5.2. Once the as-synthesized CQDs were dispersed, what was the color of the dispersion?

5.3. When you pointed the red Laser to goes through the dispersion could you see the laser in the liquid? The same can be seen when the red Laser was pointed to the beaker with no CQDs? If no, explain.

5.4. What happened when the dispersion containing the CQDs was illuminated by UV light of the 3 in 1 pointer? If some quantum phenomenon happened, explain.

5.5. The absorbance of the colloidal dispersion was measured. What can you say about the spectrum? Was it possible to observe the absorption process? If yes, explain how this process occurs.

6 REFERENCES

- (1) Filipponi, L; Sutherland, D. *Nanotechnologies: Principles, Applications, Implications and Hands-on Activities: a compendium for educators*. European Comission, **2013**, p.19.
- (2) Moore, M. N. Do nanoparticles present ecotoxicological risks for the health of the aquatic environment? *Environ. Int.*, **2006**, 32, 967-976.
- (3) Chen, X.; Schluesener, H.J. Nanosilver: a nanoproduct in medical application *Toxicol. Lett.*, **2008**, 176, 1-12.
- (4) Li, H.; Kang, Z.; Liu, Y.; Lee, S.-T. Carbon nanodots: synthesis, properties and applications *J. Mater. Chem.*, **2012**, 22, 24230.
- (5) Brown, T.; Lemay, H. E.; Bursten, B. E. *Chemistry: The Central Science*. 12th ed. Prentice-Hall: Boston, MA, **2012**, pp. 207-218.
- (6) Harris, D.C. *Quantitative Chemical Analysis*. 8th ed. W. H. Freeman and Company: New York, **2010**, pp. 393-397.
- (7) Yang, H. B.; Dong, Y. Q.; Wang, X.; Khoo, S. Y.; Liu, B.; Li, C. M. Graphene quantum dots-incorporated cathode buffer for improvement of inverted polymer solar cells *Sol. Energy Mater. Sol. Cells*, **2013**, 117, 214.
- (8) Köller, A.; Wilson, J. S.; Friend, R. H.; Fluorescence and Phosphorescence in organic Materials, *Adv. Eng. Mater.*, **2002**, pp. 453-459.
- (9) Skoog, D. A.; West, D. M.; Holler, F. J.; *Fundamentals of Analytical Chemistry*, 8th ed., Saunders College Pub: New York, 2004, pp.708-734.

(10) Myers, D. *Surfaces, Interfaces and colloids: Principles and Applications*. 2nd ed. John Wiley & Sons: New York, 1999, p.218.

6.7.2 Instructor Version

1 PRÉ-LABORATORY

1.1 What are nanoparticles?

Answer: Nanoparticles are particles in the range of 1 – 100 nm ($1 \text{ nm} = 1 \cdot 10^{-9} \text{ m}$) at least in one dimension.

1.2 What are the main types of electromagnetic radiation and which wavelengths associated with it?

Answer: Radio (10^3 m), Microwave (10^{-2} m), Infrared (10^{-5} m), Visible ($0.5 \cdot 10^{-6} \text{ m}$), Ultraviolet (10^{-8} m) X-ray (10^{-10} m) and Gamma ray (10^{-12} m).

1.3 How is the process of electronic transition in an atom?

Answer: Firstly, the electrons at the ground state level absorbs energy by interacting to the electromagnetic radiation and it goes to the high state level. This is called excitation process. Subsequently, the de-excitation process is carried and the electron must return to the ground state level, which it happens along with discard of energy.

1.4 What is absorbance?

Answer: Absorption of energy through interaction to the electromagnetic radiation, which cause an electronic transition from the ground state to the high state level.

1.5 What is emission? What is the difference between fluorescence and phosphorescence?

Answer: It is a de-excitation process where the electron discard energy (usually light) while returns to the ground state level. According to the International Union of Pure and Applied Chemistry (IUPAC), fluorescence is luminescence which occurs essentially only during the irradiation of a substance by electromagnetic radiation. By contrast, phosphorescence can be described as a long-lived luminescence. Since the spontaneous emission can be seen after removal the irradiation source. Moreover, luminescence also implies a change of multiplicity between the ground and high state.

1.6 What are Carbon Quantum Dots? Why are they considered luminescent nanoparticles?

Answer: CQDs are a new class of luminescent nanomaterials basically made from carbon. Once synthesized, CQDs can spontaneously emit light when exposures to the irradiation source like a short-wavelength ultraviolet lamp. However, the emission stops when the irradiation source is removed. This is characteristic of a quantum phenomenon called fluorescence, which is a type of luminescence. Given this, CQDs can be considered luminescent nanoparticles.

1.7 What would be a colloidal suspension?

Answer: Basically, it is a suspension containing particles having at least one dimension in the range of 1 – 1000 nm (colloidal range).

1.8. What is meant by Tyndall effect?

Answer: It is an effect observed when particles in the colloidal range scatter the light.

2 OBJECTIVE

Demonstrate quantum phenomena through luminescent nanomaterials, studying their properties and applications. Identify colloidal suspensions by Tyndall effect.

3 INTRODUCTION

Materials with size in the interval of nanometers ($1 \text{ nm} = 10^{-9}$ meters) in at least one dimension have gained significant importance in the late twentieth century, leading to the emergence and consolidation of a whole field of knowledge, today recognized as "Nanoscience and Nanotechnology"¹. Several applications can be explored, such as in the electronics area, pharmaceutical and biotechnology^{2,3}. A new and interesting class of nanomaterials is called carbon quantum dots (CQDs). The CQDs constitute a type of nanomaterial presenting size less than 10 nm and are attractive for emitting strong luminescence, which can be dependent on the excitation-wavelength⁴. To understand the properties of CQDs, it is important to know the quantum processes of absorption and emission of light. The light can be defined as an electromagnetic radiation with wave characteristics⁵. Thus, it is remarkable to observe a length (λ) and a wave frequency (ν) of the light radiation. λ can be defined as the distance between peaks or dips of a wave, while ν is associated with the number of complete λ s passing a given point per second. These quantities have an inverse proportional relationship, represented in equation (I), where c is the speed of light in vacuum ($3 \cdot 10^8 \text{ m.s}^{-1}$).

$$\nu \cdot \lambda = c \quad (\text{I})$$

In 1900, a physicist named Max Planck proposed that energy (E) could be released or absorbed by atoms in discrete amounts. Thus, he considered that E could be associated to the ν multiplied by a constant (h), later known as Planck's constant, with a value of $6,63 \cdot 10^{-34} \text{ J.s}$. Mathematically,

$$E = h \cdot \nu \quad (\text{II})$$

Relating the equations (I) and (II), it is possible to find the equation (III), by which it is possible to calculate E of electromagnetic radiation as a function of λ . The Figure 1 shows the different types of electromagnetic radiation, as well as their distribution in the electromagnetic spectrum.

$$E = \frac{h \cdot c}{\lambda} \quad (\text{III})$$

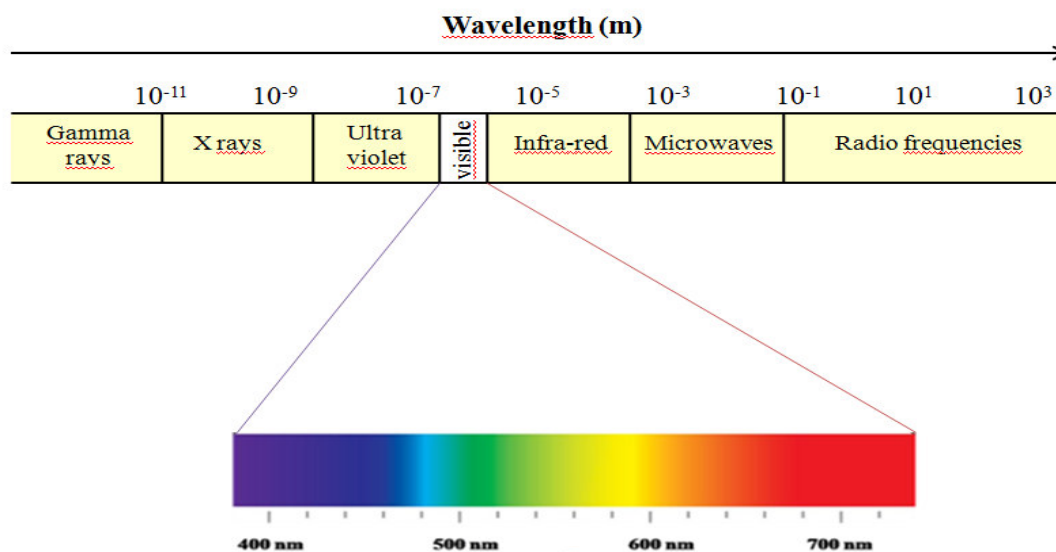


Figure 1. Wavelengths (λ) of electromagnetic radiation characteristic of various regions of the electromagnetic spectrum.

The electromagnetic irradiation can interact to the matter. For instance, the absorption process. When light is absorbed by a sample like nanoparticles, the radiant energy of the beam decreases. This can be observed calculating the transmittance (T). Mathematically, T can be calculated through equation IV.

$$T = \frac{P}{P_0} \quad (\text{IV})$$

Where P is the radiant energy and P_0 is the monochromatic energy. From the relationship presented in equation IV, it is possible to calculate the absorbance (A) of an analyte using the following equation:

$$A = -\log T = \log \frac{P_0}{P} \quad (\text{V})$$

It is well-known A is directly proportional to the concentration ($[x]$) of the chemical entities that absorb light, as well as light pathway⁶. Further, the molar absorptivity (ϵ , $\text{M}^{-1} \cdot \text{cm}^{-1}$) must also be considered. These parameters are associated in the Beer-Lambert Law, which is displayed in Equation VI.

$$A = \epsilon \cdot [x] \cdot l \quad (\text{VI})$$

On the other hand, the luminescence is defined as the emission of light as a consequence of an electronic transition where the electrons must discard energy to return to the ground state level. However, it is important to mention a process of light absorption of radiation needs to occur in order to excite the electron⁷. However, the chemical entity cannot remain in this high level state. Since it is thermodynamically unstable. Thus, the de-excitation process is carried out discarding the absorbed energy in the light form⁸. These processes of absorption and emission are diagrammed in Figure 2.

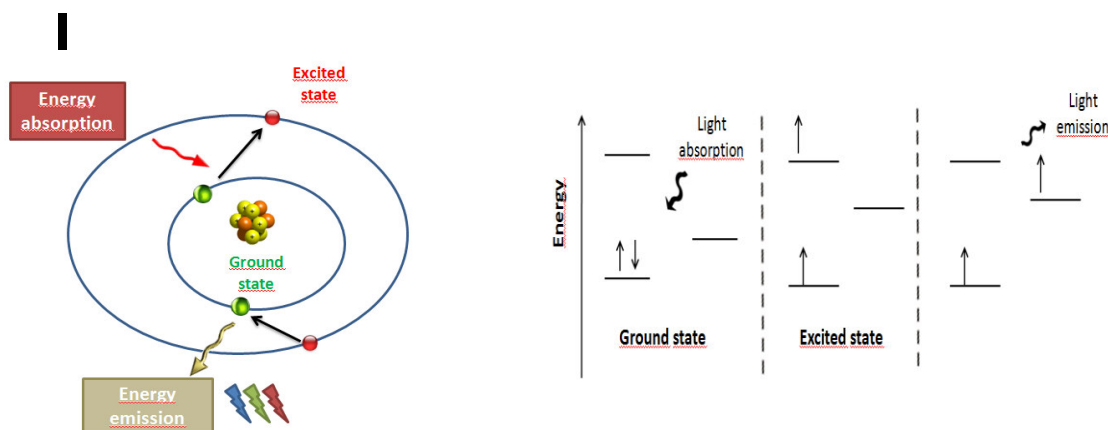


Figure 2. Schematic illustration of the electronic transition in an atom.

It is noteworthy that the emission can occur in two ways called fluorescence or phosphorescence. For fluorescence, there is a spontaneous emission of light when the chemical entity is photoexcited. This type of quantum phenomenon can be described as short-live. Since after removal of the irradiation source, no more emission can be seen. On the other hand, the phosphorescence is a long-live phenomenon. Emission can be still observed even after the removal of the irradiation source. Moreover, this type of quantum phenomenon implies a change of multiplicity between the ground and high state levels. According to the literature ⁹, the fluorescence emission features short lifetime of luminescence ($<10^{-5}$ s), while the phosphorescence has a lifetime of several seconds after the irradiation.

Beyond absorption and emission, some nanomaterials can also scatter the light. This is easily checked performing optical phenomenon known as Tyndall effect. Some types of nanoparticles, when disperses in water, can originate colloidal dispersion. Accordingly, the science of colloids is related to the study of systems in which at least one component of the mixture has a dimension in the range 1 to 1000 nm ¹⁰. In these dimensions, the particles in the colloid can act as a discontinuity in the medium. As a consequence of the interaction between light and particles, electromagnetic wave is found to be scattered, which is caused by change in their direction. This is well-known as Tyndall effect.

4 EXPERIMENTAL PROCEDURE

4.1 Weigh 500 mg of anhydrous citric acid, P.A. ($C_6H_8O_7$). Take notes about the raw product (appearance, texture, etc.).

4.2 Transfer the citric acid for a 50 mL beaker.

4.3 Lead the beaker containing the citric acid for a muffle furnace pre-heated at 180 °C and wait for 30 minutes.

Note¹: The students must be wearing temperature resistance gloves.

Note²: The students must start the timer right after place the beaker into the muffle furnace.

4.4. Upon 30 minutes, remove the beaker from the muffle furnace and naturally cool down. Take notes about the final product (appearance, texture etc.).

Note: The students must be wearing temperature resistance gloves.

4.5 Disperse the final product in 20 ml of distilled water;

Note: The students must use a volumetric flask.

4.6. Using the 3 in 1 pointer, point the red Laser to goes though the liquid. Repeat the same procedure using a beaker containing only water. Take notes summarizing what happened.

4.7 Again, using the 3 in 1 pointer, turn on the UV light and point to goes through the liquid. Take notes summarizing what happened.

Note¹: The students should realize the fluorescence emission ends once the UV lamp of the 3 in 1 red Laser pointer is turned off.

4.8. Dilute the colloidal dispersion in the ratio 1:50;

4.9 Take an aliquot of the dispersion containing the CQDs and add into a glass cuvette. Subsequently, lead the cuvette to the spectrophotometer to measure the absorbance;

5 RESULTS

Use the following questions to summarize the results:

5.1. What was the appearance of the final product upon the thermal process carried out in the muffle furnace?

Note: The final product should have a yellow/orange color upon the thermal process.

5.2. Once the as-synthesized CQDs were dispersed, what was the color of the dispersion?

Note: Yellow.

5.3. When you pointed the red Laser to goes through the dispersion could you see the laser in the liquid? The same can be seen when the red Laser was pointed to the beaker with no CQDs? If no, explain.

Note: The students should see the red Laser going through the dispersion containing the CQDs, which evidences a colloidal dispersion containing particles in the range of 1 – 1000 nm. The red Laser should not be seen in the solution with no CQDs. Since the light will not be scattered. .

5.4. What happened when the dispersion containing the CQDs was illuminated by UV light of the 3 in 1 pointer? If some quantum phenomenon happened, explain.

Note: Under UV light exposure, the colloidal dispersion should spontaneously emit a blue light. However, when the irradiation source is removed, the blue light coming out of the solution cannot be seen anymore. This is characteristics of the quantum phenomenon called fluorescence.

5.5. The absorbance of the colloidal dispersion was measured. What can you say about the graph you obtained? Was it possible to observe the absorption process? If yes, explain how this process occurs.

Note: The absorption graph should show a broad band in the range 310 - 350 nm, which is attributed to the $n-\pi^*$ transition coming from C-O bonds. This can be explained based on the excitation process where the electron absorb energy by interacting to the electromagnetic radiation and jump from the ground state to the high state level

6 REFERENCES

- (1) Filipponi, L; Sutherland, D. *Nanotechnologies: Principles, Applications, Implications and Hands-on Activities: a compendium for educators*. European Comission, **2013**, p.19.
- (2) Moore, M. N. Do nanoparticles present ecotoxicological risks for the health of the aquatic environment? *Environ. Int.*, **2006**, 32, 967-976.

- (3) Chen, X.; Schluesener, H.J. Nanosilver: a nanoparticle in medical application *Toxicol. Lett.*, **2008**, *176*, 1-12.
- (4) Li, H.; Kang, Z.; Liu, Y.; Lee, S.-T. Carbon nanodots: synthesis, properties and applications *J. Mater. Chem.*, **2012**, *22*, 24230.
- (5) Brown, T.; Lemay, H. E.; Bursten, B. E. *Chemistry: The Central Science*. 12th ed. Prentice-Hall: Boston, MA, **2012**, pp. 207-218.
- (6) Harris, D.C. *Quantitative Chemical Analysis*. 8th ed. W. H. Freeman and Company: New York, **2010**, pp. 393-397.
- (7) Yang, H. B.; Dong, Y. Q.; Wang, X.; Khoo, S. Y.; Liu, B.; Li, C. M. Graphene quantum dots-incorporated cathode buffer for improvement of inverted polymer solar cells *Sol. Energy Mater. Sol. Cells*, **2013**, *117*, 214.
- (8) Köller, A.; Wilson, J. S.; Friend, R. H.; Fluorescence and Phosphorescence in organic Materials, *Adv. Eng. Mater.*, **2002**, pp. 453-459.
- (9) Skoog, D. A.; West, D. M.; Holler, F. J.; *Fundamentals of Analytical Chemistry*, 8th ed., Saunders College Pub: New York, 2004, pp.708-734.
- (10) Myers, D. *Surfaces, Interfaces and colloids: Principles and Applications*. 2nd ed. John Wiley & Sons: New York, **1999**, p.218.

Reference

ARAIN, M. B. et al. Co-exposure of arsenic and cadmium through drinking water and tobacco smoking: Risk assessment on kidney dysfunction. **Environmental Science and Pollution Research**, v. 22, n. 1, p. 350-357, 2014. ISSN 1614-7499. Disponível em: < <http://dx.doi.org/10.1007/s11356-014-3339-0> >.

BEREZIN, M. Y.; ACHILEFU, S. Fluorescence Lifetime Measurements and Biological Imaging. **Chemical Reviews**, v. 110, n. 5, p. 2641-2684, 2010/05/12 2010. ISSN 0009-2665. Disponível em: < <http://dx.doi.org/10.1021/cr900343z> >.

BRASLAVSKY, S. E. Glossary of terms used in photochemistry, 3rd edition (IUPAC Recommendations 2006). **Pure and Applied Chemistry**, v. 79, n. 3, p. 293 - 465, 2009. ISSN 1365-3075

CHEN, B. et al. Large scale synthesis of photoluminescent carbon nanodots and their application for bioimaging. **Nanoscale**, v. 5, n. 5, p. 1967-1971, 2013. ISSN 2040-3364. Disponível em: < <http://dx.doi.org/10.1039/C2NR32675B> >.

COSTAS-MORA, I. et al. In Situ Building of a Nanoprobe Based on Fluorescent Carbon Dots for Methylmercury Detection. **Analytical Chemistry**, v. 86, n. 9, p. 4536-4543, 2014/05/06 2014. ISSN 0003-2700. Disponível em: < <http://dx.doi.org/10.1021/ac500517h> >.

CUI, L.; WU, J.; JU, H. Electrochemical sensing of heavy metal ions with inorganic, organic and bio-materials. **Biosensors and Bioelectronics**, v. 63, p. 276-286, 2015. ISSN 0956-5663. Disponível em: < <http://www.sciencedirect.com/science/article/pii/S0956566314005533> >.

DANG, H. et al. Large-Scale Ultrasonic Fabrication of White Fluorescent Carbon Dots. **Industrial & Engineering Chemistry Research**, v. 55, n. 18, p. 5335-5341, 2016/05/11 2016. ISSN 0888-5885. Disponível em: < <http://dx.doi.org/10.1021/acs.iecr.6b00894> >.

DE, B.; KARAK, N. A green and facile approach for the synthesis of water soluble fluorescent carbon dots from banana juice. **RSC Advances**, v. 3, n. 22, p. 8286-8290, 2013. Disponível em: < <http://dx.doi.org/10.1039/C3RA00088E> >.

DING, H. et al. Full-Color Light-Emitting Carbon Dots with a Surface-State-Controlled Luminescence Mechanism. **ACS Nano**, v. 10, n. 1, p. 484-491, 2016/01/26 2016. ISSN 1936-0851. Disponível em: < <http://dx.doi.org/10.1021/acsnano.5b05406> >.

DONG, Y. et al. Carbon-Based Dots Co-doped with Nitrogen and Sulfur for High Quantum Yield and Excitation-Independent Emission. **Angewandte Chemie International Edition**, v. 52, n. 30, p. 7800-7804, 2013. ISSN 1521-3773. Disponível em: < <http://dx.doi.org/10.1002/anie.201301114> >.

DONG, Y. et al. Blue luminescent graphene quantum dots and graphene oxide prepared by tuning the carbonization degree of citric acid. **Carbon**, v. 50, n. 12, p. 4738-4743,

2012. ISSN 0008-6223. Disponível em: <
<http://www.sciencedirect.com/science/article/pii/S0008622312005088>>.

DONG, Y. et al. Polyamine-Functionalized Carbon Quantum Dots as Fluorescent Probes for Selective and Sensitive Detection of Copper Ions. **Analytical Chemistry**, v. 84, n. 14, p. 6220-6224, 2012/07/17 2012. ISSN 0003-2700. Disponível em: <
<http://dx.doi.org/10.1021/ac3012126>>.

ELLIOTT, M. J.; STEWART, K. K.; LAGOWSKI, J. J. The Role of the Laboratory in Chemistry Instruction. **Journal of Chemical Education**, v. 85, n. 1, p. 145, 2008/01/01 2008. ISSN 0021-9584. Disponível em: <
<http://dx.doi.org/10.1021/ed085p145>>.

FDA. Food and Drugs. **21CFR184.1033**, Code of Federal Regulations, 2015. Disponível em: <
<https://www.accessdata.fda.gov/scripts/cdrh/cfdocs/cfcr/CFRSearch.cfm?fr=184.1033>>. Acesso em: May.

FOWLEY, C. et al. Highly luminescent biocompatible carbon quantum dots by encapsulation with an amphiphilic polymer. **Chemical Communications**, v. 48, n. 75, p. 9361-9363, 2012. ISSN 1359-7345. Disponível em: <
<http://dx.doi.org/10.1039/C2CC34962K>>.

FU, F.; WANG, Q. Removal of heavy metal ions from wastewaters: A review. **Journal of Environmental Management**, v. 92, n. 3, p. 407-418, 2011. ISSN 0301-4797. Disponível em: <
<http://www.sciencedirect.com/science/article/pii/S0301479710004147>>.

GALLOWAY, K. R.; MALAKPA, Z.; BRETZ, S. L. Investigating Affective Experiences in the Undergraduate Chemistry Laboratory: Students' Perceptions of Control and Responsibility. **Journal of Chemical Education**, v. 93, n. 2, p. 227-238, 2016/02/09 2016. ISSN 0021-9584. Disponível em: <
<http://dx.doi.org/10.1021/acs.jchemed.5b00737>>.

GAN, Z.; XU, H.; HAO, Y. Mechanism for excitation-dependent photoluminescence from graphene quantum dots and other graphene oxide derivatives: consensus, debates and challenges. **Nanoscale**, v. 8, n. 15, p. 7794-7807, 2016. ISSN 2040-3364. Disponível em: <
<http://dx.doi.org/10.1039/C6NR00605A>>.

HOFSTEIN, A.; LUNETTA, V. N. The laboratory in science education: Foundations for the twenty-first century. **Science Education**, v. 88, n. 1, p. 28-54, 2004. ISSN 1098-237X. Disponível em: <
<http://dx.doi.org/10.1002/sce.10106>>.

HOU, J. et al. Facile synthesis of carbon dots in an immiscible system with excitation-independent emission and thermally activated delayed fluorescence. **Chemical Communications**, v. 51, n. 100, p. 17768-17771, 2015. ISSN 1359-7345. Disponível em: <
<http://dx.doi.org/10.1039/C5CC08152A>>.

HOU, Y. et al. One-pot electrochemical synthesis of functionalized fluorescent carbon dots and their selective sensing for mercury ion. **Analytica Chimica Acta**, v. 866, p. 69-

- 74, 2015. ISSN 0003-2670. Disponível em: <
<http://www.sciencedirect.com/science/article/pii/S0003267015000963>>.
- HU, S. et al. Tunable Photoluminescence Across the Entire Visible Spectrum from Carbon Dots Excited by White Light. **Angewandte Chemie International Edition**, v. 54, n. 10, p. 2970-2974, 2015. ISSN 1521-3773. Disponível em: <
<http://dx.doi.org/10.1002/anie.201411004>>.
- HUI, D. et al. Nitrogen-doped carbon dots derived from polyvinyl pyrrolidone and their multicolor cell imaging. **Nanotechnology**, v. 25, n. 20, p. 205604, 2014. ISSN 0957-4484. Disponível em: <
<http://stacks.iop.org/0957-4484/25/i=20/a=205604>>.
- JIANG, C. et al. Presence of photoluminescent carbon dots in Nescafe® original instant coffee: Applications to bioimaging. **Talanta**, v. 127, p. 68-74, 2014. ISSN 0039-9140. Disponível em: <
<http://www.sciencedirect.com/science/article/pii/S0039914014000575>>.
- LANDRY, M. L. et al. Simple Syntheses of CdSe Quantum Dots. **Journal of Chemical Education**, v. 91, n. 2, p. 274-279, 2014/02/11 2014. ISSN 0021-9584. Disponível em: <
<http://dx.doi.org/10.1021/ed300568e>>.
- LI, H. et al. Carbon nanodots: synthesis, properties and applications. **Journal of Materials Chemistry**, v. 22, n. 46, p. 24230-24253, 2012. ISSN 0959-9428. Disponível em: <
<http://dx.doi.org/10.1039/C2JM34690G>>.
- LI, L.-L. et al. A Facile Microwave Avenue to Electrochemiluminescent Two-Color Graphene Quantum Dots. **Advanced Functional Materials**, v. 22, n. 14, p. 2971-2979, 2012. ISSN 1616-3028. Disponível em: <
<http://dx.doi.org/10.1002/adfm.201200166>>.
- LI, Q. et al. Photoluminescent Carbon Dots as Biocompatible Nanoprobes for Targeting Cancer Cells in Vitro. **The Journal of Physical Chemistry C**, v. 114, n. 28, p. 12062-12068, 2010/07/22 2010. ISSN 1932-7447. Disponível em: <
<http://dx.doi.org/10.1021/jp911539r>>.
- LI, X. et al. Engineering surface states of carbon dots to achieve controllable luminescence for solid-luminescent composites and sensitive Be²⁺ detection. **Scientific Reports**, v. 4, p. 4976, 2014. Disponível em: <
<http://dx.doi.org/10.1038/srep04976>>.
- LIANG, Q. et al. Easy synthesis of highly fluorescent carbon quantum dots from gelatin and their luminescent properties and applications. **Carbon**, v. 60, p. 421-428, 2013. ISSN 0008-6223. Disponível em: <
<http://www.sciencedirect.com/science/article/pii/S0008622313003515>>.
- LIM, H.-S. et al. Heavy metal contamination and health risk assessment in the vicinity of the abandoned Songcheon Au–Ag mine in Korea. **Journal of Geochemical Exploration**, v. 96, n. 2–3, p. 223-230, 2008. ISSN 0375-6742. Disponível em: <
<http://www.sciencedirect.com/science/article/pii/S0375674207000556>>. Acesso em: 2008/3//.

LIM, S. Y.; SHEN, W.; GAO, Z. Carbon quantum dots and their applications. **Chemical Society Reviews**, v. 44, n. 1, p. 362-381, 2015. ISSN 0306-0012. Disponível em: < <http://dx.doi.org/10.1039/C4CS00269E> >.

LIU, C. et al. One-step synthesis of surface passivated carbon nanodots by microwave assisted pyrolysis for enhanced multicolor photoluminescence and bioimaging. **Journal of Materials Chemistry**, v. 21, n. 35, p. 13163-13167, 2011. ISSN 0959-9428. Disponível em: < <http://dx.doi.org/10.1039/C1JM12744F> >.

LIU, Q. et al. Strong Two-Photon-Induced Fluorescence from Photostable, Biocompatible Nitrogen-Doped Graphene Quantum Dots for Cellular and Deep-Tissue Imaging. **Nano Letters**, v. 13, n. 6, p. 2436-2441, 2013/06/12 2013. ISSN 1530-6984. Disponível em: < <http://dx.doi.org/10.1021/nl400368v> >.

MEHTA, J. et al. Progress in the biosensing techniques for trace-level heavy metals. **Biotechnology Advances**, v. 34, n. 1, p. 47-60, 2016. ISSN 0734-9750. Disponível em: < <http://www.sciencedirect.com/science/article/pii/S0734975015300574> >. Acesso em: 2016/2//.

MIR, I. A. et al. Hot injection versus room temperature synthesis of CdSe quantum dots: A differential spectroscopic and bioanalyte sensing efficacy evaluation. **Colloids and Surfaces A: Physicochemical and Engineering Aspects**, v. 494, p. 162-169, 2016. ISSN 0927-7757. Disponível em: < <http://www.sciencedirect.com/science/article/pii/S0927775716300024> >.

NORDBERG, G. F. et al. Prevalence of kidney dysfunction in humans – Relationship to cadmium dose, metallothionein, immunological and metabolic factors. **Biochimie**, v. 91, n. 10, p. 1282-1285, 2009. ISSN 0300-9084. Disponível em: < <http://www.sciencedirect.com/science/article/pii/S0300908409001898> >.

PAN, D. et al. Observation of pH-, solvent-, spin-, and excitation-dependent blue photoluminescence from carbon nanoparticles. **Chemical Communications**, v. 46, n. 21, p. 3681-3683, 2010. ISSN 1359-7345. Disponível em: < <http://dx.doi.org/10.1039/C000114G> >.

PAN, D. et al. Hydrothermal Route for Cutting Graphene Sheets into Blue-Luminescent Graphene Quantum Dots. **Advanced Materials**, v. 22, n. 6, p. 734-738, 2010. ISSN 1521-4095. Disponível em: < <http://dx.doi.org/10.1002/adma.200902825> >.

PAN, L. et al. Truly Fluorescent Excitation-Dependent Carbon Dots and Their Applications in Multicolor Cellular Imaging and Multidimensional Sensing. **Advanced Materials**, v. 27, n. 47, p. 7782-7787, 2015. ISSN 1521-4095. Disponível em: < <http://dx.doi.org/10.1002/adma.201503821> >.

QU, D. et al. Highly luminescent S, N co-doped graphene quantum dots with broad visible absorption bands for visible light photocatalysts. **Nanoscale**, v. 5, n. 24, p. 12272-12277, 2013. ISSN 2040-3364. Disponível em: < <http://dx.doi.org/10.1039/C3NR04402E> >.

SAHU, S. et al. Simple one-step synthesis of highly luminescent carbon dots from orange juice: application as excellent bio-imaging agents. **Chemical Communications**, v. 48, n. 70, p. 8835-8837, 2012. ISSN 1359-7345. Disponível em: < <http://dx.doi.org/10.1039/C2CC33796G> >.

SHEN, J. et al. Effect of humic substances aggregation on the determination of fluoride in water using an ion selective electrode. **Chemosphere**, v. 159, p. 66-71, 2016. ISSN 0045-6535. Disponível em: < <http://www.sciencedirect.com/science/article/pii/S0045653516307160> >.

SUN, D. et al. Hair fiber as a precursor for synthesizing of sulfur- and nitrogen-codoped carbon dots with tunable luminescence properties. **Carbon**, v. 64, p. 424-434, 2013. ISSN 0008-6223. Disponível em: < <http://www.sciencedirect.com/science/article/pii/S000862231300729X> >.

SUN, Y.-P. et al. Quantum-Sized Carbon Dots for Bright and Colorful Photoluminescence. **Journal of the American Chemical Society**, v. 128, n. 24, p. 7756-7757, 2006/06/01 2006. ISSN 0002-7863. Disponível em: < <http://dx.doi.org/10.1021/ja062677d> >.

THEMA, F. T. et al. Synthesis and Characterization of Graphene Thin Films by Chemical Reduction of Exfoliated and Intercalated Graphite Oxide. **Journal of Chemistry**, v. 2013, p. 6, 2013. Disponível em: < <http://dx.doi.org/10.1155/2013/150536> >.

TUZEN, M.; MELEK, E.; SOYLAK, M. Celtek clay as sorbent for separation-preconcentration of metal ions from environmental samples. **Journal of Hazardous Materials**, v. 136, n. 3, p. 597-603, 2006. ISSN 0304-3894. Disponível em: < <http://www.sciencedirect.com/science/article/pii/S0304389405008605> >.

VAZ, R. et al. Preparation of carbon dots and their optical characterization: an experiment of nanoscience for undergraduate course. **Química Nova**, v. 38, n. 10, p. 1366-1373, 2015. Disponível em: < <http://dx.doi.org/10.5935/0100-4042.20150150> >.

VERHOEVEN, J. W. Glossary of terms used in photochemistry (IUPAC Recommendations 1996). **Pure and Applied Chemistry**, v. 68, n. 12, p. 2223 - 2286, 1996. ISSN 1365-3075.

WANG, L.; ZHOU, H. S. Green Synthesis of Luminescent Nitrogen-Doped Carbon Dots from Milk and Its Imaging Application. **Analytical Chemistry**, v. 86, n. 18, p. 8902-8905, 2014/09/16 2014. ISSN 0003-2700. Disponível em: < <http://dx.doi.org/10.1021/ac502646x> >.

WANG, L. et al. Common Origin of Green Luminescence in Carbon Nanodots and Graphene Quantum Dots. **ACS Nano**, v. 8, n. 3, p. 2541-2547, 2014/03/25 2014. ISSN 1936-0851. Disponível em: < <http://dx.doi.org/10.1021/nn500368m> >.

WANG, S. et al. Structural evolution of graphene quantum dots during thermal decomposition of citric acid and the corresponding photoluminescence. **Carbon**, v. 82,

p. 304-313, 2015. ISSN 0008-6223. Disponível em: <
<http://www.sciencedirect.com/science/article/pii/S0008622314010537>>.

WEN, Z.-H.; YIN, X.-B. Excitation-independent carbon dots, from photoluminescence mechanism to single-color application. **RSC Advances**, v. 6, n. 33, p. 27829-27835, 2016. Disponível em: <<http://dx.doi.org/10.1039/C5RA27172J>>.

XU, X. et al. Electrophoretic Analysis and Purification of Fluorescent Single-Walled Carbon Nanotube Fragments. **Journal of the American Chemical Society**, v. 126, n. 40, p. 12736-12737, 2004/10/01 2004. ISSN 0002-7863. Disponível em: <
<http://dx.doi.org/10.1021/ja040082h>>.

YANG, S.-T. et al. Carbon Dots for Optical Imaging in Vivo. **Journal of the American Chemical Society**, v. 131, n. 32, p. 11308-11309, 2009/08/19 2009. ISSN 0002-7863. Disponível em: <<http://dx.doi.org/10.1021/ja904843x>>.

YANG, Z.-C. et al. Intrinsically fluorescent carbon dots with tunable emission derived from hydrothermal treatment of glucose in the presence of monopotassium phosphate. **Chemical Communications**, v. 47, n. 42, p. 11615-11617, 2011. ISSN 1359-7345. Disponível em: <<http://dx.doi.org/10.1039/C1CC14860E>>.

ZHU, S. et al. The photoluminescence mechanism in carbon dots (graphene quantum dots, carbon nanodots, and polymer dots): current state and future perspective. **Nano Research**, v. 8, n. 2, p. 355-381, 2015. ISSN 1998-0000. Disponível em: <
<http://dx.doi.org/10.1007/s12274-014-0644-3>>.

ZHU, S. et al. Surface Chemistry Routes to Modulate the Photoluminescence of Graphene Quantum Dots: From Fluorescence Mechanism to Up-Conversion Bioimaging Applications. **Advanced Functional Materials**, v. 22, n. 22, p. 4732-4740, 2012. ISSN 1616-3028. Disponível em: <<http://dx.doi.org/10.1002/adfm.201201499>>.

CHAPTER 7

7 GENERAL CONCLUSIONS

The magnetic nanoparticles with chemical formula $\text{Mn}_{0.5}\text{Zn}_{0.5}\text{Fe}_2\text{O}_4$ (MnZn) and $\text{Ni}_{0.5}\text{Zn}_{0.5}\text{Fe}_2\text{O}_4$ (NiZn) were successfully synthesized by a hydrothermal method. Their structural and magnetic properties were fully investigated through PXRD, FT-IR, Mössbauer spectroscopy, VSM and TEM. The variation of experimental conditions (solvent, base concentration and hydrothermal reaction time) has been proved to have large effect under the characteristics of the studied MNPs. By changing the solvent composition, it was possible to observe the decrease of the MNPs size and saturation magnetization (M_s). For example, the crystallite size decreased from 12.1 to 3.1 nm when ethylene glycol was used as a solvent. The increase of the NaOH concentration caused bigger crystallite size, as well as higher surface disorder, which was confirmed by assuming a core-shell model for MNPs. The hydrothermal reaction time was also studied. No relevant effect was observed on crystallite size, but the morphology was found to change from truncated hexagonal to quasi-sphere structures along increase of the reaction time. As expected, the magnetic properties changed along different features of the synthesized MNPs. However, the source of the change seems to be distinct for each set of samples synthesized under different experimental conditions. The increase of crystallite size along the increase of NaOH concentration had a predominant effect on T_b . This was confirmed for MNP3 – 4. On the other hand, the surface effects played an essential role for MNP5 – 7, which were synthesized by changing the hydrothermal reaction time.

~1.5 nm NH_2 -rich CQDs were successfully synthesized in this work. Structural, morphological and surface properties of the CQDs.BPEI were fully investigated through TEM, XPS and FTIR. From XPS and FTIR measurements, it was possible to confirm the coating performed using a NH_2 -rich polymer like BPEI. The optical properties were also investigated by absorbance and fluorescence measurements. Clearly, the CQDs.BPEI work was found to be excitation-independent. Since the emission bands were no longer shifted by changing the excitation wavelength. Further, no photobleaching was observed during period of 60 min. Upon characterization, it was demonstrated the great potential of the CQDs.BPEI for detection of the proteins. In this regard, eight different proteins including metallic and non-metallic kinds were tested. The synthesized CQDs were found to be an excellent protein-responsive probe. Moreover, the fluorescent signal obtained for each protein was in a different level. Given this, a fast “nose”-

based approach was developed using materials as cheap as Cu^{2+} , EDTA and CQDs.BPEI. Both one or two-plate sensing methodology were able to successfully identify proteins, but the one-plate strategy was found to keep the level of identification being faster than the two-plate method. Therefore, the protein identification was performed in high saline environmental (PBS) using the one-plate method and six different proteins were correctly classified. A random of unknown 42 samples was performed. In this case, 90% accuracy (37 out of 42) was achieved. In order to further check the potential of the one-plate method, human serum sensing at 0.1, 0.5 and 1% (V/V) was performed. PhosA was correctly identified for both known and unknown set of samples affording 100% accuracy, which place the one-plate methodology as a potential prognostic indicator for prostate cancer and Gaucher's disease. Therefore, this methodology combined to the magnetic properties of the MNPs synthesized in this work may give rise a full methodology able to identify proteins in a dirty mixture. Since the MNPs can adsorb proteins on the surface and, subsequently, the one-plate methodology can perform the identification.

Finally, upon the utilization of CQDs for protein detection and identification, the potential of this new carbon-based nanoparticle was checked in the educational field. In this sense, a safe laboratory experiment to demonstrate quantum phenomena was developed and successfully applied for 75 undergraduate students from geology, biotechnology, engineers and pharmacy course. As a consequence, the demonstration of the light scattering, absorption and emission was successfully achieved. Once again, cheap materials were used. For instance, citric acid and a 3 in 1 Laser light pointer was utilized in the experimental procedure. Therefore, even chemistry laboratories observing lack of equipment can demonstrate the quantum phenomena for their undergraduate students. This evidences the excellent potential of the CQDs as a powerful tool in the education field to demonstrate quantum phenomena.